



UNIVERSITÀ
DEGLI STUDI
FIRENZE

**DOTTORATO DI RICERCA IN
ATOMIC AND MOLECULAR PHOTONICS**

(International Doctorate)

CICLO XXXV

COORDINATORE Prof. Diederik Wiesma

**CHIP-SCALE QUANTUM LIGHT
INFRARED EMITTERS**

Settore scientifico-disciplinare FIS/03

Dottoranda

Dott. Tecla Gabrielli

Tecla Gabrielli

Tutore

Dott. Alessandro Zavatta

Alessandro Zavatta

Coordinatore

Prof. Diederik Wiesma

Diederik Wiesma

1 Novembre 2019 – 31 Gennaio 2023

FOR THE SISTERS & THE SISTAS & THE SISTAHS
& THE SISTREN & THE WOMEN & THE WOMXN & THE WIMMIN
& THE WOMYN & OUR BRETHREN & OUR BREDRIN
& OUR BROTHERS & OUR BRUVS & OUR MEN & OUR MANDEM
& THE LGBTQIA+ MEMBERS OF THE HUMAN FAMILY
Bernardine Evaristo, "Girl, Woman, Other"



CNR-INO
ISTITUTO NAZIONALE DI OTTICA
CONSIGLIO NAZIONALE DELLE RICERCHE



Preface & Abstract

January 31, 2023

The *mid-infrared* (MIR) part of the electromagnetic spectrum is known as the molecular fingerprint region due to the abundance of fundamental rovibrational molecular absorption lines falling therein. Consequently, the MIR region has been deeply investigated for many molecular spectroscopy and sensing applications. One of the most recent scientific and technological breakthroughs in these fields is the development and demonstration of *quantum cascade lasers* (QCLs), both as MIR compact laser sources (1994, Bell Labs) and, more recently, as direct *frequency-comb* emitters (2012, ETH Zurich). Despite the importance of the MIR spectral region and the large number of applications, lasers, materials, and related technologies are still under development and far less available if compared to the visible and near-infrared spectral regions. This gap is even more dramatic if we move to the quantum world, as the MIR region nowadays lacks both non-classical light sources and suitable detectors for their investigation. This thesis, entitled *Chip-scale quantum light infrared emitters*, represents one of the first scientific attempts to push the MIR research towards *quantum technologies*. This manuscript provides a collection of experiments to which I contributed directly during my Ph.D. research activity. They all aimed at generating infrared *non-classical state of light* and developing suitable *detection systems*, paving the way to a very high-level long-term goal: the realization of the very first chip-scale quantum source based on quantum cascade laser frequency combs.

For the past three years (Nov. 2019–Jan. 2023), I have been enrolled in the three-year Ph.D. program *International Doctorate in Atomic and Molecular Photonics* organized by the European Laboratory for Non-Linear Spectroscopy (LENS) of the University of Florence (Florence, Italy). I worked in the research group (part of the Italian National Institute of Optics, CNR-INO) led by Dr Paolo De Natale under the supervision of my Ph.D. tutor, Dr Alessandro Zavatta. During this experience, I had the amazing and extremely fascinating opportunity to learn and combine some of the high-level Dr De Natale's group expertise in the fields of MIR frequency metrology, spectroscopy, and sensing, together with the high-level quantum technology skills of my tutor, Dr Zavatta. Additionally, with both of them, I had the privilege to collaborate on a large European project, the Qombs Project (<https://www.qombs-project.eu>), funded by the European Quantum Flagship. As stated in its title, the project aimed at the "Quantum simulation and entanglement engineering in quantum cascade laser frequency combs". Within the project, I had the chance to collaborate in an international partnership with researchers spread all across Europe. Furthermore, the Ph.D. international course I attended provides a period abroad. During the third year, thanks to a preexisting collaboration of my tutor with Dr Virginia D'Auria, I had the chance to spend around five months in her team at the *Institut de Physique de Nice* (INPHYNI) in Nice (France). Her group's activity is mainly focused on studying, realizing, and manipulating continuous-variable quantum states of light at telecom wavelengths. Thanks to this experience, I learned to deal with fiber-based Schrödinger's cat states and, more generally, I acquired the know-how to work with non-classical squeezed light and utilize it as a resource. Finally, I believe that this experience will allow me in the near future to apply the gained knowledge in the MIR,

creating new quantum tools in this still limited-quantum-explored region, opening the door to new joyful and fruitful collaborations between the two labs.

I am incredibly grateful to all the mentioned research groups for everything I learned during these highly stimulating years. I developed many skills related to a wide range of research topics, including frequency-comb emission control, intensity-correlation measurements, testing the properties of quantum cascade lasers, and manipulating squeezed and non-classical states of light at telecom wavelengths. What an exciting, amazing, challenging, and highly advanced scientific journey it has been!

Tecla Gabrielli

Preface & Abstract	5
Introduction	11
I.1 The mid infrared: a region rich of applications	11
I.2 QCLs: high-performance MIR laser sources	12
I.3 QCL-combs: from direct frequency comb emitters to appealing quantum resources	13
I.4 Thesis overview	16
1 Quantum optics tools	19
1.1 Free electromagnetic field quantization	20
1.2 Quantum states of light	23
1.2.1 Fock's states	23
1.2.2 Coherent state	24
1.2.3 Squeezed light	25
1.3 Linear interaction: the beam splitter	29
1.4 Non-linear phenomena	31
1.4.1 Non-linear polarization	31
1.4.2 Second-order non-linear phenomena	33
1.4.3 Third-order non-linear phenomena	35
1.4.4 Squeezing generation via non-linear phenomena	36
1.5 Electric field: from discrete to continuous modes	39
1.5.1 Narrow-bandwidth approximation	40
1.5.2 Distributed modes	42
1.6 Measurements techniques	42
1.6.1 Photodetectors	42
1.6.2 Balanced homodyne detection	44
1.7 Wigner fuction	46
2 Quantum Cascade Lasers	49
2.1 QCL working principle	49
2.2 QCL structure	51

2.2.1	The cascade process	54
2.3	QCL spectral features	54
2.3.1	Emitted wavelength	54
2.3.2	Linewidth	54
2.4	Comb emission	56
3	Shot-noise limited mid-infrared balanced homodyne detector	59
3.1	Introduction to MIR balanced detection	59
3.2	Working principle	61
3.2.1	BHD characterization	63
3.2.2	LO characterization	64
3.3	Experimental setup	64
3.3.1	Loss budget for BHD characterization	66
3.3.2	Loss budget for LO characterization	67
3.4	Results and discussion	67
3.5	Summary and remarks	72
4	Intensity correlation measurements in quantum cascade laser frequency combs	73
4.1	QCL emission: harmonic comb, dense comb and bilobed emission	74
4.2	Correlation measurements in harmonic combs	77
4.2.1	Motivations	77
4.2.2	Measurement technique	79
4.2.3	Results and discussion	83
4.2.4	Summary and final remarks	91
4.3	Correlation in bilobed emission	92
4.3.1	Device characterization	92
4.3.2	Results and discussion	97
4.3.3	Summary and final remarks	98
4.4	Conclusion and perspectives	99
5	Generation and detection of non-classical light	101
5.1	Introduction	102
5.2	Theoretical description	102
5.2.1	Squeezing generation	103
5.2.2	Kitten state preparation	103
5.2.3	Detection and quantum state reconstruction	105
5.3	Experimental setup	106
5.3.1	Heralding process	108
5.4	Results and discussion	112
5.5	Conclusion and perspectives	115
	Conclusion	117

Appendix	121
A.1 BHD with losses	121
A.2 QCL intermodal beat note measurement	123
Abbreviations	125
Bibliography	127
List of Figures	145
Curriculum vitae & Publications list	147

I.1 The mid infrared: a region rich of applications

The MIR part of the electromagnetic spectrum, spanning the range from $3\mu\text{m}$ to $50\mu\text{m}$ [1], is known as *the molecular fingerprint region* due to the abundance of fundamental rovibrational transitions of light molecules (e.g. CO_2 , N_2O , CH_4 , H_2O). These molecules have a high atmospheric and astrophysical interest, but they are also fundamental for biological processes and environmental control [2, 3]. An example of the molecular rovibrational transitions findable in the MIR is shown in Fig. I.1. Here, the absorption coefficients of air gas mixture (see the caption) are plotted in the 4–8- μm window using the HITRAN database [4]. As a natural consequence of such abundance of strong molecular bands, this spectral region has been widely used for spectroscopic and trace-gas detection applications, as food analysis [5], environment monitoring [6, 7], medical diagnostics [8], and dating biological specimens [9, 10]. Moreover, also different applications as IR-radars [11, 12] and free-space communication systems [13, 14] have started looking with interest at the MIR region [2]. The main reason lies in the presence of atmospheric transparency windows suitable for free-space communications e.g. around $4\mu\text{m}$ and around $8\mu\text{m}$ (Fig. I.1). With respect to near infrared (NIR) ($0.78 - 3\mu\text{m}$ [1]) and visible ($0.38 - 0.78\mu\text{m}$ [1]), the MIR light is less affected by particle scattering and scintillation. Moreover, the black-body radiation of the sun (peaked at 500 nm) is well-suppressed for wavelengths longer than $3\mu\text{m}$ [14–16]. In addition, MIR communication channels are more robust to losses in case of adverse weather conditions (fog, haze, clouds) than those at shorter wavelengths [14, 15, 17]. This feature is also relevant for ground-to-satellite communications [16, 18, 19].

Despite the importance of the MIR for all the above-mentioned technological applications, this spectral region lacks most of the advanced technology available, instead, both in the NIR and visible regions. These are, indeed, the spectral regions where historically the laser-correlated research has been developed and conducted [20, 21], and where high-efficiency detectors, high-power sources [3] and technological infrastructures (such as the worldwide NIR fibre-based communication links [22, 23]) have been developed. For several decades, non-linear optics has been the key tool to dab the lack of MIR mature laser technologies, providing for coherent sources with interesting

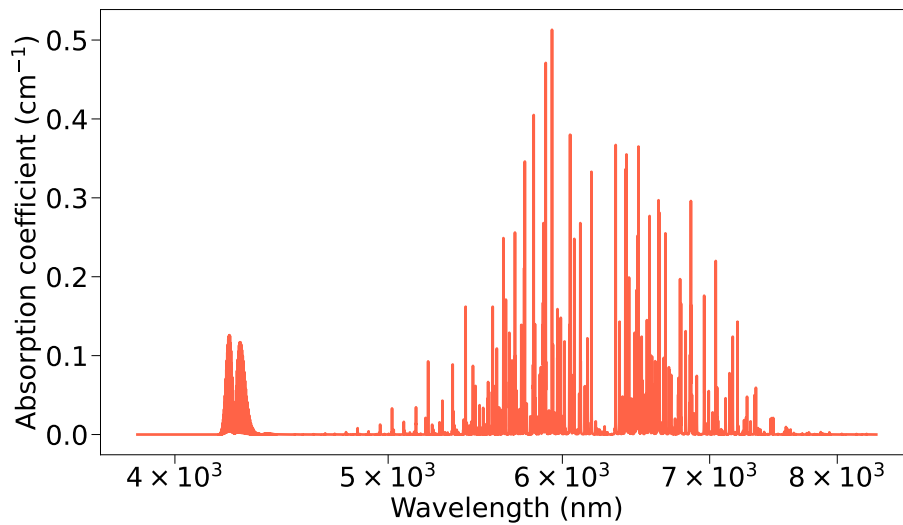


Figure I.1: Absorption coefficients of a standard air gas mixture in the MIR region from 4 μm to 8 μm , adapted by the data obtained with the HITRAN database's [4] *USA model, mean latitude, summer, $H=0$* and the following setting: $T=296\text{ K}$, $P=1\text{ atm}$, $\text{step}=0.0086\text{ cm}^{-1}$, Profile = Lorentz, Wing = 200HW, Scat = $1 \times 10^{-28}\text{ cm/mol}$. The gas mixtures of this model is by default: H_2O (1.860000%), CO_2 (0.033000%), O_3 (0.000003%), N_2O (0.000032 %), CO (0.000015%), CH_4 (0.000170%), O_2 (20.900001%), N_2 (77.206000%).

features as a wide tunability and spectral purity. As a matter of fact, via non-linear processes like Different Frequency Generation (DFG), it has been possible to develop coherent sources suitable for high-resolution MIR spectroscopy setups, by mixing NIR and visible light via non-linear crystals [24–27]. The drawback of this approach is, however, the level of generated power: standard DFG sources have a power that remains at sub-mW or mW level even in presence of high-power pump lasers [28, 29]. This represents a limit for the ultimate achievable sensitivity. Furthermore, the transparency of the available non-linear crystals limited, for a long time, the accessible wavelengths: for instance, the commonly used *Litium Niobate* (LiNbO_3) can not be used for the generation of wavelengths longer than 5.5 μm [2, 3].

In this sense, the "launch" of Quantum Cascade Lasers at Bell Lab in 1994 represented a milestone for the technological development of the MIR [30].

I.2 QCLs: high-performance MIR laser sources

Nowadays, QCLs are well-established and worldwide-used semiconductor laser sources able to operate in the mid-to-far infrared [15]. Chapter 2¹ is entirely dedicated to these devices. Here I anticipate some of the features which have allowed QCLs to emerge among the currently best-performing lasers in the MIR.

QCLs are unipolar heterostructured laser devices with chip-scale dimension² (Fig. I.2). In these devices, the fast laser transition ($\tau < 1\text{ ps}$) occurs between sub-levels of the conduction band. As a consequence, they can be engineered to emit in the mid-to-far spectral region [15] and they can be modulated up to some GHz (and

¹Further details regarding the MIR and QCLs can be found in [2, 3] and in [15, 31, 32], respectively.

²Their waveguide is a few millimetres long [15].

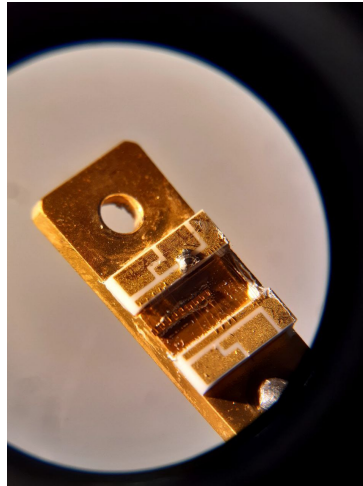


Figure I.2: Picture of a QCL fabricated at ETH Zürich taken using a mobile phone and a microscope.

above [33]), a very interesting feature for free-space communications. Furthermore, the characteristic power-magnification cascade process results in an emitted power from QCLs that can overcome the Watt [34, 35] (see chapter 2). Another advantage of QCLs is the possibility of operating at room temperature both in continuous-wave and pulse emissions [36, 37]. Furthermore, these devices benefit from a particularly small Schawlow-Townes linewidth of $\approx 100\text{Hz}$ [38, 39], making them appealing for high-resolution spectroscopy and frequency metrology applications. Since their discovery, QCLs have been deeply studied and optimized to fulfil the request of high-level sources for new technological applications and challenges such as metrological measurements [31, 40], high-resolution Doppler-free spectroscopy [38, 41, 42], high-resolution cavity ring down spectroscopy [43, 44], free-space communications [16, 45–48], quantum key distribution [49], and secure communication protocol based on chaos [50].

As it will be better discussed in the next section, the discovery of direct comb emission from QCLs [32, 51] was another tremendous conquest for MIR technologies and opened the doors to the investigation of quantum effects in QCL-emitted light. This, in particular, has significantly motivated and driven my Ph.D. research activity.

I.3 QCL-combs: from direct frequency comb emitters to appealing quantum resources

The possibility of generating frequency combs emission from coherent sources has revolutionized the field of precision measurements. Citing the Nobel laureate Theodor W. Hänsch's Nobel lecture, "the quest for an optical frequency counter is almost as old as the laser itself"; in this sense "optical frequency combs from mode-locked femtosecond lasers have revolutionized the art of counting the frequency of light" [52]. Optical Frequency Combs (OFCs) consist of several discrete frequency modes that, like comb teeth, have a fixed frequency step, the *mode spacing*, and a well-defined

phase relation. Since their first generation via mode-locked pulsed lasers [53], OFCs have been established as a powerful precision tool to measure optical frequencies, leading to the development of the first frequency ruler capable of absolute frequency measurements [54–57]. Their high stability, combined with their wide spectral coverage³, has led to both fundamental (atomic clocks) and practical applications (precision spectroscopy) [3, 58, 59].

For many years, frequency mixing in nonlinear crystals was the only approach allowing to equip the MIR with OFCs [2, 3, 60]. Indeed, in this way, it is possible to transform visible/NIR comb sources into MIR OFCs via DFG processes [27, 60–65]. Alternatively, MIR OFCs can be also generated via optical parametric oscillators (OPOs) where, e.g, a periodically poled lithium niobate (PPLN) crystal is used as non-linear medium [60, 66].

Nowadays, an alternative solution for the generation of MIR comb radiation is represented by QCLs. In the last decade, the possibility of direct frequency comb emission from QCLs (QCL-comb) has been demonstrated [32, 51, 67, 68]. In QCLs, the complex hetero-structured active medium is characterized by a large resonant $\chi^{(3)}$ (i.e. third-order non-linearity) enabling a broadband Four-Wave Mixing (FWM) due to the fast lasing upper-state lifetime [32]. These ingredients, together with a small enough Group Velocity Dispersion (GVD), have led to comb emission by broadband Fabry-Pérot QCLs [69], where the free-running multimodal emission is injection-locked by means of multiple FWM processes [32, 51]. More details about QCL-comb working principle are given in chapter 2.

The FWM process is the driving motor not only for comb emission by QCLs but even for my research activity regarding non-classical effects in the emission of these devices. Indeed, being a third-order parametric non-linear effect, FWM can induce, in principle, the generation of a non-classical state of light (chapter 1, section 1.4.4). This propriety has been proved in many different platforms: for instance FWM provides squeezing in optical fibers [70], in optical cavities [71], in rubidium vapour [72], and microring resonators [73]. In particular, considering the case of microring resonators, it is possible to evidence common elements with QCLs: they are both chip-scale photonic platforms where FWM triggers comb emission [32, 74]. Despite dense comb emissions, in both of these photonic platforms, it is also possible to find an emission regime, named *harmonic comb*, characterized by a strong central mode (the pump) and two weak sidebands (typically named signal and idler), nearby multimodal emission threshold (see section 4.2). In such a three-mode photonic state, the FWM process responsible for this emission involves two photons of the pump which generate one photon for each sideband. In this scenario, the expected correlation between signal and idler can be therefore measured by analyzing the difference of the sideband-sideband photon number signal and non-trivially interpreted [73, 75]. However, while microring resonators are passive devices (i.e. the device is optically pumped with an external laser source and presents only non-linear gain), QCLs are active devices and, as always occurs in an amplification stage, the active medium gain can introduce noise overwhelming the quantum correlation induced by FWM [76]. Moreover, QCL emission is affected by

³The near-continuous coverage of OFCs goes from microwave frequencies to the extreme ultraviolet [58].

other noise contributions typical of such devices, e.g. the $1/f$ technical noise emerging at low Fourier frequencies [75, 77, 78]. All these effects make the detection of quantum correlations a hard task. The task is even more difficult if we consider that, in the MIR, we have to fight against the lack of important technological tools necessary for the investigation of quantum properties, like high quantum efficiency detection systems [79, 80]. Moreover, low-loss optical components (e.g. optical isolators and gratings) are available only for narrow spectral MIR bands, making the challenge of detecting non-classical features in QCL-combs emission even harder. These last points will be deeply analyzed in the experimental sections dedicated to the realization of a MIR balanced detector and to the measure of amplitude correlations in MIR QCL-combs (chap. 3 and chap. 4, respectively).

For clarity, let's summarize the main points raised above:

- QCL-comb emission is given by the FWM process triggered by the active medium third-order non-linearity;
- In general, FWM is responsible for the generation of non-classical states from several photonic systems;
- QCLs are complex devices with multiple sources of noise, and the MIR is still not well equipped as the NIR for quantum measurements.

Here the non-trivial question naturally arises: Can FWM enable also squeezed state of light emitted by QCLs? This is the starting point of my work.

Aside from the interest in fundamental physics, the demonstration of possible squeezed and non-classical states emission from QCLs can lead to several new applications as well as to a sensitive improvement of all the precision applications that already exist in the MIR region. For instance, in sensing and metrology applications relying on optical field measurements, which are widely used in the MIR, the minimum detectable signal is typically constrained by the sum of photon shot noise and back-action noise [81]. In this context, establishing a MIR squeezed source, based on QCLs' technology, can lead to an ultimate precision enhancement, by taking advantage of the noise suppression below the shot-noise level typical of these state of light [81]. The use of a squeezed light can therefore enable the detection of signals that otherwise are covered by a shot-noise limited detection [82]. As a matter of fact, the squeezed light has started to be successfully employed in precision experiments such as in the famous LIGO interferometer, e.g. to increase the gravitational-wave detection sensitivity [83, 84]. In literature, there are already many proof-of-principle works involving squeezed light as a resource for sensing [81, 82] and spectroscopy [85, 86], although their practical application is still under-construction [82]. In this framework, a recent European project involving my research group has started: it is named *MULTISCALE QUANTUM BLOIMAGING AND SPECTROSCOPY* (MUQUABIS) and it is financed by the European Quantum Flagship⁴. One of the goal of this project is, indeed, the practical application of infrared squeezed light as a precision enhancement tool for the detection of biological samples.

Moreover, as already stated, the MIR is a region of interest for free-space communication, due to the presence of transparency windows and to the robustness of the MIR

⁴Grant agreement ID: 101070546.

radiation in case of adverse weather conditions. Therefore, establishing QCL-combs as non-classical-light compact sources can revolutionize MIR communications, enabling e.g. the application of quantum key distribution protocols based on squeezed states of light [87–92]. Furthermore, squeezed states of light can be used as a resource for the generation of quantum states of light such as Schrödinger’s states [93–95] which are used in the development of quantum error correction in quantum computation [96] and as a resource in advanced communication protocol like the quantum distillation [97, 98] (chapter 5).

To conclude, testing QCL radiation at the quantum level has the potential of paving the way to innovative quantum-based technologies with both fundamental and practical interest and, despite the drawback of the lack of mature quantum detection technologies in this spectral region, it is a path that worth to be explored.

I.4 Thesis overview

The first two chapters of this thesis aim to provide the theoretical background for the quantum features investigated in the experimental sections and an introduction to QCLs and QCL-combs. The last three chapters describe, instead, my experimental works and the achieved results.

In more detail, the first chapter (chap. 1) describes the theoretical quantum optics tools useful to describe quantum light and light-matter interaction from a quantum perspective. In the first part, the chapter provides the quantum optics basis for the quantization of the free electromagnetic field (section 1.1) as well as a review of some of the most common quantum states of light (section 1.2). The linear interaction via a beam-splitter (section 1.3) and the non-linear interaction via non-linear media are then presented (section 1.4). The description of the electric field in continuous modes is then introduced (section 1.5). Finally, the theory underlying photodetection techniques is given, with a focus on balanced homodyne detection (section 1.6).

In chapter 2, the working principle and the properties of QCLs are reviewed: in section 2.1, the operating principle of these devices is briefly introduced; in section 2.2 the QCL structure is described; in section 2.3 the spectral features of QCLs are presented. Finally, in section 2.4 the comb emission of these devices is described.

Chapter 3 is devoted to the description of the experimental effort made during my Ph.D. to equip the MIR with a shot-noise limited balanced detector capable of testing a non-classical state of light. The work relates to the published article [99]. There are four main sections in this chapter: in sec. 3.1 an introduction about the topic is provided; section 3.2 described the working principle and the theory at the basis of the experiment; in section 3.3 the experimental setup is described; in section 3.4 the results are discussed, with a focus on the limits and potentialities of the assembled setup. Finally, the last section (section 3.5) summarize the experimental activity, and presents some remarks and perspectives.

Chapter 4 is devoted to my experiments on intensity correlation measurements in QCL-combs. At first, a general overview of different emission regimes in QCLs is provided in section 4.1. The experimental work, published in [75], is then described in 4.2. In this work, we tested a three-mode harmonic comb generated by a MIR QCL,

with the aim of revealing a squeezed state of light in the photon difference between the two sidebands. The introduction and motivations behind these measurements are provided in section 4.2.1. In section 4.2.2, the measurement technique is described. In section 4.2.3 the results are presented and discussed. Finally, in section 4.2.4 a summary and some remarks are given, as well as a description of the limits, possible improvements, and perspectives of this type of measurement. Instead, section 4.3 is devoted to the use of the intensity-correlation setup for the analysis of QCL-comb emission operated at high driving current, characterized by a peculiar bilobed modal distribution. In section 4.3.1, the characterization of the utilized QCL-comb is described. In section 4.3.2, the correlation measurements are presented and the achieved results are discussed. Finally, the performed measurements are summarized in section 4.3.3. The fourth chapter ends with a conclusive section about intensity correlations in MIR QCLs, the section 4.4 where the perspectives of my research regarding this topic are described.

In chapter 5, the work I have done in Nice (France) regarding the generation of Schrödinger's cat state at telecom wavelength is described. This work refers to the published article [95]. The overarching goal of this research activity was to acquire the know-how and experimental expertise required to generate and detect quantum states of light from non-linear passive media, with a view to possible future applications of such methodologies to generate non-classical light in the MIR. This chapter is divided into five main sections. Section 5.1 introduces the topic; section 5.2 provides the theoretical pills needed to understand the experimental results, which are later described in section 5.4, after an experimental setup description provided in section 5.3. Conclusion, remarks and perspectives about this topic are given in section 5.5.

A final *conclusion* chapter closes the thesis, with a discussion of the experimental perspectives of the works presented in this manuscript.

CHAPTER 1

Quantum optics tools

1.1 Free electromagnetic field quantization	20
1.2 Quantum states of light	23
1.2.1 Fock's states	23
1.2.2 Coherent state	24
1.2.3 Squeezed light	25
1.3 Linear interaction: the beam splitter	29
1.4 Non-linear phenomena	31
1.4.1 Non-linear polarization	31
1.4.2 Second-order non-linear phenomena	33
1.4.3 Third-order non-linear phenomena	35
1.4.4 Squeezing generation via non-linear phenomena	36
1.5 Electric field: from discrete to continuous modes	39
1.5.1 Narrow-bandwidth approximation	40
1.5.2 Distributed modes	42
1.6 Measurements techniques	42
1.6.1 Photodetectors	42
1.6.2 Balanced homodyne detection	44
1.7 Wigner function	46

In physics, the light-matter interaction is one of the foundational phenomena. This interaction may be linear or not. For example, a linear interaction typically happens when two states of light interfere via an optical beam splitter, or when in an experiment there is a weak field used to probe some matter properties, or when an absorbed photon generates an electron in a photodetector. Instead, the interaction between a strong laser source and materials is most commonly based on non-linear processes. Many classical and quantum physics experiments depend on non-linear interactions between matter and radiation. An example of application is given in the introduction chapter, where the application of non-linear interactions (e.g. DFG) is described as a useful

method to generate OFCs in frequency range suffers from the lack of mature laser comb technologies.

This chapter goes over the quantum optics theoretical framework that I used in my experiments. The first sections provide an overview of free electric field quantization and common quantum optics states of light. Then the linear and non-linear interactions are described, focusing on the quantum perspective. Finally, the theoretical basis for the homodyne detection scheme is provided. This chapter follows the quantization presented in [100]. Other textbooks to deeply study the below-presented topics are [101–104].

1.1 Free electromagnetic field quantization

The recipe to quantize the free electromagnetic field starts from its classical decomposition in *normal modes*: The electric field can be decomposed into a sum of independent modes, and each of them is associated with a different harmonic oscillator oscillating at the mode frequency ω_k . In this description, a specific number of energy packets $\hbar\omega_k$, (i.e. photons) in the k -th electric-field normal mode corresponds to a different level of excitation of its associated harmonic oscillator.

In the case of free radiation (no electrical charges, no currents), the electromagnetic field can be fully described in terms of vector potential $\mathbf{A}(\mathbf{r}, t)$, satisfying the wave equation in the Coulomb gauge [100]:

$$\left(-\nabla^2 + \frac{1}{c^2} \frac{\partial^2}{\partial t^2}\right) \mathbf{A}(\mathbf{r}, t) = 0, \quad (1.1)$$

where c is the speed of light. Both the electric field, \mathbf{E} , and the magnetic field, \mathbf{B} , can be retrieved from the potential vector using the following formulae:

$$\mathbf{B} = \nabla \wedge \mathbf{A}, \quad (1.2)$$

$$\mathbf{E} = -\frac{\partial \mathbf{A}}{\partial t}. \quad (1.3)$$

As for the harmonic oscillator equations [100], if the potential vector is confined in a cubic cavity of a volume $V = L^3$, we can describe \mathbf{A} , \mathbf{B} and \mathbf{E} as a sum of independent modes, $A_{\mathbf{k}\lambda}$, the *normal modes*, characterized by a frequency ω_k , a wavevector \mathbf{k} , and a complex amplitude $A_{\mathbf{k}\lambda}$:

$$\mathbf{A}(\mathbf{r}, t) = \sum_{\mathbf{k}} \sum_{\lambda=1,2} \mathbf{e}_{\mathbf{k}\lambda} A_{\mathbf{k}\lambda}(\mathbf{r}, t) = \sum_{\mathbf{k}} \sum_{\lambda=1,2} \mathbf{e}_{\mathbf{k}\lambda} \left(A_{\mathbf{k}\lambda} e^{(i\mathbf{k}\cdot\mathbf{r} - \omega_k t)} + c.c \right), \quad (1.4)$$

$$\mathbf{B}(\mathbf{r}, t) = \sum_{\mathbf{k}} \sum_{\lambda=1,2} i\mathbf{k} \wedge \mathbf{e}_{\mathbf{k}\lambda} \{ A_{\mathbf{k}\lambda} e^{(i\mathbf{k}\cdot\mathbf{r} - \omega_k t)} - c.c \} = \mathbf{B}^{(+)}(\mathbf{r}, t) + \mathbf{B}^{(-)}(\mathbf{r}, t), \quad (1.5)$$

$$\mathbf{E}(\mathbf{r}, t) = \sum_{\mathbf{k}} \sum_{\lambda=1,2} i\omega_k \mathbf{e}_{\mathbf{k}\lambda} \{ A_{\mathbf{k}\lambda} e^{(i\mathbf{k}\cdot\mathbf{r} - \omega_k t)} - c.c \} = \mathbf{E}^{(+)}(\mathbf{r}, t) + \mathbf{E}^{(-)}(\mathbf{r}, t). \quad (1.6)$$

where $\omega_k = ck$, and the two unitary polarization vectors $\mathbf{e}_{1\lambda}$ and $\mathbf{e}_{2\lambda}$ are in a orthonormal

vector triad with \mathbf{k}^1 . Furthermore $\mathbf{E}^{(+)}(\mathbf{r}, t)$ and $\mathbf{E}^{(-)}(\mathbf{r}, t)$ are defined as :

$$\mathbf{E}^{(+)}(\mathbf{r}, t) = \sum_{\mathbf{k}} \sum_{\lambda=1,2} i\omega_{\mathbf{k}} \mathbf{e}_{\mathbf{k},\lambda} A_{\mathbf{k},\lambda} e^{i(\mathbf{k}\cdot\mathbf{r} - \omega_{\mathbf{k}}t)} = \left[\mathbf{E}^{(-)}(\mathbf{r}, t) \right]^* . \quad (1.7)$$

An analogue expression can be written $\mathbf{B}^{(+)}(\mathbf{r}, t)$ and $\mathbf{B}^{(-)}(\mathbf{r}, t)$ [100].

In this description, the electromagnetic field energy in the cavity V is defined as:

$$\begin{aligned} \mathcal{H}(t) &= 1/2 \int_V dV [\epsilon_0 \mathbf{E}(\mathbf{r}, t) \mathbf{E}(\mathbf{r}, t) + \mu_0^{-1} \mathbf{B}(\mathbf{r}, t) \mathbf{B}(\mathbf{r}, t)] \\ &= \sum_{\mathbf{k}} \sum_{\lambda=1,2} \epsilon_0 V \omega_{\mathbf{k}}^2 (A_{\mathbf{k},\lambda} A_{\mathbf{k},\lambda}^* + c.c.) . \end{aligned} \quad (1.8)$$

After such normal-mode decomposition, to go from the classical to the quantum description, it is sufficient to replace the field vectors and the scalar quantities of interest, with the corresponding operators, e.g. $\mathbf{A} \rightarrow \hat{\mathbf{A}}$ and $\mathcal{H} \rightarrow \hat{\mathcal{H}}$, and to substitute the amplitude field $A_{\mathbf{k},\lambda}$ with the creation of annihilation operator, $\hat{a}_{\mathbf{k},\lambda}^\dagger$ and $\hat{a}_{\mathbf{k},\lambda}$, commonly associated to the $k\lambda$ -th energetic level of the quantum harmonic oscillator:

$$A_{\mathbf{k},\lambda} \rightarrow (\hbar/2\epsilon_0 V \omega_{\mathbf{k}})^{1/2} \hat{a}_{\mathbf{k},\lambda} \quad \text{and} \quad A_{\mathbf{k},\lambda}^* \rightarrow (\hbar/2\epsilon_0 V \omega_{\mathbf{k}})^{1/2} \hat{a}_{\mathbf{k},\lambda}^\dagger . \quad (1.9)$$

By applying such substitutions to Eq. (1.8), the following quantum Hamiltonian can be retrieved:

$$\hat{\mathcal{H}} = \sum_{\mathbf{k}} \sum_{\lambda=1,2} \hbar \omega_{\mathbf{k}} (\hat{a}_{\mathbf{k},\lambda}^\dagger \hat{a}_{\mathbf{k},\lambda} + h.c.) = \sum_{\mathbf{k}} \sum_{\lambda=1,2} \hbar \omega_{\mathbf{k}} \left(\hat{n}_{\mathbf{k},\lambda} + \frac{1}{2} \right) , \quad (1.10)$$

where the photon number operator $\hat{n}_{\mathbf{k},\lambda} = \hat{a}_{\mathbf{k},\lambda}^\dagger \hat{a}_{\mathbf{k},\lambda}$ represents the number of photons of the $\mathbf{k}\lambda$ -th mode. This Hamiltonian turns out to be a sum of Hamiltonians of quantum harmonic oscillators, each of these associated with a specific $\mathbf{k}\lambda$ mode of the field [100]. In particular, the operators $\hat{a}_{\mathbf{k},\lambda}$ and $\hat{a}_{\mathbf{k},\lambda}^\dagger$ satisfy the commutation relation:

$$\left[\hat{a}_{\mathbf{k},\lambda}, \hat{a}_{\mathbf{k}',\lambda'}^\dagger \right] = \delta_{\mathbf{k},\mathbf{k}'} \delta_{\lambda,\lambda'} . \quad (1.11)$$

As for the Hamiltonian, by applying the above-mentioned quantization strategy to Eq. (1.6), the quantum electric field can be retrieved:

$$\begin{aligned} \hat{\mathbf{E}}(\mathbf{r}, t) &= \sum_{\mathbf{k}} \sum_{\lambda=1,2} \mathbf{e}_{\mathbf{k},\lambda} (\hbar \omega_{\mathbf{k}} / 2\epsilon_0 V)^{1/2} \left(\hat{a}_{\mathbf{k},\lambda} e^{-i\varphi_{\mathbf{k}}(\mathbf{r}, t)} + h.c. \right) \\ &= \sum_{\mathbf{k}} \sum_{\lambda=1,2} \mathbf{e}_{\mathbf{k},\lambda} \left(\hat{E}_{\mathbf{k},\lambda}^+(\mathbf{r}, t) + \hat{E}_{\mathbf{k},\lambda}^-(\mathbf{r}, t) \right) , \end{aligned} \quad (1.12)$$

where $\varphi_{\mathbf{k}}(\mathbf{r}, t) = \omega_{\mathbf{k}}t - \mathbf{k} \cdot \mathbf{r} - \pi/2$.

It is convenient to introduce the amplitude and the phase quadratures, respectively

¹By imposing periodical boundary condition for \mathbf{A} , the following relations are obtained:

$$A_{\mathbf{k},\lambda}(0, t) = A_{\mathbf{k},\lambda}(L, t) \quad \forall t \quad \rightarrow \quad k_i = \frac{2\pi}{L} n_i, \quad n_i = 0, \pm 1, \pm 2, \pm 3 \dots$$

where k_i is the i -th component of \mathbf{k} .

defined as:

$$\hat{X}_{\mathbf{k}\lambda} = \frac{\hat{a}_{\mathbf{k}\lambda} + \hat{a}_{\mathbf{k}\lambda}^\dagger}{2} \quad (1.13)$$

$$\hat{Y}_{\mathbf{k}\lambda} = \frac{\hat{a}_{\mathbf{k}\lambda} - \hat{a}_{\mathbf{k}\lambda}^\dagger}{2i}, \quad (1.14)$$

and their commutation rule:

$$[\hat{X}_{\mathbf{k}\lambda}, \hat{Y}_{\mathbf{k}\lambda}] = \frac{i}{2} \delta_{\mathbf{k},\mathbf{k}'} \delta_{\lambda,\lambda'}. \quad (1.15)$$

Indeed, $\hat{X}_{\mathbf{k}\lambda}$ and $\hat{Y}_{\mathbf{k}\lambda}$ are Hermitian operators and are therefore observable quantities. Eq. (1.12) can be, then, written in terms of such quantities as follows:

$$\begin{aligned} \hat{\mathbf{E}}(\mathbf{r}, t) &= \sum_{\mathbf{k}} \sum_{\lambda=1,2} \mathbf{e}_{\mathbf{k}\lambda} (\hbar\omega_{\mathbf{k}}/2\varepsilon_0 V)^{1/2} (\hat{X}_{\mathbf{k}\lambda} \cos[\varphi_{\mathbf{k}}(\mathbf{r}, t)] + \hat{Y}_{\mathbf{k}\lambda} \sin[\varphi_{\mathbf{k}}(\mathbf{r}, t)]) = \\ &= \sum_{\mathbf{k}} \sum_{\lambda=1,2} \mathbf{e}_{\mathbf{k}\lambda} (\hbar\omega_{\mathbf{k}}/2\varepsilon_0 V)^{1/2} \hat{Q}_{\mathbf{k}\lambda}(\varphi_{\mathbf{k}}), \end{aligned} \quad (1.16)$$

where:

$$\hat{Q}_{\mathbf{k}\lambda}(\varphi_{\mathbf{k}}) = \hat{X}_{\mathbf{k}\lambda} \cos[\varphi_{\mathbf{k}}(\mathbf{r}, t)] + \hat{Y}_{\mathbf{k}\lambda} \sin[\varphi_{\mathbf{k}}(\mathbf{r}, t)] \quad (1.17)$$

is the quadrature evaluated at a general phase $\varphi_{\mathbf{k}}(\mathbf{r}, t)$.

In the case of a single-mode field, neglecting the dependence upon r and k to make the notation simpler, the commutation rule for the quadrature operator \hat{Q} , evaluated in two different points of the phase space (φ_1, φ_2) , is:

$$[\hat{Q}(\varphi_1), \hat{Q}(\varphi_2)] = -\frac{i}{2} \sin(\varphi_1 - \varphi_2). \quad (1.18)$$

From which the following uncertainty principle is obtained:

$$\Delta Q(\varphi_1) \Delta Q(\varphi_2) \geq \frac{1}{4} |\sin(\varphi_1 - \varphi_2)|, \quad (1.19)$$

which is maximized for the two conjugated quadratures $\hat{X} = \hat{Q}(\varphi = 0)$ and $\hat{Y} = \hat{Q}(\varphi = \varphi/2)$:

$$\Delta X \Delta Y \geq \frac{1}{4}. \quad (1.20)$$

Finally, it is useful to introduce another observable quantity commonly measured in quantum and classical experiments: the intensity of the propagating field. In particular, the operator $\hat{I}_{\mathbf{k}\lambda}$ related to the observable intensity of the $\mathbf{k}\lambda$ -th mode is defined as:

$$\begin{aligned} \hat{I}_{\mathbf{k}\lambda} &= 2c\varepsilon_0 \hat{E}_{\mathbf{k},\lambda}^-(\mathbf{r}, t) \hat{E}_{\mathbf{k},\lambda}^+(\mathbf{r}, t) \\ &= \hbar\omega_{\mathbf{k}} \hat{a}_{\mathbf{k}\lambda}^\dagger \hat{a}_{\mathbf{k}\lambda} \\ &= \hbar\omega_{\mathbf{k}} \hat{n}_{\mathbf{k}\lambda}, \end{aligned} \quad (1.21)$$

and it is proportional to the photon number operator $\hat{n}_{\mathbf{k}\lambda}$ of the $\mathbf{k}\lambda$ -th mode.

1.2 Quantum states of light

Given a certain light source, e.g., a laser or a light bulb, the emitted light is characterized by specific photon or quadrature statistics. In quantum optics, a proper quantum state can be connected to the produced light depending on the source's statistical properties, as described in the next section. The notation used in the previous section is simplified below by considering single-mode states of light. Despite its simplicity, a single-mode state of light is, however, a good approximation for representing the light commonly used in some experiments, for instance when light beams are collimated and their transverse electric field can be, therefore, approximated by a single-mode [100].

1.2.1 Fock's states

Fock's states, $|n\rangle$, are quantum states of light characterized by a well-defined number of photons. They are, indeed, the eigenvectors of the photon number operator \hat{n} :

$$\hat{n}|n\rangle = n|n\rangle, \quad (1.22)$$

$$\hat{a}|n\rangle = \sqrt{n}|n-1\rangle \quad \text{where} \quad \hat{a}|0\rangle = 0, \quad (1.23)$$

$$\hat{a}^\dagger|n\rangle = \sqrt{n+1}|n+1\rangle. \quad (1.24)$$

where n represents the number of photons of the Fock's state $|n\rangle$, and the $|0\rangle$ identifies the vacuum state. Being states characterized by a well-defined number of photons, their statistics is characterized by a variance $(\Delta n)^2 = 0$. Furthermore, they are also eigenvectors of the single-mode Hamiltonian \hat{H} (Eq. (1.10)):

$$\hat{H}|n\rangle = \hbar\omega \left(\hat{a}^\dagger \hat{a} + \frac{1}{2} \right) |n\rangle = \hbar\omega (\hat{X}^2 + \hat{Y}^2) |n\rangle = \hbar\omega \left(n + \frac{1}{2} \right) |n\rangle. \quad (1.25)$$

Therefore, in order to evaluate the energy and the number of photons associated with a certain quantum state $|\Psi\rangle$, it is useful to decompose it in the $\{|n\rangle\}$ basis:

$$|\Psi\rangle = \sum_n C_n |n\rangle \quad (1.26)$$

where $|C_n|^2 = |\langle n|\Psi\rangle|^2$ represents the probability of having a certain number of photons n in the state $|\Psi\rangle$.

Regarding the quadratures \hat{X} and \hat{Y} (Eq. (1.13) and Eq. (1.14)), the Fock's states satisfy the following relations:

$$\langle n|\hat{X}|n\rangle = \langle n|\hat{Y}|n\rangle = 0, \quad (1.27)$$

$$(\Delta X)^2 = (\Delta Y)^2 = \frac{1}{2} \left(n + \frac{1}{2} \right). \quad (1.28)$$

From this latter relation (Eq. 1.28) the vacuum state $|0\rangle$ results to be the Fock's state characterized by the minimum quadrature uncertainty:

$$(\Delta X_0)^2 = (\Delta Y_0)^2 = \frac{1}{4}, \quad (1.29)$$

$$\Delta X_0 \Delta Y_0 = 1/4. \quad (1.30)$$

Additionally, from the above-introduced relations, it is possible to find the mean value and the variance of the generic quadrature \hat{Q} (Eq. (1.17)):

$$\langle n|\hat{Q}|n\rangle = 0 \quad \text{and} \quad (\Delta Q)^2 = \frac{1}{2} \left(n + \frac{1}{2} \right) \quad (1.31)$$

1.2.2 Coherent state

The coherent states are defined as the eigenvectors of the annihilation operator \hat{a} :

$$\hat{a}|\alpha\rangle = \alpha|\alpha\rangle \quad \text{con} \quad \langle\alpha|\alpha\rangle = 1, \quad (1.32)$$

where $\alpha = |\alpha|e^{i\theta} \in \mathbb{C}$ is the eigenvalue of the eigenvector $|\alpha\rangle$, with $\theta \in \mathbb{R}$. Using Eq. (1.26), they can be decomposed in the Fock's basis:

$$|\alpha\rangle = \exp\left(-\frac{1}{2}|\alpha|^2\right) \sum_{n=0}^{\infty} \frac{\alpha^n}{(n!)^{1/2}} |n\rangle. \quad (1.33)$$

From such relation, it is possible to calculate the number of photon number mean value, variance and probability distribution for a certain coherent state, leading to the following results:

$$\langle n \rangle = \langle \alpha | \hat{n} | \alpha \rangle = |\alpha|^2, \quad (1.34)$$

$$(\Delta n)^2 = \langle n^2 \rangle - \langle n \rangle^2 = |\alpha|^2 = \langle n \rangle, \quad (1.35)$$

$$P(n) = |\langle n | \alpha \rangle|^2 = \exp(-|\alpha|^2) \frac{|\alpha|^{2n}}{n!} = e^{-\langle n \rangle} \frac{\langle n \rangle^n}{n!}. \quad (1.36)$$

It is worth to notice that $P(n)$ is a Poissonian distribution. An example of such distribution is provided in Fig. 1.1.

It is here convenient to introduce the definition of the displacement operator $\hat{D}(\alpha)$. Via this operator, it is possible to construct a coherent state starting from the vacuum state:

$$|\alpha\rangle = \exp(\alpha\hat{a}^\dagger - \alpha^*\hat{a})|0\rangle = \hat{D}(\alpha)|0\rangle. \quad (1.37)$$

This operator is unitary and its action can be interpreted as follows: the displacement operator infers a translation in the phase space of a quantity $|\alpha|$ to the quadratures of the vacuum state without changing their variance². Indeed, the measured quadratures \hat{X} and \hat{Y} of a coherent state have the following mean values and variances:

$$\langle \alpha | \hat{X} | \alpha \rangle = \frac{1}{2} \langle \alpha | (\hat{a}^\dagger + \hat{a}) | \alpha \rangle = \frac{1}{2} (\alpha^* + \alpha) = \text{Re}[\alpha] = |\alpha| \cos \theta, \quad (1.38)$$

$$\langle \alpha | \hat{Y} | \alpha \rangle = \frac{1}{2i} (\alpha - \alpha^*) = \text{Im}[\alpha] = |\alpha| \sin \theta, \quad (1.39)$$

$$(\Delta X)^2 = (\Delta Y)^2 = \frac{1}{4}. \quad (1.40)$$

²The displacement operator moves the operator \hat{a} (\hat{a}^\dagger) of a quantity α (α^*) [100]:

$$\begin{aligned} \hat{D}^\dagger(\alpha)\hat{a}\hat{D}(\alpha) &= \hat{a} + \alpha, \\ \hat{D}^\dagger(\alpha)\hat{a}^\dagger\hat{D}(\alpha) &= \hat{a}^\dagger + \alpha^*. \end{aligned}$$

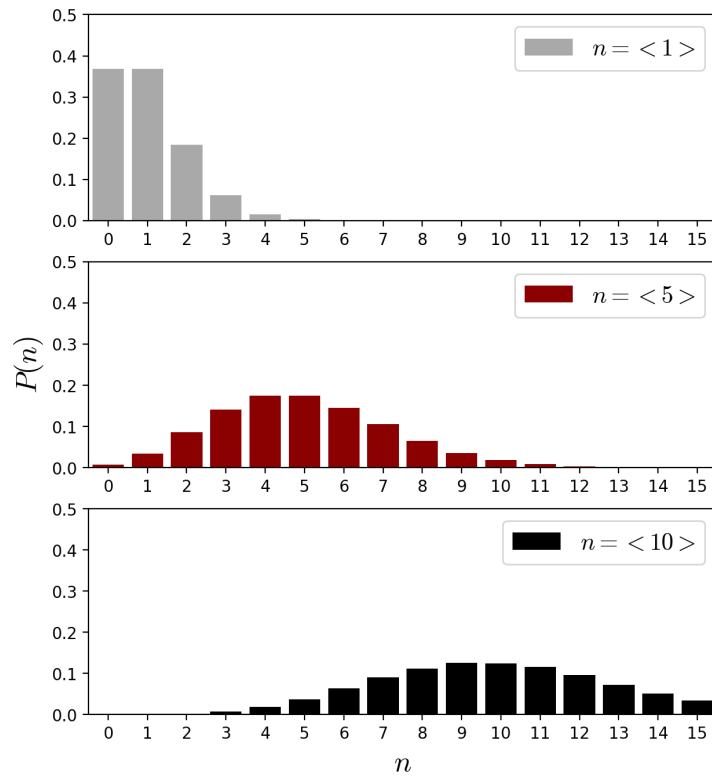


Figure 1.1: Poissonian photon-number probability distribution of a coherent state as a function of its mean number of photons $\langle n \rangle$.

The coherent state turns out to be a state with minimum quadrature uncertainty, whatever it is its average number of photons³ $|\alpha|^2$.

In general, the expectation value and the variance for the quadrature operator $\hat{Q}(\varphi)$, defined in Eq. (1.17), for a coherent state are respectively:

$$S = \langle \alpha | \hat{Q}(\varphi) | \alpha \rangle = |\alpha| \cos(\varphi - \theta), \quad (1.41)$$

$$\mathcal{N} = (\Delta Q(\varphi))^2 = \frac{1}{4}. \quad (1.42)$$

While the average amplitude of the field signal S (Eq. (1.41)) depends on the observation phase of the field φ and on the amplitude and phase of α , i.e. $S = S(\varphi - \theta, \alpha)$, the variance \mathcal{N} (Eq. (1.42)) is constant and phase-independent.

Finally, it is worth to remark that among quantum states of light the coherent state is one of particular interest, being a good representation for the radiation emitted by a laser source⁴ operating well above threshold [100].

1.2.3 Squeezed light

Although in the previously-presented states of lights the quadrature variance is independent of the observation phase φ , in this section we analyze a particular type of single-mode field excitation which vice-versa shows this phase-dependence: the

³This result is the contrary of the one obtained for the Fock's state where the variance of the quadratures is closely linked to the number of photons n , as shown in Eq. (1.31).

⁴In the here represent theoretical framework the laser source is meant to be single mode.

squeezed state of light. In general, a state of light is squeezed when for a certain φ the quadrature variance is:

$$0 \leq (\Delta Q(\varphi))^2 \leq \frac{1}{4} \quad (1.43)$$

Due to the fact that in any case the uncertainty principle must be valid, the measurement of a quadrature squeezing in a certain quadrature phase-space direction φ comes at the cost of the increment of the quadrature uncertainty observed in the relative perpendicular direction. In particular, in this section, we introduce the squeezed vacuum state of light, which is the one used in the experiment shown lately in chapter 5, and the squeezed coherent states. More info about squeezed states of light can be found in [100].

Squeezed vacuum state

Starting from the vacuum state $|0\rangle$, it is possible to generate a squeezed state of light by applying the squeezing operator⁵ $\hat{S}(\zeta)$:

$$|\zeta\rangle = \hat{S}(\zeta)|0\rangle, \quad (1.44)$$

where $\hat{S}(\zeta)$ and the squeezing parameter ζ can be defined as:

$$\hat{S}(\zeta) = \exp \left[\frac{1}{2} \zeta^* \hat{a}^2 - \frac{1}{2} \zeta (\hat{a}^\dagger)^2 \right] \quad (1.45)$$

$$\zeta = s e^{i\vartheta} \quad \text{con } s, \vartheta \in \mathbb{R}. \quad (1.46)$$

The squeezed vacuum state can be written as a superposition of (even) Fock's states:

$$|\zeta\rangle = (\text{sech}(s))^{1/2} \sum_{n=0}^{\infty} \frac{[(2n)!]^{1/2}}{n!} \left[-\frac{1}{2} e^{i\vartheta} \tanh(s) \right]^n |2n\rangle. \quad (1.47)$$

To calculate the mean value and the variance of both the photon number operator and the quadratures, it is useful to use the following transformation rules for the squeezing operator:

$$\hat{S}^\dagger(\zeta) \hat{a} \hat{S}(\zeta) = \hat{a} \cosh(s) - \hat{a}^\dagger e^{i\vartheta} \sinh(s), \quad (1.48)$$

$$\hat{S}^\dagger(\zeta) \hat{a}^\dagger \hat{S}(\zeta) = \hat{a}^\dagger \cosh(s) - \hat{a} e^{-i\vartheta} \sinh(s). \quad (1.49)$$

With these transformations, it is possible to evaluate the mean value and variance of the photon number operator onto the squeezed vacuum:

$$\langle n \rangle = \langle \zeta | \hat{a}^\dagger \hat{a} | \zeta \rangle = \langle 0 | \hat{S}^\dagger(\zeta) \hat{a}^\dagger \hat{S}(\zeta) \hat{S}^\dagger(\zeta) \hat{a} \hat{S}(\zeta) | 0 \rangle = \sinh^2(s), \quad (1.50)$$

$$(\Delta n)^2 = 2\langle n \rangle (\langle n \rangle + 1). \quad (1.51)$$

The squeezed vacuum state is characterized by a photon-number variance higher than the one retrieved for a coherent state which is equal to $\langle n \rangle$ (Eq. (1.35)). Therefore its number-photon statistics is ruled by a *Super-Poissonian distribution*.

Using the transformations reported in Eq. (1.49) and in Eq. (1.48), it is also possible to

⁵The squeezing operator is a unitary operator, therefore $\hat{S}(\zeta) \hat{S}^\dagger(\zeta) = \hat{S}^\dagger(\zeta) \hat{S}(\zeta) = 1$.

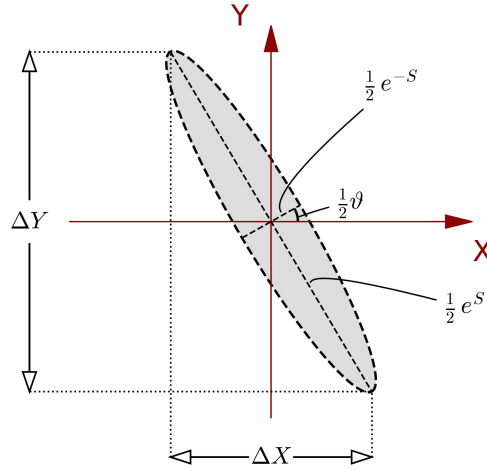


Figure 1.2: Representation of the quadrature operator's mean value and uncertainty for the squeezed vacuum state in the XY -quadrature phase space.

find the following mean values and variances for the quadrature operators:

$$\langle \zeta | \hat{X} | \zeta \rangle = \langle \zeta | \hat{Y} | \zeta \rangle = 0, \quad (1.52)$$

$$(\Delta X)^2 = \frac{1}{4} \left\{ e^{2s} \sin^2 \left(\frac{1}{2} \vartheta \right) + e^{-2s} \cos^2 \left(\frac{1}{2} \vartheta \right) \right\}, \quad (1.53)$$

$$(\Delta Y)^2 = \frac{1}{4} \left\{ e^{2s} \cos^2 \left(\frac{1}{2} \vartheta \right) + e^{-2s} \sin^2 \left(\frac{1}{2} \vartheta \right) \right\}. \quad (1.54)$$

$$(1.55)$$

A representation of a squeezed vacuum state of light in the XY -quadrature phase space is depicted in Fig. 1.2. More in general, a measurement of the quadrature $\hat{Q}(\varphi)$ of a squeezed vacuum state is characterized by a zero mean value:

$$S = \langle \zeta | \hat{Q}(\varphi) | \zeta \rangle = 0 \quad (1.56)$$

and a variance:

$$\mathcal{N} = (\Delta Q(\varphi))^2 = \frac{1}{4} \left\{ e^{2s} \sin^2 \left(\varphi - \frac{1}{2} \vartheta \right) + e^{-2s} \cos^2 \left(\varphi - \frac{1}{2} \vartheta \right) \right\}. \quad (1.57)$$

By detecting the quadrature \hat{Q} at different phases φ , it is possible to find the maximum and the minimum for \mathcal{N} which are:

$$\Delta Q_{\min} = \Delta Q \left(\frac{1}{2} \vartheta + m\pi \right) = \frac{1}{2} e^{-s}, \quad (1.58)$$

$$\Delta Q_{\max} = \Delta Q \left(\frac{1}{2} (\vartheta + \pi) + m\pi \right) = \frac{1}{2} e^s \quad \text{with } m \in \mathbb{Z}. \quad (1.59)$$

The uncertainty principle for these quadratures is therefore:

$$\Delta Q_{\min} \Delta Q_{\max} = 1/4. \quad (1.60)$$

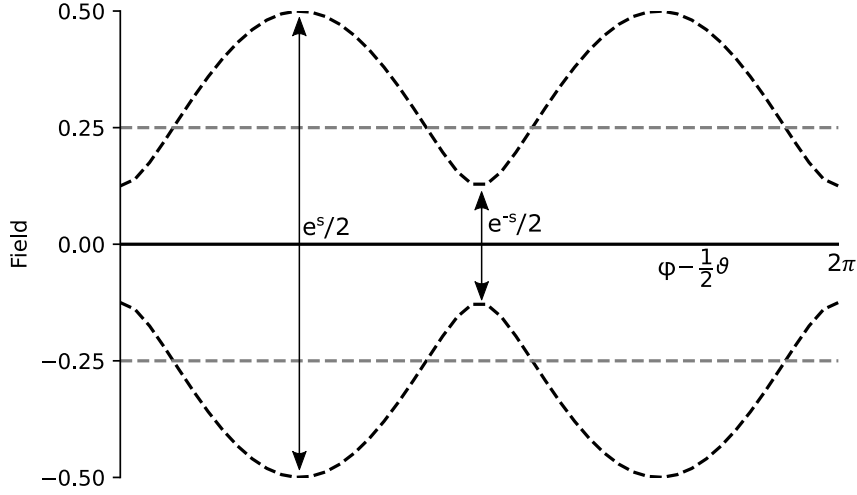


Figure 1.3: Envelope of the noise band of the field, evaluated in terms of \hat{Q} , for a squeezed vacuum state with a squeezing parameter $s = \ln(2)$ (black dashed lines) and of the vacuum state ($s = 0$, grey dashed lines) as a function of the phase. The noise band is obtained by evaluating the square root of Eq. (1.57) for the squeezed vacuum state, and of Eq. (1.31) for the standard vacuum state.

An example of the detected field quadrature \hat{Q} as a function of the phase ($\varphi - \frac{1}{2}\vartheta$) is depicted in Fig. 1.3.

Squeezed coherent states

By applying the displacement operator $\hat{D}(\alpha)$ (Eq. (1.37)) to the squeezed vacuum state (Eq. (1.44)), a squeezed coherent state is obtained:

$$|\alpha, \zeta\rangle = \hat{D}(\alpha)\hat{S}(\zeta)|0\rangle. \quad (1.61)$$

By using the following relations [100]:

$$\hat{S}^\dagger(\zeta)\hat{D}^\dagger(\alpha)\hat{a}\hat{S}(\zeta)\hat{D}(\alpha) = \hat{a}\cosh(s) - \hat{a}^\dagger e^{i\vartheta}\sinh(s) + \alpha, \quad (1.62)$$

$$\hat{S}^\dagger(\zeta)\hat{D}^\dagger(\alpha)\hat{a}^\dagger\hat{S}(\zeta)\hat{D}(\alpha) = \hat{a}^\dagger\cosh(s) - \hat{a}e^{-i\vartheta}\sinh(s) + \alpha^*, \quad (1.63)$$

it is possible to determine the mean value of the photon number operator:

$$\langle n \rangle = |\alpha|^2 + \sinh^2(s), \quad (1.64)$$

and its variance:

$$(\Delta n)^2 = |\alpha|^2 \left\{ e^{2s}\sin^2\left(\theta - \frac{1}{2}\vartheta\right) + e^{-2s}\cos^2\left(\theta - \frac{1}{2}\vartheta\right) \right\} + 2\sinh^2(s)(\sinh^2(s) + 1). \quad (1.65)$$

In particular, Eq. (1.64) is the sum of the mean values of the photon number operator evaluated on the coherent state (Eq. (1.34)) and on the squeezed vacuum state (Eq. (1.50)), respectively. Instead, the photon-number variance of Eq. (1.65) becomes the variance of the coherent state for $s \rightarrow 0$ (Eq. (1.35)), and the variance of the squeezed vacuum state for $|\alpha| \rightarrow 0$ (Eq. (1.51)).

Regarding the quadratures, for a squeezed coherent state of light \hat{X} and \hat{Y} follow the relations:

$$\langle \alpha, \zeta | \hat{X} | \alpha, \zeta \rangle = |\alpha| \cos(\theta), \quad (1.66)$$

$$\langle \alpha, \zeta | \hat{Y} | \alpha, \zeta \rangle = |\alpha| \sin(\theta), \quad (1.67)$$

$$(\Delta X)^2 = \frac{1}{4} \left\{ e^{2s} \sin^2 \left(\frac{1}{2} \vartheta \right) + e^{-2s} \cos^2 \left(\frac{1}{2} \vartheta \right) \right\}, \quad (1.68)$$

$$(\Delta Y)^2 = \frac{1}{4} \left\{ e^{2s} \cos^2 \left(\frac{1}{2} \vartheta \right) + e^{-2s} \sin^2 \left(\frac{1}{2} \vartheta \right) \right\}. \quad (1.69)$$

Their mean values are the ones found in the case of a coherent state (Eq. (1.38) and Eq. (1.39)), while their variances are the ones of a squeezed vacuum state (Eq. (1.53) and Eq. (1.55)). It is possible to generalize these results for the measurement of the quadrature \hat{Q} :

$$\mathcal{S} = \langle \alpha, \zeta | \hat{Q}(\varphi) | \alpha, \zeta \rangle = \langle \alpha | \hat{Q}(\varphi) | \alpha \rangle = |\alpha| \cos(\varphi - \theta), \quad (1.70)$$

$$\mathcal{N} = (\Delta Q(\varphi))^2 = \frac{1}{4} \left\{ e^{2s} \sin^2 \left(\varphi - \frac{1}{2} \vartheta \right) + e^{-2s} \cos^2 \left(\varphi - \frac{1}{2} \vartheta \right) \right\}. \quad (1.71)$$

A quadrature-squeezed coherent therefore has the typical signal of a coherent state $|\alpha\rangle$ (Eq. (1.41)) and the noise band suppression typical of the squeezed vacuum state $|\zeta\rangle$ (Eq. (1.57)). The maximum signal-to-noise ratio (SNR) is obtained in the following case:

$$\text{SNR} = \frac{\mathcal{S}}{\mathcal{N}} = 4e^{2s} |\alpha|^2 \quad \text{with} \quad \varphi = \theta = \frac{1}{2} \vartheta. \quad (1.72)$$

Starting from the above-mentioned relations (Eq.(1.64) and Eq. (1.65)), it is also possible to define the *amplitude-squeezed state of light* in the case of $\theta = \frac{1}{2} \vartheta$. In particular, in the case of:

$$|\alpha| \gg e^s \quad \text{and} \quad \langle n \rangle \approx |\alpha|^2, \quad (1.73)$$

the number photon variance of the amplitude-squeezed state of light is [100]:

$$(\Delta n)^2 = \langle n \rangle e^{-2s}. \quad (1.74)$$

Compared to the coherent state of light (eq. (1.35)), the amplitude-squeezed state of light has a photon-number variance reduced⁶ by a factor equal to e^{-2s} . Therefore its photon-number statistic is expected to be sub-Poissonian with a photon-number noise smaller than the corresponding shot noise [100]⁷.

1.3 Linear interaction: the beam splitter

In quantum optics experiments, a commonly used optical element is the beam splitter (BS), which is used to create linear superposition between two propagating fields

⁶The photon number variance reduction comes at the cost of an increase in the phase variance with respect to a coherent state. This magnification factor is equal to e^{2s} [100].

⁷More in general, sub-Poissonian photon-number fluctuations occur in the amplitude-squeezed coherent state when the following condition is satisfied: $|\alpha|^2 > \frac{1}{4} (e^{2s} - 1) \cosh(2s)$ [100].

impinging on it. To give an idea about the mathematics rules under such superposition we can assume that such fields are independent, monochromatic, at the same frequency and we can schematize their radiation via the corresponding annihilation operators, being $\hat{E}^+ \propto \hat{a}$ (Eq. 1.12). Referring to the Fig. 1.4, in the approximation of ideal

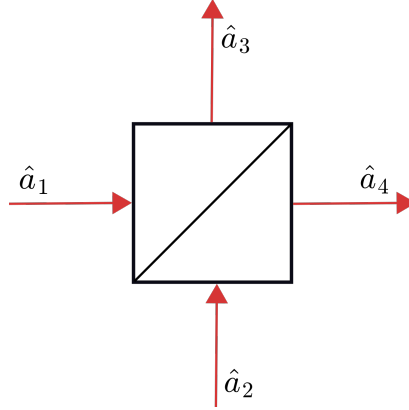


Figure 1.4: Schematic representation of an ideal beam splitter. In the figure, the annihilation operators associated with the inputs and output fields are reported and are labelled with the pair of numbers (1,2) and (3,4), respectively.

symmetric beam splitter (no losses), the relations between the input fields (\hat{a}_1, \hat{a}_2) and the outputs fields (\hat{a}_3, \hat{a}_4) are:

$$\hat{a}_3 = R\hat{a}_1 + T\hat{a}_2, \quad (1.75)$$

$$\hat{a}_4 = T\hat{a}_1 + R\hat{a}_2, \quad (1.76)$$

where R and T are the transmission and the reflection coefficients associated with the BS and, for the energy conservation, they satisfy the following relations:

$$|R|^2 + |T|^2 = 1, \quad (1.77)$$

$$RT^* + R^*T = 0. \quad (1.78)$$

All the annihilation operators introduced have to follow the commutation rules given by:

$$[\hat{a}_i, \hat{a}_j^\dagger] = \begin{cases} 1 & \text{se } i = j, \\ 0 & \text{se } i \neq j, \end{cases} \quad (i, j = 1, 2, 3, 4) \quad (1.79)$$

and the photon number operator \hat{n}_i associated to the i -th BS input/output is defined as:

$$\hat{n}_i = \hat{a}_i^\dagger \hat{a}_i \quad (i = 1, 2, 3, 4). \quad (1.80)$$

In particular, using Eq. (1.75) and Eq. (1.76), it is possible to write the outputs' photon number operators as a function of the inputs' ones:

$$\hat{n}_3 = |R|^2 \hat{n}_1 + R^* T \hat{a}_1^\dagger \hat{a}_2 + R T^* \hat{a}_2^\dagger \hat{a}_1 + |T|^2 \hat{n}_2, \quad (1.81)$$

$$\hat{n}_4 = |T|^2 \hat{n}_1 + R T^* \hat{a}_1^\dagger \hat{a}_2 + R^* T \hat{a}_2^\dagger \hat{a}_1 + |R|^2 \hat{n}_2. \quad (1.82)$$

It this way, their mean values and variances can be evaluated directly onto the input state⁸. In particular in the case of a vacuum state, $|0\rangle$, at the input 2 the photon number mean values and variances are:

$$\langle n_3 \rangle = |R|^2 \langle n_1 \rangle, \quad (\Delta n_3)^2 = |R|^4 (\Delta n_1)^2 + |R|^2 |T|^2 \langle n_1 \rangle, \quad (1.83)$$

$$\langle n_4 \rangle = |T|^2 \langle n_1 \rangle, \quad (\Delta n_4)^2 = |T|^4 (\Delta n_1)^2 + |R|^2 |T|^2 \langle n_1 \rangle, \quad (1.84)$$

It is worth noticing that in the output variance equations an extra term appears, $|R|^2 |T|^2 \langle n_1 \rangle$, with respect to the input variance, $(\Delta n_1)^2$. This term is proportional to $\langle n_1 \rangle$ and it is due to the coupling between the input state and the vacuum. Note that all the $\langle \cdot \rangle$ mentioned are evaluated onto the generic state $|\psi_1\rangle$ entering in BS input 1. To summarize, by coupling a state via a BS with the vacuum state, its photon number statistics is modified accordingly to the found relation (Eq. (1.84)). However, there is an exception: the coherent states of light. If we assume that $|\psi_1\rangle = |\alpha_1\rangle$, the BS output states will be still coherent states. E.g. it is possible to substitute in Eq. (1.84) the variance equation found in case of coherent states: $(\Delta n_1)^2 = \langle n_1 \rangle$ (Eq. 1.34). Knowing that the BS coefficients follow the relation of Eq. (1.77), the variance at the output 4 can be written as:

$$\begin{aligned} (\Delta n_4)^2 &= |T|^4 \langle n_1 \rangle + |R|^2 |T|^2 \langle n_1 \rangle = |T|^2 (|T|^2 + |R|^2) \langle n_1 \rangle \\ &= |T|^2 \langle n_1 \rangle = \langle n_4 \rangle. \end{aligned} \quad (1.85)$$

The photon number variance at output 4 is still at the *shot-noise level*, as expected by a coherent state. It can also be verified that the photon-number probability distribution at the BS outputs is still Poissonian [100]. Therefore we can conclude that in case of a coherent state the statistics it is not changed by the coupling with the vacuum field, at the cost of a reduction in terms of mean photon number⁹.

1.4 Non-linear phenomena

Non-linear phenomena are at the basis of a large number of optical techniques and technologies. In this section, the theoretical tools to deal with non-linear interactions are provided. In particular, the concept of non-linear polarization is introduced from a classical point of view, as well as some examples of second and third-order non-phenomena (section 1.4). Finally, the squeezing generation via non-linear phenomena is discussed from a quantum optics perspective (section 1.4.4). A complete theoretical description of these phenomena can be found in [101, 102, 104–106] and in [3, 107–109] from which the here provided equation toolkit is inspired.

1.4.1 Non-linear polarization

When a certain electric field $\mathbf{E}(\mathbf{r}, t)$ is applied to a dielectric material¹⁰, it generates a polarization $\mathbf{P}(\mathbf{r}, t)$ of such material, i.e. a dipole moment per unit volume [105, 106].

⁸The input state is the tensor product between the states of the beams impinging on the BS (on input 1 and input 2, respectively).

⁹Indeed: $\langle n_1 \rangle \rightarrow \langle n_4 \rangle = |T|^2 \langle n_1 \rangle$ with $|T|^2 < 1$.

¹⁰For standard dielectric materials the permanent dipole moment is zero.

In-lab produced fields are often far weaker than those that bind electrons to molecules, therefore $\mathbf{P}(\mathbf{r}, t)$ can be expanded in series with respect to the applied $\mathbf{E}(\mathbf{r}, t)$:

$$\mathbf{P} = \epsilon_0 \chi(\mathbf{E}) \mathbf{E} = \epsilon_0 (\chi^{(1)} \mathbf{E} + \chi^{(2)} \mathbf{E}^2 + \chi^{(3)} \mathbf{E}^3 + \dots) \quad (1.86)$$

where $\chi^{(j)} = \chi^{(j)}(\mathbf{E})$ is the j -th order electrical susceptibility of the material. Such equation can be expressed in tensorial form¹¹ as follows:

$$P_k(\mathbf{r}, t) = \epsilon_0 (\chi_{kl}^{(1)} E_l + \chi_{klm}^{(2)} E_l E_m + \chi_{klmn}^{(3)} E_l E_m E_n + \dots) \quad (1.87)$$

where P_k is the k -th component of the polarization, the indices l, m, n run over the three spatial coordinates x, y, z , while:

$$\chi_{1,2,\dots,j+1}^{(j)} = \frac{1}{j! \epsilon_0} \frac{\partial^j P_1}{\partial E_2 \partial E_3 \dots \partial E_{j+1}} \quad (1.88)$$

is the electrical susceptibility tensor of rank $j + 1$ [106]. In Eq. (1.86), the linear term can be separated from the non-linear term leading to the relation [110]:

$$\mathbf{P}(\mathbf{r}, t) = \epsilon_0 \chi^{(1)} \mathbf{E}(\mathbf{r}, t) + \mathbf{P}_{(\text{NL})}(\mathbf{r}, t), \quad (1.89)$$

where $\mathbf{P}_{(\text{NL})}(\mathbf{r}, t)$ represents the non-linear polarization part. To understand the role of the non-linear response of the material, it is useful to combine Maxwell's equations, under the assumption of no magnetization of the material and far away from charges or currents, to determine the following wave equation [105]:

$$\nabla^2 \mathbf{E} = \mu \epsilon \frac{\partial^2}{\partial t^2} \mathbf{E} + \mu \frac{\partial^2}{\partial t^2} \mathbf{P}_{(\text{NL})} \quad (1.90)$$

with $\epsilon = \epsilon_0 (1 + \chi^{(1)})$ where ϵ_0 is the dielectric constant in vacuum, while μ is the magnetic permeability constant. This equation can be written in a scalar form under the assumption $\mathbf{P}_{(\text{NL})} \parallel \mathbf{E}$:

$$\nabla^2 E = \mu \epsilon \frac{\partial^2}{\partial t^2} E + \mu \frac{\partial^2}{\partial t^2} P_{(\text{NL})} \quad (1.91)$$

If now we expand the electric field in normal modes propagating along the z as in sec. 1.1, each of them characterized by the frequency ω_i , the following equation can be obtained:

$$E(z, t) = \sum_i \frac{1}{2} [E_i(z) e^{i(k_i z - \omega_i t)} + c.c.] \quad (1.92)$$

Replacing Eq. (1.92) in Eq. (1.91) and comparing the left and right terms characterized by the same electric field power, it clearly emerges that the non-linear term *mixes* the components at different frequencies¹² [3, 106].

¹¹Here the Einstein summation convention is adopted. The summation over repeated indices is implied.

¹²This mixing takes place since the field is multiplied by itself, therefore terms related to different frequencies multiplies among each other [3, 106].

1.4.2 Second-order non-linear phenomena

For the interpretation of second-order non-linear phenomena, only the second-order term in Eq. (1.87) must be considered, as well as only three plane waves in Eq. (1.86). We can assume that two of them are applied to the material, $E_1(z, t)$ and $E_2(z, t)$, and that the third one, $E_3(z, t)$, is the result of their non-linear interaction [106]. The three fields are defined according to Eq. (1.92) as:

$$\frac{1}{2}[E_i(z) e^{i(k_i z - \omega_i t)} + c.c.] \quad \text{with } i = 1, 2, 3. \quad (1.93)$$

By replacing in the second order term, $P^{(2)} \propto E^2$, of Eq. (1.86) the sum of the two electric fields $E_1(z, t)$ and $E_2(z, t)$ as E , we can find terms oscillating at $2\omega_1$ and $2\omega_2$ (*second-harmonic generation* - SHG), $\omega_1 + \omega_2$ (*sum-frequency generation* - SFG), and $|\omega_1 - \omega_2|$ (*difference-frequency generation* - DFG) [3]. All of these phenomena are capable of generating a new field at ω_3 . The relation among the frequencies is given by the energy conservation law [106]. Instead, the relation among the three fields can be found via Eq. (1.91). In the case of a SFG process, neglecting the second derivative of the field with respect to z in Eq. (1.91) (slowly varying amplitude approximation [106]), recalling that $k_3 = \frac{n_3 \omega_3}{c}$ where $n_3 = \sqrt{\epsilon_3 / \epsilon_0}$ is the refractive index ($\epsilon_3 = \epsilon(\omega_3)$), the following relation can be found [106]:

$$\frac{d}{dz} E_3 = 2i \frac{\omega_3}{n_3 c} d_{\text{eff}} E_2 E_1 e^{i\Delta k z}, \quad (1.94)$$

where, for energy conservation, the following relation must be satisfied:

$$\omega_3 = \omega_1 + \omega_2, \quad (1.95)$$

and the *phase-mismatch factor*¹³ Δk satisfies the relation:

$$\Delta k = (k_1 + k_2) - k_3, \quad (1.96)$$

and where d_{eff} is the effective value of the non-linear constant and it depends on the non-linearity $\chi^{(2)}$, as well as on the fields' geometry [106]. The value of d_{eff} can be calculated from the definition of the non-linear constant $d_{klm} = \frac{1}{2} \chi_{klm}^{(2)}$ (defined from Eq. (1.87)) as described in details in reference [106]. An equation similar to Eq. (1.94) can be found for the other fields, when a sum of three plane waves is introduced in Eq. (1.91). The three field amplitudes are coupled via the non-linear constants d_{eff} . It is worth remarking that Eq. (1.94) can represent a good description of second-order non-linear phenomena in the low conversion efficiency regime where the source fields are not significantly depleted [106].

To find the equation for E_3 we can integrate Eq. (1.94) assuming that E_1 and E_2 hit at $z = 0$ the surface of a $\chi^{(2)}$ non-linear crystal of length L and that $E_3(z = 0) = 0$ [106].

¹³For the other second-order non-linear processes the phase-mismatch factor is defined in the same way with just a different distribution of the signs.

The obtained result is:

$$E_3(L) = 2i \frac{\omega_3}{n_3 c} d_{\text{eff}} E_2 E_1 \frac{e^{i\Delta k L} - 1}{i\Delta k}, \quad (1.97)$$

and the related intensity is [106]:

$$I(L) = 2n_3 \epsilon_0 c E_3(L) E_3^*(L) = 8\epsilon_0 \frac{\omega_3^2 (d_{\text{eff}})^2}{n_3 c} |E_2|^2 |E_1|^2 L^2 \frac{\sin^2(L\Delta k/2)}{(L\Delta k/2)^2}. \quad (1.98)$$

Phase matching

From Eq. (1.98), we can see that:

$$I(L) \propto \text{sinc}^2\left(\frac{L\Delta k}{2}\right) = \frac{\sin^2(L\Delta k/2)}{(L\Delta k/2)^2} \xrightarrow{\Delta k \rightarrow 0} 1. \quad (1.99)$$

In case of $\Delta k = 0 \rightarrow I(L) \propto L^2$, the intensity increases quadratically with the crystal length¹⁴. Otherwise, this function oscillates with a spatial period given by the *coherence length* $l_c = \pi/\Delta k$, as shown in Fig. 1.5. There are different techniques to fulfil the

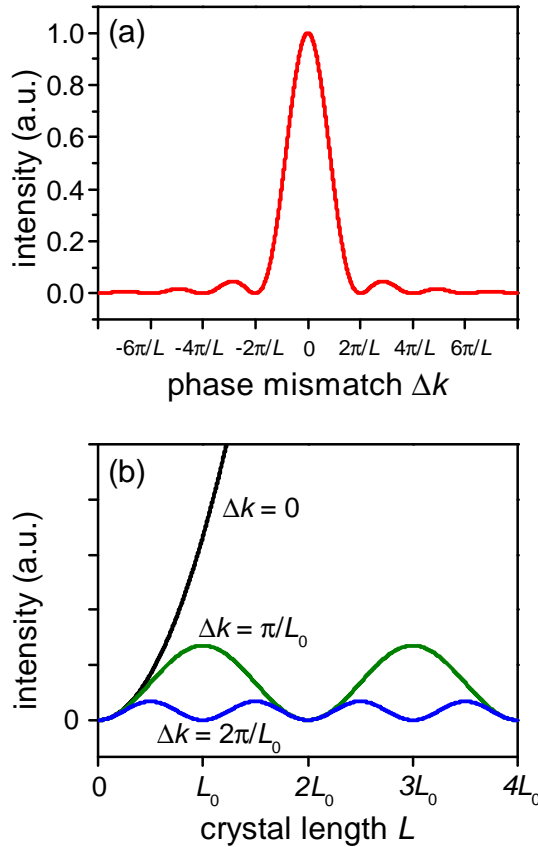


Figure 1.5: a) Phase-matching curve (Eq. (1.99)) as a function of the phase-mismatch factor Δk , with a fixed crystal length L . b) Generated intensity (Eq. (1.98)) as a function of the crystal length L for different fixed values of the phase-mismatch factor Δk . The crystal length L is expressed in terms of a reference length L_0 . figures adapted from [3].

phase-matching condition like the *birefringent phase matching* and the *quasi-phase*

¹⁴This is true in the approximation of plane waves. For Gaussian beam $I(L) \propto L$ [3].

matching [106]. Here the latter technique is described¹⁵.

The so-called *quasi-phase matching* exploits the potential of periodically reversing one of the crystal's principal optical axes, resulting in a modulation of the sign of the nonlinear constant d_{eff} . If this modulation has a spatial period, i.e. the *poling period*, $\Lambda = 2l_c$, the generated power oscillates but grows with each oscillation [3, 106]. Formally, the new phase-matching condition is the following:

$$\Delta k' = k_3 - k_2 - k_1 - \frac{2\pi}{\Lambda} = 0 \quad (1.100)$$

In this new phase matching equation, the parameter to be finely selected is Λ which depends on the crystal fabrication¹⁶. For a fixed phase-matching condition, a key indicator to consider in the non-linear conversion processes is the *phase-matching bandwidth*, which is how much the frequency of the generated radiation can be modified while still having a meaningful amount of power [106]. Supposing that the tunable frequency is ω_2 , via Eq. (1.95) it is possible to write the phase-mismatch factor (Eq. (1.96)) as a function of the other two frequencies by applying the following substitution $\omega_2 \rightarrow \omega_3 - \omega_1$. By comparing this result with Eq. (1.100), it is possible to determine the following equation of mismatching in case of a quasi-phase-matching condition:

$$\omega_3(n_3 - n_2) - \omega_1(n_1 - n_2) - \frac{2\pi c}{\Lambda} = c\Delta k. \quad (1.101)$$

Observing the phase-mismatch function (Eq. 1.99 and Fig. 1.5), we can assume as a limit for having the generation its first zero, i.e. $L\Delta k/2 = \pi$, yielding to the following relation for the crystal length $L < 2\pi/\Delta k = 2l_c$. The bandwidth of the generated radiation at ω_3 is now obtained subtracting member by member Eq. 1.101, one time evaluated in phase-matching condition $\Delta k = 0$ and the other one in the limit condition $\Delta k = 2\pi/L$, under the assumption that the tuning of ω_2 does not affect the refractive index, which remains constant¹⁷. The resulting phase matching bandwidth $\Delta\omega_3$ is therefore:

$$\Delta\omega_3 = \frac{2\pi c}{L \Delta n_{32}}. \quad (1.102)$$

This result depends only on the difference of the refractive indices $\Delta n_{32} = n_3 - n_2$ and on the crystal length L .

1.4.3 Third-order non-linear phenomena

The third-order term in Eq. (1.86) (or in Eq. (1.87)) must be considered, as well as four plane waves ($i = 1, 2, 3, 4$ in Eq. (1.92)) for the description of third-order non-linear phenomena. The resulting third-order susceptibility $\chi_{klmn}^{(3)}$ is, in general, a fourth-rank tensor [106]¹⁸. For simplicity, we can assume that the non-linear crystal used to model the third-order non-linear effect is isotropic: in this way the number of independent

¹⁵The advantages of the quasi-phase matching are an overall higher conversion efficiency and higher flexibility in reaching the phase-matching condition [3].

¹⁶In the experiment such parameter can be slightly adjusted by changing the crystal temperature.

¹⁷In general $n_i = n(\omega_i)$ and therefore the refractive index can change by changing the frequency of the radiation, however, if the tuning is small, it is possible to assume it constant [106].

¹⁸For low-symmetry crystals, all terms are independent and can be nonzero. In contrast, the number of independent elements is greatly reduced in high-symmetry materials, arriving at just three independent elements in isotropic materials [3, 106].

elements of the tensor is reduced at three [106]. Considering E_1 the resulting element of the non-linear process, in the corresponding third-order non-linear polarization $P^{(3)}$ there are, for instance, terms oscillating at $3\omega_2$ (*third-harmonic generation*), $\omega_2 + \omega_3 + \omega_4$ (*sum-frequency generation*), and $|\omega_3 + \omega_4 - \omega_2|$ and permutations (*four-wave mixing* - FWM) [3, 106]. All of them are capable of generating a new field at ω_1 , where the conservation of energy provides the relation among the mixed frequencies. With an analogue derivation to that of section 1.4.2, an expression equivalent to Eq. (1.94) can be retrieved in case of third-order process involving a FWM [3, 102, 106]:

$$\begin{aligned} \frac{d}{dz}E_1 = i \frac{\omega_1^2 \mu \epsilon_0 \chi^{(3)}}{8k_1} & \left[\underbrace{6E_3E_4E_2^* e^{i\Delta k z}}_{\text{four-wave mixing}} + \right. \\ & \left. + 6E_1 \underbrace{\left(\frac{1}{2}|E_1|^2 + |E_2|^2 + |E_3|^2 + |E_4|^2 \right)}_{\text{Kerr}} \right] \end{aligned} \quad (1.103)$$

Similar formulae occur for the other three fields, and the four amplitudes are related via the $\chi^{(3)}$ parameter. In particular, the *four-wave mixing* (FWM) term comes from the mixing of the other three waves¹⁹, while the *Kerr* term comes from the quadratic sum of the field, i.e. of their intensities and it is proportional to E_1 . Therefore, the Kerr term only modifies the propagation constant of the wave associated with the normal mode E_1 by determining an increment of the refractive index [3, 106].

By integrating Eq. (1.103) and computing the intensity, a dependency from the phase-mismatch factor Δk of the same type as Eq. (1.99) is obtained, along with a corresponding phase-matching bandwidth [106].

1.4.4 Squeezing generation via non-linear phenomena

Non-linear effects are powerful tools to generate squeezed radiation. In the sections below such phenomena are described using quantum formalism. The models here provided are simple, however, despite their simplicity, it clearly emerges the possibility of squeezing generation via non-linear processes. More info can be found in [101, 102, 104, 107–109].

Squeezing via Spontaneous Parametric Down Conversion

A common way to generate squeezing is via the second-order non-linear process named *Spontaneous Parametric Down Conversion* (SPDC) which is the reverse process of the above described SFG (section 1.4.2). In case of a non-degenerate process, a field $E_3(\omega_3)$ is applied to a $\chi^{(2)}$ non-linear crystal to generate two field $E_2(\omega_2)$ and $E_1(\omega_1)$ such that $\omega_1 + \omega_2 = \omega_3$.

From a quantum perspective, it is useful to associate to each field a quantised normal mode as already seen in section 1.1. Supposing that the fields have a defined polarization λ and propagate in the same direction z , it is possible to simplify the notation of Eq. (1.12), defining for each of them a couple of operators $\hat{a}_i, \hat{a}_i^\dagger$ ($i = 1, 2, 3$) which create/destroy photons at the field frequency. We can then build, from a

¹⁹The factor 6 in front of it comes from the degeneracy given by the interchangeability of the three fields [106].

phenomenological perspective, an interaction Hamiltonian for the non-linear process made by two terms: the first term represents the SPDC process and it creates a couple of photons at the frequency ω_2 and ω_1 at the cost of a photon ω_3 ; while the second term is its *c.c.* and describes the opposite process, i.e. the SFG. The overall Hamiltonian can be represented by a free-evolving term (\hat{H}_0) plus the interacting one [104]:

$$\hat{H} = \hat{H}_0 + \hat{H}_I = \sum_{i=(1,2,3)} \left(\hat{a}_i^\dagger \hat{a}_i + \frac{1}{2} \right) + \hbar k \left(\hat{a}_1 \hat{a}_2^\dagger \hat{a}_3^\dagger + \hat{a}_1^\dagger \hat{a}_2 \hat{a}_3 \right), \quad (1.104)$$

where $k \propto \chi^{(2)}$. If we forget about the H_0 part, we can consider just the interaction part to understand how the squeezing is generated from this process. In a fully quantum mechanics interaction picture under the rotating wave approximation and the hypothesis of a bright coherent single-mode pump (approximated with a classical mode), the interaction Hamiltonian can be seen as [102]:

$$\hat{H}_I = \hbar k |\alpha_1| \left(e^{-i\varphi} \hat{a}_2^\dagger \hat{a}_3^\dagger + e^{i\varphi} \hat{a}_2 \hat{a}_3 \right) = -\hbar \frac{i}{2} k' \chi^{(2)} |\alpha_1| \left(e^{-i\varphi} \hat{a}_2^\dagger \hat{a}_3^\dagger + e^{i\varphi} \hat{a}_2 \hat{a}_3 \right), \quad (1.105)$$

where $k = -\frac{i}{2} k' \chi^{(2)}$ and the operator \hat{a}_1 has been replaced with $|\alpha_1| e^{-i\varphi}$. From such Hamiltonian we can define the unitary evolution operator [104, 108]:

$$U_I = e^{iH_I t/\hbar} = \exp \left[\frac{k'}{2} \chi^{(2)} |\alpha_1| \left(e^{-i\varphi} \hat{a}_2^\dagger \hat{a}_3^\dagger + e^{i\varphi} \hat{a}_2 \hat{a}_3 \right) t \right], \quad (1.106)$$

where t is the time of interaction. It is immediately clear that this operator is of the same form of $S(\zeta)$ (section 1.2.3), when it is defined in the case of two modes [101, 102]. In the degenerative process where $\omega_2 = \omega_3 = \omega_1/2$ it is possible to find the same type equation with a square dependence on the annihilation and creation operator, as shown in chap. 5.

Despite its simplicity and limitation, this intuitive approach gives a taste of how squeezing can be generated via a non-linear process. A more formal approach can be found in [101, 102, 104].

Squeezing via four-wave mixing

As mentioned in the introduction chapter, we aim to study the FWM process in the case of QCL harmonic combs characterized by a bright single central mode and two weak sidebands. The quantum model for a QCL dynamics is quite complex: gain, losses, and other coupling terms (e.g. mode competition) occur between the modes. However, the motivation under the statement about the capability of FWM of generating a squeezed state of light can be provided starting from a simple scenario considering an interaction Hamiltonian similar to the case of χ^2 passive medium ²⁰.

In the case of a FWM process where two photons of a bright pump (ω_p) generate two photons of two sidebands (ω_{s1} and ω_{s2}) such that: $2\omega_p = \omega_{s1} + \omega_{s2}$, we can find

²⁰This model does not take into account about the gain, the losses, and the coupling between different modes due to phenomena like gain competition. However, it is an intuitive and easy way to get the squeezing generation in the case of a simple toy model.

an interaction Hamiltonian similar to the case of SPDC [101, 102]:

$$\hat{H}_I = \hbar k \left(\hat{a}_p^2 \hat{a}_{s1}^\dagger \hat{a}_{s2}^\dagger + \hat{a}_p^{\dagger 2} \hat{a}_{s1} \hat{a}_{s2} \right) \quad (1.107)$$

where now $k \propto \chi^{(3)}$. If we schematize the pump as a classical bright coherent state, we end up with an expression identical to the SPDC one, apart from a multiplicative constant. Therefore, we can have the generation of a two-mode squeezing state also via FWM. A more formal approach can be found in [101, 102, 104].

In particular, in the experiment presented in chapter 4, we aim to measure the presence of squeezing in the photon number difference of the two side modes. About this topic, we can compare the QCL-comb platform to the Kerr-comb emitted by micro-resonator where such squeezed difference signal has been found [73, 111].

In the case of Kerr comb generated via micro-resonator, it has been shown that this sideband-sideband photon-number difference, evolving via a Hamiltonian characterized by a FWM term, leads to a difference photon-number squeezed state [111]. The theoretical dissertation presented in [111] uses the quantum mechanics Heisenberg picture, where the states are kept constant in their initial value, e.g. $|\Psi\rangle = |\Psi(0)\rangle$, and the time evolution is applied to the operators²¹. In particular, if we define the operator of sideband-sideband photon-number difference as \hat{n}_- , its evolution in the Heisenberg picture can be written as [100]:

$$\frac{d}{dt} \hat{n}_-(t) = \frac{i}{\hbar} [\hat{H}_{tot}, \hat{n}_-(t)] + \frac{\partial}{\partial t} \hat{n}_-, \quad (1.108)$$

where, as described in [111], the Hamiltonian \hat{H}_{tot} has a free part evolution (analogue to H_0 defined above), a part linked to the external pump, H_{pump} , and, finally, an interaction part, H_{Kerr} . In particular, H_{Kerr} is composed by three terms: the FWM part, H_{FWM} , the self-phase modulation part, $H_{SPM} \propto \sum_m (\hat{a}_m^\dagger)^2 (\hat{a}_m)^2$, and the cross-phase modulation part $H_{CPM} \propto \sum_{m < l} (\hat{a}_m^\dagger) (\hat{a}_l^\dagger) (\hat{a}_m) (\hat{a}_l)$ [111].

In the specific case of bright pump and weak sidebands²², the interaction Hamiltonian can be approximated as the one defined in Eq. (1.107) [111]. By doing the proper calculations and evaluating the Fourier Power Spectrum $S(\omega)$ ²³ related to the sideband-sideband photon-number difference²⁴, and by normalizing it to the shot-noise, the following equation can be obtained [111]:

$$S(\omega) = 1 + \rho \frac{4k_c^2}{\omega^2 + k_c^4}, \quad (1.109)$$

where k_c is linked to the laser pump detuning with respect to the micro-ring resonator cavity resonance, and ρ is a parameter that represents a direct indicator of the squeezing

²¹At the contrary, in case of the Schrodinger picture the state of light $|\psi(0)\rangle$ evolves in the time leading to $|\psi(t)\rangle = \hat{U}(t) |\psi(0)\rangle$ and the operator remains constant at the initial value. $U(t)$ is the evolution operator [100], which is the one applied to the operator \hat{A} to find $\hat{A}(t)$ in case of Heisenberg picture : $\hat{A}(t) = \hat{U}^\dagger(t) \hat{A} \hat{U}(t)$.

²² $\langle n_p \rangle \gg \langle n_\pm \rangle$ where n_\pm is the sideband-sideband sum (+) and difference (-) photon number operator and n_p is the photon number operator associated to the pump mode.

²³Given a certain signal $A(t)$, the power spectrum is defined as $|A(\omega)|^2$, where $A(\omega)$ is the Fourier Transform of $A(t)$.

²⁴In [111], the sideband-sideband photon-number difference operator is defined taking into account also the losses which lead to a coupling between the side modes and the vacuum state.

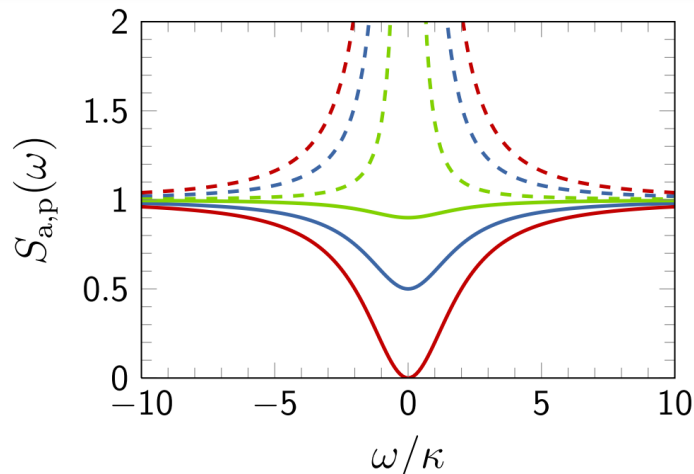


Figure 1.6: Power spectra of pure amplitude and phase quadratures for different values of the squeezing parameter ρ . The solid curves refer to the sideband-sideband photon difference spectrum section 1.4.4, whose spectrum equation is equal to the one found for the power spectrum amplitude quadrature described in the main text as \hat{X} . The dashed-line curves refer to the spectra found for the phase quadrature described in the main text as \hat{Y} . Figure taken from [111].

efficiency. $\rho \rightarrow 1$ leads to a perfect squeezed state, $\rho \rightarrow 0$ to no squeezing in the whole spectrum. This parameter depends on the cavity experimental parameter such as the cavity factor and the coupling losses and so dependence on the cavity manufacture and coupling efficiency [111]. An example of the Lorentzian spectral shape of $S(\omega)$ is provided in Fig. 1.6 where the squeezed state curve is represented with a solid line.

Explaining all the theories under the theoretical model presented in [111] is quite complex and out of the scope of this experimental thesis. The aim of the work presented in this manuscript is indeed to study possible non-classical features in QCLs. These devices have some common features with microring resonators like the presence of a cavity, comb emissions and the FWM, However, they are also quite different from them, being active media. Furthermore, the sideband-sideband photon-number difference measurements presented in chapter 4 do not evidence the presence of correlations at the quantum level between the QCL's sidebands. The noise difference of their photon numbers signal remains, indeed, well above the corresponding shot-noise level. However, by describing the possibility of having a squeezed state of light in the sideband-sideband photon-number difference in a three-mode comb triggered by a FWM process, the here presented brief introduction can help to understand the motivation under the experiment described in chapter 4.

A complete and elegant theoretical dissertation about the quantum features of Kerr comb out of micro-resonator can be found in [111].

1.5 Electric field: from discrete to continuous modes

The quantum optics derivation described in the sections above refers to the ideal case of a time-independent single-mode quantum optics state. However, in the experiments, we have to deal with travelling quantum states of light with time-dependent properties and, in general, their field is characterised by a certain spectral bandwidth. The first step

for a better description is to pass from a discrete modes' decomposition to continuous modes one [100].

Let's assume that in our experiment we are dealing with the radiation of an optical beam characterized by a transverse area A and by a well-defined polarization which is propagating in free space from the emitting source to a detector in the z -direction parallel to the optical table. It is convenient to model the propagation path as a fictitious cavity of length L , extending in the direction parallel to the optical table. From a discrete-mode decomposition perspective, the electrical field of the beam can be seen as a sum of normal modes as in the case of Eq. (1.6), where the sum runs only over the variable k , indeed the direction of propagation and the polarization of the beam are fixed. Passing to a continuous mode description, we can now associate to the k -mode the continuous quantity ω_k and determine the distance between two normal modes in terms of frequency as:

$$\Delta\omega = 2\pi c/L, \quad (1.110)$$

where $L \rightarrow \infty$ in case of free-space propagation beam, transforming the discrete sum into an integral over the frequency:

$$\sum_k \rightarrow \frac{1}{\Delta\omega} \int d\omega. \quad (1.111)$$

Similarly to the derivation done for discrete normal modes, here it is possible to associate to the electric field the operators $\hat{a}^\dagger(\omega)$ and $\hat{a}(\omega)$ which have now to satisfy the commutation relation:

$$[\hat{a}(\omega), \hat{a}^\dagger(\omega')] = \delta(\omega - \omega'), \quad (1.112)$$

where the Kronecker's delta $\delta_{k,k'}$ of Eq. (1.11) is substituted with the continuous Dirac delta function $\delta(\omega - \omega')$. By doing the following substitutions in Eq. (1.12) :

$$\hat{a}_k \rightarrow \sqrt{\Delta\omega} \hat{a}(\omega), \quad (1.113)$$

$$\hat{a}_k^\dagger \rightarrow \sqrt{\Delta\omega} \hat{a}^\dagger(\omega), \quad (1.114)$$

the electric field can be written as:

$$\hat{E}(\varphi) = \int_0^\infty d\omega \left(\frac{\hbar\omega}{4\pi\epsilon_0 c A} \right)^{1/2} \left(\hat{a}(\omega) e^{-i\varphi} + \hat{a}^\dagger(\omega) e^{i\varphi} \right) \quad (1.115)$$

where

$$\varphi = \omega \left(t - \frac{z}{c} \right) + \frac{\pi}{2}. \quad (1.116)$$

In this derivation, the photon number operator becomes:

$$\hat{n} = \int d\omega \hat{a}(\omega) \hat{a}^\dagger(\omega). \quad (1.117)$$

1.5.1 Narrow-bandwidth approximation

For a single-mode optical beam characterized by a central frequency ω_0 and by a narrow bandwidth ($\Delta\omega_{\text{optical beam}} \ll \omega_0$) it is possible to approximate $\omega \approx \omega_0$ and to

extend the frequency integral²⁵ introduced in the previous paragraph from $-\infty$ to ∞ . In this narrow-bandwidth approximation [100], the temporal-dependent operator $\hat{a}(t)$ can be defined as the Fourier Transform of the operator $\hat{a}(\omega)$:

$$\hat{a}(t) = (2\pi)^{-1/2} \int_{-\infty}^{\infty} d\omega \hat{a}(\omega) e^{-i\omega t}, \quad (1.118)$$

$$\hat{a}(\omega) = (2\pi)^{-1/2} \int_{-\infty}^{\infty} dt \hat{a}(t) e^{i\omega t}, \quad (1.119)$$

and in the same way it is possible to define a Fourier-Transform-based relation between $\hat{a}^\dagger(t)$ and $\hat{a}^\dagger(\omega)$. These temporal-dependent operators must satisfy the commutation relation:

$$[\hat{a}(t), \hat{a}^\dagger(t')] = \delta(t - t'). \quad (1.120)$$

Furthermore, as in the case of discrete modes, the vacuum state satisfies the condition:

$$\hat{a}(t) |0\rangle = \hat{a}(\omega) |0\rangle = 0. \quad (1.121)$$

It is also possible to define the photon number operator \hat{n} in terms of photon flux operator $\hat{f}(t) = \hat{a}^\dagger(t)\hat{a}(t)$ as:

$$\hat{n} = \int dt \hat{a}^\dagger(t)\hat{a}(t) = \int dt \hat{f}(t), \quad (1.122)$$

and to evaluate its mean value by averaging the flux operator:

$$\begin{aligned} \langle n \rangle &= \int dt f(t) = \int dt \langle \hat{f}(t) \rangle dt = \\ &= (2\pi)^{-1} \int dt \int d\omega \int d\omega' \langle \hat{a}^\dagger(\omega)\hat{a}(\omega') \rangle \exp[i(\omega - \omega')t]. \end{aligned} \quad (1.123)$$

Finally, in this narrow-bandwidth approximation, the electric field and the intensity associated with the optical beam can be respectively written as:

$$\begin{aligned} \hat{E}(z, t) &= \left(\frac{\hbar\omega_0}{2\epsilon_0 c A} \right)^{1/2} \left\{ i\hat{a} \left(t - \frac{z}{c} \right) - i\hat{a}^\dagger \left(t - \frac{z}{c} \right) \right\} \\ &= \hat{E}^+(z, t) + \hat{E}^-(z, t) \end{aligned} \quad (1.124)$$

and:

$$\begin{aligned} \hat{I}(z, t) &= 2c\epsilon_0 \hat{E}^-(z, t)\hat{E}^+(z, t) \\ &= \frac{\hbar\omega_0}{A} \hat{a}^\dagger \left(t - \frac{z}{c} \right) \hat{a} \left(t - \frac{z}{c} \right) \\ &= \frac{\hbar\omega_0}{A} \hat{f} \left(t - \frac{z}{c} \right). \end{aligned} \quad (1.125)$$

The here retrieved expressions are analogues to the ones found in the discrete mode decomposition, with the difference that now both the annihilation and construction are time-dependent, and the quantity associated with the intensity operator is the photon flux.

²⁵In general, this integral should be positive being the frequency a positive quantity.

1.5.2 Distributed modes

A further step in the description of a real propagating state of light is to associate with it a certain frequency spectrum $g(\omega)$, peaked at the frequency ω_0 , accordingly to its photon-number statistical distribution which can be for instance Gaussian or Lorentzian. In this scenario, it is useful to define the operators:

$$\hat{a}_g^\dagger = \int d\omega g(\omega) \hat{a}^\dagger(\omega), \quad (1.126)$$

$$\hat{a}_g = \int d\omega g^*(\omega) \hat{a}(\omega), \quad (1.127)$$

which respectively create e destroy a photon in the wave-packet of the propagating state of light characterized by a certain shape given by the distribution $g(\omega)$ which must be normalized:

$$\int d\omega |g(\omega)|^2 = 1 \quad (1.128)$$

to satisfy the commutation relation rule:

$$[\hat{a}_g, \hat{a}_g^\dagger] = 1. \quad (1.129)$$

From this derivation, it is possible to find results similar to the one found for single-mode states of light in section 1.2. A complete description of distributed quantum states of light can be found in [100].

1.6 Measurements techniques

In this section, the mathematical tools useful for describing typical photon-detection schemes are provided. In particular, the homodyne detection technique is here introduced and described.

1.6.1 Photodetectors

In the case of direct photodetection using photovoltaic detectors, the flux of photons characterizing the beam incident on the detector area is measured in terms of photocurrent. In the following description, we assume that the detector is ideal, with no saturation and that it works in the linear responsivity regime, with a conversion efficiency between incident photons and generated electrons, commonly called quantum efficiency, of 1:1: i.e. for each incident photon the detector generates an electron. From a quantum point of view the photocurrent $\hat{I}(t)$ is proportional to the $\hat{f}(t)$ defined in Eq. 1.122:

$$\hat{I}(t) = q\hat{f}(t). \quad (1.130)$$

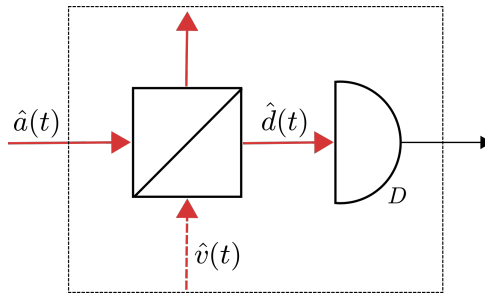


Figure 1.7: Representation of a real detector with quantum efficiency $\eta < 1$, schematized as an ideal detector (D) preceded by an ideal and symmetrical beam-splitter which couples the field under investigation $\hat{a}(t)$ to the vacuum field $\hat{v}(t)$. The resulting field is described via $\hat{d}(t)$. The beam-splitter is described via the coefficients $T = \sqrt{\eta}$ and $R = i\sqrt{1-\eta}$.

where q is the electron charge. The number of photons²⁶ arriving to the detector in the measuring time \mathcal{T} is given by the operator:

$$\hat{M}(t, \mathcal{T}) = \int_t^{t+\mathcal{T}} dt' \hat{f}(t') = \int_t^{t+\mathcal{T}} dt' \hat{a}^\dagger(t') \hat{a}(t'). \quad (1.131)$$

This model, however, does not represent a real detector where the quantum efficiency $\eta < 1$: in fact, a real detector is affected by losses (e.g. the photons are reflected from the detector surface or not absorbed in the sensitive region and/or the loss of electrons as a result of ionization processes). This leads to a conversion of photons in electrons lower than 1:1. In quantum optics, the losses can be schematized with a BS as shown in Fig. 1.7. This BS couples the field of interest (described via the operator $\hat{a}(t)$) with the vacuum field ($\hat{v}(t)$), and it is characterized by a transmission coefficient and a reflection coefficient both expressed in terms of η : $T = \sqrt{\eta}$ and $R = i\sqrt{1-\eta}$, respectively. Therefore, a real detector can be seen as an ideal one (D in Fig. 1.7) preceded by the BS schematizing the losses. By using the beam splitter relations presented in sec. 1.3, the output field $\hat{d}(t)$ can be written as:

$$\hat{d}(t) = (\eta)^{1/2} \hat{a}(t) + i(1-\eta)^{1/2} \hat{v}(t), \quad (1.132)$$

and the detected number of photons can be defined as:

$$\hat{M}_D(t, \mathcal{T}) = \int_t^{t+\mathcal{T}} dt' \hat{d}^\dagger(t') \hat{d}(t'). \quad (1.133)$$

Accordingly to Eq. (1.84), the mean number of detected photons and its variance are:

$$\langle m \rangle = \eta \langle \hat{M}(t, \mathcal{T}) \rangle, \quad (1.134)$$

$$(\Delta m)^2 = \eta^2 \langle [[\Delta \hat{M}(t, \mathcal{T})]^2] \rangle + \eta(1-\eta) \langle \hat{M}(t, \mathcal{T}) \rangle. \quad (1.135)$$

The mean number of photons is the one of the incident beam, scaled by the quantum efficiency. The variance has instead an extra term, i.e. $\eta(1-\eta) \langle \hat{M}(t, \mathcal{T}) \rangle$, with respect to the one of the incident beam. This extra term is due to the coupling with the vacuum.

²⁶This quantity $\hat{M}(t, \mathcal{T})$, as defined in Eq. (1.131), remains a finite quantity even in the case of a stationary beam, being \mathcal{T} a finite amount of time [100]. Vice-versa for non-stationary light the photon flux depends on the position of the detector z_d which can be explicited in the introduced relation by doing the substitution $t \rightarrow t - \frac{z_d}{c}$ [100].

1.6.2 Balanced homodyne detection

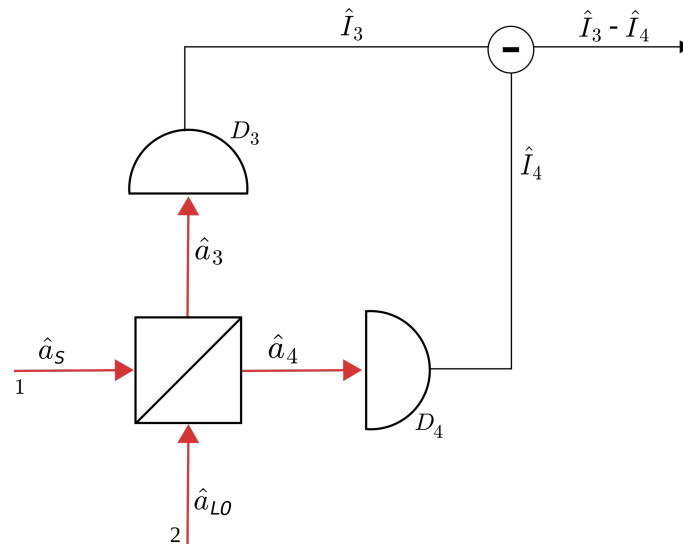


Figure 1.8: Scheme of the homodyne detection. The signal field is indicated by \hat{a}_S , that of the local oscillator by \hat{a}_{LO} . The output fields are respectively indicated with \hat{a}_3 and \hat{a}_4 to which the currents \hat{I}_3 and \hat{I}_4 are associated, revealed by the two detectors. The measured quantity is $\hat{I}_3 - \hat{I}_4$, which we call \hat{I}_- in the text.

In quantum optics, the balanced homodyne detection is a commonly used technique that allows the measurement of the electric field of a specific state of light and, therefore, of the associated observable \hat{Q} (Eq. (1.17)). This technique involves the mixing of the signal of interest with a reference radiation, via a 50/50 BS (i.e. $|R|^2 = |T|^2 = 1/2$, sec. 1.3) and a differential measurement performed between the output signals of two identical photodetectors located at the two 50/50 BS outputs, as shown in Fig. 1.8.

In the following discussion the fields are assumed in a single mode, with the same frequency and polarization²⁷. Another prerequisite for efficient homodyne detection is that the two states must have the same spatial and spectral shape. This requirement can be experimentally obtained, for example, from beams generated by the same or identical sources (an example of this detection scheme is described in chap. 5). Furthermore, in the following description, we assume to have an ideal symmetric BS. Referring to Fig. 1.8, in a typical balanced homodyne detection scheme the signal of interest \hat{a}_S is mixed via a 50/50 (ideal and symmetric) BS (i.e. $R = T$) with a signal of reference \hat{a}_{LO} , commonly called *Local Oscillator* (LO). While the signal state $|\Psi_s\rangle$ is a generic one, the LO is typically a strong coherent state $|\alpha_{LO}\rangle$. The homodyne detection consists of transforming the BS output signals, \hat{a}_3 and \hat{a}_4 , in two photocurrent signals (\hat{I}_3 and \hat{I}_4 , respectively) via two identical (ideal) photodetectors and performing the difference between this latter retrieved quantities. By writing the coefficients of the 50/50 BS as $T = i/\sqrt{2}$ and $R = 1/\sqrt{2}$, from the BS equation found in sec. 1.3 (Eq. 1.75

²⁷Throughout the discussion, the temporal dependencies are left implicit, assuming that the various operators are valued at the same instant in the measure. In this discussion, the concepts introduced in the previous paragraphs are also taken for granted (definition of the various operators, rules of the beam-splitter, etc.).

and Eq. 1.76), it is possible to retrieve the equations for the outputs signals:

$$\hat{a}_3 = \frac{1}{\sqrt{2}}(\hat{a}_S + i\hat{a}_{LO}), \quad (1.136)$$

$$\hat{a}_4 = \frac{1}{\sqrt{2}}(\hat{a}_{LO} + i\hat{a}_S). \quad (1.137)$$

The two detectors' photocurrent signals can be schematized through the operators:

$$\hat{I}_3 \propto \hat{a}_3^\dagger \hat{a}_3 = \frac{1}{2}(\hat{a}_S^\dagger \hat{a}_S + i\hat{a}_S^\dagger \hat{a}_{LO} - i\hat{a}_L^\dagger \hat{a}_S + \hat{a}_L^\dagger \hat{a}_{LO}) \quad (1.138)$$

$$\hat{I}_4 \propto \hat{a}_4^\dagger \hat{a}_4 = \frac{1}{2}(\hat{a}_S^\dagger \hat{a}_S - i\hat{a}_S^\dagger \hat{a}_{LO} + i\hat{a}_L^\dagger \hat{a}_S + \hat{a}_L^\dagger \hat{a}_{LO}) \quad (1.139)$$

Therefore, the differential current operator \hat{I}_- , representing the differential measurement done at the two detectors' outputs, can be written as:

$$\hat{I}_- = \hat{I}_3 - \hat{I}_4 \propto i(\hat{a}_S^\dagger \hat{a}_{LO} - \hat{a}_{LO}^\dagger \hat{a}_S). \quad (1.140)$$

In the approximation of strong coherent LO its beam can be considered classical and in the latter equation the operator \hat{a}_{LO} can be replaced with $|\alpha_{LO}|e^{i\varphi_{LO}}$ leading to:

$$\hat{I}_- \propto |\alpha_{LO}|(\hat{a}_S^\dagger e^{i(\varphi_{LO} + \pi/2)} + e^{-i(\varphi_{LO} + \pi/2)} \hat{a}_S) = |\alpha_{LO}| \hat{Q}_S \left(\varphi_{LO} + \frac{\pi}{2} \right). \quad (1.141)$$

Therefore, it is immediately visible that a measurement of \hat{I}_- gives information about the quadrature \hat{Q}_S of the signal. Moreover, by controlling the LO phase φ_{LO} it is possible to scan the quadrature signal in the quadrature phase space. This procedure corresponds to a scan of the electric field \hat{E} in the time domain if we consider $r = 0$ in Eq. (1.12). Furthermore, in the balanced homodyne detection, the measured quadrature signal \hat{Q}_S is amplified by a factor proportional to the LO amplitude. This can be useful to get access to small quadrature fluctuations that are covered by the detector background noise otherwise (see chap. 3 for a practical explanation).

The equations above presented do not take into account the measuring time \mathcal{T} and the presence of losses. If we assume that the overall detection efficiency of the assembled balanced detector is η , with the two real detectors identical and schematized as in Fig. 3.1, following the formalism introduced to describe the real detector, the measured quantity with the balanced homodyne detection can be written as:

$$\hat{M}_{HD}(t, \mathcal{T}) = \int_t^{t+\mathcal{T}} dt' \left(\hat{d}_3^\dagger(t') \hat{d}_3(t') - \hat{d}_4^\dagger(t') \hat{d}_4(t') \right), \quad (1.142)$$

where $\hat{d}_3(t)$ and $\hat{d}_4(t)$ have a definition analogue to the one reported in Eq. (1.132), evaluated in terms of $\hat{a}_3(t)$ and $\hat{a}_4(t)$, respectively. It is possible to demonstrate that the mean value and the variance of \hat{M}_{HD} are [100]:

$$\langle m \rangle = i\eta \langle \hat{M}_-(t, \mathcal{T}) \rangle = i\eta \int_t^{t+\mathcal{T}} dt' \langle \hat{a}_S^\dagger(t') \hat{a}_{LO}(t') - \hat{a}_{LO}^\dagger \hat{a}_S(t') \rangle, \quad (1.143)$$

$$(\Delta m)^2 = \eta^2 (\Delta M_-(t, \mathcal{T}))^2 + \eta(1 - \eta) \int_t^{t+\mathcal{T}} dt' \langle \hat{a}_{LO}^\dagger(t') \hat{a}_{LO}(t') + \hat{a}_S^\dagger \hat{a}_S \rangle \quad (1.144)$$

Where $\hat{M}_-(t, \mathcal{T})$ is the homodyne measured quantity corresponding to the temporal integration of the one previously introduced in Eq. (1.140), and $(\Delta M_-(t, \mathcal{T}))^2$ is its variance. In this derivation, it is useful to introduce the homodyne-field operator [100] as:

$$\hat{E}_{HD}(\varphi, t, \mathcal{T}) = \frac{1}{2\mathcal{T}} \int_t^{t+\mathcal{T}} \left(\hat{a}_S^\dagger(t') e^{i(\varphi - \omega_S t')} + \hat{a}_S(t') e^{-i(\varphi - \omega_S t')} \right) \quad (1.145)$$

where ω_S is the frequency of the signal-of-interest field. By making again the assumption that the LO is a strong (bright) coherent state, and by doing the approximation $\hat{a}_{LO} \rightarrow |\alpha_{LO}| e^{i(\theta_{LO} - \omega_{LO} t)}$, where $\omega_{LO} = \omega_S$ is the frequency of the LO radiation²⁸, it is possible to find the following results:

$$\langle m \rangle = 2\eta |\alpha_{LO}| \mathcal{T}^{1/2} \langle \hat{E}_{HD}(\varphi, t, \mathcal{T}) \rangle \quad (1.146)$$

$$(\Delta m)^2 = \eta \mathcal{T} |\alpha_{LO}|^2 \left[(4\eta (\Delta E_{HD}(\varphi, t, \mathcal{T}))^2 + (1 - \eta)) \right] \quad (1.147)$$

where $\varphi = \pi/2 + \theta_{LO}$. The results are similar to the ones that we can get via Eq. (1.141). However, we can see here the presence of an extra-term due to the coupling with the vacuum in the variance of the homodyne measured signal.

1.7 Wigner fuction

As described in the previous section homodyne detection is a technique that allows the measurement of the quadrature signal of a certain quantum state of light under investigation. Regarding the state of light characterization, another useful quantity related to its quadrature signal is the so-called *Wigner function*, which is a quasi-probability function commonly used in quantum optics to asset the non-classicality of light states [112]. Moreover, this quantity can be reconstructed starting from the quadrature measurements done via the homodyne detection scheme as described below.

In general, the Wigner function for a single-mode pure state $|\Phi\rangle$ is defined as [101, 112, 113]:

$$W(x, p) = \frac{1}{\pi\hbar} \int_{-\infty}^{+\infty} \Phi^*(x+q) \Phi(x-q) e^{2iqp/\hbar} dq \quad (1.148)$$

where x and p are the two conjugated variables representing the position and the momentum operators \hat{x} and \hat{p} satisfying the commutation rules $[\hat{x}, \hat{p}] = i\hbar$ [100]. Starting from this definition, the Wigner function can be adapted to represent any couple of conjugated quadrature operators [109] like the quadratures \hat{X} and \hat{Y} defined in Eq. (1.1), used to describe the space phase of the electric field. In this manuscript \hat{X} and \hat{Y} are defined following the description of [100], while their commutator is $[\hat{X}, \hat{Y}] = i/2$. Therefore, it is possible to define $W(X, Y)$ starting from Eq. (1.148) by doing the following substitutions $x \rightarrow X$, $p \rightarrow Y$ and $\hbar \rightarrow 1/2$, yielding to the equation:

$$W(X, Y) = \frac{2}{\pi} \int_{-\infty}^{+\infty} \Phi^*(X+q) \Phi(X-q) e^{4iqY} dq. \quad (1.149)$$

²⁸As already mentioned, the two light states have the same frequency.

This description holds for pure states of light. However, in a real experiment quantum states of light are typically contaminated by the losses, therefore it is no more possible to describe them as a single pure state of light $|\Phi\rangle$ [100]. To give a suitable description of a realistic quantum state, it is better to use the density matrix ($\hat{\rho}$) formalism [100, 101]. In this formalism, a quantum state is, indeed, described as a superposition (mixture) of pure states of light $\{|\psi_i\rangle\}$ [100, 101, 108]:

$$\hat{\rho} = \sum_i P(\psi_i) |\psi_i\rangle\langle\psi_i| \quad (1.150)$$

where $P(\psi_i)$ is probability associated to the pure state $|\psi_i\rangle$.

In this scenario, it is possible to generalize Eq. (1.148) for a generic state described by the density matrix $\hat{\rho}$ [101] as follows:

$$W(X, Y) = \frac{2}{\pi} \int_{-\infty}^{+\infty} \langle X+q | \hat{\rho} | X-q \rangle e^{4iqY} dq. \quad (1.151)$$

As for the density matrix, the Wigner function gives us a complete description of the associated state of light²⁹ [103]. In particular, the Wigner function gives us a description of the density matrix in the XY -phase space [100, 103].

As mentioned at the beginning of this section, the Wigner Function is a quasi-probability distribution that gives information about the light state under investigation: in fact, if $W(X, Y) < 0$ the state is quantum [114]. Therefore, by reconstructing this quantity in our experiment we can asset the non-classicality of the state under study. However, in an experiment, the quantities that we can measure are actually the marginal probability distributions $P(X)$ and $P(Y)$ of \hat{X} and \hat{Y} , respectively. Such quantities are linked to $W(X, Y)$ via the following relations [103, 112, 113]:

$$\int_{-\infty}^{+\infty} W(X, Y) dY = P(X), \quad (1.152)$$

$$\int_{-\infty}^{+\infty} W(X, Y) dX = P(Y). \quad (1.153)$$

In a more general picture, we can think of shifting of a quantity θ the quadratures in XY -phase space, yielding the following shifted quadratures:

$$X_\theta = X \cos(\theta) + Y \sin(\theta), \quad (1.154)$$

$$Y_\theta = -X \sin(\theta) + Y \cos(\theta). \quad (1.155)$$

Following the new notation, the marginal distribution probability of measuring a certain value X_θ for the observable defined via the operator \hat{X}_θ is therefore:

$$P(X_\theta) = \int_{-\infty}^{+\infty} W(X_\theta, Y_\theta) dY_\theta. \quad (1.156)$$

In the same way, it is possible to define the marginal distribution for \hat{Y}_θ .

To re-construct the marginal probability distribution of both quadratures, we have to do a statistical-significant repetition of measurements of these quantities, e.g. via a

²⁹In case of pure state $\hat{\rho} = |\Phi\rangle\langle\Phi|$ and from Eq. (1.151) it is possible to retrieve Eq. (1.148).

homodyne detection scheme. After that, we can invert the corresponding equations (Eq. (1.152) or Eq. (1.153)) to get $W(X, Y)$. This is the philosophy under the *quantum state tomography* that allows via an inversion process to reconstruct the quantum state of light under investigation [103]. An example of this procedure is provided in the experimental work described in chapter 5.

CHAPTER 2

Quantum Cascade Lasers

2.1 QCL working principle	49
2.2 QCL structure	51
2.2.1 The cascade process	54
2.3 QCL spectral features	54
2.3.1 Emitted wavelength	54
2.3.2 Linewidth	54
2.4 Comb emission	56

QCLs are hetero-structured semiconductor lasers, characterized by a complex structure composed of multiple semiconductor layers of nanometric thickness. This peculiar structure enables the development of devices capable of producing coherent radiation at the desired wavelength in the spectral range from mid- to far-infrared. This chapter describes the QCLs' working principles and their key characteristics. More info about such devices are available in [15] and in [2, 3]. A review of comb operation in these devices is given in [32].

2.1 QCL working principle

Conventional semiconductor lasers (e.g. diode lasers) are distinguished by an emission based on an interband transition that occurs inside the active medium between the conduction and valence bands. The wavelength of the emitted radiation is determined by the difference in energy between the two bands, the so-called *energy gap*, and it is thus an intrinsic property of the active medium. Due to the hard availability of semiconductors characterized by sufficiently small energy gap and, at the same time, easy to implement and sufficiently robust¹, the typical semiconductor lasers cannot emit at wavelengths above $\sim 3\mu\text{m}$ [2]. In bipolar diode lasers, each electron injected

¹For example, lead-salt diode laser are semiconductor devices characterized by a small energy gap, however, these devices have to work at cryogenic temperature. Furthermore, these devices are characterized by a low efficiency of conversion between pumping current and emitted optical power [15].

2.1 QCL working principle

into the active zone, recombining with a hole, can generate a single photon, and the output power from each of the two facets of the laser cavity is equal to [110]:

$$P = \frac{1}{2e} h\nu \eta (I - I_{th}), \quad (2.1)$$

where e is the electron charge, I is the supplied laser current, I_{th} is the lasing threshold current, $h\nu$ is the photon energy, while $0 \leq \eta \leq 1$ is a parameter that depends on the cavity properties, as the losses, the cavity length and the reflectivity. The factor $1/2$ is, instead, due to the equipartition of the output power between the two cavity facets. By fixing all the parameters, with the exception of the emission frequency, from this equation it is immediately possible to notice that the emission power decreases by increasing the laser wavelength (λ), being $\nu \propto 1/\lambda$. Furthermore, typically the losses increase by increasing the wavelength, and η decreases consequently. This gives, therefore, an idea about the inefficiency of using standard bipolar laser for the MIR wavelength [3].

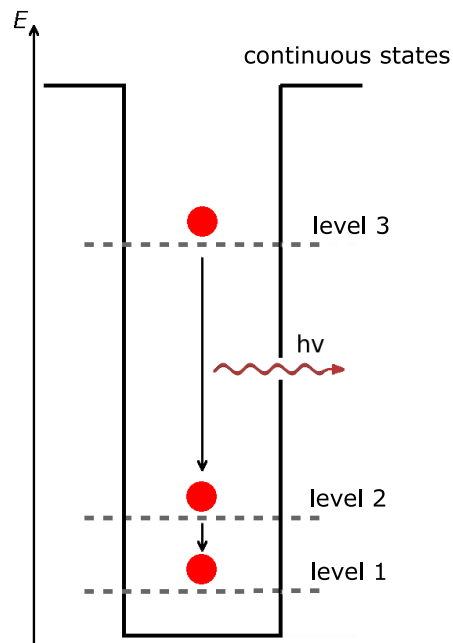


Figure 2.1: Energy-level scheme of a quantum well. The depicted quantum well is characterized by three discrete energy levels: in the electronic transition between levels 3 and 2, a photon of energy $h\nu$ is emitted. Non-radiative processes are, instead, at the basis of the transition between level 2 and level 1.

Unlike what happens for bipolar semiconductor lasers, the wavelength emitted by quantum cascade lasers does not depend on the size of the gap, but on the confinement of the electrons in well-defined energy levels of sub-bands of the conduction band [15, 30, 115]. The active medium of such devices is composed of different layers of semiconductor materials, which are grown via the molecular beam epitaxy (MBE) technique. This technique allows the growth of single layers of different chemical compositions with a nanometric thickness. In the case of QCLs, this results in a variation of the electric potential encountered by electrons as they propagate through the active medium, which can be represented as a series of wells and barriers (quantum

wells). This determines a division of the conduction band in discrete sublevels, as depicted in Fig. 2.1. Referring to this figure, the QCL lasing transition occurs between two of these sublevels (level 1 and level 3): electrons are injected in level 3 and they relax in level 2 via stimulated emission. A non-radiative relaxation process (electron-phonon scattering), then, assures that level 2 is quickly and efficiently emptied into level 1. The gap between such levels, and therefore the emitted wavelength, is determined by the material and the thickness of the layer composing the active medium [15].

Furthermore, QCLs are able to emit high power, even above the Watt level, thanks to a cascade mechanism. The heterostructured active medium is, indeed, characterized by multiple *active regions* (multiple quantum wells) connected by *injection regions* serving as channels for electrons. Therefore, each electron, flowing into the active medium, contributes multiple times to the laser transition. Furthermore, differently from the bipolar standard semiconductor laser, QCLs are *unipolar devices* because the electrons are the only charge carriers engaged in the lasing process. This, together with their particularly fast dynamics, has consequences also in the QCLs' intrinsic linewidth, which is much lower than that of bipolar junction lasers [116].

2.2 QCL structure

Demonstrated in 1994 [30], the first QCLs were created by alternating layers of InGaAs with layers of InAlAs on a substrate of InP. Today, they are manufactured almost the same way, and they can be engineered to emit wavelengths ranging from 3.4 μm to 24 μm [15]. A few years later, GaAs-AlGaAs devices were developed with an emission wavelength ranging from 8 μm to 80 μm [15, 117–119]. However, the actual structure of these devices is more complex with respect to the simple quantum-well model introduced in the previous section. An example of the typical QCL structure is reported in Fig. 2.2. More specifically, the layers in which the laser action occurs (composing the active region in Fig. 2.2a and b) form a waveguide. The beam propagates parallel to the layers and the facets of the guide are cut perpendicular to the direction of the beam, forming the semi-reflection mirrors² of the laser cavity (Fig. 2.2 c). As shown in Fig. 2.2, the electrons are injected in the waveguide via gold (Au) connections. Here they experience the N -stage cascade³ of the heterostructure active medium (each stage width is of the order of 50 nm, as depicted in Fig. 2.2 c). Each stage is divided into an electron injection region and an active region in which the laser transition takes place (Fig. 2.2 c and Fig. 2.3). The operating principle of this complex system is based on the confinement of an electron in a potential well, its Schrödinger equation leads to a discrete system of energy levels [2, 3, 15]. Additionally, if two adjacent wells are characterized approximately by the same energy and the barrier between them is quite thin, the electron wave function is no longer localized. The new wave function is given by the linear combination of the previous ones, which extends into the two wells. Moving from the example of two wells to numerous layers of semiconductor material of ad-hoc-chosen composition and thickness, i.e. to multiple wells, the possibilities for

²The used waveguide semiconductors have a typical refractive index of the order of 3, while air has a refractive index of around 1: these conditions cause a reflection of the intracavity (i.e. intra-waveguide) propagating beam about 30%, sufficient to guarantee the laser action [15].

³The number of stages typically range between 10 and 100 [15].

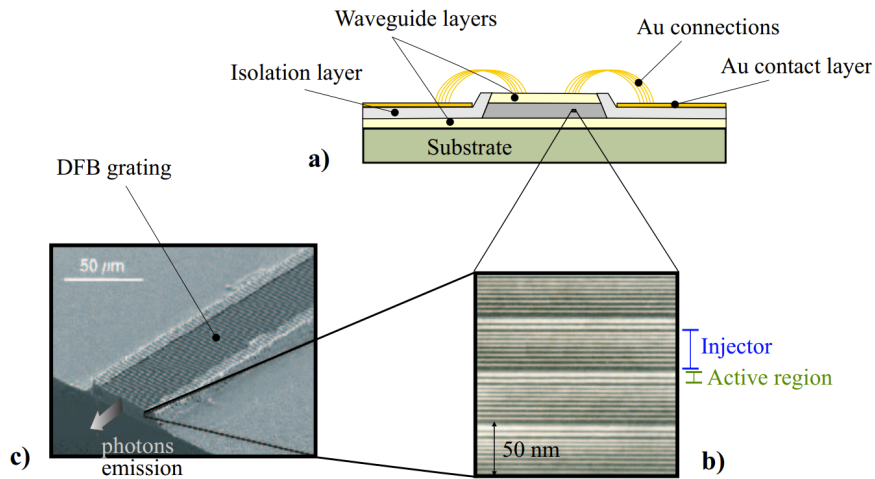


Figure 2.2: (a) A QCL representation from the front facet. Bottom: two images of a QCL taken via an electronic microscope. In (b), there is an image from above of a QCL, and in (c) of its active medium seen from the front. Image taken from [2].

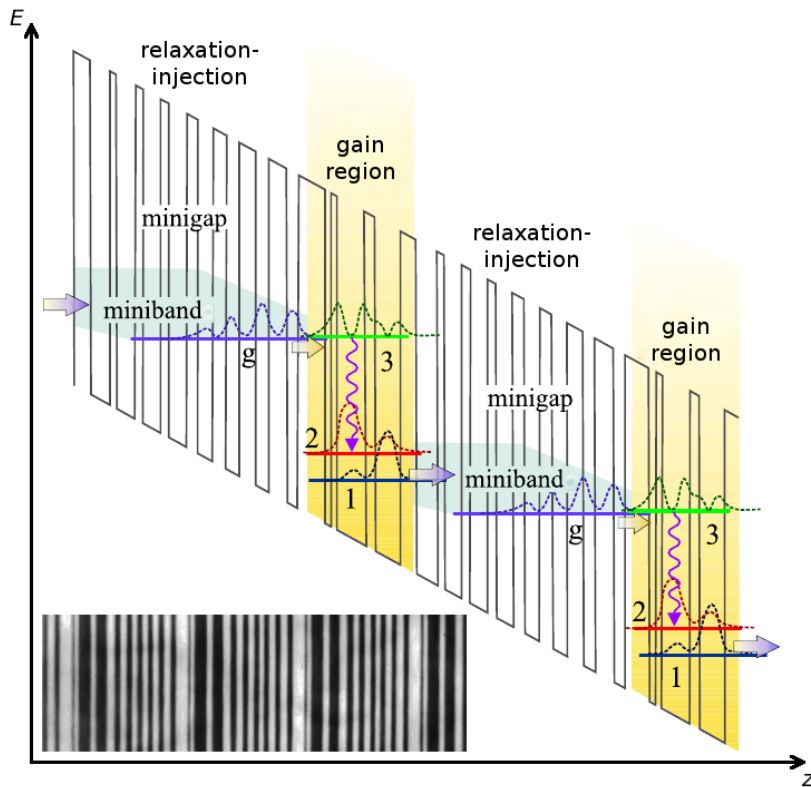


Figure 2.3: Scheme of a QCL's band structure. A three-quantum-well vertical-transition architecture is depicted in the scheme. There are two time periods displayed. The square moduli of the electronic wavefunctions are shown alongside the superlattice. The externally applied electric field determines the overall slope. The thick arrows represent electron transport, whereas the thin wavy arrows represent laser transition. The ground-state miniband in the relaxation-injection area is denoted by g . A TEM micrograph of a clived cross-section of an active region of the same type is shown, similarly to the one shown in Fig. 2.2 c. Light regions are AlInAs barriers, while dark regions are GaInAs wells. Pictures taken from [3].

manipulating the wave functions and the levels structures emerge quite clearly. Indeed, these latter quantities can be really discrete as in the case of the active region (Fig. 2.3),

or they can determine the formation of *minibands* where the electrons flow freely⁴, as in the case of the injection/relaxation regions. In particular, the electron injection region is composed of quantum wells separated by very thin barriers, characterized by thicknesses of the order of 1 – 3 nm [15], forming a *super-latex* structure. As a result, the electronic wave functions stretch into several layers, generating narrow minibands separated by minigaps and with a low state density. According to [15], the number of states in a miniband equals the number of quantum wells. Furthermore, when a strong electric field⁵ is applied to the active region, it causes a cascade of the potential wells. The electrons in the miniband of an injection region have the same energy as the level 3 of the adjacent active region, where they migrate by a tunnelling effect. To prevent the electron escape from the active region via thermal excitation, the materials are selected so that the energy of level 3 is sufficiently below the top of the potential well⁶. As already explained in the previous section via Fig. 2.1, the lasing process takes place between level 3 and level 2. To guarantee the lasing transition, it is necessary to maintain a population inversion between these two levels: the requirement is therefore that the average level-2 lifetime must be significantly lower than the level-3 ones. In general, the electron's average lifetime in these levels depends on the emission of optical phonons: an increment of the energy gap between these levels, with respect to the average energy of the phonons, increases the level-3 average lifetime [15]. Commonly the energy gap between the lasing levels is selected to be an order of magnitude higher than the energy of such photons, which is typical of the order of 35 meV [3, 15]. This leads to a typical average lifetime for the higher level (level 3) of the order of ps. Instead, the energy gap between levels 1 and 2 is of the order of the optical photons' energy. Therefore, the time scale decay of electrons from level 2 to level 1 is of the order of tenths of ps, allowing a quite fast emptying of level 2. From an experimental point of view, the described fast dynamics allows modulating the radiation of QCLs up to GHz and above [15, 33], making such devices appealing for communications. The last barrier of the active zone is often quite thin to promote the depletion of the 1 level, favouring the electron tunnel effect to the adjacent injection region. In this region, due to the miniband structure, the electrons quickly relax to the ground state, where they are injected to the next active region⁷.

The three-level conduction band works well in QCL with wavelength shorter than 11 μm [2, 15]. A variety of issues come up with longer wavelengths, but the challenge of obtaining population inversion stands out: the energy difference between levels 3 and 2 must decrease contextually as the wavelength is increased; once this difference reaches the typical energy of optical phonons, the electrons decay non-radiatively, which prevents the laser transition. Being the collisions between electrons the most efficient mechanism for emptying the lower level, in these conditions, the most suitable implementation for the active region is to use a two-level system for the lasing transition

⁴The latter case is obtained when the states are engineered so that the separation between the levels is less than the electrons' thermal energy.

⁵The applied electric fields vary from 1 to 10 kV/mm [15].

⁶To have QCL capable of operating even at room temperature, it is crucial that the energy difference between the top of the quantum well and the level in question is significantly greater than the energy of the phonons in the crystal. Otherwise, these electrons would be excited towards continuous states outside the hole and there would be no laser transition[15].

⁷Here a minigap prevents the opposite injection, i.e. from the level 3 of an active region to the ground state of the previous injection region.

made by two successive minibands. For more information see [2, 3, 15].

2.2.1 The cascade process

The so-called cascade process enables QCLs to achieve high output powers [15]: once an electron emits a laser photon in an active region, it goes through the adjacent injection region and then ends up in the next active region, where it emits a new photon⁸. For these devices, the Eq. 2.1 still holds as long as the right side of the equation is properly multiplied by the number of stages N_s of the active medium. Therefore, a higher number of stages leads to a proportionally higher emitted power. This feature, combined with the fact that the semiconductor materials composing QCLs have large gaps supporting high current flows (up to 1 A), allows QCLs to achieve output powers up to a thousand times greater than the common diode lasers hypothetically engineered to emit at the same wavelength [120].

2.3 QCL spectral features

2.3.1 Emitted wavelength

In the active region, the depth of the wells limits the shortest wavelength that QCLs can emit. By placing level 3 too close to the top of the holes, electrons are easily stimulated to continuum states. It has been experimentally confirmed that the energy of the emitted photons cannot exceed half the depth of the potential wells in devices suitable to work nearby room temperature [121]. Variations in the active medium's temperature have the effect of changing the active medium's refractive index and, as a result, tuning the wavelength emitted by these devices [15]. In particular, when the temperature rises, the refraction index rises, increasing the emitted wavelength. An analogous effect is achieved by changing the supplying current.

2.3.2 Linewidth

In general, when we talk about the laser linewidth, we mean the full width at half maximum (FWHM) of the laser's spectral emission profile over a given timescale. There are several effects which can contribute to the laser linewidth, some due to fundamental laws of physics and some due to additional technical noise. Temperature and (driving) current fluctuations are two of the most significant technical contributions. When the linewidth is only due to fundamental mechanisms (essentially the spontaneous emission of photons), we speak of *intrinsic linewidth* and its value is calculated with the Schawlow-Townes formula [122]. The intrinsic linewidth of QCLs is predicted to be significantly narrower than that of a conventional semiconductor laser [123]. This is because, in the conventional semiconductor laser, the laser transition occurs between the conduction band and the valence band, which have dispersion curves with opposite concavities when viewed in the space of the wave vectors, as shown in Fig. 2.4a. In QCLs, on the other hand, the laser transition occurs between two

⁸The photons are emitted by electron via stimulated emission. Therefore, they have the same energy, propagation direction, and phase as the stimulating photons.

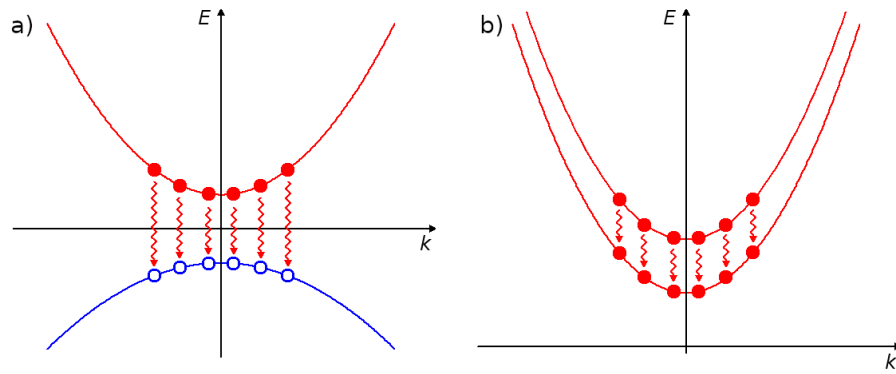


Figure 2.4: Scheme of the band of transition in the case of a standard semiconductor laser (a) and of a QCL (b) in the $E - k$ space. a) The conduction band and the relative electrons are depicted in red, while the valence band and the relative holes are represented in blue. The two bands are characterized by an opposite concavity. As a consequence, their energy gap increases as k increases from $k = 0$. This leads to the emission of photons at higher frequencies. (symbolized by arrows of greater length). (b) Scheme of two QCL sub-bands: These have the same curvature and, therefore the emitted frequency remains constant for overall the k represented.

sub-bands (or sublevel as described in the previous sections) of the same band, i.e. the conduction band. These subbands are characterized by the same curvature (Fig. 2.4b). As a consequence, the emission is expected to be narrower, similar to what happens in solid-state lasers [110]. This prediction has been experimentally confirmed by Bartalini *et al.* [122]. In their experiment, by exploiting an absorption line of the CO_2 molecule

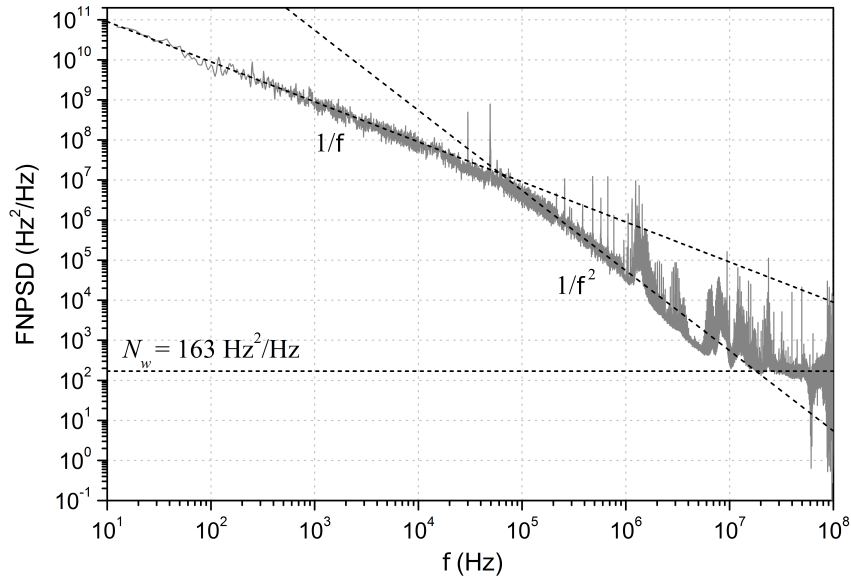


Figure 2.5: Frequency noise power spectral density (FNPSD) of a MIR QCL, in double logarithmic scale [122]. The noise profile is characterised by a $1/f$ trend for Fourier transform frequencies lower than 50 kHz, and by a $1/f^2$ trend for frequencies up to 10 MHz. For higher frequencies, the noise becomes flat, at the white noise level of $N_w = 163 \text{ Hz}^2/\text{Hz}$. The line profile that belongs to this latter noise component is purely Lorentzian with an FWHM of $\pi N_w = 510(160) \text{ Hz}$. Figure taken from [122].

to convert frequency fluctuations into amplitude fluctuations, the frequency spectral

noise density of a MIR QCL⁹ was analyzed (Fig. 2.5). In particular, they observed that the measured Frequency Noise Power Spectral Density (FNPSD) has a profile characterized by three different trends: a $1/f$ trend at low Fourier frequencies, followed by a $1/f^2$, and a final flattening to a constant value (N_w in Fig. 2.5) for frequencies higher than 10 MHz, which is typical of white noise. According to the theory of frequency noise, the line profile that belongs to the white noise component is purely Lorentzian, with a FWHM value of πN_w . This corresponds to the intrinsic linewidth mentioned above, and in the case of QCLs¹⁰ is of the order of 500 Hz [38]. From the linewidth measurement, it is also possible to retrieve the typical coherence time, τ_c , of these devices, expected to be the inverse of the linewidth itself. However, in general, the technical noise contributions (mostly depending on the characteristics of the power supply or on the temperature stabilization) strongly enlarge the actual laser linewidth. This leads to a QCL actual linewidth ranging from hundreds of kHz to few MHz[15] and to a corresponding coherence time $\tau_c \sim 1 - 10 \mu\text{s}$.

2.4 Comb emission

Optical frequency combs OFCs are particular multifrequency coherent photonic states consisting, in the frequency domain, of a series of equally spaced modes having a well-defined phase relationship [52]. The *mode-locking mechanism* converts the group of independent modes into a set of modes with fixed reciprocal phases and modal spacing. The frequency components of such a spectrum can be therefore described in the following way [3]:

$$\nu_N = N f_s + f_o, \quad (2.2)$$

where f_s is the *mode spacing*, f_o is the *offset frequency*, while N is a large integer¹¹. Frequency combs are typically generated by stabilized mode-locked pulsed lasers [56, 57, 124, 125]. Such lasers' modes can be utilised as accurate frequency references in the visible and NIR spectral regions, proving a direct link between optical frequencies (which are not directly measurable with a counter) and radio frequencies. Due to this capability, they have become essential instruments in many fundamental and practical studies [52, 126].

To expand the applicability of frequency combs in the fields of telecommunications, molecular spectroscopy and gas detection, significant efforts have been made towards both the miniaturization of comb sources and the extension of their operation towards new spectral regions (e.g., mid and far infrared, ultraviolet) [2, 3]. As already mentioned in the introduction chapter, the lack of fs pulsed laser in the MIR has required the use of non-linear processes to transfer OFCs generated at lower wavelengths in the MIR. Matching the two requirements of being compact sources and emitting in the mid-to-far infrared spectral region, QCLs have been soon considered as valid candidates for frequency comb generation in this wavelength range. Due to the structure and working

⁹The tested QCL emission is centred around $4.33 \mu\text{m}$.

¹⁰The intrinsic linewidth of a QCL is comparable with the natural linewidth of the rovibrational transitions of molecules in the infrared: these devices can be successfully used to perform precision spectroscopic measurements.

¹¹The notation used is: ν for optical frequencies, f for radio-frequencies.

principle of their active region, in QCLs the upper laser level lifetime (≈ 0.5 ps) is much shorter than the optical cavity round-trip time (≈ 130 ps for devices with 6 mm long waveguide) [15, 32]. Consequently, the energy cannot be accumulated during the round-trip propagation in the cavity. Therefore, the maintenance and amplification of optical pulses are not possible and the locking between the modes with the losses' modulation (*passive mode locking*) is not feasible [32, 51, 127]. An alternative to passive mode locking is the active locking between the modes by means of gain modulation, successfully demonstrated in [77, 128–130]. However, this technique has several limits: it needs extensive and complex optical apparatus; the devices must be powered slightly beyond the threshold to avoid gain saturation, which drastically limits the available power; moreover, the duration of the pulses has a lower bound, preventing them from reaching the inverse of the gain band.

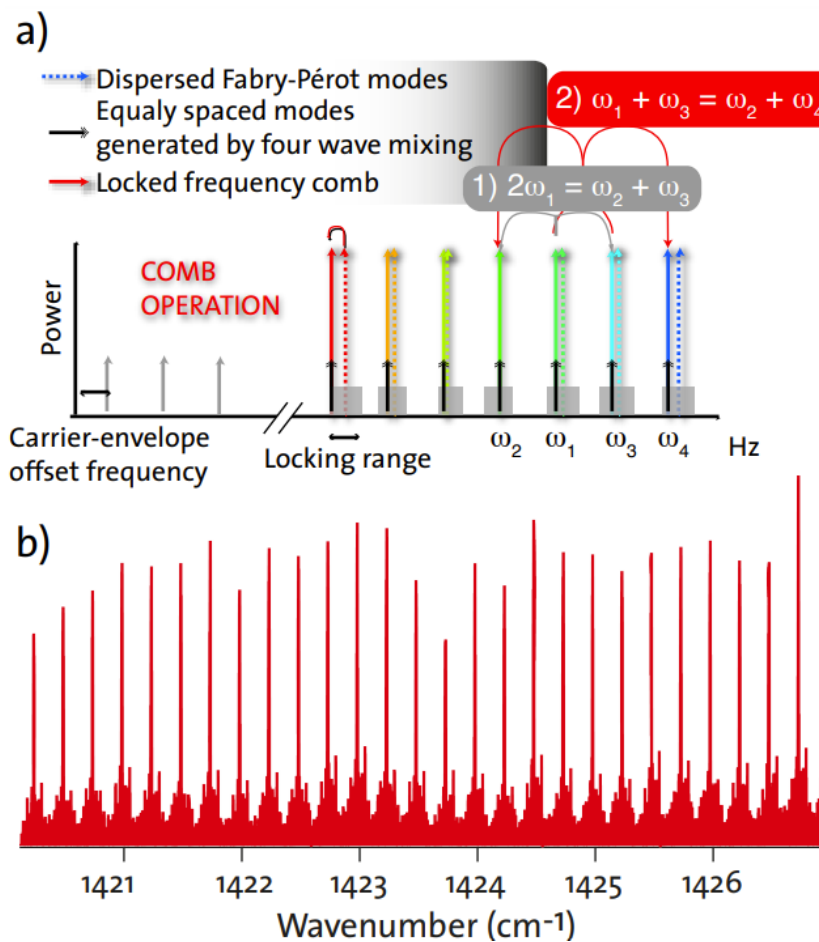


Figure 2.6: a) Scheme of the FWM process in Fabry-Pérot QCL. The dashed arrows indicate the frequency modes emitted by a multimodal Fabry-Pérot QCL. To these modes are added the secondary modes (black lines with double arrow) generated by the degenerate FWM (example 1 in grey) to the non-degenerate FWM (example 2 in red). In the case of degenerate FWM, accordingly to the grey example, two photons competent in the mode ω_1 mix to generate a pair of photons competent one in the mode ω_2 and the other ω_3 . While the red example, should a non-degenerate FWM process where two photons of independent modes (ω_1 and ω_2) combine to generate a pair of photons competent to the other two modes (ω_3 and ω_4). This process involves phase locking between the modes of the QCL (Fabry-Pérot modes are phase-locked to the modes generated by the FWM by optical injection). The result is a frequency comb with phase-locked and equally spaced modes in the frequency domain (modes represented by solid line arrows). b) Example of a comb emitted by a Fabry-Pérot QCL. Figure adapted from [32].

Quite surprisingly, in the last decade, the possibility of direct comb emission from free-running multimode Fabry-Pérot¹² QCLs (QCL-combs) has been demonstrated [32, 51, 68]. These devices are engineered to have low group velocity dispersion¹³ [32]. In these devices, the comb emission is due to the third-order non-linearity of the laser active medium which triggers a FWM process. This process optically injects the independent longitudinal modes emitted spontaneously by Fabry-Pérot devices, coupling them with those generated by the mixing process itself. This induces a strong correlation among these modes. The result is a frequency combs generation with equally spaced modes and with a fixed phase relation given by the non-linear process. The spacing between the modes corresponds to the FSR of the cavity. In particular, the comb emission out of a QCL-comb is more a quasi-continuous emission rather than a pulse [32]. The working principle of the QCL-comb generation is depicted in Fig. 2.6. Many advanced techniques have been employed to demonstrate the effective phase-coherence of QCL-comb multimodal emission. Among these techniques, I would like to mention the well-known intermodal beat note spectroscopy [51], the Shifted Wave Interference Fourier Transform Spectroscopy (SWIFTS) [131–133], the characterization of the emitted modes both individually and in groups [134, 135], the Vernier technique, which employs an optical cavity for the characterization of frequency noise [136], as well as the characterization, via Fourier transform, of the frequency combs generated by QCLs with respect to a reference comb (FACE) [137]. All these techniques confirmed the existence of phase coherence among the modes of QCL-combs compatible with the one observable in a standard frequency comb.

¹²Fabry-Pérot QCLs are devices characterised by a simple waveguide in semiconductor material as laser cavity. In general, these devices have multimode emissions, as there is no selection mechanism for the emitted frequency. Instead in the so-called distributed *feedback* QCLs, the waveguide has a grating engraved on it which acts as a frequency filter inducing a single-mode emission [15].

¹³The group velocity dispersion (GVD) of the cavity plays a crucial role in four-wave mixing's capacity to produce mode proliferation and, ultimately, comb operation. E.g. for an active region characterized by a gain bandwidth of 100 cm^{-1} the number of modes emitted by a Fabry-Pérot QCL is about 300 modes for a 3 mm laser waveguide. If we consider a cavity finesse of about 5, it is possible to find the following upper bound for keeping the modes efficient coupling by FWM: $\text{GVD} < 560\text{ fs}^2/\text{mm}$ [32].

CHAPTER 3

Shot-noise limited mid-infrared balanced homodyne detector

3.1	Introduction to MIR balanced detection	59
3.2	Working principle	61
3.2.1	BHD characterization	63
3.2.2	LO characterization	64
3.3	Experimental setup	64
3.3.1	Loss budget for BHD characterization	66
3.3.2	Loss budget for LO characterization	67
3.4	Results and discussion	67
3.5	Summary and remarks	72

This chapter is dedicated to my experimental work regarding the realization of a MIR shot-noise-limited balanced detector as a tool for quantum measurement in this spectral region. The presented setup and results refer to the work published in 2021 in *Optics Express* [99].

The chapter is organized as follows: the first part is dedicated to the motivation at the basis of the implementation of a shot-noise-limited balanced detector working in the MIR (sec. 3.1); then, the theoretical working principle of the detector characterization is introduced (sec. 3.3), followed by the presentation and discussion of the achieved results (sec. 3.4); finally, a brief summary and the final remarks are given (sec. 3.5).

3.1 Introduction to MIR balanced detection

Balanced homodyne detection is a measurement technique widely spread and used in quantum optics [100, 138–144]. From a quantum perspective, this technique can prove the non-classicality of a light state via an electric field quadrature measurement. As described in sec. section 1.6,a balanced homodyne detector (BHD) relies on a

differential measurement performed with two identical detectors, detecting at the two outputs of a 50/50 BS a combination of the signal of interest with a reference radiation (the LO). Due to the equal splitting of the signal in two different but identical paths (i. e. the two paths must have the same length and the same type of detector), the common noise (e. g. correlated noise due to the photon-generation process or amplification or $1/f$ -noise in case of QCLs) is, in principle, suppressed when the balanced difference is performed¹. Therefore, in a BHD any extra classical noise affecting the measurement can be cancelled out² and it is possible to achieve the detection sensitivity requested by the standard quantum limit [145]. In the linear responsivity regime, the variance of the measured differential signal is proportional to the product between the variance of the tested field quadrature and the amplitude of the LO (section 1.6.2). As a consequence, in the limit given by the saturation of the detection system, increasing the LO amplitude results in a quadrature variance magnification and it can allow for measuring even small fluctuations (variance) of the tested signal [100]. Given all these benefits, BHDs have been massively utilized in NIR quantum optics schemes [100, 140–142, 146, 147], and, in particular, in CV quantum communication both in optical fibers and free-space links [148–150]. A BHD can be a valid tool to explore the quantum feature of the MIR CV light emitted by QCLs, as well.

The aim of the work described and published in the manuscript [99] is to explore the extension of MIR balanced homodyne to the quantum level. In this spectral region, balanced detection has already been investigated in many classical applications such as frequency-modulation spectroscopy [151], difference-frequency laser spectroscopy [152], balanced radiometric detection [153], and Doppler-free spectroscopy [38]. Other optical schemes suitable for single-photon quantum applications, such as coincidence measurements [154] or free-space Quantum Key Distribution with discrete variables [49], have so far been studied. The general goal of the implemented BHD is to equip the MIR with a tool suitable for testing CV states of light at the quantum level. In particular, the here-presented BHD has been tested with a MIR QCL, with the aim of realizing a novel tool allowing the investigation of QCLs-radiation quantum properties which are yet unexplored.

The implemented setup, as described in the following sections, is a versatile setup that allows not only to perform the balanced differential measurement required by the balanced homodyne detection scheme but can be used to compute different operations with the same stream of acquired data (dataset) thanks to a post-processing data analysis approach. This method has allowed characterizing at the same time both the BHD performance in terms of noise suppression and amplitude noise of the used LO, by analysing the difference and the sum of the output signals from the detectors. The BHD characterization procedure is described in detail in the next sections, from both a theoretical and experimental point of view. More details concerning the theory under such application can be found in [100], in chapter 1, and in Appendix A.1.

¹This is true up to the limit given by the maximum extinguishable noise achievable with the implemented setup, typically expressed in term of CMRR (see the sections below for a detailed explanation and analysis)

²If the extra classical noise does not exceed the maximum CMRR, otherwise it can be at least reduced.

3.2 Working principle

The sketch of the working principle of a real balanced detector is reported in Fig. 3.1a. It consists of a 50/50 BS and two identical photovoltaic detectors (real detectors D_1 and D_2). To characterize a BHD, it is sufficient to send the LO radiation, described via its field operator \hat{a} , onto the 50/50 BS, measuring the sum and the difference of the photocurrents generated by the two photovoltaic detectors (\hat{I}_{3D} and \hat{I}_{4D})³. In this way, it is possible to test the noise suppression performance of the system via the measurement of the maximum achievable Common-Mode Rejection Ratio (CMRR) and to prove that the differential detection is shot-noise limited. Furthermore, the possibility of measuring sub-shot-noise non-classical signals (e.g. as the one expected by squeezed states of light [100]) is tested by demonstrating that the clearance (i.e. the ratio between the shot-noise level, retrieved via the differential measurement, and the background noise) is significantly larger than one. In the following dissertation, we assume that the detectors are identical with no saturation and with instantaneous and linear responsivity. In the creation and annihilation operators, any time dependence is neglected. Furthermore, the detection system is assumed to be perfectly balanced to benefit from the advantages of a balanced detection in terms of noise suppression [100, 145]. The two identical photovoltaic detectors (in our case two MIR MCT detectors) generate a photocurrent that, in the linear responsivity regime, is proportional to the incident power. As a consequence, by studying the statistical properties of the output photocurrent (e.g. mean value, variance), it is possible to get information about the statistics of the incident light. In an ideal scenario, a perfect photovoltaic detector (D_3 and D_4) generates an electron for each incident (and absorbed) photon (section 1.6.1). However, in a real detector losses occur and, as a consequence, the translation rate between incident photons and generated electrons, known as quantum efficiency (η_{eff}), is lower than one (section 1.6.1). In quantum optics, real photodetector losses can be modelled a BS⁴ which couples the incident radiation (e.g. the output radiation from the 50/50 BS described via the operators \hat{a}_3 and \hat{a}_4 , fig. 3.1) with the vacuum field (e.g. \hat{v}_3 and \hat{v}_4), as described in sec. 1.6.1 [100]. Furthermore, in a real optical setup, the propagating optical radiation is attenuated due to absorption and reflection from optical components. Also in this case it is possible to model the losses as a BS mixing the propagating beam with the vacuum field. The loss budget on the implemented BHD should be, therefore, carefully addressed in order to give the right interpretation of the data, taking into account all the losses contributions that may affect the measurements. For instance, if we want to characterize the implemented balanced detector to test its applicability as BHD for quantum light characterization, the LO losses are not relevant, being just the reference radiation, and we must take into account only the optical losses that affect the path (named *input* in Fig. 3.1) in which the possible quantum state under investigation propagates [100] (e.g. the losses of the 50/50 BS, of the photodetectors and of the other optical elements that may be placed in the two 50/50 BS output paths). Differently, if the goal is to characterize the implemented balanced

³Referring to Fig. 3.1a the LO radiation enters via the *LO* path of the BS, while no radiation is sent in the *Input* path. Therefore, the *LO* is mixed with the vacuum state.

⁴as described in sec. 1.6.1. The losses' BS is described via the transmission coefficient $T_L = \sqrt{\eta_{\text{eff}}}$ and the reflection coefficient $R_L = i(\sqrt{1-\eta_{\text{eff}}})$.

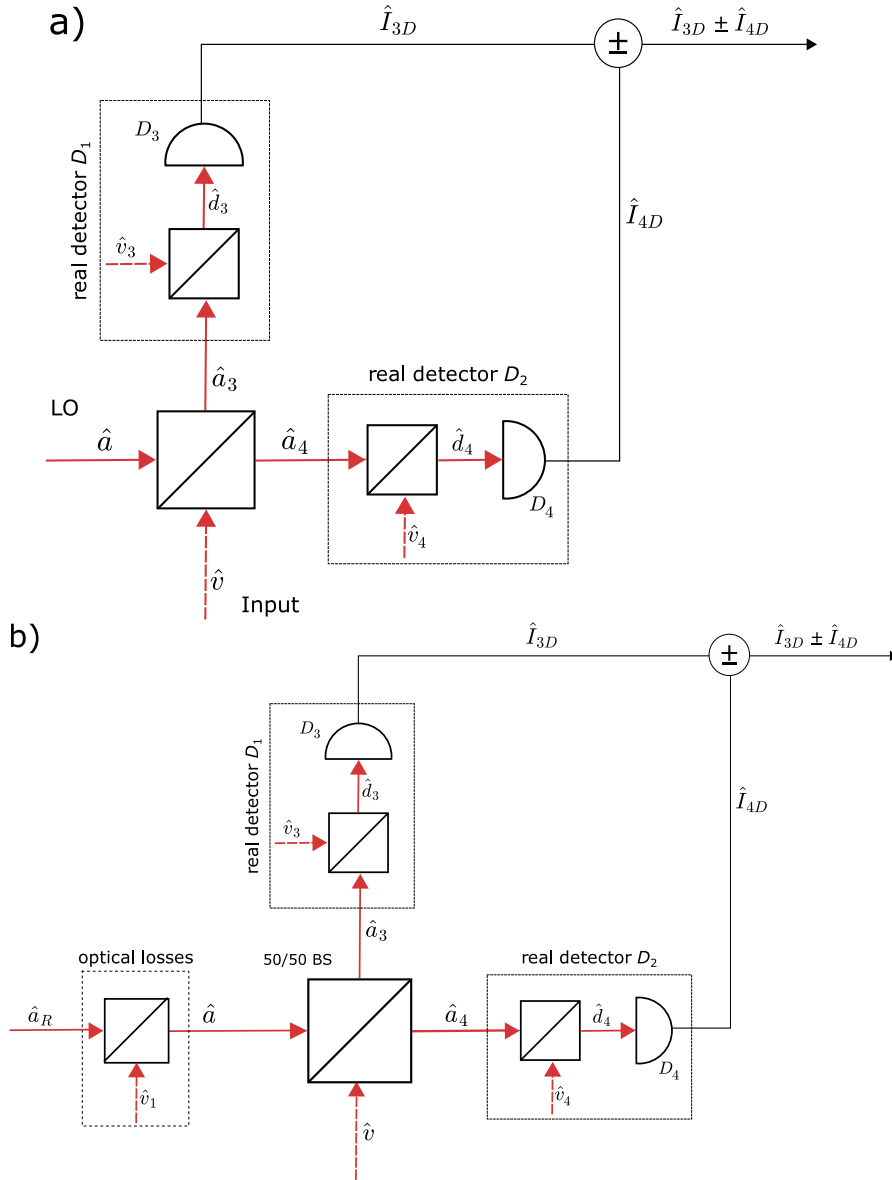


Figure 3.1: Conceptual working scheme for a real balanced detector with losses (a) and of the real balanced detector used to characterize the amplitude noise of a certain source (b). In (a) the LO radiation (LO), represented by the operator \hat{a} , is mixed via a 50/50 BS with the vacuum field (\hat{v} , Input), generating the output fields (\hat{a}_3 and \hat{a}_4) that are collected by two real detectors (D_1 and D_2). Each real detector is schematized with an ideal detector (D_3 and D_4) and a BS that accounts for the losses by mixing the incident field with the vacuum field (\hat{v}_3 and \hat{v}_4). The collected power radiation described via the operator \hat{d}_3 and \hat{d}_4 is transformed in a proportional photocurrent (\hat{I}_{3D} and \hat{I}_{4D}) by the photovoltaic detectors. The measured photovoltaic signals are used to retrieve information regarding the shot-noise level (by measuring the difference) and the overall amplitude noise (by measuring the sum) of the collected radiation. In (b) it is added the part of optical losses (described again via a BS that couples the radiation with the vacuum \hat{v}_1) affecting the LO radiation, which is now described with the operator \hat{a}_R .

detector for testing the statistic of the LO itself, we must address an optical loss budget taking into account also the optical losses experienced by the LO, as it becomes the radiation under investigation. In Fig. 3.1 and in the following paragraphs we describe both scenarios. In particular, Fig. 3.1a refers to the characterization of the BHD, while 3.1b refers to the application of the balanced detector for LO characterization.

3.2.1 BHD characterization

In the characterization of the BHD as a shot-noise-limited detector, the losses that matter are those affecting the input light described by the operator \hat{v} , as shown in Fig. 3.1. Therefore, the loss budget must take into account all the optical losses experienced in the two output paths of the BS into account, including the losses of the BS itself, and also the detection efficiency of the two photovoltaic detectors. By defining η_1 as the overall optical transmission of each of the two paths⁵, we can incorporate such contribution in the transmission coefficient of the BSs simulating in 3.1a the lossy photodetectors, i.e. $\eta = \eta_1 \cdot \eta_{\text{eff}}$. As already stated, in the BHD characterization the measured quantities are the sum and the difference of the photovoltaic detectors' photocurrents (\hat{I}_{3D} and \hat{I}_{4D}) that are proportional to the flux of incident photons. This latter quantity, once integrated in the measured time, gives the mean value of the incident photons and information concerning the photon number statistics of the tested light (section 1.6). Therefore, in the case that the input mode \hat{v} is the vacuum field, the mentioned quantities leads to the following results:

$$\langle \hat{N}_+^D \rangle = \eta \langle \hat{n} \rangle, \quad (3.1)$$

$$(\Delta N_+^D)^2 = \eta^2 (\Delta n)^2 + \eta(1-\eta) \langle \hat{n} \rangle, \quad (3.2)$$

$$\langle \hat{N}_-^D \rangle = 0, \quad (3.3)$$

$$(\Delta N_-^D)^2 = \eta \langle \hat{n} \rangle, \quad (3.4)$$

where \hat{N}_+^D (Eq. (3.1) and Eq. (3.2)) is the sum of the detected photon-number signals, \hat{N}_-^D (Eq. (3.3) and Eq. 3.4) is their difference, and \hat{n} is the number of photons emitted by the LO source⁶. The expectation values $\langle \cdot \rangle$ are calculated over the state of the LO. More details concerning this calculation can be found in Appendix A.1. From this simple derivation, it is clear that measuring the variance of the differential measurement allows estimating the shot-noise level of the incident radiation collected by the BHD. If the LO is a perfect coherent state, the variance of the sum is equal to the variance of the difference, being $(\Delta n)^2 = \langle \hat{n} \rangle$. From the presented model, it is also clear that the losses play a fundamental role in this type of measurement: by coupling the radiation with the vacuum field, the losses add an extra term in Eq. (3.2) that is proportional to the losses factor $1-\eta$. If the losses are too high, the retrieved amplitude noise of the LO is covered by the shot-noise term, and/or both the sum and difference measurements (section 3.2.1) can be covered by the background noise. In this sense, the noise floor given by the sum/difference⁷ of the backgrounds of the two photovoltaic detectors⁸ sets the limit of sensitivity in terms of measurable shot-noise level. As a consequence, in order to have the best signal-to-noise ratio in terms of measured shot-noise level the best operating scenario for the BHD is to work with the maximum power of the LO tolerated by the detectors, avoiding their saturation. This means having the best clearance. Moreover, the clearance itself contributes to the overall detection efficiency [155]: the effective

⁵The losses in the two output paths of the BS are assumed to be equal.

⁶Typically the LO is a coherent state, i.e. with a variance in terms of photons equal to the number of emitted photons: $(\Delta n)^2 = \langle \hat{n} \rangle$, where $\hat{n} = \hat{a}^\dagger \hat{a}$ is the number of incident photons.

⁷Due to the fact that the two detectors are independent the noise of the sum and of the difference of the two background signals are equal.

⁸The background noise is due to both electronics and dark current noise.

detection efficiency of the photodetectors is given by the product of their quantum efficiency and the equivalent optical efficiency (as defined in [155]) calculated as $\eta_{ee} = \frac{1-C}{C}$, where C is the measured clearance.

The simple model here described gives us another possible path of investigation: by comparing Eq. (3.2) with Eq. (3.4) it is also possible to understand how much the LO statistics deviate from the coherent state one, in case of a signal not dominated by vacuum fluctuations. By the way, for studying the statistics of the LO, a specific loss budget must be addressed, as reported below.

3.2.2 LO characterization

As already stated in the previous section, with the implemented balanced detector, it is possible to characterize also the statistics of the LO radiation. In this case, the loss budget includes also the optical losses in the LO arm, as sketched in Fig. 3.1b. It is possible to achieve the same results found in the above equations by including in the η the transmission efficiency η_{LO} experienced by the LO before impinging on the BS ($\eta \rightarrow \eta = \eta_{LO} \cdot \eta_1 \cdot \eta_{eff}$) and by redefining \hat{a} in terms of the new operator \hat{a}_R associated to the LO field before that optical losses occur ($\hat{a} \rightarrow \hat{a} = \sqrt{\eta_{LO}} \hat{a}_R + i(\sqrt{1-\eta_{LO}}) \hat{v}$). By doing these substitutions, it is possible to write Eq. (3.1), Eq. (3.2), Eq. (3.3) and Eq. (3.4) in terms of the new LO photon number operator (\hat{n}_R) and its variance by doing the following substitutions: $\hat{n} \rightarrow \hat{n}_R = \hat{a}_R^\dagger \hat{a}_R$ and $(\Delta n)^2 \rightarrow (\Delta n_R)^2$. For the LO characterization, it is important to remark that the retrieved sum signal relates to the LO properties only if the quantum efficiency is high enough (i.e. the signal is not dominated by the vacuum fluctuations). In this scenario, by comparing Eq. (3.2) with Eq. (3.4), it is possible to verify if the LO radiation is shot-noise limited and/or how far it is from an ideal coherent state.

3.3 Experimental setup

The implemented MIR detection system is schematically shown in Fig. 3.2. The core of the BHD consists of a 50/50 CaF₂ BS (BSW510, Thorlabs) working in the wavelength range 2-8 μm and of two MCT (MgCdTe) commercial photovoltaic detectors (PVI-4TE-5-2x2-TO8-wAl203-36+MIP-10-250M, VIGO System) characterized by a nominal bandwidth of 180 MHz and covering the spectral range between 2.5 and 5 μm . The detectors have a two-stage preamplifier consisting of a DC transimpedance stage and an AC-coupled second stage with a measured voltage gain of 26.5. The detectors are set at a working temperature of 200 K via a 4-stage Peltier system driven via the temperature cooler provided within the detectors (PTCC-01-BAS, VIGO System)⁹. The AC and DC photocurrent signals generated at the outputs of the photodetectors are

⁹The detectors' DC outputs have been added in house. Indeed, these detectors are commercialized with only the AC output. The AC-coupled amplifier works nominally in the range 10 Hz-250 MHz. From the producer final test, the nominal bandwidth of the detector plus amplifier is estimated to be 180 MHz. Moreover, they have a declared time constant $\tau \leq 80\text{ns}$, a transimpedance of $1.95 \times 10^4\text{ V/A}$ and an output noise density of $400\text{ nV}/\sqrt{\text{Hz}}$ ((averaged over 1 MHz to high cut-off frequency of 180 MHz), measured on a load $R_{LOAD} = 50\Omega$. Notice that the data shown in this thesis and in [99] have been acquired using the oscilloscope in high-input-resistance mode with $R_{LOAD} = 1\text{ M}\Omega$. Other specs of these detectors are available from the [VIGO System website](#).

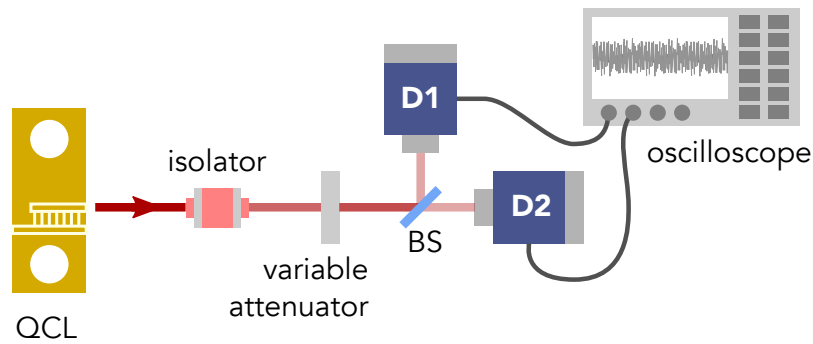


Figure 3.2: Sketch of the implemented BHD. The radiation emitted by a single-mode QCL working in the MIR ($\lambda = 4.47 \mu\text{m}$) is used as LO to test the performance of the assembled BHD. An isolator is used to avoid feedback and the power impinging on the BHD is controlled via a variable attenuator. The BHD is composed of a 50/50 BS and two identical photovoltaic detectors D1 and D2. The photocurrent signal generated by the two photodetectors is acquired in the time domain using different channels of an oscilloscope.

acquired simultaneously by 4 channels of a 200 MHz-bandwidth oscilloscope (MSO44, Tektronix) with a sample rate of 625 Ms/s and a 1-ms acquisition time. In the assembled BHD, the 50/50 splitting of the LO radiation is done with a precision $|R|^2 - |T|^2 = 0.2\%$, calculated via DC signals obtained via the oscilloscope. Furthermore, the overall measured bandwidth of the implemented system at -3-dB-cutoff (oscilloscope and detectors) results to be 120 MHz¹⁰. Thanks to the double outputs available from each detector, it is possible to measure both the mean value of the generated photocurrents via the DC output and its fluctuations amplified by the AC gain stage, at the same time. The BHD has been characterized for two different wavelengths, using two continuous-wave (CW) Fabry-Pèrot QCLs emitting at 4.47 μm and 4.72 μm , respectively. These lasers have been provided by the group led by Jérôme Faist settled at ETH Zürich (Switzerland). To characterize the noise response of the BHD avoiding possible extra-noise from the MIR sources, the QCLs' working conditions have been fixed at specific values of driving current and temperature ($I = 712 \text{ mA}$, $T = 18^\circ\text{C}$ for the 4.72- μm -wavelength QCL; $I = 490 \text{ mA}$, $T = 20^\circ\text{C}$ for the 4.47- μm -wavelength QCL). In these conditions, the devices operate in single-mode emission, as far as possible from the threshold to avoid any extra-noise contribution (e.g. due to spontaneous emission)¹¹. To test the BHD in different noise regimes, the power impinging onto the BHD is varied by means of an optical variable attenuator (Fig. 3.2). Furthermore, in the LO path an isolator (wavelength working range 4.5-4.7 μm) is set to prevent possible intensity fluctuations due to the feedback from the BHD optical elements. To minimise the technical noise, the lasers are driven by ultra-low-noise current drivers (QubeCL 15-P, PpqSense S.r.l.) characterized by a current noise density of $200 \text{ pA}/\sqrt{\text{Hz}}$.

As a first step in the BHD characterization, the responsivity of two photodetectors has been measured at both the tested wavelengths, as shown in Fig. 3.3. At fixed working conditions of the QCLs, the attenuation is varied via the variable attenuator to test the current response of the photodetectors for different values of incident power. By

¹⁰The actual bandwidth evaluated at 3-dB-cutoff is, therefore, lower than the nominal bandwidth of 180 MHz declared by the producer.

¹¹At the selected temperature, the lasing threshold current is 450 mA for the 4.47- μm -wavelength QCL and 620 mA for the 4.72- μm -wavelength QCL, respectively.

3.3 Experimental setup

fitting the acquired data with a linear curve (orange lines), it is possible to estimate the responsivity \mathcal{R}_i , with $i = 1, 2$, of the two detectors in the linear regime for both the laser wavelengths. Their quantum efficiency is calculated as $\eta_{qe} = \mathcal{R}_i hc / (\lambda e)$, where h is the Planck constant, c is the speed of light, and e is the electron charge. At $\lambda = 4.72 \mu\text{m}$ the responsivity for Detector 1 is $\mathcal{R}_1 = 1.24(2) \text{ A/W}$ and $\mathcal{R}_2 = 1.25(2) \text{ A/W}$ for Detector 2. The corresponding quantum efficiency is $33(1) \%$. At $\lambda = 4.47 \mu\text{m}$ the detectors

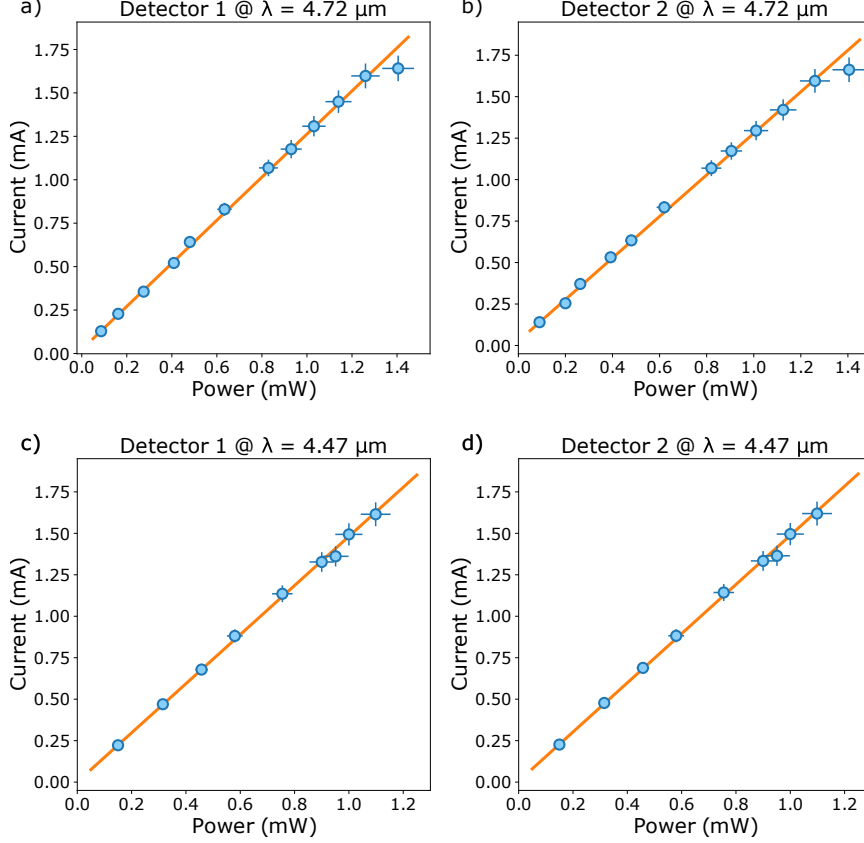


Figure 3.3: Current response of the two photovoltaic detectors (Detector 1 and 2) for different values of incident power at $4.72 \mu\text{m}$ (a, b) and $4.47 \mu\text{m}$ (c, d). In the graphs, the raw data with their error are represented in blue. At low power, the error bars are covered by the data spot size (blue circles). Via the linear fit of the data (orange line) is possible to retrieve the responsivity of the detectors, corresponding to the slope of the fitted lines: at $4.72 \mu\text{m}$ the responsivity for Detector 1 is $\mathcal{R}_1 = 1.24(2) \text{ A/W}$ (a) and for Detector 2 is $\mathcal{R}_2 = 1.25(2) \text{ A/W}$ (b), at $\lambda = 4.72 \mu\text{m}$ they are $\mathcal{R}_1 = 1.48(1) \text{ A/W}$ (c) and $\mathcal{R}_2 = 1.48(2) \text{ A/W}$ (d), respectively. In graphs (a) and (b), it is possible to see the saturation of the detectors for $P > 1.2 \text{ mW}$.

have the response peak, as stated by the producer, and their measured responsivity is $\mathcal{R}_1 = 1.48(1) \text{ A/W}$ and $\mathcal{R}_2 = 1.48(2) \text{ A/W}$, respectively. Therefore, the corresponding quantum efficiency is $41(1) \%$.

3.3.1 Loss budget for BHD characterization

To get a preliminary value for the detector efficiency, we must consider both the estimated quantum efficiencies and the optical transmission experienced by the light due to the 50/50 BS and the other optical elements placed in the paths from the BS output to the detectors (e.g. lenses in front of the two detectors). The overall optical losses due to optical elements are estimated to be 2% for both paths. As a result, the

detection efficiency is 40 % at $\lambda = 4.47\ \mu\text{m}$, and 32 % at $\lambda = 4.72\ \mu\text{m}$. These values must be multiplied for the *equivalent optical efficiency* of the detector (as stated in sec. 3.2), retrieved via the clearance measurement obtained from the calculation of the detector CMRR, as explained in sec. 3.4. However, we can already observe from this preliminary estimation that in the MIR region we have to face lower quantum efficiency than that at lower wavelengths (e.g. optimized Silicon and InGaAs photodetectors have a quantum efficiency higher than 90%). As a consequence, Wigner function analysis of complex quantum states, such as single-photon Fock's state and cat states (chapter 5), is not possible with available MIR detectors, requiring an efficiency higher than 50% to observe non-classical features [156]. The efficiency of the MCT detectors is not intrinsically limited by the material but by its purity. Moreover, in the MIR, a large loss contribution is due to the Fresnel reflection of the utilized materials, typically characterized by a large refractive index [99]. Some anti-reflection coatings are available but are expensive and in general less effective than the ones available at lower wavelengths (visible and NIR light). Besides the coatings, further improvements can be achieved by placing a golden surface on the back of the semiconductor medium acting as a retro-reflector. A more detailed analysis of the possible measurements available with such detector efficiency is given in the *Results and Discussion* section (sec. 3.4).

3.3.2 Loss budget for LO characterization

As already described in sec. 3.2, it is possible to utilize this balanced detection scheme to study the amplitude noise of the laser source used as LO. In this case, being the LO itself the light under study, all the optical losses affecting the LO arm must be included in the loss budget done for the BHD characterization. At the maximum transmission value achievable with the variable attenuator, taking into account the contribution from all the optical elements (attenuator, isolator, beam splitter, lenses, mirrors) placed between the QCLs and the photovoltaic detectors, the total optical transmission is 47(1) % at $4.72\ \mu\text{m}$ and 55(1) % at $4.47\ \mu\text{m}$. In general, a limitation for this loss budget is represented by the attenuation of the LO power required to avoid the detectors' saturation. For example, Figs. 3.3a and b show that at $4.72\ \mu\text{m}$ both the detectors saturate at an incident power higher than 1.2 mW. With this transmission ratio, the achieved detection efficiency for the LO is around 23%. If the LO emission is lower than this value, and in case of optimal alignment (no feedback), there is no need for the optical attenuator or the isolator, characterized by a transmission of 70 % (65%) at $4.47\ \mu\text{m}$ ($4.72\ \mu\text{m}$). In this scenario, the LO characterization detection efficiency can increase up to 40 %.

3.4 Results and discussion

The goal of the BHD characterization is to prove its eligibility as a shot-noise-limited detector suitable for quantum measurements. To this purpose, for each incident power value selected via the variable attenuator (Fig. 3.2), the time-domain AC signals retrieved at the outputs of the photovoltaic detectors are added/subtracted and then

translated in the FTT domain. In particular, the variance of these two signals is studied in the frequency domain via the computation of the Intensity Noise Power Spectral Density (INPSD), retrieved via a Python analysis code¹². Therefore, the INPSD of the sum provides information regarding the intensity noise¹³ of the LO radiation (sec. 3.2, Eq. (3.2)), while the INPSD of the difference should give us the shot-noise level corresponding to the incident radiation power (sec. 3.2, Eq. (3.4)). This is true in the BHD linear responsivity regime, when the extra noise does not exceed the limit given by the maximum CMRR of the detectors, and when the shot-noise level is higher than the noise floor given by the detector background. An example of the calculated INPSDs of the sum (difference) is shown in orange (blue) in Fig. 3.4a. The traces refer to a LO incident power of 2.2 mW (1.1 mW for each photovoltaic detectors) obtained using as source the CW single-mode QCL working at 4.72 μm . Both the INPSDs (orange and blue traces) lay above the background noise of the BHD, obtained as the INPSD of the sum of the two detectors (grey trace), and of the oscilloscope, obtained as the INPSD of the sum of the two oscilloscope channels (petroleum trace). In particular, since the oscilloscope background noise is approximately 20 dB lower than that of the detector background, it is negligible and, in practice, does not affect the measurements.

In Fig. 3.4, the difference INPSD (blue trace) perfectly lies on the expected shot-noise level (dashed black-line) calculated from the DC signals as $PSD_{\text{shot-noise}} = 2eI$, where e is the electron charge and I is the sum of the photocurrent mean values measured at the two DC photovoltaic detector outputs [157]¹⁴. With this evidence, it is possible to conclude that, for the tested LO power and under the LO amplitude noise condition shown by the orange trace, the assembled BHD is therefore shot-noise limited in the differential measurement and has a clearance above one (the measured shot-noise level is above the background noise floor) and flat response for a wide FFT frequency range (1-100 MHz). Fig. 3.4a allows also to estimate the actual bandwidth of the measurement system (photovoltaic detectors plus the oscilloscope) that is 120 MHz, calculated at the signal -3dB-cutoff. Because of the limited bandwidth, all the measured traces drop below the estimated shot-noise level at FFT frequencies higher than 100 MHz. Moreover, it is worth noticing that with the introduced analysis, it is possible to have information regarding the noise of the LO. The example shown in Fig. 3.4 shows that for the used QCL the measured intensity noise (INPSD of the sum) remains above the corresponding shot-noise level in the tested FFT frequency range. Moreover, there is the presence of a peak at around 3 MHz related to the laser dynamics. This is just an example of how adaptable the setup in use is and of how different analyses may be performed using the same set of data. By the way, in this experiment, the focus is not on QCLs as "noisy LO" but rather on testing the BHD

¹²The INPSDs are calculated as twice the value obtained via the *matplotlib* Python library function *matplotlib.mlab.psd()*. We applied the Hanning windowing and normalized the data to the noise bandwidth. The *NFFT* parameter, i.e. the number of data points used in each block for the FFT is 1/50 of the length of the input data. The input data are the AC current signals scaled by the AC gain

¹³With the expression *intensity noise* we refer in the text to the optical power noise of the laser beam. Indeed, the measured quantity using the photodetector is the power impinging onto the detector and its fluctuation, via the generator of a proportional photocurrent.

¹⁴Actually at the DC output of the photovoltaic detector the measured quantity is the mean value of the voltage drop experienced by the transimpedance for a certain value of incident power. Knowing that the transimpedance circuit has a unitary voltage gain and that the transimpedance is 2.2 k Ω , it is possible to retrieve the mean value of the corresponding photocurrent.

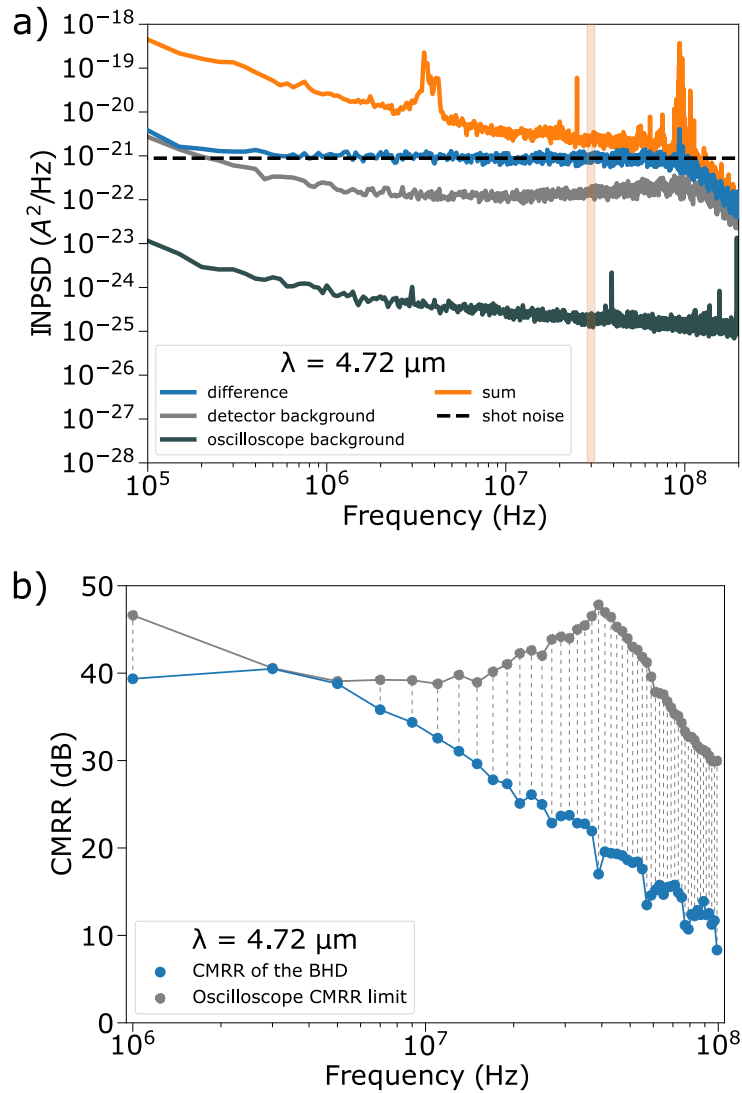


Figure 3.4: (a) Example of INPSDs calculated for a certain value of incident power (2.2 mW) and laser wavelength (4.72 μm). The INPSD of the sum is shown in orange and the difference one in blue. The INPSD of the detector background and the INPSD of the difference between the two oscilloscope channels' backgrounds are the grey and the petroleum traces, respectively. The dashed black line represents the theoretical one-sided PSD shot-noise level for an ideal detector with an infinite bandwidth. For frequencies higher than 100 MHz, the drop of the measured spectra below the theoretical curve is ascribable to the finite detector bandwidth, characterized by a -3-dB-cutoff at 120 MHz. The orange area of 3 MHz centred at 30 MHz is an example of the frequency window in which the data are analysed. The excess noise at 100 MHz is a spurious noise compatible with FM radio signals. Moreover, it is far from the frequency ranges selected for data analysis, therefore it is not relevant for the purpose of the BHD characterization. b) Common-Mode Rejection Ratio (CMRR) of the BHD (blue circles) and of the oscilloscope (grey circles), measured with a square-wave modulation of the signals. The CMRR data are shown in the flat response FFT frequency window 1-100 MHz of the detector respect to noise subtraction, as emerged from (a).

performance for potential quantum applications. As a consequence, the BHD rather than the QCLs is the focus of the analysis described below.

In order to characterize the maximum noise extinction ratio of the assembled BHD, i.e. the maximum CMRR, we have modulated the laser current and, therefore its emission, simultaneously at multiple frequencies with a square wave signal centered at 1 MHz, whose FFT spectrum is characterized by FFT odd harmonic components, shown

as blue spots in Fig. 3.4b. In particular, for each tested frequency we have measured the CMRR as the ratio between the INPSD of the sum and the INPSD of the difference. To correctly evaluate the CMRR at each frequency component of the square-wave signal, the modulation signal amplitude has been selected to guarantee the presence of a residual noise component after the subtraction in the INPSD of the difference. The CMRR of the BHD (blue trace) is compared with the CMRR of the oscilloscope that represents the ultimate limit for the measurements (grey trace). In particular, to measure the CMRR of the oscilloscope we have sent the modulation directly into the two oscilloscope channels used to acquire the detectors' AC outputs in the measurement procedure. As shown in Fig. 3.4, for frequencies lower than 5 MHz the CMRR is

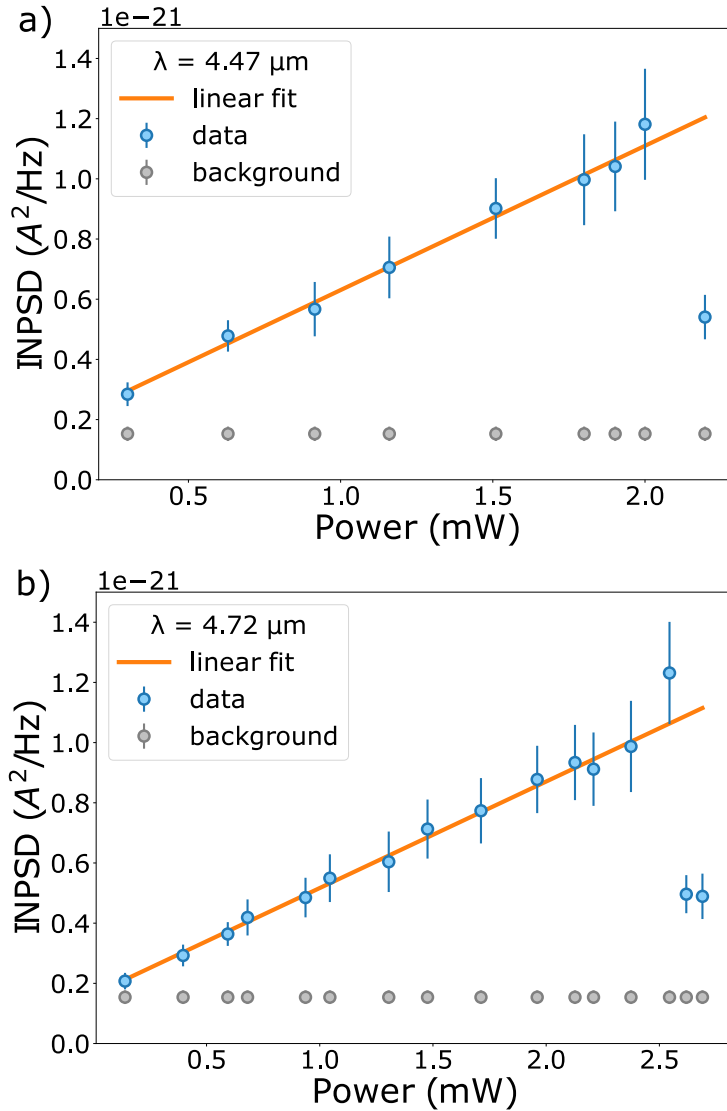


Figure 3.5: INPSD of the difference of the AC output signals as a function of the incident power impinging onto the BHD. Each point corresponds to the average level in the frequency window of 3 MHz centred at 30 MHz, evidenced in orange in 3.4a. The BHD performances are tested via two single-mode QCLs, emitting at 4.47 μm (a) and 4.72 μm (b), in fixed working conditions (temperature and current). The incident power is changed via the variable attenuator depicted in Fig. 3.2

limited by the oscilloscope and it is over 30 dB, while for higher frequencies the CMRR decreases. By the way, it is possible to find a high-frequency region around

30 MHz where the CMRR is still over 20 dB. Starting from this consideration and to get a deep analysis about the BHD performance, with the laser at fixed condition, the INPSD is calculated for different incident power values obtained via the variable attenuator depicted in 3.2. To evaluate the linear responsivity in the BHD differential measurements, for each acquired dataset, we computed the INPSD of both the sum and the difference and, in particular, we averaged the INPSD of the difference in a Fourier frequency window of 3 MHz set around 30 MHz, retrieving the data points shown in blue in Fig. 3.5. The data are compared to the background INPSD level, averaged in the same Fourier frequency window. For an impinging radiation wavelength of 4.47 μm (Fig. 3.5a), the BHD saturates for an incident power higher than 2 mW (1 mW for each photovoltaic detector) while at 4.72 μm it starts to saturate for power higher than 2.4 mW (Fig. 3.5b). This result is in agreement with the responsivity peak of the MCT detector expected at 4.5 μm . To increase the saturation level of detectors, one possible solution could be increasing the surface size of the photodetectors. By the way, this later change can lead to a decrease in the detection bandwidth. The analysis shown in Fig. 3.5 proves the linear responsivity of the assembled BHD, as expected by a shot-noise limited detector whose INPSD of the difference increases proportionally to the incident power. Furthermore, from both the plots it is possible to conclude that the BHD is suitable for sub-shot noise measurements and, therefore, for possible quantum state characterization. Indeed the retrieved INPSDs (blue dots) are above the BHD noise (grey dots). A more quantitative spectral analysis of the BHD clearance and linearity, performed for several values of incident power, is shown in Fig. 3.6. In Fig. 3.6a and Fig. 3.6b, the clearance FFT spectra are shown in the flat responsivity window previously identified in Fig. 3.4. At 4.47 μm the saturation clearly emerges for a LO incident power of 2.20 mW, and a maximum clearance of 8, corresponding to 9.0 dB, is found. At 4.72 μm the clearance is slightly lower, reaching a value of 7 (\approx 8.5 dB) for an incident power of 2 mW, approximately. For higher powers (i.e. 2.54 mW) the BHD starts to saturate for Fourier frequencies higher than 40 MHz. The BHD linearity has been also tested in several Fourier frequency windows of 3 MHz, centered at different frequencies, as explained in the legend of Fig. 3.6c and Fig. 3.6d. The clearance and saturation power level previously mentioned are confirmed by this analysis. In summary, from Fig. 3.6c and d it is possible to conclude that the detector shows a linear behavior with the incident power until the saturation level is achieved, for different Fourier frequencies going from 10 MHz to 80 MHz. In addition, the plots show that the clearance decreases by increasing the central frequency of such analysis. The best performance for homodyne application is achieved for a LO emitting at 4.47 μm , in the Fourier frequency window centered at 10 MHz. Here the clearance reaches the value of 8, corresponding to an equivalent optical efficiency (as defined in sec. 3.2) of 87.5%. From the responsivity characterization (section 3.3) the quantum efficiency at this wavelength is 41%, thus the total overall detection efficiency is 36%. Given the best clearance, this is the best scenario for a future investigation of MIR quantum states of light.

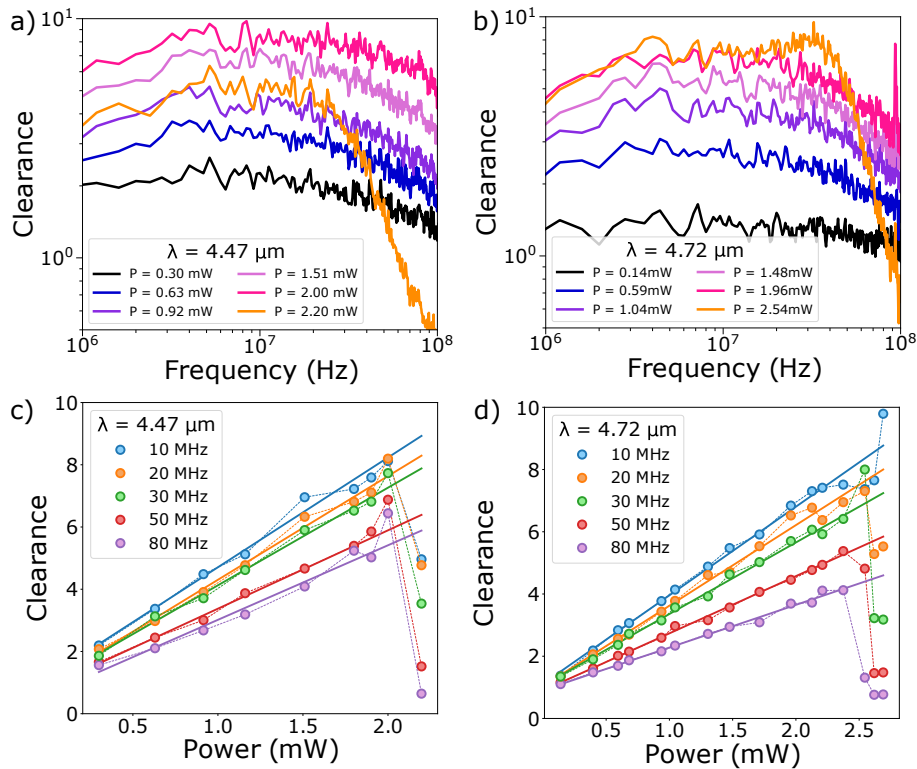


Figure 3.6: BHD FFT spectral response in terms of Clearance measured at $4.47 \mu\text{m}$ (a) and $4.72 \mu\text{m}$ (b), for several values of incident power on the BHD. In graphs (c, d), the clearance spectra have been integrated over a frequency window of 3 MHz centered at different values (written in the legend) and plotted as a function of the incident power. The experimental data are shown as a circle. Each dataset has been fitted via a linear function for testing the linearity of the BHD in the different FFT frequency windows analysed. In particular, graph (c) refers to the data acquired for an incident radiation wavelength of $4.47 \mu\text{m}$, and graph (d) of $4.72 \mu\text{m}$.

3.5 Summary and remarks

To conclude, the achieved results confirm the possibility of using the presented balanced detector for future quantum applications, enlightening the optimal working conditions in terms of clearance and LO incident power. Moreover, the presented analysis method allows multiple operations with the same set of data. In the presented analysis, just the sum and the difference have been computed, but even more complex operations can be performed, as well as correlation measurements by computing the product between the two detector outputs. However there are also some limits: even if the achieved values of overall detection efficiency and clearance are promising and suitable for possible non-classical states characterization such as squeezed states of light, due to the limited detection efficiency it is however not possible to use the BHD to test the non-classicality of a state of light via the Wigner Function reconstruction, requiring efficiencies above 50% to certify its non-classicality [156]. Nevertheless, with a quantum efficiency lower than 50% more sophisticated procedures can be applied to certify it [158]. Also, for quantum information processing, e.g. CV quantum teleportation [159] or long-distance CV free-space quantum communications (e.g. satellite-based [160]), the overall detection efficiency needs to be improved.

To prove the versatility of the implemented BHD, in the next chapter its application to the analysis of multimodal emissions by MIR QCLs is discussed.

CHAPTER 4

Intensity correlation measurements in quantum cascade laser frequency combs

4.1 QCL emission: harmonic comb, dense comb and bilobed emission	74
4.2 Correlation measurements in harmonic combs	77
4.2.1 Motivations	77
4.2.2 Measurement technique	79
4.2.3 Results and discussion	83
4.2.4 Summary and final remarks	91
4.3 Correlation in bilobed emission	92
4.3.1 Device characterization	92
4.3.2 Results and discussion	97
4.3.3 Summary and final remarks	98
4.4 Conclusion and perspectives	99

In this chapter, the characterization of different types of QCL emission is presented. In particular, the measurements of intensity correlations in multimodal regimes emitted by QCLs are described. The core of this chapter is represented by the work published in 2022 in *Advanced Photonics Research* [75]. The work shows an application for the balanced detector described in chap. 3 to investigate the presence of intensity correlations in the harmonic combs generated by QCLs. A harmonic comb is a peculiar comb emission regime with a limited number of lasing modes (e.g. three-five modes) characterized by a modal spacing that is a multiple of the standard FSR findable when the device is operated in the dense comb regime (made by tens of modes) [161], as described in the next sections. In particular, the study reported in [75] concerns a three-mode harmonic-comb emission from a MIR QCL, consisting of two weak sidebands and an intense central mode which is considered the pump of a FWM non-linear generation process.

The chapter is organized into different sections. A brief introduction regarding QCL emissions is provided in sec. 4.1, where different emission regimes are presented.

Then the motivations for studying intensity correlations in QCLs' harmonic combs are provided in sec. 4.2. As proof of the versatility of the implemented intensity-correlation detection setup, in sec. 4.3 unpublished results concerning the intensity correlations in QCL bilobed emission are presented. This particular emission regime is present in some broadband QCLs, typically at high values of driving current, nearby the saturation. Finally, a final remark and perspective section concludes the chapter (sec. 4.4).

Disclaimer and Acknowledgment. The lasers presented in this "intensity-correlation" chapter have been produced and provided to P. De Natale's lab by the group of Jérôme Faist (ETH Zürich) for scientific collaboration purposes. Here I want also to mention that the ongoing work regarding the characterization of harmonic comb has been, in particular, carried via a strong and close collaboration between Francesco Cappelli and myself with Mathieu Bertrand from ETH Zürich, with continuous supervision and scientific discussion with the group leaders and other members of both the research groups. Instead, the ongoing investigation regarding the characterization of bilobed emission regimes has been possible thanks to a collaboration between our group and one of Carlo Sirtori working at *Ecole Normale Supérieure* (Paris), and in particular, among the researchers, I want to mention Baptiste Chomet, the researcher in charge for this joint project of characterization. All the here-presented unpublished measurements, analysis and results have been done in our lab, mainly by myself and Francesco Cappelli, with the supervision and collaboration of all the other group members and of my tutor.

I would like to personally thank all the collaborators here cited for the amazing work done together.

4.1 QCL emission: harmonic comb, dense comb and bilobed emission

Depending on the device structure and the working conditions, broadband QCLs can emit both in single mode and/or in multimodal regimes (as already stated and presented in the introduction chapter and chapter 2). During my lab activity, all the tested QCL emissions are characterized by a single spatial mode and one, few or many frequency modes that, in principle, can be spatially split with a proper diffraction grating, as shown in the next sections. To characterize the spectral emission of QCLs, it is possible to use commercial interferometer-based optical spectrum analyzers. In particular, Fig. 4.1 shows the setup I have used to characterize MIR QCL emissions via the optical spectrum analyzer *FTIR 721 Spectrum Analyzer* produced by Bristol. The working principle of this spectrum analyzer is based on the Fourier transform infrared spectroscopy (FTIR): using a Michelson interferometer with a moving mirror, the interferogram of the light is measured and, by translating the raw data in the frequency domain via the FFT algorithm, the spectral emission is obtained [162]. The radiation under study has been attenuated during these measurements to prevent the

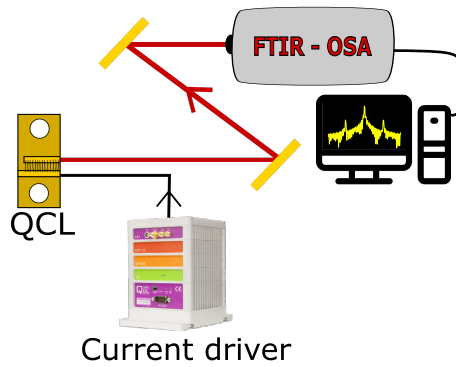


Figure 4.1: Scheme of the experimental setup used for the measurements of QCL emission spectra: The laser is driven via an ultra-low noise current driver (QubeCL, PpqSense) and the spectra are measured with an optical spectrum analyzer (OSA) based on FTIR spectroscopy (Fourier Transform Infrared Spectroscopy). The optical path of the laser beam is shown in red, two golden mirrors are depicted in dark yellow, and in the computer icon, the emission is sketched in yellow which is retrieved via the dedicated software provided by the FTIR producer company.

FTIR saturation¹. The data have been acquired with a sampling of $\Delta\lambda_c = 0.3 \text{ nm}$ and a spectral resolution $\Delta\nu_{\text{ris}} = 6 \text{ GHz}$ ². In general, this spectral resolution is sufficient to

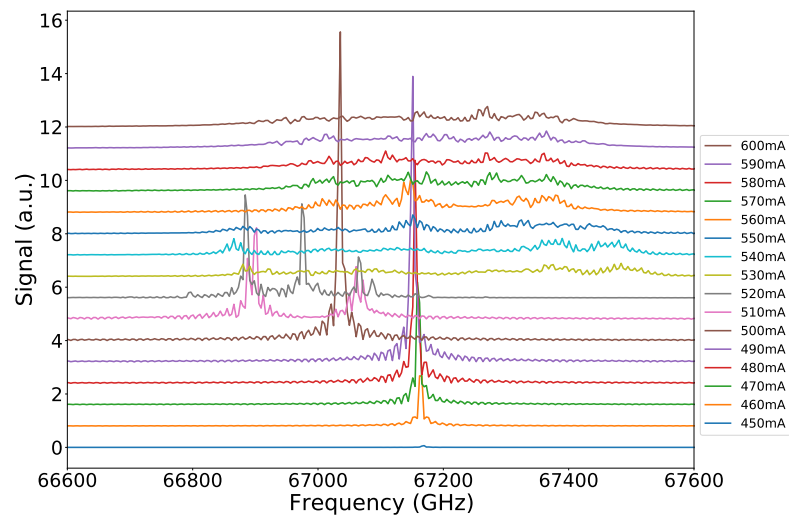


Figure 4.2: QCL spectral emissions acquired via the setup shown in Fig. 4.1. The tested laser is a MIR CW Fabry-Pérot QCL emitting around $4.5 \mu\text{m}$. The laser working temperature is set at $20 \text{ }^\circ\text{C}$, and the driving current is scanned to evidence different emission regimes.

measure even dense combs emitted by MIR Fabry-Pérot QCLs. Their FSR depends on the laser waveguide length: in the tested devices, the waveguide length goes from 4 to 6 mm, and the typical FSR is around 6-10 GHz. Although the detection is possible, due to limited FTIR resolution, each mode cannot be resolved properly. Therefore, to distinguish each mode, a longer-arm spectrometer or alternatively more sophisticated

¹This instrument operates both as a spectrometer and a wavemeter. The saturation of the instrument is visible in the wavemeter mode via a sort of loading bar that saturates. In the spectrometer mode, the saturation is characterized by some aliasing effects resulting in a distortion of the spectrum (e.g., some extra-modes can appear), therefore it must be carefully avoided in order to get the right information.

²With this spectral resolution, if we consider, for example, a laser emission peaked around a wavelength of $\lambda \approx 4.6 \mu\text{m}$, the corresponding wavelength resolution is $\Delta\lambda_{\text{ris}} \approx \frac{\lambda^2}{c} \Delta\nu_{\text{ris}} \approx 0.4 \text{ nm}$, where c is the speed of light.

precise measurements are required (e.g. dual-comb multiheterodyne detection [137]). To get different emission regimes from multimodal QCLs, it is possible to play with their driving current and temperature. An example of this trend is shown in Fig. 4.2. By changing the driving current, reported in the legend of the figure, it is possible to go from single-mode emissions ($I < 510$ mA), to few-mode emissions ($I = 510$ mA, $I = 520$ mA) and, finally, at high gain and driving current the dense comb emission, made by dozens of modes, is reached ($I > 520$ mA). By precisely playing with the two parameters mentioned above, it is also possible to find the working condition where several devices show a harmonic comb emission. This emission regime is characterized by a few lasing modes separated by a multiple of the FSR of standard dense combs [161, 163, 164], which is advantageous for spatial mode separation and analysis. Indeed, while standard QCL-comb emissions are characterized by dozens

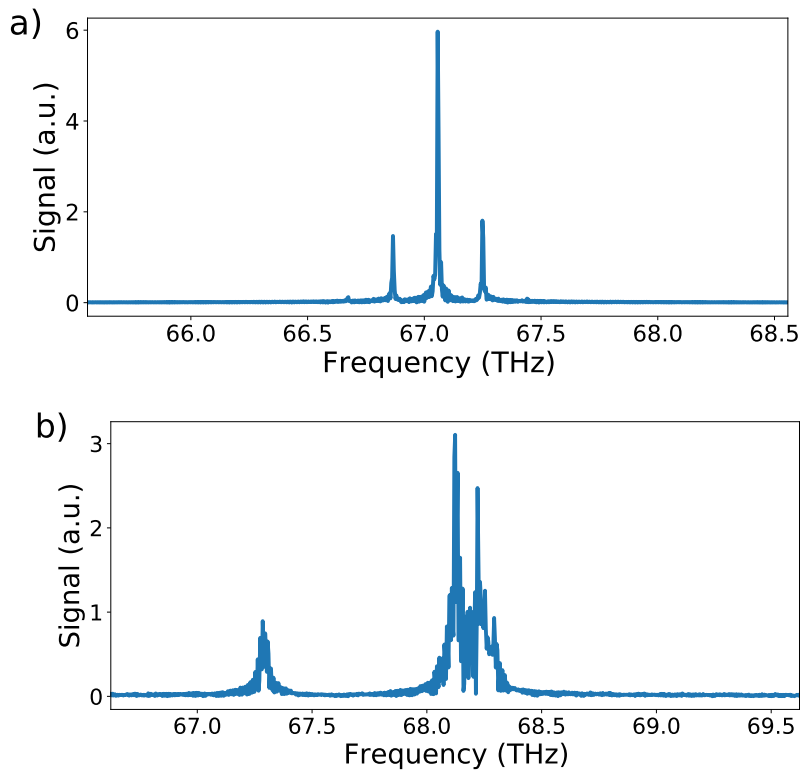


Figure 4.3: a) Example of five-mode harmonic comb emission by a QCL operating around $4.5\ \mu\text{m}$. The device working conditions are a driving current of 550 mA and a working temperature of $-15\ ^\circ\text{C}$ (as a reference, the lasing threshold at this temperature is 390 mA). b) Example of bilobed emission out of a Fabry-Pèròt QCL emitting around $4.4\ \mu\text{m}$. The laser is operated at a temperature of $-5\ ^\circ\text{C}$ and at a current of 770 mA, nearby the saturation (that occurs for $I > 770$ mA), while the laser threshold is around 530 mA at the tested temperature.

of modes, which cannot be properly distinguished via the setup shown in Fig. 4.1, the harmonic comb emission can be, instead, completely resolved due to wider mode spacing. Fig. 4.3a shows an example of a five-mode harmonic comb. Despite their simplicity, harmonic comb regimes are the most promising for investigating intensity correlations, indeed the low number of modes removes the ambiguities on the origin of the FWM process generating the correlations. It thus makes the experiment much easier to be interpreted and useful for future research. However, harmonic combs

need fine tuning to be found in standard QCL-combs and are not always available. Recently some devices have been optimised to emit in the harmonic regime, by properly engineering the laser waveguide for instance by acting on the reflection coatings of the laser waveguide facets [161]. In the section dedicated to correlation measurements in harmonic combs (section 4.2), the presented data regard a standard Fabry-Pérot QCL, able to emit both in harmonic and dense comb regime. Even if the device is not optimized for harmonic-comb emission, it shows a current range of several mA where the analysis of correlations in a three-mode harmonic-comb state has been possible. To complete the global picture of multimodal QCLs emission regimes that I measured during my research activity, Fig. 4.3b shows an emission spectrum characterized by bilobed or bicolor emission: the spectrum presents indeed two macroscopic emission area, the two lobes. These two lobes are multimodal and characterized by the same FSR. A characterization of intensity correlations in this type of emission is provided in section 4.3.

The here-presented emission spectra are just some examples of the deep spectral investigation that I performed searching for promising emission regimes where to test the presence of intensity correlations. In particular, the driving motor behind this type of research is presented in the following section.

4.2 Correlation measurements in harmonic combs

The work presented in this section refers to our work already published in 2022 in *Advanced Photonics Research* [75].

4.2.1 Motivations

The research of new laser sources capable of generating non-classical light is essential for its applications in quantum information processing, which is in high demand globally [165]. For this purpose, the intensity noise of the light emitted by semiconductor lasers has been studied in depth in the last decades, also in the perspective of controlling it at the quantum level [166–168]. A fundamental step for these studies is to understand the operation mechanism of the different laser devices, focusing on the different contributions that affect the intensity noise of the emitted light. Among semiconductor devices, QCLs deserve a particular mention, presenting an interesting possibility for developing novel quantum technologies operating in a spectral region, the MIR, so far much less explored than the telecom wavelength range. In such devices as stated in chap. 2, their complex heterostructure and their working principle, based on fast electrons' transitions in quantum well and on their recycling in a cascade process, determine the noise contributions and the intensity noise behaviour of the emitted light [168–171]. These devices show a $1/f$ -trend in the low-frequency intensity noise due to electron tunnelling through the multi-barrier structure [172, 173]. Moreover, the high-frequency noise of these devices is typical of class A lasers, due to their very fast upper-state lifetime [174]. Their complex conduction band structure makes difficult the observation of quantum features in the emitted light even when the driving

current is sub-shot-noise [175]³. However, in recent years, the demonstration of the presence of FWM⁴ as the responsible mechanism for the frequency-comb generation [32, 51, 68, 69, 176] (chapter 2) has boosted again the research regarding QCLs towards the quantum limit. This is also the purpose of the already mentioned *Qombs Project*⁵, where novel quantum simulations platforms, based on ultracold atoms [177], have been proposed and developed with the goal of optimizing the QCL structure and dynamics targeting at the emission of quantum states of light. However, the FWM has never been investigated as a driving motor for non-classical emission in QCLs, nor the presence of potential non-classical intensity correlation in such devices. On this trial, a recent pre-printed manuscript by M. Frankiè has demonstrated the possibility of increasing the $\chi^{(3)}$ non-linearity in such devices by acting onto three parameters: a larger dipole moment, a narrower transition, and a lower the angular frequency (the susceptibility resonance frequency of the material, as defined in [106]) increase the nonlinearity, as well as the chances of generating non-classical light [178]. However, a Hamiltonian derivation capable of modelling the FWM, as well as all of the other gain and loss terms present in QCLs, is still lacking.

The study of possible intensity correlations due to FWM phenomenon motivated the work presented below, with the perspective of achieving the quantum level in the near future. In particular, in the next sections, the presence of classical intensity correlations ascribable to FWM are proved. The correlations have been studied in harmonic combs emitted by MIR QCLs made by three modes, an intense central emission mode (the pump) and two weaker sidebands [179], which are equally spaced from the central one. In particular, harmonic QCL-combs serve as a test bed for investigating intensity correlations caused by FWM. In this sense, the tested three-mode emission represents the simplest system accessible for experimentally characterizing the presence of intensity correlations owing to FWM where two photons of the pump are expected to be destroyed at the cost of producing two other photons, one for each sideband. In this FWM process, the two sidebands must be equally spaced from the pump mode to fulfil the energy conservation. Furthermore, they are expected to exhibit intensity squeezing in their photon-number difference signal if this emission is solely the result of the FWM non-linear process and the losses are not too high (see section 1.4.4) [111]. However, additional noise sources must also be considered in a real active system, like a QCL [168], besides losses [76], as well as the intrinsic noise contribution proper of such devices (e.g. $1/f$ technical noise chapter 2), already mentioned above. Indeed, QCLs are active devices: therefore, also the amplification caused by the lasing process, as well as the eventual modes' competition process, can destroy or partially conceal possible quantum correlations [76, 168, 175]. In this framework, the first experimental proof of the existence of FWM intensity correlations between the two side modes is the detection of intensity correlations at the classical level. This proof can also pave the

³As described in [175], in QCLs, the suppression of the noise affecting the driving current, obtained by correlating the electrons (i.e. getting a sub-shot-noise current), does not lead to squeezed light emitted by such devices. Indeed the main contribution to the photon intensity noise comes from the non-radiative electronic disexcitation (see chap. 2) that is proportional to the bias current, and this suppresses the amount of photon number squeezing achievable in QCLs compared to semiconductor diode lasers, where the non-radiative channels are much less efficient.

⁴As already explained in the introduction chapter and in section 1.4.4, this non-linear process can generate quantum state on light.

⁵This is the European project where my work over the last years has been primarily focused.

way for the development of new theoretical models and it may also drive technological research on lasers and detection systems toward the quantum level, favouring the existence and detectability of non-classical effects.

4.2.2 Measurement technique

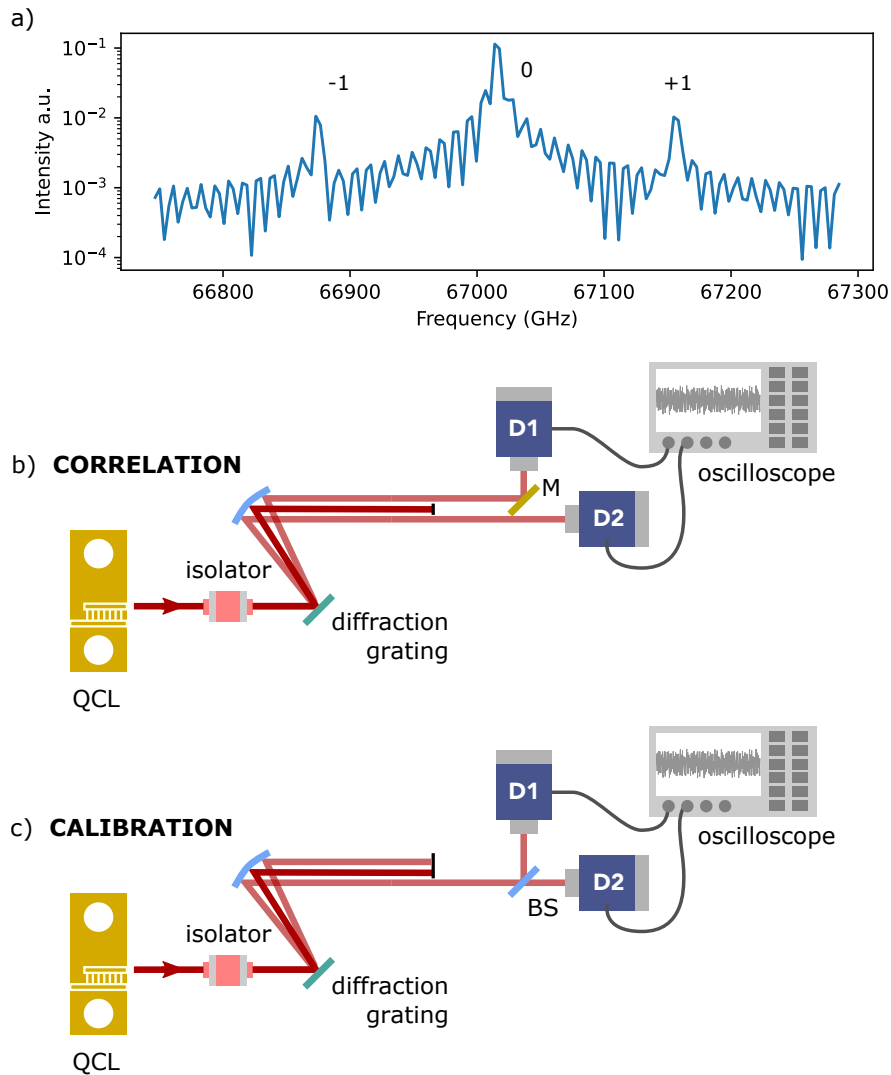


Figure 4.4: a) An example of the three-mode emission by the Fabry-Pérot QCL-comb emitting at $4.5\ \mu\text{m}$. The spectrum is measured via the setup shown in Fig. 4.1, using an optical spectrum analyzer. The measurement resolution is 6 GHz. b) Sketch of the experimental setup for correlation measurements. The QCL-comb three-mode emission is split via a diffraction grating. The two side modes are selected (the third one is blocked) and each of them is sent to different photovoltaic detectors, and the generated photocurrent signals are acquired simultaneously in the time domain via two different channels of an oscilloscope (MSO44, Tektronix). The data analysis is performed digitally in post-production. c) Sketch of the experimental setup for noise calibration, where we replaced the mirror M , shown in b, with a 50/50 beam-splitter (BS), to reconstruct the balanced detector depicted in Fig. 3.2. The used isolator provides isolation of 40 dB at the laser wavelength resulting in a stable laser emission. No significant feedback effect is observed.

The goal of the experimental work here presented is to test three-mode harmonic frequency combs emitted by a MIR QCL, where the central, intense, mode is expected to act as a pump in the FWM process generating two weaker sidebands (Fig. 4.4a).

The used device is a Fabri-Pérot QCL, fabricated at ETH Zurich, with a waveguide length of 4.5 mm operating at a wavelength of 4.5 μm [75]. The laser is kept at 23 °C, where the lasing threshold is 470 mA, and driven in the current range between 512 mA and 517 mA, where the laser operates in a three-mode harmonic comb regime, as shown in Fig. 4.4a. Here the modes are labelled with the numbers +1, -1 and 0 to indicate the two side modes (the sidebands) and the central mode, respectively⁶. In the depicted emission, the distance between two neighbouring modes is, approximately, of 100 GHz (Fig. 4.4a), about ten times the waveguide FSR⁷. To verify that the tested emission is really harmonic combs, i.e. no sub-cluster of modes are present under each detected mode, we checked via a radio-frequency spectrum analyzer the absence of the intermodal beat-note at the FSR frequency value expected in the case of dense combs (i.e. around 10 GHz for the tested device)⁸ (for further info see Appendix sec. A.1). In this work, the interest is in characterizing the sideband-sideband intensity correlations using the experimental setup depicted in Fig. 4.4b. In this setup, a diffraction grating with a groove density of 300 grooves/mm spatially separates the three modes. At the laser wavelength, the measured transmission of the grating is of the order of 60%. One of the modes is blocked, and the other two are detected (e.g. the two sidebands or one sideband and the central mode) via the balanced detector described in chap. 3. In practice, each mode is collected via one of two preamplified photovoltaic detectors. The detectors are extensively characterized and described in the previous chapter (chap. 3), but here some highlights are reported: they have both a DC output and an AC output; they have a quantum efficiency of up to 41%, and a maximum clearance (ratio between the observable shot-noise level and the dark-noise level) of 8, leading to an effective quantum efficiency of 36%. The detection system effective bandwidth is 120 MHz, the CMRR is up to 30 dB and at 4.5 μm the maximum power impinging on the BS tolerated to have a linear response is 2 mW. Via the detectors' DC output, the mean value of the incident radiation intensity and the corresponding shot-noise level are retrieved. This latter level is used as a reference for the intensity noise measured at the AC outputs. As in the BHD setup (sec. 3.4), also for the correlation measurements the DC and AC output signals are acquired simultaneously in the time domain via a four-channel oscilloscope with a sample rate of 625 MS/s. The duration of each acquisition is 1 ms. Referring to Fig. 4.4b, according to the harmonic comb FSR the position of the mirror M and the distance between the diffraction grating and the detectors can be adjusted to properly collect the reflected mode (the ultimate limit is given by the grating's dispersion power). In all the measurements, the system has always been kept in the linear responsivity regime to maintain a direct link between the

⁶In the characterized device, by changing the driving current, the sideband gain changes, as shown later in the measurements of correlation taken at several sideband powers (Fig. 4.8). For each value of driving current, we monitored the spectral emission via the spectrum analyzer. However, we acquired just one of these spectral emissions as an example and reference. A flip mirror, located in the setup (Fig. 4.4a) after the isolator, directs the radiation onto the FTIR in an analogous path to the one depicted in Fig. 4.1.

⁷This device, when operates as a dense comb, has a free spectral range of:

$$FSR = \frac{c}{2 \cdot n_g \cdot L} \simeq 1e-9 \frac{3e8}{2 \cdot 3.4 \cdot 4.5e-3} \text{GHz} \simeq 10 \text{GHz},$$

where c is the speed of light, n_g is the group dispersion index, and L is laser waveguide length.

⁸Such beat-note is acquired using the laser current. This measurement is possible thanks to the QCLs' fast gain dynamics allowing the modulation of the carrier population up to tens of GHz. The intermodal beating, being an intermodal modulation due to the comb emission, can be read out from the bias line, i.e. from the laser driving current [180]. For further info have a look at Appendix sec. A.1.

statistics of the tested photocurrent and the incident radiation power.

For the correlation measurements, a two-step characterization has been applied: first, the shot noise calibration of impinging radiation is performed; then the intensity correlations are measured and referred to the calibrated level of shot noise. The methods and the expected results for the two characterization steps are described in the two following paragraphs, entitled *Single-mode noise and relative shot-noise level calibration* and *Intensity correlation measurements*. The same nomenclature is used in the section dedicated to the presentation of the obtained results (sec. 4.2.3).

Single-mode noise and related shot-noise level calibration. As a first step in the setup characterization, we performed a noise calibration of the system in terms of shot noise. To accomplish this, a single mode is chosen using the diffraction grating, and the mirror M in Fig. 4.4b is replaced with a 50/50 BS (Fig. 4.4c). This allows us to equally split the single-mode intensity onto the two detectors, recreating the balanced detector shown in chap. 3 and in [99]. The balanced detector is used to estimate the shot-noise level for each mode using a differential measurement, and its match with the predicted theoretical value, retrieved via the DC output, is checked. After the calibration, the reference shot-noise level in correlation measurements is computed directly using the mean value of the detectors' DC outputs for a particular incident power⁹ ¹⁰.

As already anticipated in sec. 3.2, the balanced detector can also measure the intensity noise of the mode under study by computing the INPSD of the sum of the AC signals retrieved at the two detectors' outputs. Moreover, by removing the grating, the three modes are no longer spatially separated, and the balanced detector can be used to study the intensity noise or the whole unsplit emission. The comparison of the intensity noise level of each single mode with that of the whole unsplit three-mode signal offers information on the modes' relationships and on the presence of correlations. In particular, an INPSD level of the unsplit three-mode emission lower than that of each mode measured singularly indicates the presence of intensity correlations.

However, there is an inherent limitation in this type of measurement and comparison: the balanced setup system can only measure one mode at a time, whereas the correlation setup can test two modes out of three at the same time. As a result, only a post-production (asynchronous) comparison is possible to compare the three modes' intensity noise and their correlations rather than a simultaneous one. However, the simultaneous acquisition of the noise of each of the three modes requires a much more complex and expensive system: a minimum of three detectors is necessary to test at the same time the intensity noise of each mode and the correlation between each couple of modes, while for the simultaneous acquisition of the shot noise of each mode, three BSs and six detectors are requested. Furthermore, all the acquisitions should also be synchronized (e.g., six detectors, each with two outputs, required, in principle, a twelve-channel acquisition card). We can confidently state, however, that the implemented setup is a good compromise between having a good analysis and keeping the budget

⁹In the calibration phase, we also verified that sending a single mode onto one detector did not saturate its outputs.

¹⁰In this chapter, the term incident power refers to the incident power impinging on the balanced detector in the case of single-mode noise measurements or on the single detector in the case of correlation measurements.

and implementation complexity at a reasonable level. Indeed, despite the limitations, the three-mode emission shows good repeatability and stability for the entire time required to acquire all the measurements¹¹ and, therefore, it is reasonable to compare acquisitions taken asynchronously.

Intensity-correlation measurement. Via the implemented intensity-correlation setup (Fig. 4.4b), both the measurements of sideband-sideband and of sideband-pump correlations are possible. The grating horizontal alignment allows for the selection of the mode incident on $D2$, whilst the position of mirror M allows the desired mode reflected on $D1$ to be selected. The implemented setup enables the detection of the intensity noise of each of the two selected modes in the time domain using the dedicated detectors. In the same vein as the analysis performed for the BHD characterization (chap. 3), the AC time-domain data are added or subtracted, and the INPSD of the result is computed. Depending on the type of correlation (i.e. if the tested quantities are correlated or anti-correlated), by performing the sum or the difference, the common-noise terms in the intensity noise of the two selected modes are subtracted or added up: if the level of the sum INPSD is above (below) the level of the difference INPSD, the two beams are (anti-) correlated¹². Therefore, it is possible to evidence and demonstrate the presence of correlation via the comparison between the INPSD of the sum (named *sum INPSD* in the following text and analysis) with the INPSD of the difference (named *difference INPSD* in the following text and analysis). In the case of a non-linear phenomenon that generates the sidebands (i.e. FWM), where two photons of the pump are translated into one photon for each sideband, the intensities of such modes are correlated and increase together. We can also imagine them as two modes synchronously fluctuating in intensity; therefore, they are expected to be correlated and to have a difference INPSD lower than the sum INPSD. In the ideal scenario expected for non-classical correlation, the difference INPSD should lay below the corresponding shot-noise level as demonstrated for passive media [73]. In practice, the light originating from a laser active region experiences several noise contributions and losses (such as $1/f$ noise, gain, modes' competition, and waveguide loss) both in the optical path and in the detection that may affect the intensity noise of the sidebands, their intensity correlation and create intensity unbalancing between the two modes. Furthermore, if each sideband noise is far from the matching shot-noise level, a greater level of correlation is necessary

¹¹A typical measurement cycle in which we test several emissions from a harmonic comb lasts a working day, including alignment and overall measurement time. The repeatability means that it is possible to achieve the same emission state on different days, in the same current range, by adjusting the laser driving current by a few mA.

¹²As already stated in chap. 3, the INPSD allows via the Parseval theorem the estimation of the variance of the measured signals, at the cost of an integration. With this in mind, let's assume the quantity A and B are correlated. If we have now to calculate the variance of the sum of the two quantities $A + B$ depending if they are correlated (+) or anti-correlated (-) we get the following error propagation [181]:

$$[\Delta(A + B)]^2 = (\Delta A)^2 + (\Delta B)^2 \pm 2 \cdot \text{cov}(A, B)$$

where $\text{cov}(A, B)$ is the covariance between the two quantities A and B . An analogue formula can be retrieved for the difference, where the sign of the correlation part will be opposite to the one in the sum. Now let's assume that the quantity A and B are the number of photons of two sidebands, then if they are shot-noise limited, the variance of each of them is proportional to the square of the number of photons (e.g. $(\Delta A)^2 = \sqrt{A}$). Therefore, in case of correlation (+), while the sum should lie above the sum of the two shot-noise levels, the difference should lie below. This is a simple and limited derivation of the results, however, it helps in the general comprehension of the measurements.

to get a sub-shot-noise level differential signal, as well as a high detectors' quantum efficiency and CMRR. If their noise is instead close to the shot-noise level, the system can detect even a reduced amount of squeezing in the sideband-sideband difference measurement and requests a lower CMRR. In addition, the background noise of the used detectors is added on top of the INPSD contributions, and this may compromise the detection of weak signals. While in the case of a balanced homodyne detection, the LO acts as an amplifier for the noise of the light understudy (section 1.6.2), in this application the balanced detector has no LO. Indeed both of the detector's paths are illuminated with the harmonic-comb signals in order to test the amount of correlation. If the sidebands' signals are too weak, the corresponding shot-noise level may lie below the detector background. In this case, there is no chance of observing non-classical effects and other techniques need to be explored¹³.

To sum up, the demonstration of quantum-level correlations requires that the difference INPSD signal lies below the reference shot-noise level. This implies that the detection system must have a clearance significantly larger than 1 [73, 99].

4.2.3 Results and discussion

Single-mode intensity noise and relative shot-noise level calibration

As described in sec. 4.2.2 and in Fig. 4.4c, we calculated the INPSD of the sum and difference of the two detectors' output signals, respectively, to assess the intensity noise and the associated shot-noise level of a single mode (orange and blue traces, Fig. 4.5 a). In the measured harmonic emission, the sidebands are quite weak in comparison to the central mode: their power generally varies from a few μW to hundreds of μW , whereas the central mode power is on the scale of dozens of mW. As a consequence, the central mode has been attenuated in the measurements performed via the balanced detector to avoid saturation (the saturation for each detector at the laser wavelength occurs for an incident power $P > 1 \text{ mW}$), while no attenuation is necessary¹⁴ for the weak sidebands. On the other hand, the low intensity of the sidebands (e.g. the minimum tested sideband power is $P \simeq 0.08 \text{ mW}$) may translate into a shot-noise level (black dashed line) lying below the background noise (grey trace), as shown in Figure 4.5. This limit prevents unveiling possible quantum correlations, as already stated in sec. 4.2.2. At higher gain (i.e. at higher driving current with fixed temperature), the sidebands' power can reach a value over $200 \mu\text{W}$ (e.g. this is the case of the relative intensity-noise (RIN) spectra depicted in Fig.4.6), leading to a shot-noise level above the background noise as expected by the detector calibration presented in the previous chapter (chap. 3). However, at $4.5 \mu\text{m}$, even when the power of the sidebands is maximum (i.e. $P = 0.25 \text{ mW}$ in Fig. 4.6), the detection clearance remains below 3

¹³E.g. as an alternative a balanced homodyne detector can be employed with an appropriate multimodal LO, like as a second QCL with the same polarization, harmonic emission, and spatial mode. In this case, to test several values of phase between the LO and the test harmonic state of light, an appropriate method for varying the LO phase must be found [182].

¹⁴The sideband-sideband correlation is used to assess the presence of non-classicality, and, because of their weak intensity, no attenuation is required in their detection. In the case of pump-sideband correlation measurement, on the other hand, attenuation is required. In this measurement, the system is completely unbalanced: the pump is much more intense than each of the sidebands, and most of the pump photons do not participate in the non-linear process. In a certain sense, the attenuation can help to re-balance the measurement, at the cost of adding vacuum coupling to the pump state.

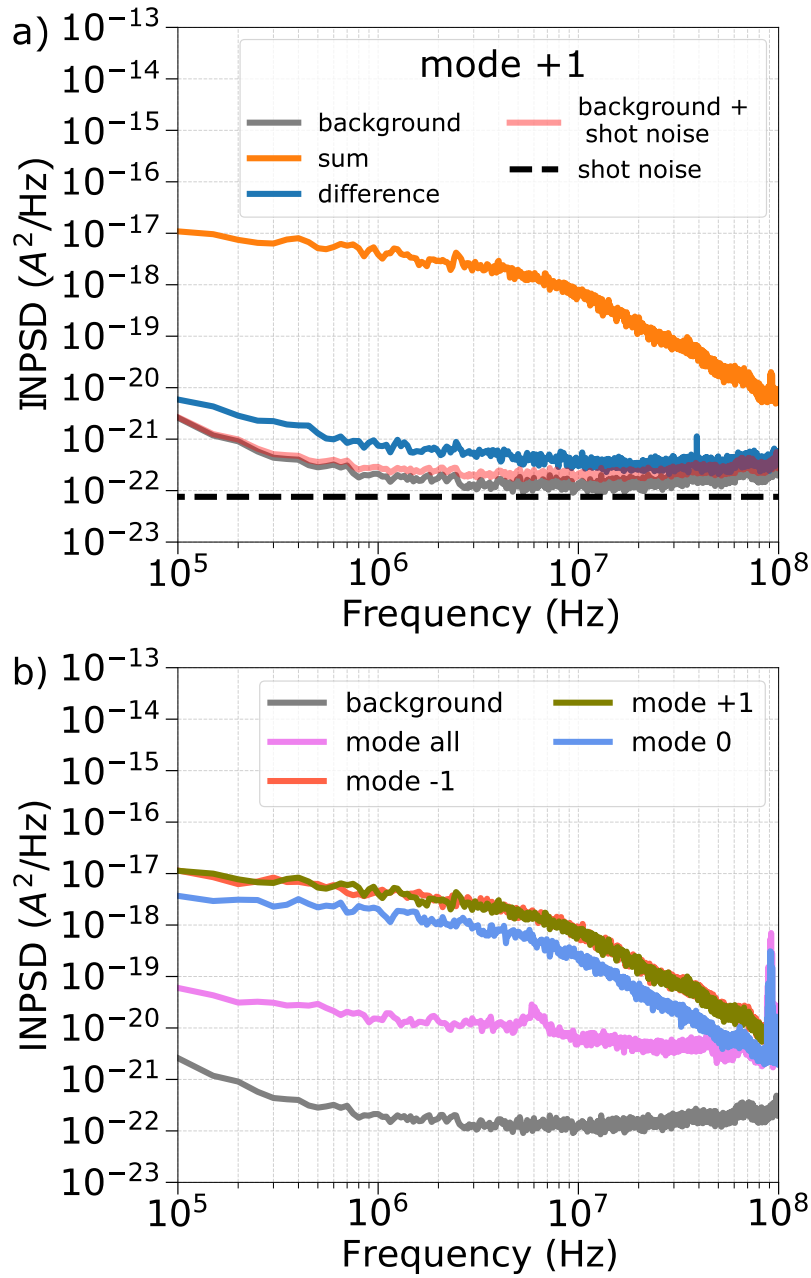


Figure 4.5: a) INPSD of the single sideband "mode +1" detected via the 50/50 balanced detector. The INPSD of the sum (orange trace) is compared to the measured INPSD of the difference (blue trace), to the computed level of the shot noise (black dashed lines) and to the background noise of the detector. The achievement of the shot-noise level is limited by the background. However, the sum of the expected shot-noise level and of the background noise (light red trace) is still compatible with the INPSD of the difference, which lies slightly above the background noise. b) Comparison among the sum INPSDs of each individual mode of the tree-mode emission (+1 and -1 denote the sideband, 0 the central mode) and the sum INPSD of the whole signal obtained by sending the unsplit three-mode radiation (mode all) on the balanced detector (no grating, no modal dispersion). A spurious noise around 100 MHz, compatible with FM radio broadcasting signals, is detected in case of mode all and mode 0.

(Fig. 3.6a), limited by the reduced amount of available power. Moreover, the performed analysis reveals that the sideband intensity noise (orange trace in Fig. 4.5a) is well above the corresponding shot-noise level. Regarding the calibration, by adding up the expected shot-noise level and the background noise (light red trace in Fig. 4.5a) we can

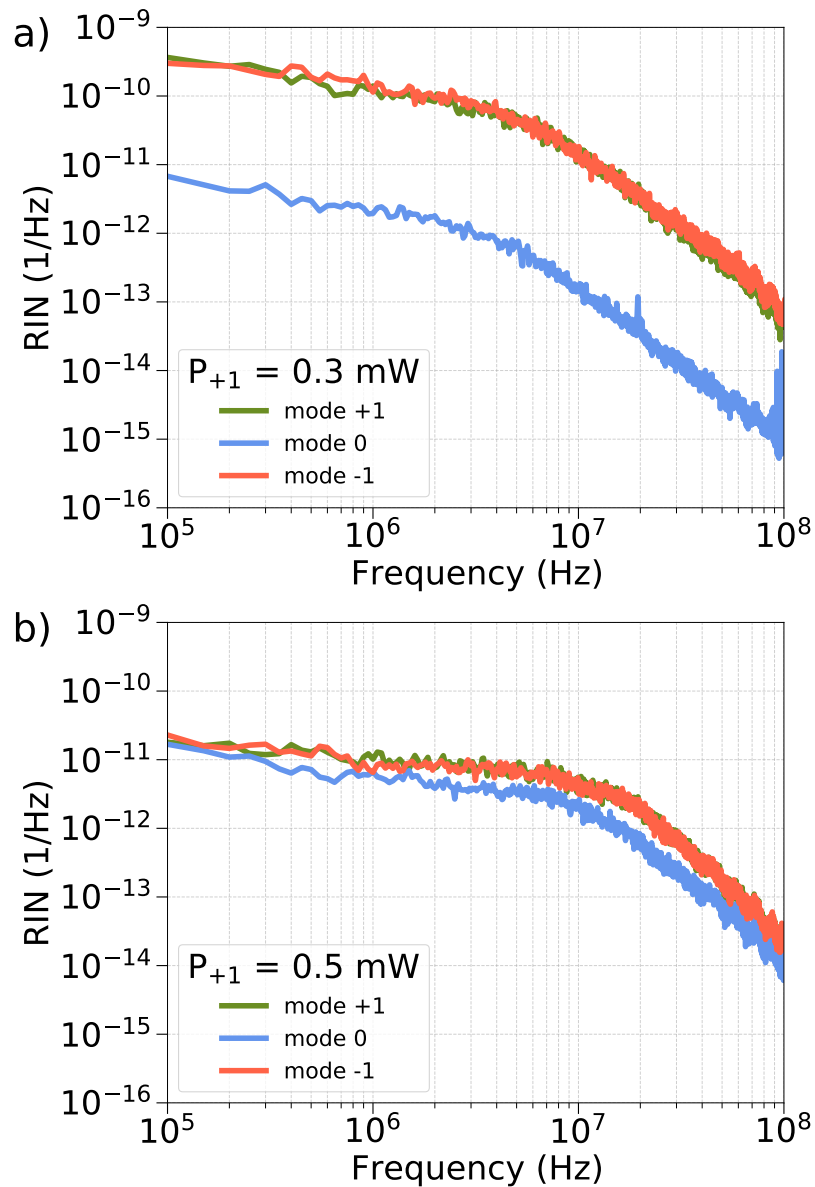


Figure 4.6: RIN of each individual mode of the three-mode emission for two different values of the single sideband power (P_{+1}). In both cases, the RINs of the two sidebands (mode +1, green trace and mode -1, dark orange trace) are overlapped and above the level of noise of the central mode (mode 0, blue trace). The excess noise around 100 MHz visible in graph a) is compatible with FM radio broadcasting signals.

still estimate the experimental shot-noise level (blue trace in Fig. 4.5a), that in case of a very weak sideband is slightly above the background noise. Given the above-mentioned limitations, the solution seems to be working at higher sideband power to have higher clearance. Anyway, it is worth noticing that higher powers mean higher gains that may degrade the correlations.

By using the balanced detector setup (Fig. 4.4c), it is also possible to measure the INPSDs of each single mode and, by removing the grating, to compare them to the INPSD of the whole unsplit signal. Fig. 4.5b shows the INPSD of each sideband in case of a very weak power ($P \simeq 0.08 \mu\text{m}$) (modes +1 and -1, green and dark orange traces). These quantities are compared with the central-mode INPSD (mode 0, blue

trace) and with the INPSD of the whole unsplit three-mode signal (mode all, pink trace). The INPSD of the whole signal is lower than that of the signal of each single mode, and this seems to indicate the presence of at least classical correlations¹⁵. To understand this result we can write the expected results in terms of their variances¹⁶. If we assume the presence of correlation between the intensity of each pair of modes, from the error theory analysis the variance σ_{all}^2 of the total intensity is given by [181]:

$$\sigma_{\text{all}}^2 = \sigma_{+1}^2 + \sigma_{-1}^2 + \sigma_0^2 + 2\sigma_{+1,-1} + 2\sigma_{+1,0} + 2\sigma_{0,-1} \quad (4.1)$$

where σ_i^2 is the i -th mode variance, and $\sigma_{i,j}$ is the covariance between mode i and mode j with $i, j = +1, 0, -1$ and it can be positive or negative, depending on the type of correlation. Therefore, the measurement of an INPSD of the whole unsplit signal (pink trace in Figure 4.5b) below each single-mode INPSD is a proof of non-negligible correlation. Knowing that the variance of each quantity gives a positive contribution being the square of the fluctuation, this lead to a negative contribution from the sum of the covariance term in Eq. (4.1) to match our experimental results:

$$(\sigma_{+1,-1} + \sigma_{+1,0} + \sigma_{0,-1}) < 0. \quad (4.2)$$

At this point, classical intensity correlations are expected, and a deep analysis of such correlations is needed to understand the sign of each term of correlation. Furthermore, analyzing the noise of each individual mode under different gain conditions (e.g., far or close to the sidebands' threshold) can indicate what is the most convenient regime for observing strong correlations, as the gain is one of the parameters that can contribute to the deterioration of correlations. In particular, at a fixed operation temperature, the laser driving current can be spanned to experience several gain conditions of the sideband modes. An anticipation of the results is offered by Fig. 4.6, where the RINs of both the sidebands (renamed mode +1 and -1 in the figure) and of the central mode (renamed mode 0) are displayed for two different values of sideband gain represented in terms of single-sideband incident power. In particular, when the sidebands are weak (Fig. 4.6a), their RIN is clearly higher than the one of the central mode. While at a higher gain (corresponding to a sideband power $P = 0.5 \text{ mW}$, Fig. 4.6b) the gap among these two noise levels almost disappears (Figure 4.6b). Interestingly, the RIN of the two sidebands is overlapped in both configurations, evidencing the same amount of noise, and indicating that the modes are balanced.

To summarize, the low-gain regime seems to be the most relevant condition for studying sideband-sideband correlations, as shown in the following section.

¹⁵It is worth noticing that, usually, to perform this comparison we should calculate the RIN of these quantities, by normalizing the retrieved INPSDs to the corresponding incident powers, indeed in case of central mode and whole signals measurements the radiation has been attenuated. However, the measured incident power, which is equal to the product between the attenuation factor and the actual power, results higher for these latter two signals than for the weak sidebands. To have a reference, the incident power for the overall signal is around 1.12 mW, and the one of the central mode is around 0.7 mW. Therefore the comparison among the INPSDs does not alter the results. Indeed, the central mode and the overall signal should be normalized to higher power values with respect to the sidebands, and thus the gaps between the INPSDs are expected to widen.

¹⁶Via the Parseval theorem [183], we can extract information about the variance of the signal by measuring its INPSD.

Intensity-correlation measurement

We investigated the sideband-sideband correlations and sideband-pump correlations using the apparatus depicted in Fig. 4.4b and the measurement methods described in Sec. 4.2.2. An example of both patterns is shown in Fig. 4.7 at two distinct single sideband power levels, $P_{+1} = 0.08 \text{ mW}$ for sideband-sideband correlation and $P_{+1} = 0.21 \text{ mW}$ for pump-sideband anti-correlation. In fact, graph (a) shows a partial sideband-sideband correlation since the difference INPSD lies up to 20 dB below the sum INPSD, but still over 20 dB above the shot-noise level. Instead, in graph (b), the difference INPSD is higher than the sum INPSD, indicating the presence of a partial anti-

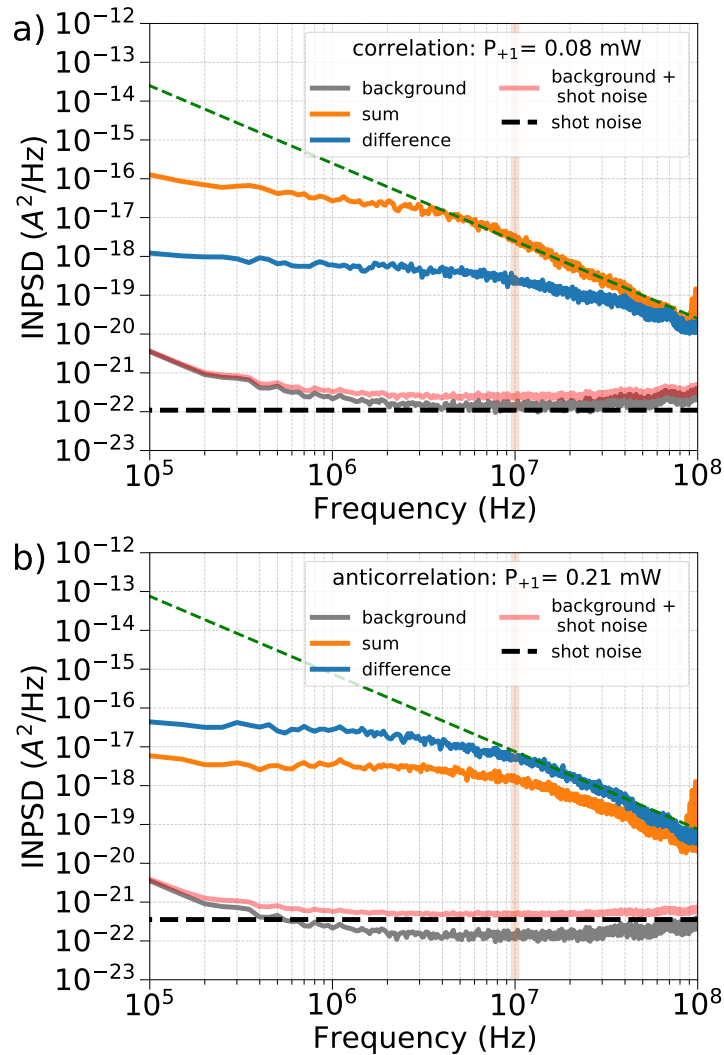


Figure 4.7: INPSD analysis of the sideband-sideband correlation (a) and sideband-pump anti-correlation (b) for different values of the single sideband power (P_{+1}), present in the three-mode harmonic comb emitted by a MIR QCL. The INPSD of the difference (blue trace) and the INPSD of the sum (orange trace) are compared with both the expected level of shot noise (black dashed lines) and the background noise of the balanced detector. In both graphs, the 1-1 MHz frequency window set around 10 MHz, and used in the CMRR analysis shown in Fig. 4.8, is coloured in dark orange. In this window, the CMRR of the setup is optimal (over 30 dB) and the highest clearance is reached [99] (chap. 3). The green dashed line indicates a 10-MHz frequency cut-off present in such correlation data in the INSPD of the sum (a) and of the difference (b). This cut-off is far from the -3-dB-cutoff of the detector and therefore it is ascribable to the laser dynamics dominating such emission.

correlation between the two investigated modes. Even in this situation, both INPSDs remain significantly higher than the background and shot-noise levels. However, unlike the sideband-sideband case, due to the presence of much more intense modes (the sideband power is of $P_{+1} = 0.21$ mW, and the one of the central mode of $P = 0.51$ mW, Fig. 4.7b) the shot-noise level is above the background noise. Interestingly, in both graphs (a) and (b), a 10-MHz-frequency cut-off is present (green dashed line), which is highlighted in the sum in the case of correlation, while in the case of anti-correlation in the difference. This cut-off is far enough from the detector's limited-bandwidth -3-dB-cut-off set at 120 MHz (sec. 3.3). As a result, we may conclude that this effect is caused by the intermodal laser dynamics that define this sort of emission. This latter assumption is supported by the fact that this cut-off appears in both the correlation graph and in the single mode INPSDs (Fig. 4.5b), but not in the INPSD of the whole unsplit signal (pink trace, Fig. 4.5b).

Prolonging the cut-off dashed green line trends in Fig. 4.7, the shot-noise level is expected to be reached at a few GHz. Furthermore, the appearance of a 10-MHz cut-off in the difference/sum INPSD shows that evaluating the signals for a shorter time frame (i.e. at a higher frequency) can be advantageous in terms of noise reduction, increasing the probability of revealing non-classicality. However, it is difficult to find a detector with GHz bandwidth suitable for such measurements: some commercial fast detectors with a few GHz bandwidth are available, but at the cost of a smaller detector area, resulting in earlier saturation in comparison to the used detectors, while the background noise remains at the same level. This situation results in a lower dynamical range for faster detectors, which is inadequate to have a satisfactory clearance or even to detect the shot noise. To meet all of the requirements of these intensity-correlation measurements, new optimized detectors have to be implemented.

To provide a comprehensive picture of the revealed correlation and anti-correlation, we examined such quantities at various single-sideband gains and powers, spanning the driving current in the range 512-517 mA while maintaining the temperature constant. In particular for such analysis, we estimated the *correlation-measurement CMRR* as the ratio of the sum INPSD and the difference one in the dark orange frequency region depicted in Fig. 4.7, i.e. $\text{correlation-measurement CMRR} = \frac{\langle \text{sum INPSD} \rangle}{\langle \text{difference INPSD} \rangle}$. With this definition, a $\text{CMRR} > 1$ indicates the presence of correlation, while a $\text{CMRR} < 1$ of anti-correlation¹⁷. As shown in Fig. 4.8, the correlation-measurement CMRR is mapped as a function of the single sideband emission power, both in the case of pump-sideband anti-correlation (a) and sideband-sideband correlation (b). This analysis evidences that the two types of correlations have an opposite trend with the sideband power (gain). The sideband-sideband correlation decreases while the sideband power increases, indeed, their trend tends to 1. On the contrary, the sideband-pump anti-correlation increases with a trend tending to get away from 1. These patterns suggest that the lowest gain condition tested, i.e. near the sideband formation threshold, is the optimal situation for measuring strong correlations between the two sidebands. Indeed, as the sideband gain rises, so does the anti-correlation with the central mode, indicating the presence of mode competition between the sideband and the pump.

¹⁷This CMRR should not be confused with the one previously introduced in chap. 3 that was defined as the ratio between the shot-noise level and the background noise.

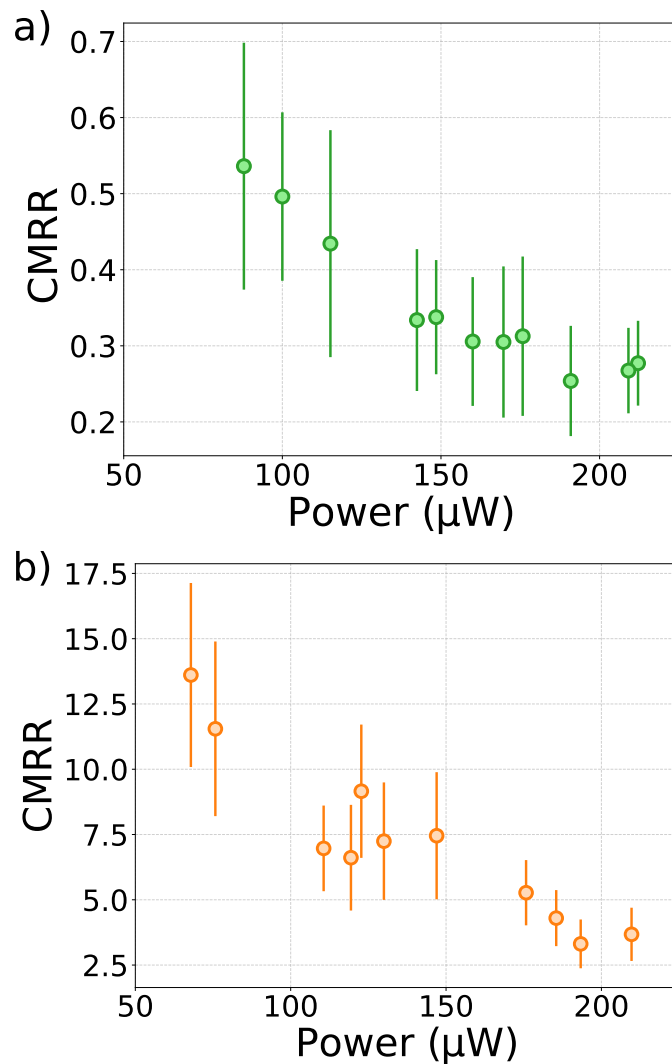


Figure 4.8: CMRR between sum and difference in the measurements of sideband-pump correlation (a) and sideband-sideband correlation (b) vs the power of the single sideband. The laser used is a Fabry-Pérot QCL emitting at $4.5\ \mu\text{m}$, working at room-temperature ($23\ ^\circ\text{C}$). The data are obtained spanning the laser current in the range from 512 mA to 517 mA. To calculate the CMRR (named in the text *correlation-measurement* CMRR), the sum and difference INPSDs have been averaged in a 1-MHz-FFT window centred around 10 MHz and the ratio between the two has been computed. The data shown in these graphs refer to the Fabry-Pérot laser emitting at $4.5\ \mu\text{m}$.

Aside from losses, it appears that gain and mode competition are the two components that reduce the correlation between the two sidebands and prevent the detection of non-classicality. In general, the values obtained in the correlation-measurement CMRR graphs confirm the correlation sign found in the characterization shown in Fig. 4.7, i.e. the presence of correlation between the sidebands which result both anti-correlated with the central mode. Such results are summarized in Table 4.1 where the sign + is associated with correlation, and sign - with anti-correlation¹⁸. As already stated in the previous section, it is worth once again noting that we were only able to use two detectors for observation of these correlations (anti-correlations), and therefore, to

¹⁸The results for the anti-correlation shown in the graph of this chapter concern specifically the sideband mode +1 and the central mode 0, but identical results for the tested anti-correlation with the other sideband mode (-1) have been found, as expected by the tested symmetrical emission state.

	mode +1	mode -1	mode 0
mode +1	+	+	-
mode -1	+	+	-
mode 0	-	-	+

Table 4.1: Correlation sign between the modes. The sign + indicates the presence of correlations, and the sign - indicates anti-correlations.

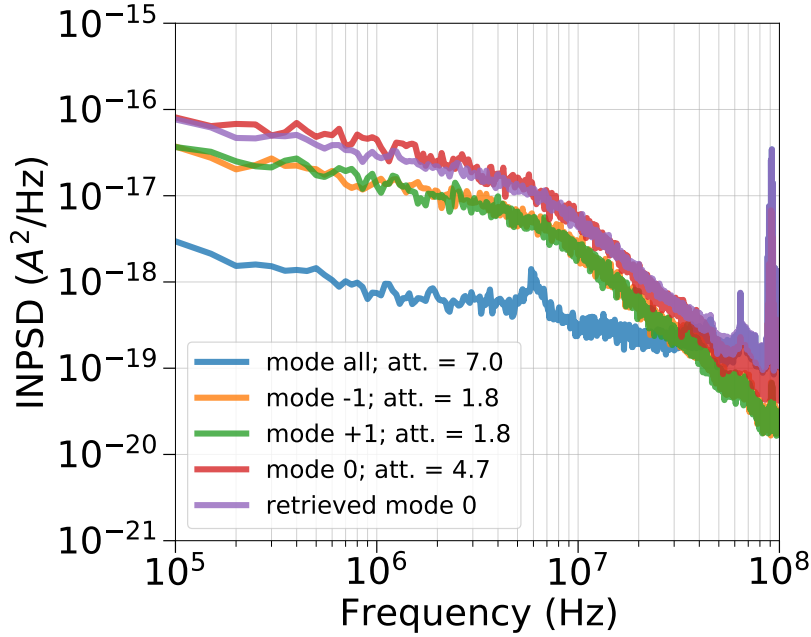


Figure 4.9: INPSD of each individual mode of the three-mode emission and of the whole three-mode signal sent to the balanced detector without modal dispersion (no grating). The spectra have been compensated for the related optical attenuation as reported in the legend. The *retrieved mode 0* spectrum has been obtained by adding the spectrum of mode +1, -1 and of the whole signal (*mode all*) according to Eq. (4.3). The excess noise around 100 MHz visible in the plot is compatible with FM radio broadcasting signals.

monitor the correlation between only two modes at a time. A more deep investigation may arise from the implementation of a three-synchronised-detectors scheme where the correlation between the three modes can be monitored at the same time. Furthermore, with a three-detector scheme, it is also possible to test the correlation between one mode, e.g. the pump, and the sum of the other two. We have already deeply described the increase of complexity of such measurements in the previous section, however, the implementation of a more sophisticated detection system can be a target for near-future investigations. In the meantime, the comparison with asynchronous data remains a valid alternative in the case of stationary and reproducible emission (and noise) which is the case of the harmonic state tested. To prove it, we decided to recombine the single mode signal knowing the sign of correlation (Table 4.1) to highlight that the overall signal can be retrieved and, therefore, the asynchronous data can be compared. For this comparison, we need to normalize the INPSDs displayed in Fig. 4.5b for the different attenuation factors affecting their measurements. The attenuation factors are the ones shown in the legend of Fig. 4.9 and are defined as the ratio between the real

power and the measured incident power onto the detection system. In particular, all the single modes are affected by the grating losses (attenuation of 1.8). The central mode is attenuated with a glass, leading to a global attenuation of 4.7. The overall radiation has no grating attenuation but it is attenuated by a factor of 7 (using two glasses) to prevent detector saturation. Given these factors, starting from the dataset of Fig. 4.5, it is possible to obtain the normalized INPSD traces depicted in Fig. 4.9. Then, by combining these INPSDs following the correlation sign expected by the two-mode correlations, it is possible to combine three of the cited spectra to obtain the fourth one. E.g., if we want to reconstruct the mode 0 (*retrieved mode 0*, violet trace in Fig. 4.9) we should combine the spectra as follows:

$$\text{INPSD}_{+1} + \text{INPSD}_{-1} + \text{INPSD}_{\text{all}} = \text{INPSD}_0. \quad (4.3)$$

The correspondence between the measured mode 0 and the retrieved one shows the validity of such analysis¹⁹.

4.2.4 Summary and final remarks

In this section, the correlations between pairs of modes have been investigated in a three-mode harmonic comb emitted by a MIR QCL. The origin of this investigation comes from the presence of FWM in QCL-combs that, besides inducing comb emission out of these devices, has also potential as a non-linear process able to induce non-classical correlation.

In particular, the tested harmonic emissions are characterized by an intense central mode and two sidebands. The performed analysis shows the presence of correlation between the side modes, and each of them results anti-correlated with the central mode. In particular, the harmonic emission is tested for different levels of gain obtained by changing the laser driving current at a fixed temperature condition. When the gain and the sideband power rise, the pump-sideband anti-correlation increases at the cost of decreasing the sideband-sideband correlation. With the ultimate goal of reach the sub-shot noise level, this analysis suggests that the best scenario for investigating the correlation between the sidebands is the emission configuration in which the sidebands are very weak and nearby their threshold. Indeed, the gain seems to promote their competition with the central mode while decreasing the correlation level. The presence of sideband-sideband correlation is in accordance with what is expected by the presence of a FWM processes where two photons of the pump are mixed to generate one photon for each sideband. However, with the performed analysis, only classical correlations have been unveiled. Indeed, in case of sideband-sideband INPSD analysis, the difference lies below the sum but still remains up to 20 dB above the corresponding shot-noise level. An analogue result is obtained in case of the sideband-pump anti-correlation, where the sum lays below the difference but it is still far from the reference shot-noise level. In the perspective of observing quantum correlations, the present setup can be successfully used for a single-sideband power above 0.1 mW, as suggested

¹⁹It is worth noticing that Eq. (4.3) is valid as long as the sideband-sideband correlation and sideband-pump anti-correlation are dominant with respect to the intrinsic noise of each mode (see Eq. (4.1)), which is the case of the tested harmonic comb emission.

by the characterization of the clearance of our detection system reported in chap. 3. Although the presented measurements remain at a classical level, this analysis is a valid benchmark to prove FWM-induced correlations. Furthermore, by enlightening their limitations, it is possible to set a strategy for future unveiling of FWM correlation in QCLs targeting the quantum level. First of all, the analysis shows the presence of a 10-MHz frequency cut-off in both the INPSDs of the correlation measurements and of the single modes. This cut-off is ascribable to the internal dynamics of QCLs and it can help in two improvement directions. By studying the causes of such internal dynamics, a new generation of QCLs can be optimized to minimize the extra noise coming from this intermodal dynamical process. On the other hand, new detectors with higher bandwidth (of the order of a few GHz) can be assembled to test the correlation in the frequency region where the evidenced excess of this $1/f$ noise is expected to reach the shot-noise²⁰. Furthermore, this detector should match the request of having a dynamical range large enough to have a clearance well above one even in the case of very weak sidebands. Another key parameter is the quantum efficiency which should be as high as possible to increase the chance of unveiling non-classicality. Finally, a theoretical model with a full quantum approach will substantially contribute to correctly describing the correlation measurement data and to clarify which are the structural key parameters to be optimized to increase non-classical emission out of QCLs.

4.3 Correlation in bilobed emission

As a final application for the balanced detector, I would like to briefly mention its use in testing the emission of a Fabry-Perot QCL emitting around $4.41\ \mu\text{m}$ with a peculiar bilobed comb emission at high driving current, as shown in Fig. 4.3b. This peculiar emission is likely due to some inhomogeneity in the gain and/or to its saturation, which favors the emission in two separate (but close) spectral regions, the two lobes, at the cost of the extinction of the emission modes in the gap between the two. Before going into more detail about the preliminary results, I want to make clear that the goal of this research is not to test the light's quantum state but rather to comprehend the dynamical process that created the two lobes in QCLs, especially whether and how they are related.

4.3.1 Device characterization

The LIV (Light power (L) - current (I) - voltage (V)) curve of the tested device is depicted in Fig.4.10, at a working temperature $T = -5^\circ\text{C}$, where the bilobed emission is present for high driving current (nearby the saturation) as already anticipated in Fig. 4.3. After the LIV characterization, the emission spectra of the laser are tested for several values of the driving current using the setup of Fig. 4.1. The measured spectral emissions are shown in Fig. 4.11. Depending on the driving current (I), the laser emission switches from a single mode emission ($I < 630\ \text{mA}$), to dense comb emission ($I < 630\ \text{mA}$), reaching nearby the laser saturation the bilobed emission

²⁰For instance, a reasonable detection bandwidth should not exceed the QCL cavity linewidth that gives a frequency limit of 5 GHz in case of 5-mm-waveguide QCL [75].

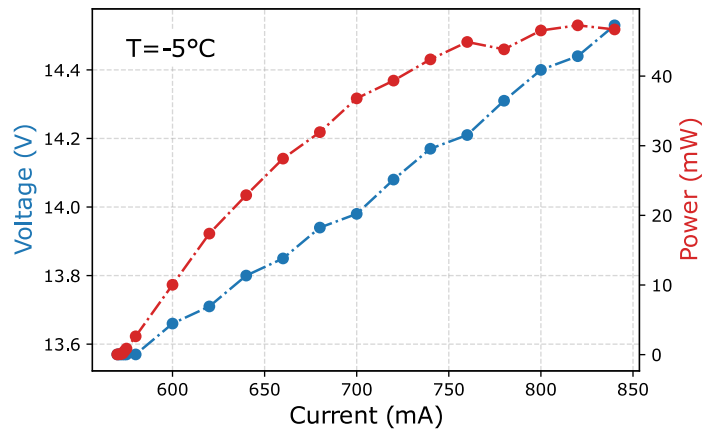


Figure 4.10: LIV curve of the ETH-fabricated Fabry-Perot QCL emitting around $4.41 \mu\text{m}$ at a temperature of $T = -5^\circ\text{C}$, where the laser exhibits a bilobed emission. The laser voltage drop (blue trace) and the emission power (red trace) are plotted for several values of laser driving current. The laser power saturates for a current around 800 mA. The power is measured at the laser output via a standard power meter, and the voltage is read out via the software provided by ppqSense to pilot the QubeCL current driver used to drive the laser.

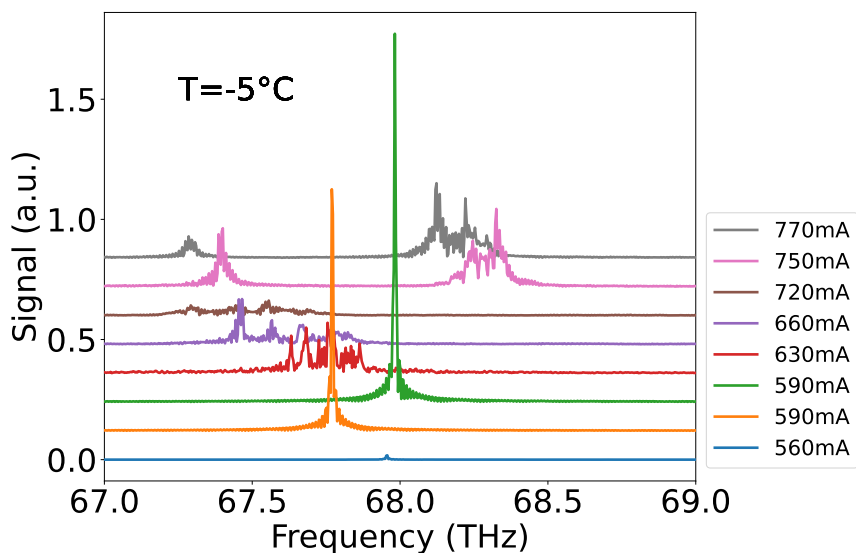


Figure 4.11: Fabry-Pèrot QCL emission spectra at several values of current (see the legend) at a fixed temperature of $T = -5^\circ\text{C}$. The laser operation wavelength is around $4.4 \mu\text{m}$, corresponding to 68 THz, approximately. As shown in the graph, the wavelength changes depending on the working condition.

($I = 750\text{mA}$ and above). In the case of bilobed emission, two multimodal lobes appear, separated by around 1 THz. This distance allows for the measurement of correlations between the two via the technique explained in sec. 4.2, being the distance between these modes a factor 10 wider than the distance between harmonic-comb modes. Before performing this measurement, the intermodal beat note of the laser has been monitored via an RF spectrum analyzer with a radio bandwidth $\text{RBW} = 100 \text{Hz}$ (see Fig. 4.12) directly from the laser bias current, as described in the Appendix sec. A.2. Additionally, for all the tested driving-current values, the QCL intensity noise has

4.3 Correlation in bilobed emission

been characterized via the balanced detector widely described in chap. 3. An example

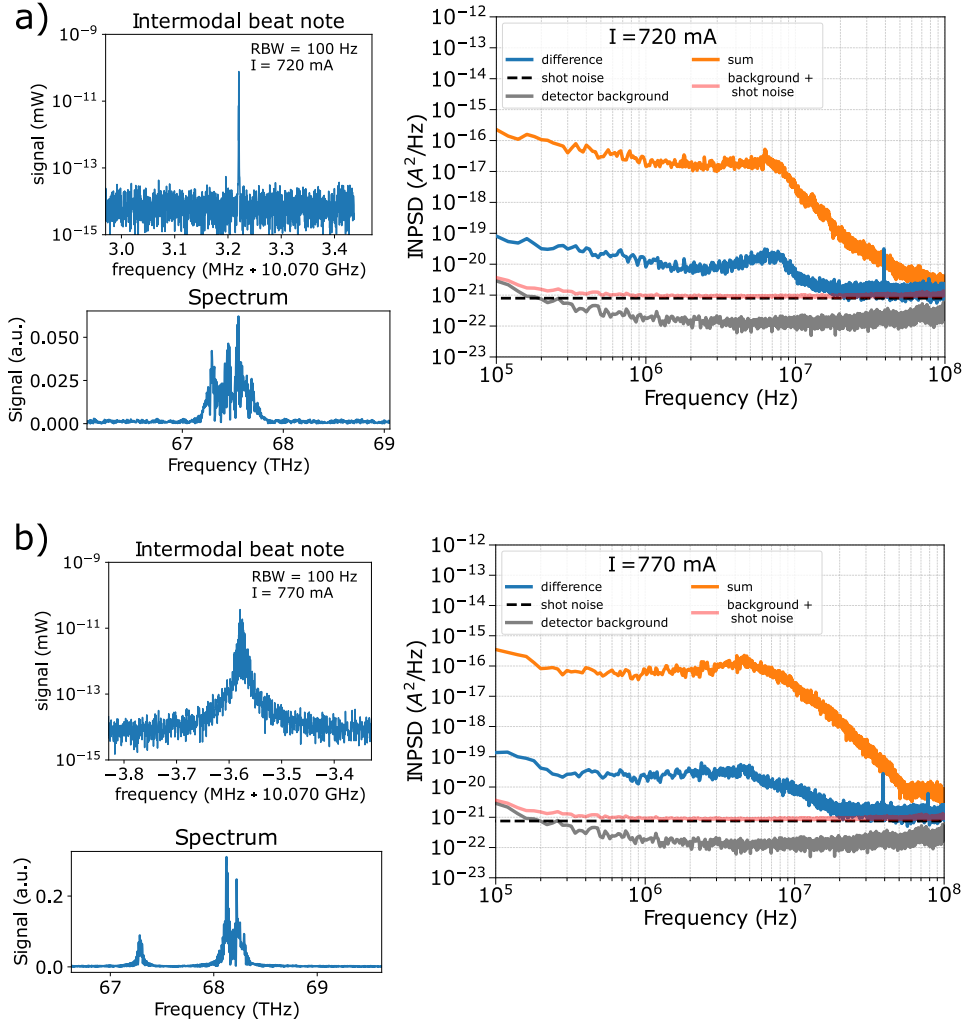


Figure 4.12: Intermodal beat note, spectrum, and INPSD of the sum (orange trace) and of the difference (blue trace) referred to the shot-noise level (black dashed line), the background noise (grey trace) and to the sum of the two (shot noise + background, red trace) in case of a driving current of 720 mA (a) and 770 mA (b). The beat notes are acquired via an RF spectrum analyzer (Fig. A.1) with a resolution bandwidth (RBW) of 100 Hz. The spectral emissions are acquired via an optical spectrum analyzer (Fig. 4.1), while the intensity noise of the two emission modes is measured via the balanced detector shown in Fig. 3.2. The measured incident power sent onto the balanced detector, in both cases, is around 1.8 mW. Referring to the INPSDs plots: the sum INPSD is shown in orange, the difference INPSD in blue and these quantities are compared to the background noise (grey trace), shot-noise level (dashed black line) and to the sum of the latter two noises (red trace). These quantities are computed following the procedure described in chap. 3.

of the characterization of these three mentioned parameters (i.e. the intermodal beat note, the spectrum and the intensity noise) is provided in Fig. 4.12 at a working temperature of -5°C . In particular, in (a) the parameters for the dense comb at a driving current (I) of $I = 720$ mA are shown, while in (b) the characterization of the bilobed emission for $I = 770$ mA is reported. By comparing the two beat notes, it is clear that the one of the bilobed emission (b) is broader than the standard comb one (a), suggesting a less coherent emission (sec. A.2): In case of bilobed emission, the FWHM of the intermodal beat note is 50 kHz approximately, while the one of the tested dense comb emission is, around a factor of 10 narrower. Focusing on the

spectral emissions depicted in 4.12, it is possible to note that the standard dense comb spectrum (a) is composed of a continuum of modes located in the frequency windows 67-68 THz, while in the bilobed case (b) there is a huge gap between the two lobes being around 1 THz far away. In particular, the low-frequency lobe falls around 67.3 THz, corresponding to a wavelength of 4.46 μm , while the high-frequency lobe falls around 68.2 THz corresponding to 4.40 μm . For the intensity noise characterization reported in (a) and (b) the whole (unsplit) radiation is measured with the balanced detector (as described in section 1.6): the sum INPSD (orange trace) has a cut-off in the trend around a few MHz, then the intensity noise decreases reaching the shot-noise level (blue trace) in the case of dense comb, while it remains slightly above it in the case of the bilobed comb. These two emissions are characterized by a high power (Fig. 4.11) over 30 mW, therefore they had to be importantly attenuated to prevent the saturation of the detection system. Besides the large attenuation (over 90%), in both the emissions the noise remains so high that, due to the CMRR limitation, the estimated shot-noise level (black dashed line) is reached only at high Fourier frequencies (over 10 MHz). As for the other INSPD graphs shown in this manuscript, the above-mentioned quantities are also compared to the background noise of the detector (grey trace), and to the sum between this latter noise and the expected shot-noise level (red trace). A better overview

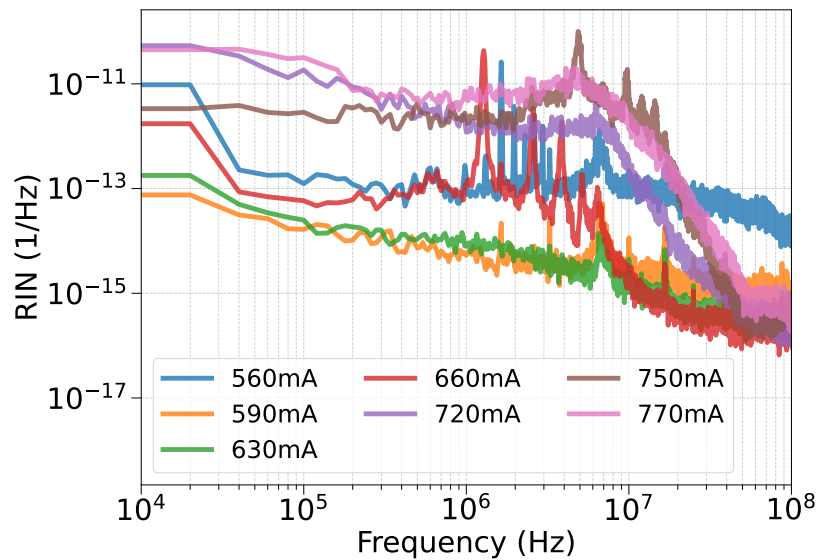


Figure 4.13: RIN (Relative Intensity Noise) at different values of driving current of the MIR QCL, whose spectra emission are depicted in 4.11. The RIN is calculated as the sum INPSD signal retrieved via the balanced detector analysis procedure presented in chap. 3, normalized to the square of the mean value of the photocurrent measured at the DC outputs of the detectors.

regarding the laser intensity noise is given in Fig. 4.13, where the QCL RIN²¹ is plotted for several values of driving current. Nearby the lasing threshold ($I = 560\text{mA}$) the RIN is quite high, then it decreases to lower values in case of single-mode emission, to rise again in the dense comb emission, reaching the highest values in the bilobed emission. The analysis remarks also the presence of a frequency cut-off around a few MHz only in case of multimodal emission, and it is probably due to some collective dynamics

²¹As already defined, the RIN here depicted is obtained normalizing the computed sum INPSD to the square of the mean value of the measured photocurrent.

4.3 Correlation in bilobed emission

effects affecting this type of emissions, however, further investigations are needed to draw a clearer picture.

By adding a grating before the balanced detector we also tested the intensity noise of each single lobe composing the bilobed emission, as shown in Fig. 4.4c. An example

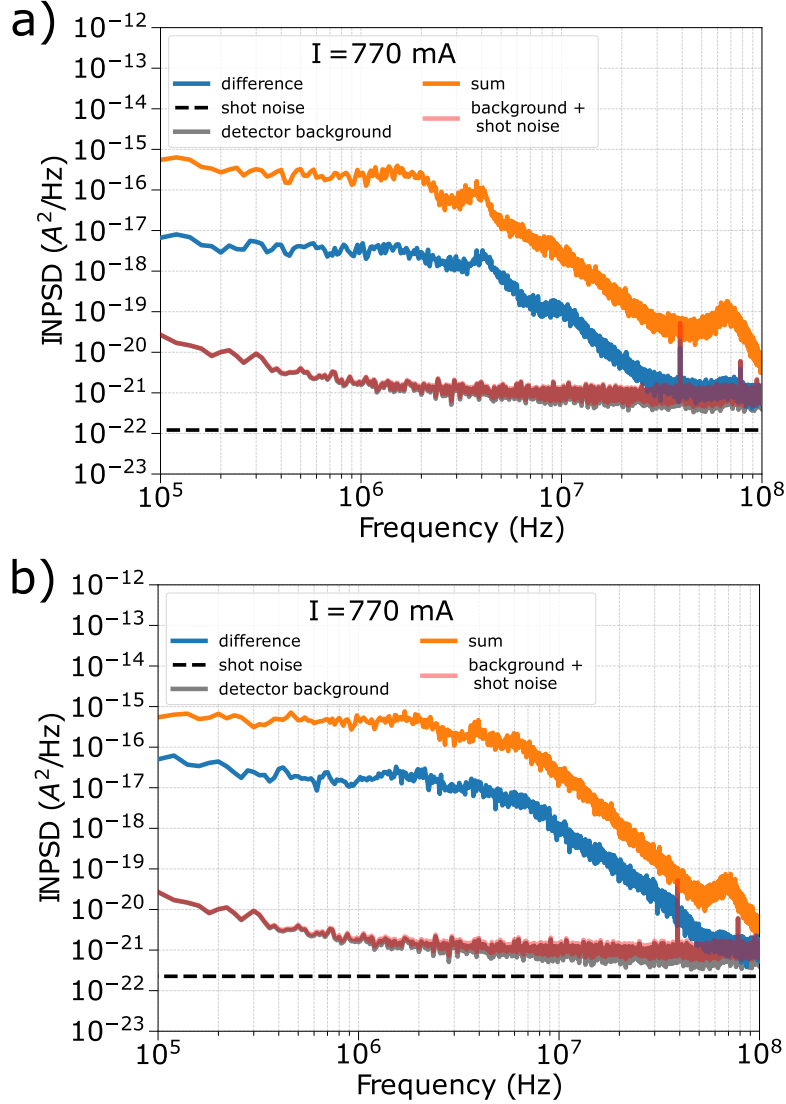


Figure 4.14: INPSD of the single lobe composing the QCL bilobed emission found at a driving current of 770 mA and a working temperature of -5°C shown in Fig. 4.11. The single-lobe noise detection has been possible by using the variant of the implemented balanced detector where a grating is set before the BS enabling the selection of one lobe at a time (Fig. 4.4c). The INPSDs graph (a) is the one of the weaker lobe (the left one in the depicted spectrum), while (b) refers to the other one. In both the plots the sum INPSD is shown in orange and the difference INPSD in blue. These quantities are compared to the background noise (grey trace), shot-noise level (dashed black line) and to the sum of the latter two noises (red trace). The measured incident power impinging onto the detector is 0.4 mW for (a), 0.7 mW for (b), approximately.

of the retrieved INPSDs, as well as the corresponding shot-noise level is given in Fig. 4.14. It is worth noticing that the intensity noise related to the two lobes is higher compared to the one characterizing the sidebands in the harmonic three-mode emission. For this reason, we were forced to use a higher oscilloscope scale with respect to the other measurements shown in this chapter. This scale is characterized by a higher background noise that limits the clearance of the measurement preventing

the differential measurements to reach the shot-noise level and it totally overcomes the background noise (grey trace) of the balanced detector that is now limited by the oscilloscope contrary to what was observed in the BHD characterization shown in chap. 3 or in its application in the correlation measurement in the case of harmonic combs (sec. 4.2). To overcome this problem, we could use a commercial power combiner to compute the difference between the AC outputs of the two photodetectors and a RF spectrum analyzer. However, due to the fact that in this application we were more interested in testing the intensity noise (sum INPSD) of the lobes, rather than the detector ability of noise suppression, I do not believe that the faced instrumental limitation has excessively impacted the measurement quality, in particular in the case of the bilobed emission, where the sum INPSD still lay above the corresponding shot-noise level. To complete the general overview of this single lobe noise measurements, we can notice for both the lobes the presence of a frequency cut-off after a few MHz: in Fig. 4.14 (a) the cut-off occurs around 2 MHz, in (b) around 6 MHz. Furthermore, in both the sum INPSDs a peak around 70 MHz is present. Finally, it is worth to remark the different power of the two lobes: the left lobe has a power of 0.4 mW, the other one of 0.7 mW, the unbalance between the two is therefore of around 30%. This may impact the operation of the balanced detection in the correlation measurements.

4.3.2 Results and discussion

By adapting the position of the mirror M and the distance between the detectors and the grating in the correlation setup depicted in Fig. 4.4b it is possible to match the frequency gap between the two lobes. Therefore, the correlations between them are retrieved, using the same methodology described in case of the three-mode harmonic comb (sec. 4.2). Each lobe has been directed to a different photodetector and both the INPSD of the sum and the difference are computed starting from the two AC detector output signals. An example of the computed INPSDs is shown in Fig. 4.15, where the bilobed correlation is tested for both the bilobed emission shown in Fig. 4.11 at a driving current of 750 mA (a) and 770 mA (b). Both the plots show an anti-correlation behaviour between the two lobes: the sum INPSD lays below the difference INPSD until a few MHz (for Fourier frequencies < 10 MHz) and also nearby the 70-MHz peak registered also in the single lobe spectra (Fig. 4.14). This anti-correlation behaviour suggests a competition of modes between the two lobes. It is worth remarking that the bilobed system is unbalanced in terms of measured photocurrent (and therefore of power). By the way, even with this constraint, we were able to detect such anti-correlation²². As in the case of single lobe INPSD analysis, the intensity noise was so high that we were forced to increase the oscilloscope scale during the acquisition. This has prevented reaching the expected shot-noise at the tested power values (i.e. 1 mW a and 0.7 mW). However, the detection of anti-correlation was still possible. Furthermore, the detected noise stays above such background noise limit for almost all the tested Fourier frequency range, reaching it around 100 MHz, nearby the limit given by the detector bandwidth (i.e. 120 MHz, chap. 3). Even in with the enlightened

²²We also verified that by balancing the signal in post-production we obtained the same results. The post-production balancing is obtained by renormalizing the AC fluctuations of one of the lobe using the ratio between the two mean values of the measured current.

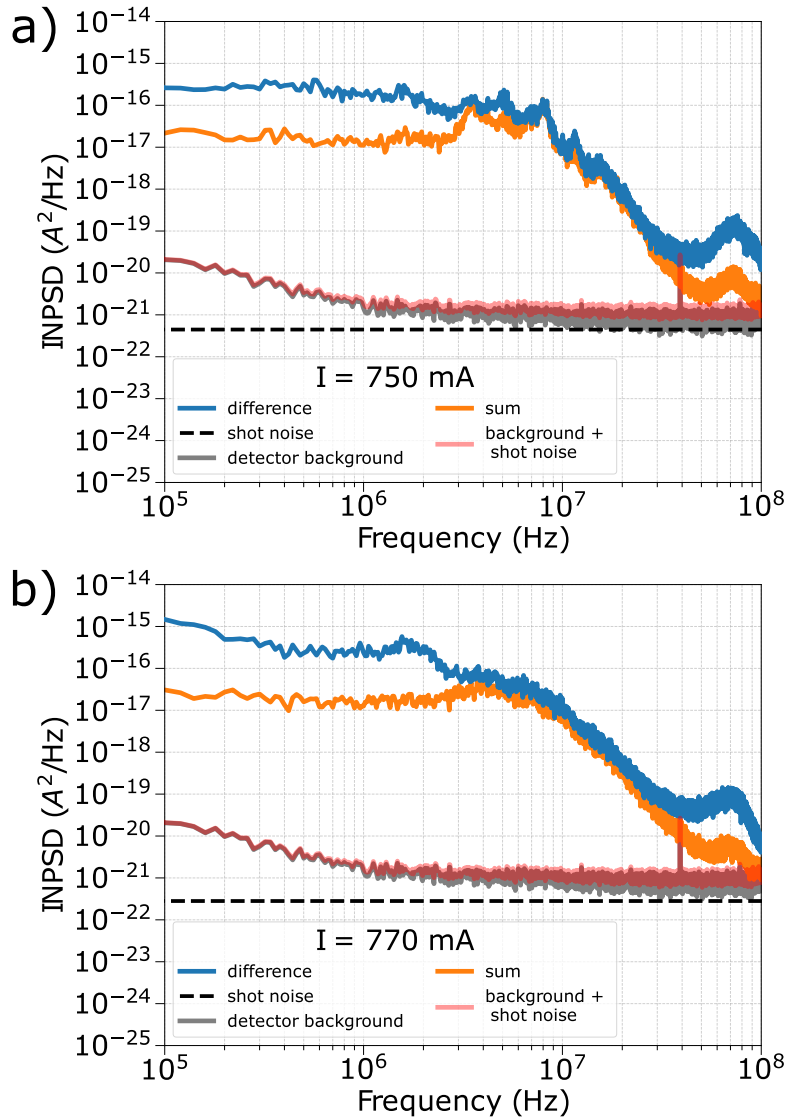


Figure 4.15: INPSD analysis of the lobe-lobe correlation at a driving current of 750 mA (a) and of 770 mA (b) at a fixed temperature of -5°C . The INPSD of the difference (blue trace) and the INPSD of the sum (orange trace) are compared with both the expected level of shot noise (black dashed lines) and the background noise of the balanced detector. In (a) the total incident power onto the balanced detector is 1 mW, and in (b) is 0.7 mW.

limitations, we believe that the detection of the anti-correlated behaviour between the two lobes is already an interesting result, to be deepened in the near future.

4.3.3 Summary and final remarks

This section presents an unpublished application regarding the correlation setup shown in section 4.2. In the presented application, the detector is used to test the correlation in a specific comb emission made of two different multimodal lobes characterizing the spectral emission of a MIR Fabry-Pérot QCL driven at high current (nearly its saturation). Differently from standard dense combs, this emission is characterized by two lobes that are separated by around 1 THz, likely due to some inhomogeneity in the gain and/or its saturation, which favours the emission in the two specific spectral

regions. At first, the balanced detector has been applied to measure the intensity noise of both the whole unsplit bilobed signal and of each single lobe. The bilobed emission is characterized by a general high-noise level compared to the RIN measured in the other emission regimes of the laser (e.g. in cases of single mode or standard dense comb emission). This is also in accordance with the intermodal beat note analysis, where a larger FWHM of the note has been measured in the case of bilobed emission with respect to a standard comb emission regime. Furthermore, the two lobes have different average powers, with an unbalance of around 30%. Another limitation with this high-noise regime emission is that in the case of the INPSD analysis performed for each of the two lobes, the fluctuations required a higher oscilloscope scale. As a consequence, in these measurements the background noise of the detector is limited by the oscilloscope background, making it impossible to reach the shot-noise level corresponding to the tested power (around 1 mW). However, even with this limitation, we were able to test the intensity noise of the devices operated in this peculiar regime at a classical level. The same limits are present even in the correlation measurement performed between the two lobes. By the way, the performed analysis interestingly reveals the presence of anti-correlation between the two lobes, suggesting a competition between the two of them. In the near future, in order to improve the measurement quality, a RF spectrum analyzer and a power splitter can be combined to measure the INPSD of the difference/sum between the two lobes. These instruments are typically characterized by low-level background noise and therefore the chances of reaching the shot-noise level are higher. The disadvantage of this detection system is that it can only perform one fixed measurement (i.e. sum or difference) at a time, whereas our balanced detector has the advantage of performing multiple operations with the same dataset (as described in chap. 3). However, I want to remark that while the target for harmonic state emission was to test the correlation at the quantum level (section 4.2), this was not the case for this type of investigation. In this case, we were more interested in understanding the nature of correlation that may characterize this type of emission, in particular, searching for anti-correlation between the two modes in the view of creating a proper theoretical model able to describe the origin of this type of emission in QCLs. Therefore, I consider the achieved results already satisfactory.

4.4 Conclusion and perspectives

In this chapter the balanced detector presented in chap. 3 has been applied to investigate the emission of multimodal MIR QCLs. As a first application, the balanced detector has been used to test three-mode harmonic comb emissions out of a MIR QCL, characterized by an intense central mode and two sidebands (sec. 4.2), with a first-neighbour mode separation of around 100 GHz. The ultimate goal of such measurement is to prove the presence of non-classical correlation between the sideband modes expected by the FWM process that takes place in the QCL-combs waveguide. Interestingly, the obtained results show classical correlations between the sideband modes, but the non-classical level was never reached. However, this work has set a benchmark for future investigations, enlightening the next steps to take for testing these correlations at the quantum level.

The second application shown in this chapter (sec. 4.3) regards the application of the implemented balanced detector in the measurement of correlation in the case of bilobed emission out of MIR QCLs. This peculiar emission is characterized by two clusters of modes, the two lobes, separated by around 1 THz, and is present at a high driving-current value. Such emission might be due to the saturation of the laser gain and/or its inhomogeneity. From the results, we can conclude that this emission is characterized by a high-intensity noise regime and that the two modes are anti-correlated. In this case, we were not interested in measurements at the quantum level, but rather more in a classical characterization of this type of emission with the perspective of developing a proper theoretical model.

Finally, to accomplish the task of pushing the MIR and QCL technologies to the quantum level I am going to take the following steps:

1. Gaining the expertise in dealing with squeezing and quantum state generation at standard wavelengths with passive optical devices;
2. Developing a non-linear passive device able to generate MIR squeezed light to test the developed detector's ability to measure non-classical effects;
3. Creating a theoretical model able to schematize the non-linearity of QCLs from a quantum point of view, enabling the engineering of devices optimized for enhancing the quantum features;
4. Working with scientific groups and manufactures able to provide a new generation of MIR detectors that, following the prescriptions evidenced in both sec. 3.3 and sec. 4.2, should have higher quantum efficiency ($> 50\%$) and higher bandwidth ($> 1\text{ GHz}$) while keeping a good dynamical range in terms of clearance and power saturation;
5. Testing new emerging devices such as Interband Cascade Lasers (ICLs), which recently have emerged as a valid alternative to QCLs.

In the following chapter, the work that I have already done concerning the first step is described.

CHAPTER 5

Generation and detection of non-classical light

5.1 Introduction	102
5.2 Theoretical description	102
5.2.1 Squeezing generation	103
5.2.2 Kitten state preparation	103
5.2.3 Detection and quantum state reconstruction	105
5.3 Experimental setup	106
5.3.1 Heralding process	108
5.4 Results and discussion	112
5.5 Conclusion and perspectives	115

The work described in this chapter regards the experiment done during my research abroad period, spent in Nice (France), with the aim of generating CV quantum states of light (i.e. Schrödinger’s cat state [184]) via a chip-scale passive non-linear medium, a PPLN ridge waveguide (PPLN/RW). In particular, the specific tasks of this work were to generate, manipulate and detect small-amplitude cat states (named *kitten states* [93]) with a plug-n-play approach to a CV-quantum-optics experiment based on off-the-shelf components coming from the telecom (1.55 μm) and non-linear optics. The work here mentioned has been already published in *Optics Express* [95].

In a global view of generating non-classical states of light in the MIR, this work gave me the know-how necessary for dealing with non-classical states of light at standard wavelength, out of a passive medium.

In this chapter, a brief introduction about kitten state generation is provided in section 5.1; a theoretical description regarding this topic is then given in section 5.2. In 5.3, the experimental setup is described and in section 5.4 the obtained results are shown and discussed.

Disclaimer and Acknowledgement All the work described in the next sections has been carried out at the Institut de Physique de Nice¹ (France) under the supervision

¹<https://inphyni.univ-cotedazur.eu/>

of Dr Virginia D’Auria², in cooperation with the Ph.D. student Mohamed Melalkia³. This chapter offers a general overview of the work done in the five months that I have spent there. A complete and rigorous theoretical approach to this argument is reported in [108], as well as a detailed description of the data analysis done for the Wigner state reconstruction. I have to thank all of the coauthors of [95] for giving me the opportunity to view my first squeezed state and my first non-classical state with a negative Wigner function in such a short amount of time.

5.1 Introduction

Squeezed states of light [185, 186] are a commonly used Gaussian resource in CV quantum optics that can be applied in quantum communication and computation protocols [88, 90, 91]. Furthermore, these states of light can be manipulated to generate non-Gaussian quantum states of light such as Schrödinger’s cat states [187, 188], consisting in a macroscopic superposition of two coherent states of opposite phase [184], and Schrödinger’s kitten states, with smaller amplitudes [93]. These non-Gaussian states of light allow the generation of advanced communication protocols like quantum distillation [97, 98]. At standard wavelength, i.e. in the telecom spectral region where the worldwide-fiber communication system is based, the generation of squeezing is commonly obtained via OPO or Optical Parametric Amplifier (OPA), based on non-linear PLNN crystal or waveguide implemented both in bulk optics setup [189, 190] and in fully-guided system [191] where the elements are compact and integrated with a plug-and-play approach [192–194]. These compact and integrated systems are of particular interest in view of out-of-lab applications, e.g. for the application of quantum communication systems in the urban fiber-based communication network. From an experimental point of view, Schrödinger’s kitten states can be obtained by subtracting a single photon from a squeezed vacuum state [93]. Recently a PPLN/RW-based setup has been proven to be able to generate Schrödinger’s kitten state [94]. However, in this experiment, the single photon subtraction and the detection of the prepared non-Gaussian state of light are made in bulk optics, where the mode matching and the spatial alignment are critical issues to be addressed to get good results. In the work done in Nice, we realized a plug-and-play setup to overcome these issues: in the experiment, the squeezing generation, the subtraction, as well as the detection, are all obtained via fiber-based components [95].

5.2 Theoretical description

In this section, the theoretical description and the references to understand the principles behind the experiment are provided.

²<https://inphyni.univ-cotedazur.fr/a-propos-dinphyni/annuaire/virginia-dauria>

³<https://inphyni.univ-cotedazur.fr/a-propos-dinphyni/annuaire/mohamed-melalkia>

5.2.1 Squeezing generation

In our experiment we used a PPLN/RW to generate vacuum squeezing via a degenerate Spontaneous Parametric Down Conversion (SPDC) process: referring to the theoretical section 1.4.4, one photon of the pump ω_p generates two photons at half of its frequency $\omega_s = \omega_i = \omega_p/2$. In case of a single-mode strong pump, its mode can be treated as a classical coherent state and its depletion can be neglected, i.e. $\hat{a}_p \rightarrow |\alpha\rangle e^{-i\varphi}$, and the Hamiltonian of interaction for the degenerative SPDC process in the rotation wave approximation can be modelled as [102]:

$$H_I = \hbar k |\alpha| \left(e^{-i\varphi} \hat{a}^{\dagger 2} + e^{i\varphi} \hat{a}^2 \right) = -\frac{i}{2} k' \hbar \chi^{(2)} |\alpha| \left(e^{-i\varphi} \hat{a}^{\dagger 2} + e^{i\varphi} \hat{a}^2 \right) \quad (5.1)$$

where $\chi^{(2)}$ is the second-order non-linearity of the non-linear crystal, the operator \hat{a} (and the h.c.) is associated to the generated state of light and $k = -\frac{i}{2} k' \chi^{(2)}$ is the coupling constant of the non-linear process that depends on $\chi^{(2)}$. The evolution of the state can be described via the unitary operator U_I as [101, 102, 108]:

$$U_I = e^{iH_I t/\hbar} = \exp \left[\frac{nLk'}{2c} \chi^{(2)} |\alpha| \left(e^{-i\varphi} \hat{a}^{\dagger 2} + e^{i\varphi} \hat{a}^2 \right) \right] = \exp \left[\frac{1}{2} \zeta^* \hat{a}^2 - \frac{1}{2} \zeta (\hat{a}^\dagger)^2 \right] \quad (5.2)$$

where $t = nL/c$ is the interaction time where L is the crystal length, n is the refractive index and c the speed of light and the squeezing parameter is defined as $\zeta = s e^{i\varphi}$ where $s = \frac{nLk'}{2c} \chi^{(2)} |\alpha|$. This interaction toy model allows us to immediately recognize the possibility of squeezing generation via a SPDC process. In particular, in the experiment presented in [95] a squeezing vacuum state is generated at the output of the PPLN/RW.

It is worth noticing that in the experiment the PPLN/RW is pumped in the CW regime, therefore the generated squeezed vacuum state is characterized by a certain temporal wave-packet amplitude, defined by the non-linear crystal. A complete theoretical treatment of this topic is provided in [195].

5.2.2 Kitten state preparation

In single-mode quantum optics, a cat state is a non-Gaussian state of light generated by a macroscopic superposition of two coherent states characterized by opposite phases ($|\alpha\rangle$ and $|\alpha\rangle$) and the same amplitude [101]:

$$|\Psi\rangle = \frac{1}{C} (|\alpha\rangle + e^{i\varphi} |\alpha\rangle) \quad (5.3)$$

where $C = \sqrt{2 [1 + e^{-2|\alpha|^2} \cos(\varphi)]}$ is a normalization constant, φ is the relative phase⁴ and α is the amplitude of the coherent state $|\alpha\rangle = e^{(\alpha \hat{a}^\dagger + \alpha^* \hat{a})} |0\rangle$. The operators \hat{a}^\dagger and \hat{a} , appearing in the definition of the coherent state, are the construction and annihilation operator, respectively and they fulfil the commutation rule $[\hat{a}, \hat{a}^\dagger] = 1$ (section 1.2). In particular, starting from this definition, we can call a *kitten state* a low-amplitude cat state [93], as already mentioned. In particular, it is possible to generate a kitten state

⁴Depending on φ we can define different types of cat states: for $\varphi = 0$ we have the *even cat state*, $\varphi = \pi$ the *odd cat state* and for $\varphi = \pi/2$ we have the so-called *Yurke-Stoler state*. These three states are eigenvectors of \hat{a}^2 [101].

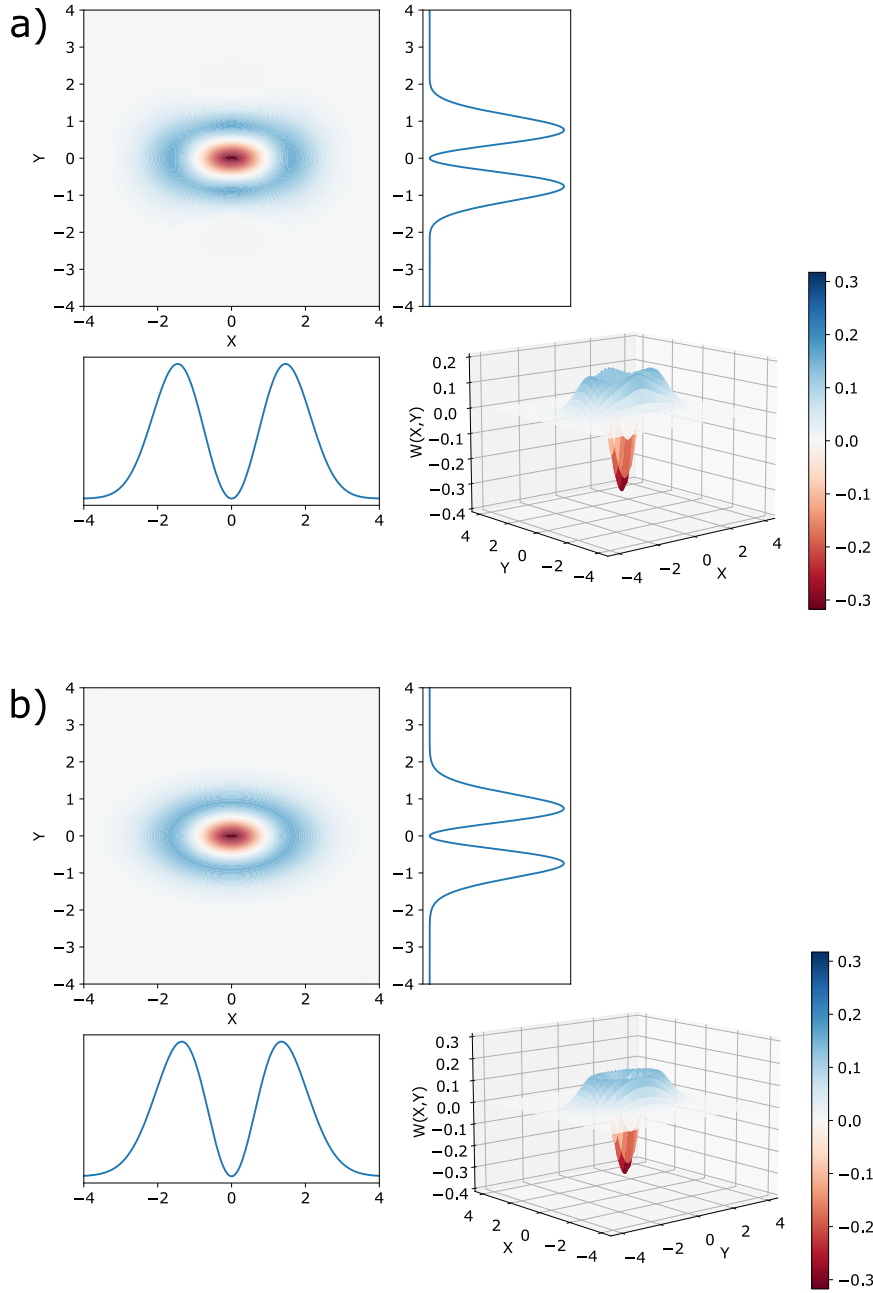


Figure 5.1: a) Wigner Function of a cat state of low amplitude $|\alpha|^2 = 1$, with $\varphi = \pi$ (eq. 5.3). b) Wigner Function of a cat state of low amplitude generated by subtracting a photon from a squeezing state of 2.7 dB (eq. 5.4). The simulation has been done with the Python library **QuTiP**. In both figures (a) and (b) two main elements are depicted: On the left, there is the projection of Wigner Function $W(X,Y)$ in the XY -plane with marginal probability distributions, shown in the two graphs surrounding the XY -plane projection of $W(X,Y)$ (they are obtained integrated the $W(X,Y)$ over the conjugated quantity); On the right, the 3D representation of the $W(X,Y)$ with the corresponding colour-bar is shown.

$|\Psi_k\rangle$ by subtracting a photon from a squeezed vacuum state ($\hat{S}(\zeta)|0\rangle$) [93]:

$$|\Psi_k\rangle = \hat{a}\hat{S}(\zeta)|0\rangle \quad (5.4)$$

where $\hat{S}(\zeta) = \exp\left[\frac{1}{2}\zeta^* \hat{a}^2 - \frac{1}{2}\zeta (\hat{a}^\dagger)^2\right]$ is the squeezing operator [100] (section 1.2). Indeed, this state is comparable to a cat state of low amplitude (eq. (5.3)), as shown in

Fig. 5.1: The two graphs show the Wigner function [101, 112] (sec. 1.7) of the two states in terms of the field quadrature X and Y ⁵. Both the depicted Wigner functions are characterized by a negative part, that reaches the minimum (i.e. -0.3) at $X=Y=0$. The negative of the Wigner function proves the state's non-classicality [112, 114]. The analogy between the two states (Eq. (5.4) and Eq. (5.3) in case small amplitude) allows from an experimental point of view to get a way to construct a kitten state: via a non-linear crystal it is possible to generate a squeezing vacuum state and, then, an unbalanced BS with a low reflectivity can be used as for the photon subtraction. This is the working principle of the here presented experiment.

5.2.3 Detection and quantum state reconstruction

The detection technique used in this experiment is based on a homodyne detection measurement. The theory of this technique is described in chap. 1 (section 1.6). As already mentioned this technique allows to measure a current signal I_θ proportional to the quadrature $\hat{Q}(\theta) = \hat{X}_\theta$ of the electric field associated at the state of light under investigation:

$$I_\theta \propto \hat{X}_\theta = \hat{X} \cos(\theta) + \hat{Y} \sin(\theta). \quad (5.5)$$

By performing multiple measurements of states identically generated, we can measure the marginal probability distribution $P(\hat{X}_\theta)$ associated to the quadrature \hat{X}_θ , which is also the marginal of the Wigner function (sec. 1.7) [113]:

$$P(\hat{X}_\theta) = \int_{-\infty}^{+\infty} W(X_\theta \cos(\theta) - Y_\theta \sin(\theta), Y_\theta \cos(\theta) + X_\theta \sin(\theta)) dY_\theta. \quad (5.6)$$

From here, by inverting the relation, we can reconstruct the Wigner function of the tested state [103].

In the experiment, the max likelihood algorithm is used to reconstruct the prepared state of light [196], consisting in the estimation of the state (described via the density matrix) that best represents the obtained results, by maximizing the probability of obtaining them. The description of this algorithm is out of the scope of this thesis, however, the principle of work of the data analysis done in Nice is provided in the sec. 5.4. Further information about this algorithm is provided in [108, 196].

Impact of the experimental losses

All the theoretical framework here presented neglects the losses contribute. As shown in the theoretical part of this manuscript (chap. 1), the presence of losses affects the measurement of the quadrature of the state. Therefore, a careful analysis of the losses is needed to understand the limits of the experimental setup.

By recalling the theory introduced in chap. 1 (sec. 1.6), in a real setup the measured quadratures are affected by the losses $(1 - \eta)$ and the measured variance for a squeezed

⁵ X and Y are respectively the real and complex part of the operator \hat{a} (or of the electric field if multiplied for the proper scale factor [100](see chap. 1)), and are therefore observable.

vacuum state $(\Delta X_M)^2$ of the quadrature $\hat{X}_M = (\hat{X}_\theta)_{\text{measured}}$ is given by:

$$\begin{aligned} (\Delta X_M)^2 &= (\Delta X_0)^2 \left[\eta (\Delta X_\theta)^2 + (1 - \eta) \right] \\ &= (\Delta X_0)^2 \left[\eta \{e^{2s} \sin^2(\theta) + e^{-2s} \cos^2(\theta)\} + (1 - \eta) \right] \end{aligned} \quad (5.7)$$

where $(\Delta X_0)^2 = 1/4$ is the quadrature variance of the vacuum state (section 1.2) and $(\Delta X_\theta)^2 = (\Delta X_0)^2 \{e^{2s} \sin^2(\theta) + e^{-2s} \cos^2(\theta)\}$ is the variance of the squeezed vacuum state (without losses). Like in the other presented experiments, the losses can compromise the detection of the squeezing. Furthermore, if the overall efficiency (including generation, transmission and detection) is lower than 50%, it is not possible to achieve a negative value in the reconstructed Wigner function [156].

By recalling $(\Delta X_0)^2 = \sigma_0^2$ to simplify the notation, in this lossy scenario the minimum, $(\Delta X_M)^2|_{\min} = \sigma_{\min}^2$, and the maximum, $(\Delta X_M)^2|_{\max} = \sigma_{\max}^2$, of the variance $(\Delta X_M)^2$ (Eq. (5.7)) are respectively [108]:

$$\sigma_{\min}^2 = \sigma_0^2 [\eta e^{-2s} + (1 - \eta)], \quad (5.8)$$

$$\sigma_{\max}^2 = \sigma_0^2 [\eta e^{2s} + (1 - \eta)]. \quad (5.9)$$

In the experiment, starting from the measured maximum and minimum values of the quadrature variance, it is possible to retrieve the squeezing parameter $\mathcal{S} = e^{-2s}$ and the efficiency η by inverting the above mentioned relations:

$$\mathcal{S} = \frac{1 - \sigma_{\min}^2/\sigma_0^2}{\sigma_{\max}^2/\sigma_0^2 - 1}, \quad (5.10)$$

$$\eta = \frac{(\sigma_{\max}^2/\sigma_0^2 - 1)(1 - \sigma_{\min}^2/\sigma_0^2)}{\sigma_{\max}^2/\sigma_0^2 + \sigma_{\min}^2/\sigma_0^2 - 2}. \quad (5.11)$$

5.3 Experimental setup

A schematic representation of the utilized setup for generating Schrödinger's kitten states is depicted in Fig. 5.2. A CW fiber-coupled laser produced by μQuans ⁶ is used as laser source. The laser has three outputs: a 780.2-nm amplified output and two 1560.4-nm outputs, but only one of them is amplified. Referring to the setup area named *squeezing generation*, the emitted power of the 780.2-nm output is controlled via a commercial fiber-coupled Variable Optical Attenuator (VOA) and its polarization is adjusted via a polarization controller (PC). Then the radiation is sent to a commercial pigtailed PPLN/RW produced by NTT Electronics corporation. Here the 780.2-nm beam acts as a pump for the generation of a single-mode squeezed vacuum state at 1560.4 nm by degenerate SPDC process. In particular, the used commercial PPLN/RW module is equipped with a thermistor and a thermoelectric cooler to control and stabilize

⁶In this device, the 1560.4-nm radiation is produced via a diode laser. the 780.2-nm light is generated via a SHG process enabled by a PPLN/RW which is located inside the μQuans laser. A portion of the generated SHG radiation is used to lock the diode to a ⁸⁵Rb transition. The remaining SHG radiation and a portion of the 1560.4-nm radiation are amplified via an Erbium doped fiber amplifier and they are sent to two amplified polarize-maintaining-fiber outputs. Finally, the residual part of the 1560.4 nm radiation is sent without amplification at the third polarize-maintaining-fiber output. This latter output radiation is characterized by a linewidth of 8 kHz. More details can be found in [108].

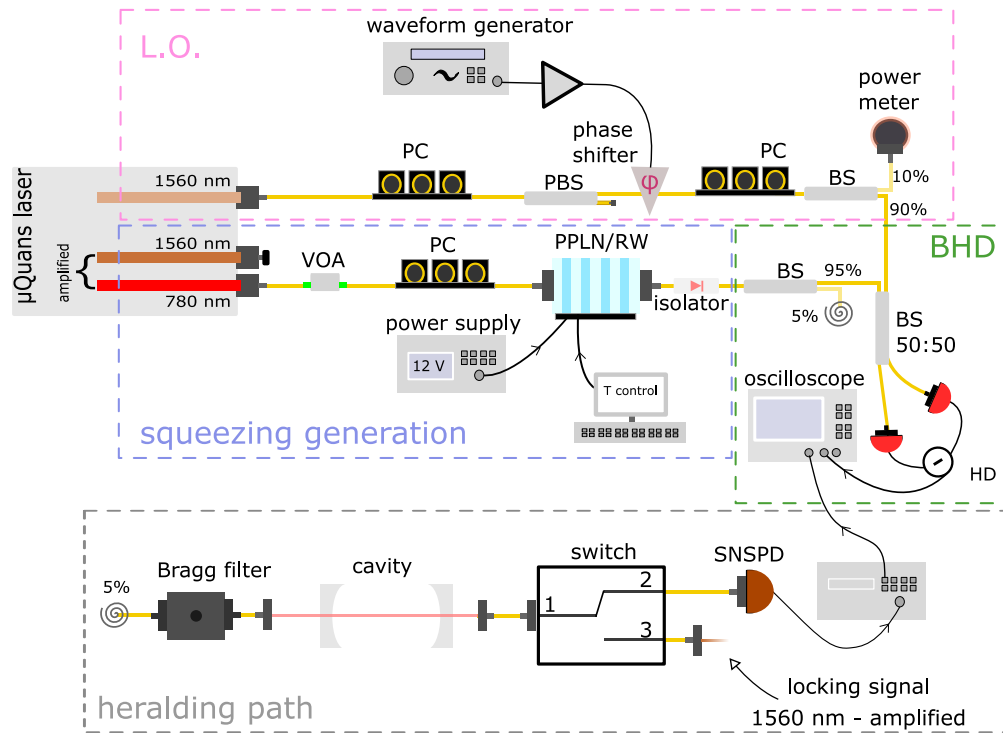


Figure 5.2: Overview of the experimental setup. The source is a μ Quans laser able to emit both at $\lambda = 1560.4$ nm (red and beige laser outputs) and at $\lambda = 780.2$ nm (brown output). The setup is divided into four main areas: in the *squeezing generation* part, the laser amplified output at $\lambda = 780.2$ nm is used to pump a non-linear PPLN/RW, generating a single-mode 1560.4 nm-squeezed vacuum state. The PPLN/RW is stabilized in the temperature via a temperature controller (T control), while the intensity and the polarization of the pump are controlled via a Variable Optical Attenuator (VOA) and a polarization controller (PC), respectively. By subtracting the 5% of the generated squeezed state via a 5/95 BS, a non-Gaussian photon-subtracted squeezed state is then generated. The prepared state (expected to be a kitten state), obtained at the 95%-output of the BS, is then measured via a BHD (BHD, green area). In the BHD, this state is mixed via a 50/50 BS with the LO reference radiation which is obtained via the non-amplified μ Quans's output at $\lambda = 1560.4$ nm (sketched in beige). Before reaching the 50/50 BS, the LO radiation passes through a phase shifter and a PC (L.O., pink area). At the two outputs of the 50/50 BS, the signal is then acquired via a homodyne detector (HD) where the difference is electronically computed. Furthermore, the 5% output of the subtracting BS is used for heralding the photon-subtracted squeezed state detection (*heralding path*, grey area). This 5%-beam passes through a Bragg filter and a cavity in order to match the bandwidth of the HD. Through an optical switch (link 1-2) the heralding photons reach a superconducting nanowire single-photon detector (SNSPD), where the signal is converted via a time-to-digital converter (TDC) and used to herald (trigger) the detection of the kitten state done via an oscilloscope. The link 3-1 of the switch is used to lock the cavity using the amplified laser output at $\lambda = 1560.4$ nm. More details about the filtering process and the setup are provided in the main text.

the PPLN temperature via an external driver. In our case, we used a commercial thermoelectric cooler (MTD451T, Thorlab).

After the squeezing generation, a non-Gaussian photon-subtracted squeezed state (i.e. our "kitten state") is then generated by subtracting a part of the squeezed light via a 5/95 BS. A BHD detector is then used to detect its quadrature signal (green area, Fig. 5.2), by mixing its radiation with that of the LO via a 50/50 BS. The LO radiation is taken from the 1560-nm output of the laser source, where the polarization is controlled via a PC (pink area, 5.2). In addition, the LO phase is scanned via a commercial phase shifter produced by General Photonics⁷. Furthermore, by using a PC combined with

⁷During the quadrature measurement done via the BHD, it is possible to scan the quadrature of the signal of interest in the phase space by scanning the LO phase.

a 10/90-polarized BS, the LO power is monitored during the measuring process via a power meter located at the 10% output of the BS. The remaining 90% part of the LO beam is sent to the BHD.

Regarding the detection system, the homodyne detector (HD) is a commercial detector produced by Insight Photonic Solutions characterized by a bandwidth of 300 MHz and a quantum efficiency $\eta_{pd} = 0.80$. This detector has been characterized via the same procedure shown in chap. 3.3. In the experiment, the HD was used in the linear responsivity regime with a LO power of 3.1 mW corresponding to a clearance of 14 dB between the related shot-noise level and the background noise, leading to an equivalent efficiency $\eta_{el} = 0.96$. To compute the overall detection efficiency for the prepared state propagating inside the implemented setup, the overall optical transmissivity is also taken into account. By considering both the optical losses affecting the propagating radiation before the BHD and the one of the 50/50 BS, we get an overall optical transmissivity $\eta_t = 0.94$. Therefore, the effective detection efficiency is: $\eta_d = \eta_t \cdot \eta_{el} \cdot \eta_{pd} = 0.72^8$. In the implemented setup, the 5% output of the subtraction stage is used to herald the detection of the generated non-Gaussian state, as described in [94, 197], where it is shown that a low-reflectivity BS can be used in combination with single-photon detector to herald the homodyne detection of the prepared state.

In the heralding channel (grey area 5.2), a filter (composed by a Bragg grating filter and a custom-made Fabry-Peròt cavity) is used to match the heralding bandwidth with one of the homodyne detection. The filtering stage is then followed by an optical switch, connecting via link 1-2 the 5%-filtered beam to the superconducting nanowire single-photon detector, SNSPD, (Id281 SNSPD, IDQuantique), whose output signal is sent to a time digital converter, TDC, (Id900, IDQuantique) and it is then used as a trigger for the kitten state balanced homodyne detection measurements, acquired via an oscilloscope (HDO6104A, Teledyne Lecroy).

The filtering stage and the cavity locking are described in the next section.

5.3.1 Heralding process

As already described, to herald the detection of the prepared non-Gaussian state, the 5% output of the subtraction BS is used, i.e. the detection of the single photon (idler) heralds the kitten state. However, in general, in the SPDC process the signal and idler photons can be generated at two different frequencies within the crystal bandwidth, which is of 12 THz, centered around 192.5 THz (corresponding to 1557.3 nm), as shown in Fig. 5.3. This means that, in principle, a detected single photon, along the heralding path, can herald the detection of a state whose LO beating is outside the 300-MHz bandwidth of the HD. Therefore, the heralding signal needs to be filtered to match the bandwidth constraint given by the HD. The filtering process is made via a cascade of two optical filters: a Bragg grating filter and a custom-made Fabry-Pèrot cavity. In particular, The Bragg filter is a commercial adjustable ultra-narrow transmission filter (Advanced Optics Solutions GmbH). This filter has the maximum of transmission around 1560.5 nm and its bandwidth is 585 MHz⁹. Therefore a further reduction is

⁸More details about the HD characterization are available in [95].

⁹The bandwidth is measured in terms of FWHM of the spectral transmission, the measurements are available in [108].

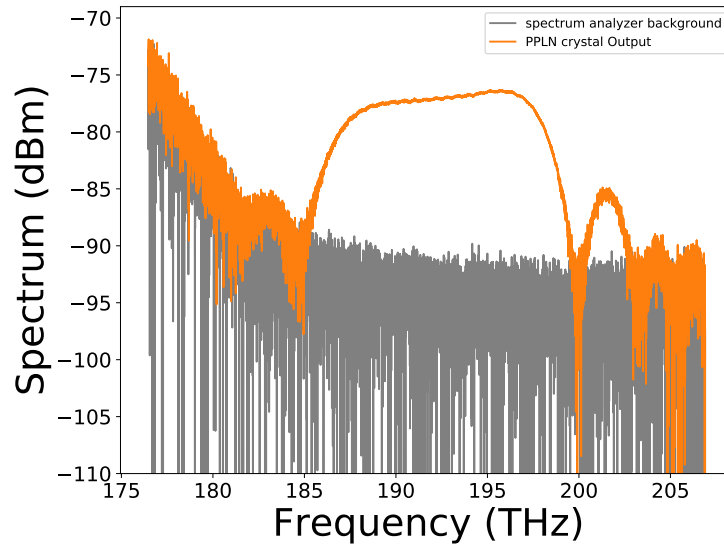


Figure 5.3: Spectrum of the PPLN/RW (orange trace) acquired with an optical spectrum analyzer, compared to the instrument background (grey trace).

needed to match the HD bandwidth. In order to accomplish this task we inserted a custom-made in-house Fabry-Pèrot cavity in the setup. It is worth mentioning that the used Fabry-Pèrot cavity is the only bulk part of the experiment. However, it can be substituted with a proper compact system, e.g. a thin etalon cavity or a sharper Bragg filter, to create a more compact and fully plug-and-play setup.

Fabry-Pèrot cavity

The cavity has been designed in the following way [107]: in order to filter the output light from the Bragg filter, the cavity modes have to be spaced more than two times the filter bandwidth. This guarantees that only one cavity mode is inside the Bragg filter mode width. Therefore, in our case, the cavity FSR must fulfil the following relation: $FSR \geq 1$ GHz [108].

In particular, the mounted Fabry-Pèrot cavity is composed of a plane mirror with a reflection coefficient $R_P = 0.98$ and a curved one (attached to the piezo, PZ, in Fig. 5.4) with a curvature radius of 1 m and a reflection coefficient $R_C = 0.99$. The expected finesse \mathcal{F} is therefore [198]:

$$\mathcal{F} \approx \pi \frac{\sqrt[4]{R_C \cdot R_P}}{1 - \sqrt{R_C \cdot R_P}} \approx 208. \quad (5.12)$$

The distance¹⁰ between the two mirrors is set at $L_C = 7$ cm. Therefore the expected single mode width $\Delta\nu$ is:

$$\Delta\nu = \frac{c}{2\mathcal{F}L_C} = 10 \text{ MHz}, \quad (5.13)$$

where c is the speed of light, while the expected cavity FSR is:

$$FSR = \frac{c}{2 \cdot L_C} = 2 \text{ GHz}. \quad (5.14)$$

¹⁰The cavity has been designed in this configuration taken into account of the available space in the optical table and the available optical elements [108].

Therefore the designed cavity matches the requirement mentioned above. In order to get a stable filtering process the cavity has been locked (link 3-1 of the switch, Fig. 5.2).

Cavity locking

The cavity-locking working principle is depicted in Fig. 5.4. The locking and the measurement processes are not simultaneous, but one follows the other in a repeated cycle. This cycle is iterated for all the measurements acquisition and it is obtained via an optical switch (OSW12-1310E MEMS 1x2 Fiber Optic Switch Kit, Thorlabs): the period of this cycle is 1 s divided in 0.2 s of cavity locking (switch in the position 1-3 as depicted in Fig. 5.4) and in 0.8 s of heralding photon detection (switch in the position 1-2 as depicted in Fig. 5.2). The details of the synchronization needed for this switching cycle are provided after the cavity locking description.

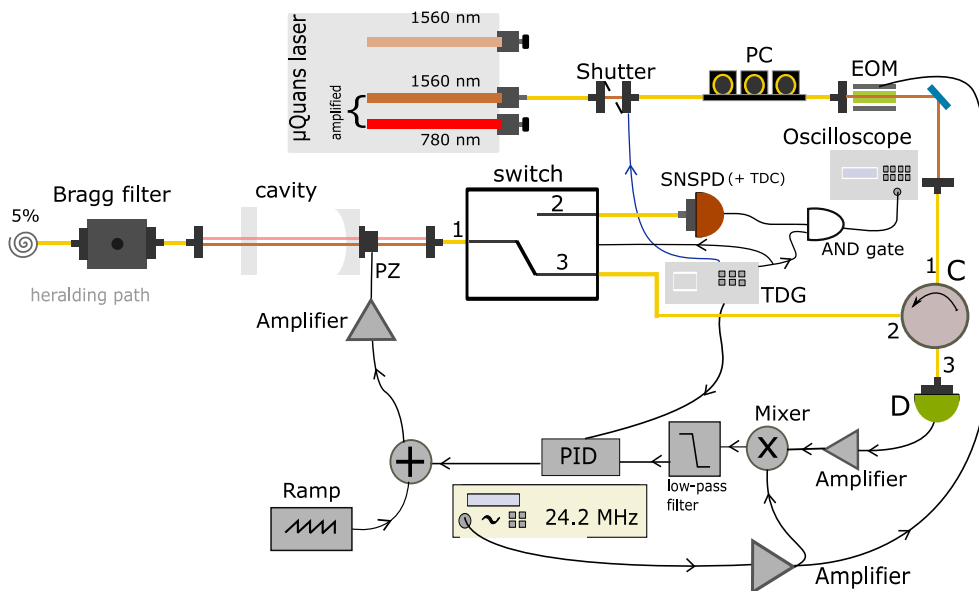


Figure 5.4: Sketch of the cavity setup both from optical and electronic points of view. Some elements are already introduced in Fig. 5.2. The details of the setup are explained in the main text. The principle of work is here summarized: The amplified 1560-nm radiation is used as a reference for the cavity locking. When switch ports 1 and 3 (link 1-3) are connected the system is in the locking part of the cycle. The 1560-nm passes through a shutter and a PC and it is modulated via an EOM at 24.5 MHz. The modulated radiation arrives at the switch and then at the cavity, passing through the circulator C (input 1- output 2). The reflection signal from the cavity is used in the PDH locking method to stabilize the cavity. Through the switch and the circulator (input 2- output 3), the reflection signal is collected via an AC detector. The detected signal is amplified and beaten via a mixer with the modulation signal and filtered via a low-pass filter. After an amplification stage, the obtained PHD error signal is then sent via a PID controller to a piezo (PZ) mounted onto the curved cavity mirror. This mirror is moved accordingly to the PHD signal, keeping the cavity stabilized.

The method used for the cavity locking is the Pound-Drever-Hall (PDH), consisting in monitoring the cavity stabilization via the derivative of the cavity output signal[199] (in our case we used the reflected signal). In the assembled setup, the amplified 1560-nm beam is used to lock the cavity. For this purpose, it is modulated at 24 MHz¹¹ via an

¹¹The modulation signal is obtained via a clock generator breakout board (Si5351, Adafruit) combined with Arduino Uno R3 chip [108]. Before reaching both the mixer and the EOM, this signal is amplified (Amplifier 15 dB ZX60-100VH+, Mini-Circuits).

electro-optic modulator (EOM) (PM7-SWIR, QUBIG GmbH). The modulated radiation passes through a fiber circulator (C, Fig. 5.4) and, from the output 2, it reaches the cavity passing through the switch link 1-3. The reflected light from the cavity comes back reaching the circulator from the same switch link (link 1-3). Here, the reflected light entering via port 3 of the circulator reaches the 100-MHz-bandwidth AC detector (PD100, Koheron) (D, Fig. 5.4). The AC-detected signal is used in the error correction of the PDH locking process. For this scope, such signal is amplified of 20 dB and mixed via a commercial mixer (ZX05-1MHW-S+ mixer, Mini-Circuits) with the modulation signal at 24 MHz, properly delayed. The resulting beat signal is then filtered via a low-pass filter (BLP-2.5+ from Mini-Circuits) and sent to the PID controller (Teensy 3.2)¹². The PID control signal is, then, amplified (TD250 amplifier, PiezoDrive) and

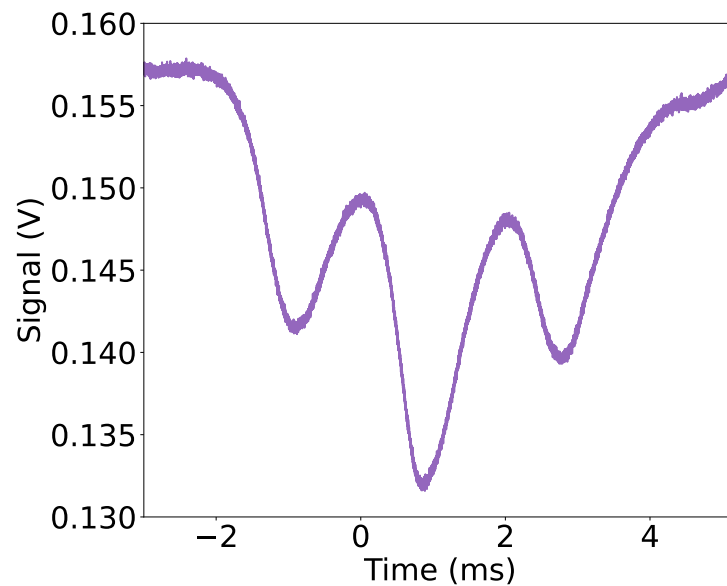


Figure 5.5: Reflection signal from the cavity showing the cavity mode (central peak) used for the lock-in and the sidebands due to the EOM modulation.

sent to the piezo (PZ in Fig. 5.4) mounted on the curved mirror to keep the cavity locked to its resonance position. Moreover, a ramp signal generated by a servo controller (Toptica) is added to the PID control signal to scan the cavity during the alignment. An example of the reflection cavity signal obtained during a ramp scan is shown in Fig. 5.5. Here both the central mode and the two EOM sidebands are visible. Knowing that the EOM sidebands are distant 24.5 MHz from the central mode, corresponding to 2 ms approximately in Fig. 5.5, it is possible to retrieve the FWHM of the central signal which is 12.2 MHz, in good agreement with the value expected from Eq. (5.13).

Synchronization

As a side effect, the presence of the optical switch has the problem of cross-talk between the two link channels that must be removed to guarantee a heralding signal that comes from the subtraction process, only. To avoid this cross-talk, a shutter is placed before the EOM in the 1560-nm beam path (SH05, Thorlabs). The shutter, the

¹²In order to have an error signal readable by the used PID controller, the signal is shifted via a DC offset to have only positive input value at the Teensy entrance.

switch and the PID are synchronized using a time delay generator (TDG) (DG535, Stanford Research). Furthermore, to ensure that the trigger signal received by the oscilloscope comes only from the SNSPD detection of a subtracted single photon, an AND gate is placed between the TTL signal generated by TDG and the SNSPD. The synchronization is made with the following logic:

a) During the measurement process (0.8 s):

- the TTL signal sent to the shutter and the PID is 0, which blocks the shutter, while the PID controller maintains the last control signal until the next locking cycle activation;
- Simultaneously, a TTL signal 1 is sent to the switch, to activate the link 1-2, and to the AND gate, to get a trigger from the detection of a single photon.

b) During the locking process (0.2 s):

- the TTL signal sent to the shutter and the PID is switched to 1, opening the shutter and activating the PID controller;
- Simultaneously, a TTL signal 0 is sent to the switch, to activate the link 1-3, and to the AND gate, to avoid any trigger in the locking phase.

With this scheme, the measured single-photon overall detection efficiency is 6%. During the measurements, the SNSPD count rate is 3 kHz, while the dark count rate is 80 Hz, giving an SNR = 17.5 dB.

5.4 Results and discussion

As already stated, the scope of the data analysis is to reconstruct the Wigner function of the photon-subtracted squeezed state. In the experiment, 43k 5- μ s-long quadrature traces $x_i(t)$ are acquired via the oscilloscope with a sample rate of 5 Gs/s. The LO phase, spanning with a speed of $9\pi/s$, results constant over each single i -th homodyne acquisition. To reconstruct the Wigner function of the prepared state we have to estimate both its quadrature X_i and the corresponding LO phase θ_i . From the filtering process, we know that the heralding bandwidth is around 10 MHz (given by the cavity). Therefore, during the 5 μ s acquisition most of the collected data regards the squeezed vacuum state and not the heralded states [108]. Being its quadrature phase dependent (chap. 1), it is possible to calculate the variance σ_{sq}^2 of each measured $x_i(t)$ ¹³ and used them to extract the corresponding θ_i [108]. An example of this procedure is shown in Fig. 5.6(a). In this figure, the squeezing variance calculated for 1000 acquired homodyne traces $x_i(t)$ is displayed. The data are plotted via a sinusoidal function¹⁴ allowing to retrieve the phase θ_i for each computed squeezed state variance, and therefore for each acquired trace x_i . Via this analysis, the dependence of the squeezed state variance as a function of the LO phase is therefore reconstructed (Fig. 5.6b). As a consequence, it has been possible to identify the maximum and the minimum value of the squeezed state variance. In particular, from Fig. 5.6b we can determine a

¹³The variance is calculated over all the 5 μ s trace $x_i(t)$.

¹⁴The used fit function is $f(t) = A\cos(a \cdot t^2 + b \cdot t + c) + B$ [108].

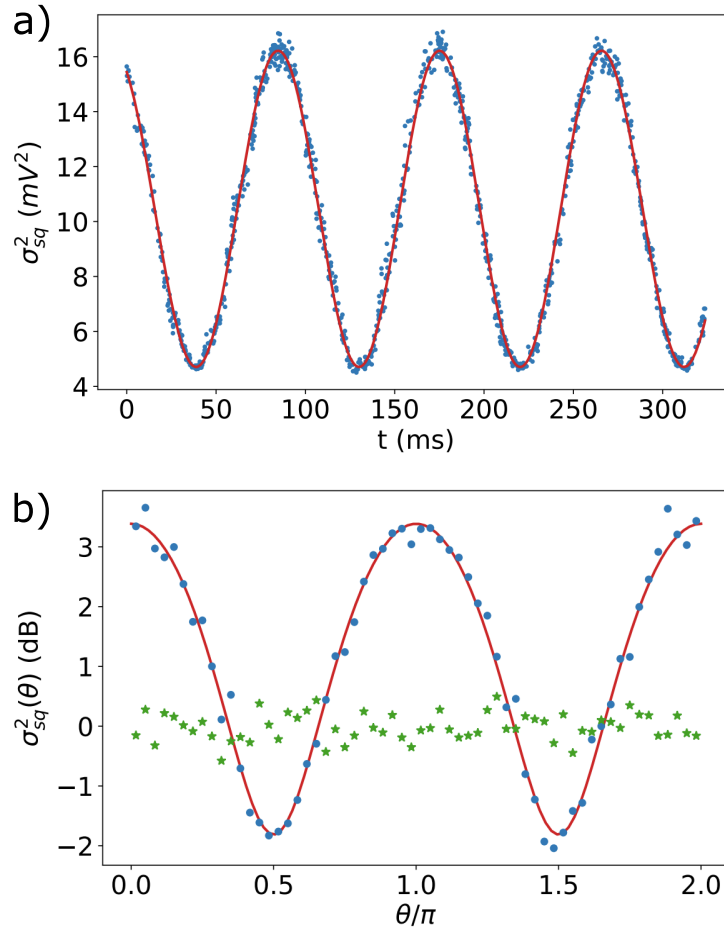


Figure 5.6: (a) Squeezed variance σ_{sq}^2 computed for 1000 measured quadratures x_i . The sinusoidal fit used to extract the phase θ_i associated with each acquired quadrature trace x_i , is displayed in red. (b) Squeezed variance σ_{sq}^2 (blue dots) as a function of the LO phase. The data are compared to the shot-noise level of the LO (green data) and are fitted via the equation Eq. (5.7) (red curve). Figures adapted from [108].

minimum value of -1.81 dB and a maximum value of 3.36 dB. From these values using the relations of Eq. (5.10) and Eq. (5.11), an initial squeezing amount of -5.37 dB is expected (evaluated via the parameter S , Eq. (5.10)) and an overall transmission efficiency $\eta = 0.48$ (Eq. (5.11)). At this point it is useful to explicate the definition of η applied to our experiment: $\eta = \eta_d \cdot \eta_{wg} \cdot \eta_s$ (Eq. (5.11)) where $\eta_d = 0.72$ is the overall homodyne detection efficiency calculated in sec. 5.3, $\eta_s = 0.96$ is the transmission of the subtracting $5/95$ BS and η_{wg} takes into account both propagation losses and losses due to the guide-fiber coupling occurring in the PPLN/RW. In particular, we can estimate a $\eta_{wg} = 0.69$ from the retrieved value of η .

As already described in the case of the BHD presented in chap. 3, it is worth noticing that with this efficiency ($\eta < 0.5$) there is no chance of observing a negative Wigner function, however, it is still possible to unveil a non-Gaussian state corresponding to the lossy kitten state.

As already anticipated, together with the phase, the other key parameter to reconstruct the Wigner function is the quadrature of the heralded state X_i . The procedure is the one presented in [195, 200]. In this experiment, indeed we have to face the fact that, we are

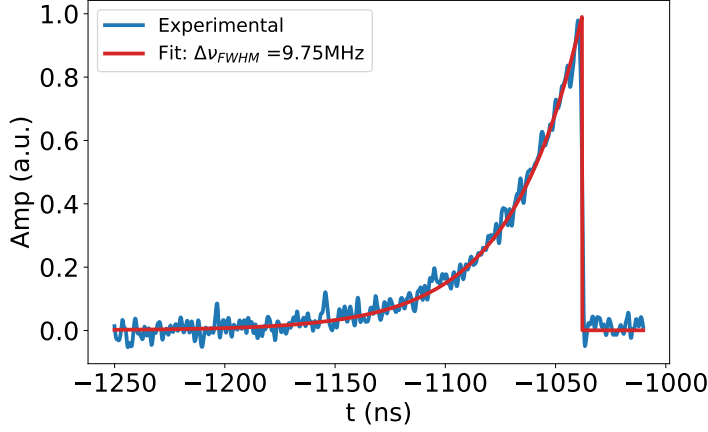


Figure 5.7: Temporal mode obtained as the eigenvector $f(t)$ with the highest eigenvalue (blue trace) fitted with the expected theoretical rising exponential function.

dealing with CW travelling quantum state of light. As shown in [195, 200], in the CW regime it is possible to extract the quadrature of interest X_i by knowing the temporal profile of the heralded state $f(t)$, i.e. its wave-packet, which in our experiment is given by the filtering process done in the heralding path. In particular, X_i can be extracted by the homodyne raw data x_i using the equation:

$$X_i = \int f(t) \cdot x_i(t) dt. \quad (5.15)$$

To retrieve the $f(t)$ function, the auto-correlation function of the acquired quadrature segments is calculated [108, 200]: $g(t, t') = \langle x_i(t)x_i(t') \rangle$. The method involves, then, the calculation of eigenvalues and eigenvectors of the auto-correlation function $g(t, t')$. In particular, as demonstrated in the manuscript [200], the eigenvector $f(t)$ with the highest eigenvalue is the proper temporal mode to use in the analysis¹⁵. In our experiment, based on the fact that the squeezed bandwidth is higher than the filter one, the temporal function should be a rising exponential function [108]. An example of the obtained results is shown in Fig. 5.7, where the function $f(t)$ related to the highest eigenvalue is fitted with the theoretical rising exponential function¹⁶. Via the fit procedure, a FWHM of approximately 10MHz is found, as expected by the filtering process (dominated by the cavity mode FWHM). Once known $f(t)$, the quadrature X_i are retrieved via Eq. (5.15) and used, together with the phases θ_i , in the maximum likelihood algorithm to extract the Wigner function¹⁷[108, 201, 202]. In Fig. 5.8 the retrieved Wigner function (a) is compared with the Wigner function corrected for the

¹⁵Indeed, this eigenvector maximizes the variance of the quadrature X which can be defined as:

$$\sigma^2(X) = \int \int f(t)f(t') \cdot g(t, t') dt dt'.$$

This method is based on the fact that the variance of the heralded non-Gaussian state is greater than the squeezed vacuum one [101, 108].

¹⁶The used fit function is:

$$f(t) = \Theta(-t)e^{2\pi\nu t},$$

where $\Theta(-t)$ is the Heaviside function [108].

¹⁷For the maximum likelihood application, the number of interaction done is 200 [95]. The description of this method is out of the scope of this thesis, indeed the code for the tomography reconstruction has been developed by Dr Melalkia and the details can be found in its manuscript[108].

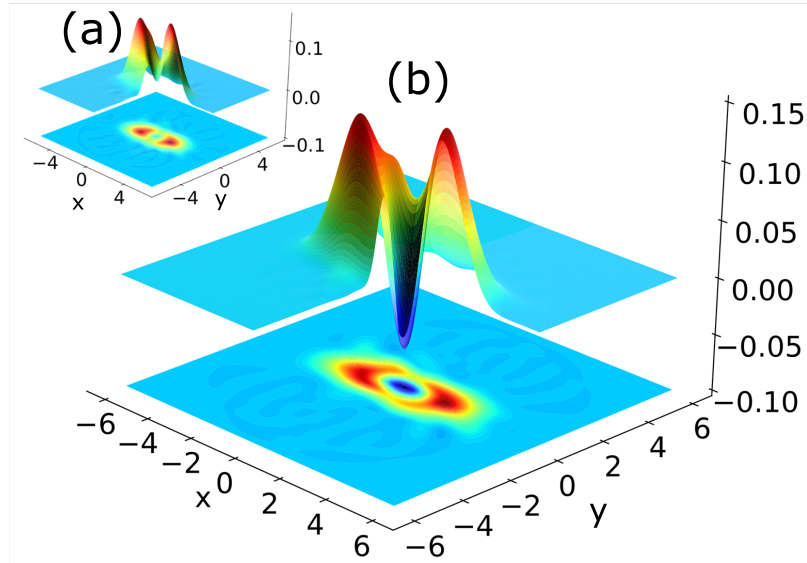


Figure 5.8: (a) Reconstructed Wigner function used the maximum likelihood method [108]. The reached minimum is $W_a(0,0) = 0.016 \pm 0.004$. (b) Wigner Function corrected for the detection efficiency the minimum is negative and reached at $W_b(0,0) = -0.065 \pm 0.004$.

detection efficiency ($\eta_D = 0.72$). As expected from the retrieved overall efficiency *eta* (<50 %), in Fig. 5.8a the Wigner function is always positive (the minimum value is, indeed, $W_a(0,0) = 0.016 \pm 0.004$), but with a non-Gaussian shape. Instead, in Fig. 5.8b the Wigner function is corrected for the detection efficiency (η_d) and therefore it has negative values, as expected (sec 5.2) for a kitten state. In particular, the minimum value reached is $W_b(0,0) = -0.065 \pm 0.004$.

The setup can be improved: for instance by splicing together all the fibered components the losses in the experiment can be reduced and, in particular, the PPLN/RW design can be improved and integrated to increase the transmission efficiency being one of the key parameter limiting the achievement of a negative Wigner function.

5.5 Conclusion and perspectives

The here presented work refers to the kitten state generation experiment done in Nice whose results are published in [95]. Here a non-linear PPLN/RW, pumped in CW regime, is used to generate a squeezed state of light at telecom wavelengths (i.e. 1560 nm). The kitten state is then generated via a photon subtraction done on a squeezed state of light. The prepared state is then detected via a BHD. Even though the state tomography performed on the acquired data reveals a Wigner function compatible with a Non-Gaussian state, this function never reaches a negative value, due to the limited overall transmission efficiency (<50%). To retrieve the expected negativity, the data are corrected for the detection efficiency ($\eta_d = 0.72$). The corrected Wigner function shows a negative value in the origin as expected for a kitten state. This work presents some limits that may be overcome by integrating and splicing the fibered components, which should increase the overall transmission efficiency.

As a perspective, this work has given me the methods necessary to deal with CV

non-classical state of light. The goal for my near future research is to apply such gained knowledge to the construction of an innovative MIR setup, based on a non-linear crystal, able to generate quantum states of light. This will allow having a controllable system able to produce non-classical states of light to test the detection setups shown in chap. 3 and in chap. 4. These applications will be a benchmark for the improvement of the implemented setups, with the final goal of detecting non-classical CV quantum states in the MIR.

Conclusion

The main goal of the research activity presented in this thesis is to test the properties of MIR radiation at the quantum level by using QCLs as efficient MIR coherent light emitters. As described in the introduction, the MIR is a region of interest for many applications spanning from spectroscopy and sensing to free-space communication. In this context, the demonstration of non-classical properties of the light emitted by QCLs can open the doors to many revolutionary quantum-technology innovations. For instance, the availability of a MIR non-classical light can lead to an enhancement of the ultimate sensitivity in spectroscopic and sensing measurements and to the development of quantum secure free-space communication links based on non-classical states of light. In this scenario, QCLs optimised for frequency-comb emission (QCL-combs) seem to be promising non-classical-light compact sources. In multimodal QCLs, the comb emission is, indeed, induced in the laser waveguide by a FWM process triggered by the third-order non-linearity of the active medium. As introduced in chapter 1, this phenomenon has also a quantum interest since FWM is a non-linear process able to generate squeezed states of light.

Although the MIR lacks mature quantum-detection technologies, the above-mentioned fundamental and practical interests in testing the MIR light at the quantum level have driven my research activity.

This thesis starts with a theoretical chapter introducing the quantum optics tools needed for describing light-matter linear and non-linear interaction, as well as the measurement techniques. To complete this methodological overview, in chapter 2 the working principle of QCLs is briefly reviewed. Instead, the remaining three chapters are fully devoted to describing three different experiments I performed during my Ph.D. research activity dealing with detection systems for quantum light characterization and quantum sources:

- In chapter 3, the published work [99] is presented. This experimental work focuses on the realization and characterization of a shot-noise-limited MIR balanced detector able to test MIR light at the quantum level. The overall detection bandwidth is 120 MHz. The best performance is achieved for a wavelength of 4.5 μm , where the best clearance (9 dB) and overall detection efficiency (36%) are obtained. Even though these values are lower compared with respect to the

ones achieved at shorter wavelengths (700-800 nm), this is a good starting point to stimulate their improvement for the optimal detection of non-classical states of lights, e.g. squeezed light.

- In chapter 4, intensity-correlation measurements in frequency combs emitted by QCLs are presented. In the first part, section 4.2, the already-published experimental work [75] is described. It reports on the measurement of the sideband-sideband and sideband-pump intensity correlations in the case of a MIR QCL-comb operating in a three-mode harmonic-comb emission characterized by a bright central mode (the pump) and two weak sidebands. The results show the presence of correlation between the two sidebands, ascribable to FWM process. However, this correlation remains at the classical level within the detection bandwidth. The best scenario to detect such correlation is proved to be the operation of the harmonic comb nearby sideband-threshold. Indeed, increasing the sidebands' gain seems to favour the mode competition with the central mode at the cost of reducing the correlation factor. In this work, some suggestions about the improvements needed to achieve the quantum level are provided. For instance, an increase in detection bandwidth may allow exploring the correlation in the regime of reduced $1/f$ noise. Furthermore, a comprehensive quantum theoretical model for QCL emission is still missing. Indeed, a precise model could help not only in the data interpretation but also to unveil the key parameters that must be improved in the next generations of QCL-combs to optimise the emission of quantum-featured light. The second part of this chapter (section 4.3) describes, instead, the application of the correlation setup to study the anti-correlated behaviour of the two frequency lobes present in a MIR QCL-comb operated in bilobed emission.
- Finally, in the last chapter (chap. 5), the experiment that I have realized during my research period at the *Institut de Physique de Nice* (France) is presented. The experiment, published in *Optics Express* [95], describes the generation and the detection of Schrödinger's cat states at telecom wavelength (1560 nm). In this work, by correcting the data for the losses, a Schrödinger's kitten state with a negative Wigner function is observed. Negative values of the Wigner function clearly show the non-classical behaviour of the generated state. Along with the results achieved, this experiment has been highly formative, giving me the know-how necessary to generate, manipulate and detect quantum states of light.

As already anticipated in section 4.4, the next step that I would like to pursue to make the generation and detection of MIR quantum light effective are:

- To generate MIR squeezed-light via a passive non-linear media. In particular, currently in my lab, we are realizing and characterizing a quasi-degenerate doubly-resonant OPO following the work presented in [203].
- To collaborate with quantum-optics-expert theoretical teams, to develop the very first model describing the emission of QCL-combs with a fully quantum approach.

- To collaborate with teams devoted to the fabrication of detectors and devices, to favour the development of a new generation of devices improved for quantum-technology applications.
- To test other emerging MIR laser devices, i.e. interband cascade lasers which seem to be a valid alternative to QCLs, being also characterized by the presence of FWM.

Finally, the very last topic that I would like to investigate in the next years is the application of MIR light sources in free-space communication, pointing to quantum-secure protocols. As already explained in the introduction, the MIR is a valid and competitive alternative to standard NIR wavelengths, in particular in case of adverse weather conditions, being less affected by losses. For this scope, I have already contributed to two proof-of-concept works where QCLs are used as free-space communication sources [16, 46]. In the first cited work [16], we studied the noise contribution to the overall free-space communication system due to a QCL operated in different conditions of attenuation (high attenuation regime and low attenuation regime) and in different points of the LIV curve of the laser source, i.e. nearby threshold and well-above it. In the second cited work [46], we proved the possibility of exploiting the intermodal beat note of a QCL-comb to carry in parallel both an analog and a digital signal via FM and AM, respectively. The next step will be a feasibility study and practical implementation of QKD protocols in a QCL-based free-space communication link.

A.1 BHD with losses	121
A.2 QCL intermodal beat note measurement	123

A.1 BHD with losses

Here the calculations underpinning the equations of sec. 3.2 are reported. Starting from Fig. 3.1a and knowing the BS rules (sec. 1.3 and sec. 1.6), it is possible to retrieve the following relations for the annihilation operators associated to the field at the inputs (\hat{a} and \hat{v}) and outputs (\hat{a}_3 and \hat{a}_4) of the BS¹⁸:

$$\hat{a}_3 = R\hat{a} + T\hat{v}, \quad (\text{A.1})$$

$$\hat{a}_4 = T\hat{a} + R\hat{v} \quad (\text{A.2})$$

where R and T are the complex reflection and transmission coefficient of the BS. In particular, for a 50/50 BS they satisfy the relation: $|R| = |T| = 1/\sqrt{2}$. It is possible to determine the following equation for the photo-number operators associated with the two BS outputs:

$$\hat{n}_3 = \hat{a}_3^\dagger \hat{a}_3 = |R|^2 \hat{n} + R^* T \hat{a}^\dagger \hat{v} + R T^* \hat{v}^\dagger \hat{a} + |T|^2 \hat{n}_v, \quad (\text{A.3})$$

$$\hat{n}_4 = \hat{a}_4^\dagger \hat{a}_4 = |T|^2 \hat{n} + R T^* \hat{a}^\dagger \hat{v} + R^* T \hat{v}^\dagger \hat{a} + |R|^2 \hat{n}_v, \quad (\text{A.4})$$

where \hat{n} is the photon number operator defined for the LO state, and \hat{n}_v for the vacuum state (section 3.2). In this way, we are able to calculate the expectation values on the input states. In particular, in the case of vacuum state in the input 2, $|0\rangle$, knowing the commutation rules $[\hat{a}_i, \hat{a}_j^\dagger] = \delta_{i,j}$ ¹⁹ and that the expectation value of the photon number operator is zero when evaluated on the vacuum state²⁰, the expectation value

¹⁸In this description, the input beams are monochromatic, at the same frequency and independent. Furthermore, their propagating field is described via the annihilation operator referring to the part of the field operator at positive frequency $\hat{E}^+ \propto \hat{a}$ [100].

¹⁹In all the other cases is zero. This means that each operator of annihilation/creation commutes with itself and with all the operators referring to a different field ($i \neq j$) [100].

²⁰ $\hat{v}|0\rangle = 0$, where \hat{v} is the annihilation operator referring to the vacuum state.

and the variance of the outputs' photon-number operators are:

$$\langle n_3 \rangle = |R|^2 \langle n \rangle, \quad (\Delta n_3)^2 = |R|^4 (\Delta n_1)^2 + |R|^2 |T|^2 \langle n_1 \rangle, \quad (\text{A.5})$$

$$\langle n_4 \rangle = |T|^2 \langle n \rangle, \quad (\Delta n_4)^2 = |T|^4 (\Delta n)^2 + |R|^2 |T|^2 \langle n \rangle, \quad (\text{A.6})$$

where the expectation values $\langle \cdot \rangle$ are calculated on the LO state, impinging onto the BS via input 1.

Following the same strategy, it is possible to determine analogue relations for the operators \hat{d}_3 and \hat{d}_4 describing the incident radiation onto the two photodetectors:

$$\hat{d}_3 = \sqrt{\eta} \hat{a}_3 + i(\sqrt{1-\eta}) \hat{v}_3, \quad (\text{A.7})$$

$$\hat{d}_4 = \sqrt{\eta} \hat{a}_4 + i(\sqrt{1-\eta}) \hat{v}_4 \quad (\text{A.8})$$

where η is the photodetectors' quantum efficiency, assumed to be equal for both the photodetectors (see 3.2 for a better explanation regarding this latter parameter). Combining all the rules and equations mentioned above, it is possible to find the following equations for the mean values and variances of the number of photons impinging on the two detectors:

$$\langle \hat{n}_{3D} \rangle = \eta \langle \hat{n}_3 \rangle, \quad (\text{A.9})$$

$$(\Delta n_{3D})^2 = \langle (\hat{n}_{3D})^2 \rangle - (\langle \hat{n}_{3D} \rangle)^2 = \eta^2 (\Delta n_3)^2 + \eta(1-\eta) \langle \hat{n}_3 \rangle, \quad (\text{A.10})$$

$$\langle \hat{n}_{4D} \rangle = \eta \langle \hat{n}_4 \rangle, \quad (\text{A.11})$$

$$(\Delta n_{4D})^2 = \eta^2 (\Delta n_4)^2 + \eta(1-\eta) \langle \hat{n}_4 \rangle. \quad (\text{A.12})$$

The two quantities of interest for our measurements are the sum and the difference measured between the two photodetectors' output signals, which are:

$$\hat{N}_+^D = \hat{n}_{3D} + \hat{n}_{4D} = \hat{d}_3^\dagger \hat{d}_3 + \hat{d}_4^\dagger \hat{d}_4, \quad (\text{A.13})$$

$$\hat{N}_-^D = \hat{n}_{3D} - \hat{n}_{4D} = \hat{d}_3^\dagger \hat{d}_3 - \hat{d}_4^\dagger \hat{d}_4. \quad (\text{A.14})$$

Their mean values and variance are therefore:

$$\langle \hat{N}_+^D \rangle = \langle \hat{n}_{3D} \rangle + \langle \hat{n}_{4D} \rangle, \quad (\text{A.15})$$

$$(\Delta N_+^D)^2 = (\Delta n_{3D})^2 + (\Delta n_{4D})^2 + 2[\langle \hat{n}_{3D} \hat{n}_{4D} \rangle - \langle \hat{n}_{3D} \rangle \langle \hat{n}_{4D} \rangle], \quad (\text{A.16})$$

$$\langle \hat{N}_-^D \rangle = \langle \hat{n}_{3D} \rangle - \langle \hat{n}_{4D} \rangle, \quad (\text{A.17})$$

$$(\Delta N_-^D)^2 = (\Delta n_{3D})^2 + (\Delta n_{4D})^2 - 2[\langle \hat{n}_{3D} \hat{n}_{4D} \rangle - \langle \hat{n}_{3D} \rangle \langle \hat{n}_{4D} \rangle]. \quad (\text{A.18})$$

$$(\text{A.19})$$

At this point, combining all the here presented results regarding the variances and the expectation values, and knowing from [100] (see the Hambury-Twiss calculations) that $\langle \hat{n}_{3D} \hat{n}_{4D} \rangle = \langle \hat{n}_3 \hat{n}_4 \rangle = \langle \hat{n}(\hat{n}-1) \rangle$, the results presented in sec. 3.2 are obtained with basic calculations..

A.2 QCL intermodal beat note measurement

To demonstrate that a QCL multimodal emission is realistically a frequency comb, the simplest and most immediate measurement consists in measuring the intermodal beat note among its spectral modes [32, 51]. This beat note corresponds to the amplitude modulation resulting from the interference among the frequency comb modes: its frequency coincides with the mode spacing, i.e. the FSR, while its width gives information on the phase coherence between the modes of the comb under examination. In general, a narrow beat note, i.e. characterized by a width much smaller than the modes' linewidth²¹, is a symptom of a high coherence between the modes themselves. The intermodal beat note is usually detected with a fast photodetector and observed with a radio frequency spectrum analyzer [32]. However, in QCLs, it is possible to detect such quantity directly as a modulation of the bias current used to drive the laser. Indeed, the fast lifetime of such devices (chapter 2) results in a very strong coupling between the light intensity in the cavity and the population of the levels. As a consequence, the intermodal modulation of the laser intensity can be measured as voltage modulation in the carrier flux directly at QCL circuitual terminals [15, 32]. However, the observation of a narrow intermodal beat note does not guarantee, a priori, the phase-coherence among the QCL-comb spectral modes. To demonstrate that the QCL multimodal emission is actually a coherent frequency comb, more advanced techniques are required, such as the SWIFTS [131–133] and the FACE [137]. However,

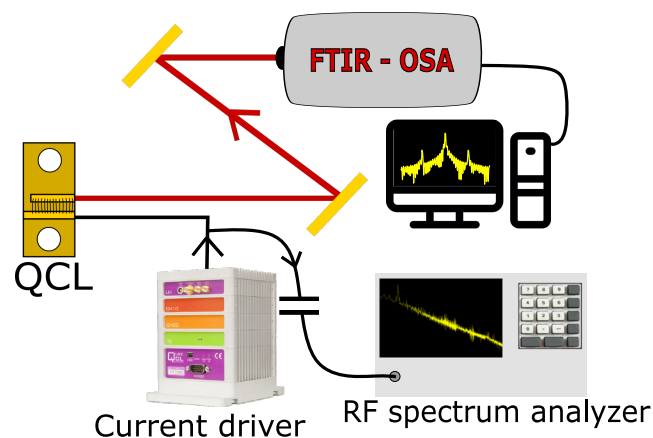


Figure A.1: FTIR setup depicted in Fig. 4.1, where the part of detection relative to the beat note has been added. As already described, the optical spectral emission of QCLs is measured via a FTIR Optical spectrum analyzer produced by Bristol using the dedicated software that transforms, via a Fourier Transform process, the temporal interferogram in the spectrum, as shown in the PC depicted in the figure. Instead, The intermodal beat note is measured as modulation in the bias current of the laser directly with a radio-frequency spectrum analyzer.

the measurements performed with such techniques have shown that only in the high coherence regime a QCL frequency comb shows narrow intermodal beat notes (kHz). In practice, we can consider the presence of a narrow beat note as a sufficient clue for the presence of a comb emission. For the purposes of this thesis work, therefore, the detection of the beat note has been utilized for a preliminary study of the characteristics

²¹In general, the modes of QCL-combs have linewidths equivalent to those of a single-mode QCL, so they are affected by technical noises impacting the QCL (thermal fluctuations, driving current noise etc.) Their linewidth typically ranges from hundreds of kHz to a few MHz, according to [15].

A.2 QCL intermodal beat note measurement

of the frequency comb emitted by the QCL. An example of the setup commonly used in my lab for monitoring both the spectral emission via a FTIR optical spectrum analyzer and the intermodal beat note via the driving current of the device is depicted in Fig. A.1.

Abbreviations

BHD	Balanced Homodyne Detector
BS	Beam Splitter
CV	Continuous Variable
CW	Continuous Wave
DFG	Difference-Frequency Generation
EOM	Electro-optic modulator
FACE	Fourier-transform Analysis of Comb Emission
FFT	Fast Fourier Transform
FIR	Far Infrared
FNPSD	Frequency Noise Power Spectral Density
FSR	Free Spectral Range
FTIR	Fourier Transform Infrared spectroscopy
FWHM	Full Width at Half Maximum
FWM	Four-Wave Mixing
HD	Homodyne Detector
ICL	Interband Cascade Laser
LIV	Light power (L) - current (I) - voltage (V) curve
LO	Local Oscillator
MBE	Molecular Beam Epitaxy
MCT	Mercurium Cadium Telluride
MIR	Mid Infrared
NIR	Near Infrared
NPSD	Noise Power Spectral Density
OFC	Optical Frequency Comb
OPA	Optical Parametric Amplifier

Abbreviations

OPO	Optical Parametric Oscillator
PDH	Pound-Drever-Hall
PID	(Proportional-Integral-Derivative
PLL	Phase-Locked Loop
PPLN	Periodically-Poled Lithium Niobate (LiNbO ₃)
PPLN/RW	Periodically-Poled Lithium Niobate (LiNbO ₃) Ridge Waveguide
PZ	Piezo
QCL	Quantum Cascade Laser
QCL-comb	Quantum Cascade Laser emitting frequency comb
PDH	Pound-Drever-Hall
RBW	Radio BandWidth
RF	Radio Frequency
RIN	Relative Intensity Noise
RMS	Root Mean Square
SFG	Sum-Frequency Generation
SHG	Second-Harmonic Generation
SPDC	Spontaneous Parametric Down Conversion
SNR	Signal-to-Noise ratio
SNSPD	Superconducting Nanowire Single-Photon Detector
SWIFTS	Shifted Wave Interference Fourier Transform Spectroscopy
TDC	Time Digital Converter
TDG	Time Delay Generator
VOA	Variable Optical Attenuator

Bibliography

- [1] ISO 20473:2021 – Optics and photonics – Spectral bands. 11
- [2] S. Borri, *High-sensitivity and high-precision spectroscopic techniques using quantum cascade lasers*. . Ph.d. thesis, Università degli Studi di Firenze, 2006. 11, 12, 14, 49, 51, 52, 53, 54, 56
- [3] F. Cappelli, *Mid-infrared single- and multi-frequency coherent sources for high-resolution molecular spectroscopy*. . Ph.d. thesis, Università degli Studi di Firenze, 2015. 11, 12, 14, 31, 32, 33, 34, 35, 36, 49, 50, 51, 52, 53, 54, 56
- [4] Harvard-Smithsonian Center for Astrophysics (CfA), V. E. Zuev Institute of Atmospheric Optics (IAO). HITRAN on the Web. <http://hitran.iao.ru/>, 2012. 11, 12
- [5] R. Wilson and H. Tapp. Mid-infrared spectroscopy for food analysis: recent new applications and relevant developments in sample presentation methods. *TrAC Trends in Analytical Chemistry*, **18**, 85–93, 1999. 11
- [6] T. Miyasaka and T. Watanabe. Enhanced CO₂ greenhouse to compensate for reduced solar luminosity on early earth. *Nature*, **277**, 22, 1979. 11
- [7] D. A. Lashof and D. R. Ahuja. Relative contributions of greenhouse gas emissions to global warming. *Nature*, **344**, 529–531, 1990. 11
- [8] W. Petrich. Mid-infrared and Raman spectroscopy for medical diagnostics. *Applied Spectroscopy Reviews*, **36**, 181–237, 2001. 11
- [9] I. Galli, S. Bartalini, S. Borri, P. Cancio, D. Mazzotti, P. De Natale, and G. Giusfredi. Molecular gas sensing below parts per trillion: Radiocarbon-dioxide optical detection. *Phys. Rev. Lett.*, **107**, 270802, 2011. 11
- [10] I. Galli, S. Bartalini, P. Cancio, P. De Natale, D. Mazzotti, G. Giusfredi, M. Fedi, and P. A. Mandó. Optical detection of radiocarbon dioxide: First results and AMS intercomparison. *Radiocarbon*, **55**, 213–223, 2013. 11

- [11] F. Hanson, P. Poirier, and M. A. Arbore. Single-frequency mid-infrared optical parametric oscillator source for coherent laser radar. *Optics Letters*, **26**, 1794–1796, 2001. 11
- [12] P. F. McManamon, Laser radar development. in *15th Annual AESS/IEEE Dayton Section Symposium. Sensing the World: Analog Sensors and Systems Across the Spectrum (Cat. No. 98EX178)*. , 53–60, IEEE, 1998. 11
- [13] K.-D. F. Büchter, H. Herrmann, C. Langrock, M. M. Fejer, and W. Sohler. All-optical Ti: PPLN wavelength conversion modules for free-space optical transmission links in the mid-infrared. *Optics Letters*, **34**, 470–472, 2009. 11
- [14] Y. Su, W. Wang, X. Hu, H. Hu, X. Huang, Y. Wang, J. Si, X. Xie, B. Han, H. Feng, Q. Hao, G. Zhu, T. Duan, and W. Zhao. 10 Gbps DPSK transmission over free-space link in the mid-infrared. *Optics Express*, **26**, 34515–34528, 2018. 11
- [15] J. Faist. *Quantum cascade lasers*. Oxford University Press, Oxford, UK, 2013. 11, 12, 49, 50, 51, 53, 54, 56, 57, 58, 123
- [16] M. Seminara, T. Gabbrielli, N. Corrias, S. Borri, L. Consolino, M. Meucci, P. D. Natale, F. Cappelli, and J. Catani. Characterization of noise regimes in mid-IR free-space optical communication based on quantum cascade lasers. *Optics Express*, **30**, 44640–44656, 2022. 11, 13, 119
- [17] P. Corrigan, R. Martini, E. A. Whittaker, and C. Bethea. Quantum cascade lasers and the Kruse model in free space optical communication. *Optics Express*, **17**, 4355–4359, 2009. 11
- [18] R. Martini, C. Bethea, F. Capasso, C. Gmachl, R. Paiella, E. Whittaker, H. Hwang, D. Sivco, J. Baillargeon, and A. Cho. Free-space optical transmission of multimedia satellite data streams using mid-infrared quantum cascade lasers. *Electronics Letters*, **38**, 1, 2002. 11
- [19] L. Flannigan, L. Yoell, and C. Q. Xu. Mid-wave and long-wave infrared transmitters and detectors for optical satellite communications—a review. *Journal of Optics*, **24**, 043002, 2022. 11
- [20] T. H. Maiman. Stimulated optical radiation in ruby. *Nature*, **187**, 493–494, 1960. 11
- [21] H. W. Mocker and R. J. Collins. Mode competition and self-locking effects in a Q-switched ruby laser. *Appl. Phys. Lett.*, **7**, 270–273, 1965. 11
- [22] I.-T. R. G.983. A broadband optical access system with increased service capability by wavelength allocation. 11
- [23] B. E. Saleh and M. C. Teich. *Fundamentals of photonics*. John Wiley & Sons, 2019. 11

-
- [24] D. Lancaster, D. Richter, and F. Tittel. Portable fiber-coupled diode-laser-based sensor for multiple trace gas detection. *Applied Physics B*, **69**, 459–465, 1999. 12
- [25] F. Minardi, G. Bianchini, P. C. Pastor, G. Giusfredi, F. S. Pavone, and M. Inguscio. Measurement of the helium $2^3p_0 - 2^3p_1$ fine structure interval. *Phys. Rev. Lett.*, **82**, 1112–1115, 1999. 12
- [26] D. Mazzotti, S. Borri, P. Cancio, G. Giusfredi, and P. D. Natale. Low-power Lamb-dip spectroscopy of very weak CO_2 transitions near $4.25 \mu\text{m}$. *Opt. Lett.*, **27**, 1256–1258, 2002. 12
- [27] P. Maddaloni, P. Malara, G. Gagliardi, and P. De Natale. Mid-infrared fibre-based optical comb. *New J. Phys.*, **8**, 1–8, 2006. 12, 14
- [28] P. Maddaloni, G. Gagliardi, P. Malara, and P. De Natale. A 3.5-mW continuous-wave difference-frequency source around $3 \mu\text{m}$ for sub-doppler molecular spectroscopy. *Applied Physics B*, **80**, 141–145, 2005. 12
- [29] K. Krzempek, G. Sobon, and K. M. Abramski. Dfg-based mid-ir generation using a compact dual-wavelength all-fiber amplifier for laser spectroscopy applications. *Optics Express*, **21**, 20023–20031, 2013. 12
- [30] J. Faist, F. Capasso, D. L. Sivco, C. Sirtori, A. L. Hutchinson, and A. Y. Cho. Quantum cascade laser. *Science*, **264**, 553–556, 1994. 12, 50, 51
- [31] M. S. Vitiello, G. Scalari, B. Williams, and P. D. Natale. Quantum cascade lasers: 20 years of challenges. *Optics Express*, **23**, 5167–5182, 2015. 12, 13
- [32] J. Faist, G. Villares, G. Scalari, M. Rösch, C. Bonzon, A. Hugi, and M. Beck. Quantum cascade laser frequency combs. *Nanophotonics*, **5**, 272–291, 2016. 12, 13, 14, 49, 57, 58, 78, 123
- [33] R. Paiella, F. Capasso, C. Gmachl, H. Y. Hwang, D. L. Sivco, A. L. Hutchinson, A. Y. Cho, and H. C. Liu. Monolithic active mode locking of quantum cascade lasers. *Applied Physics Letters*, **77**, 169–171, 2000. 13, 53
- [34] A. Lyakh, R. Maulini, A. Tsekoun, R. Go, S. V. der Porten, C. Pflügl, L. Diehl, F. Capasso, and C. K. N. Patel. High-performance continuous-wave room temperature $4.0\text{-}\mu\text{m}$ quantum cascade lasers with single-facet optical emission exceeding 2 w. *Proceedings of the National Academy of Sciences*, **107**, 18799–18802, 2010. 13
- [35] B. Schwarz, C. A. Wang, L. Missaggia, T. S. Mansuripur, P. Chevalier, M. K. Connors, D. McNulty, J. Cederberg, G. Strasser, and F. Capasso. Watt-level continuous-wave emission from a bifunctional quantum cascade laser/detector. *ACS photonics*, **4**, 1225–1231, 2017. 13
- [36] M. Silva, D. Sonnenfroh, D. Rosen, M. Allen, and A. Keefe. Integrated cavity output spectroscopy measurements of no levels in breath with a pulsed room-temperature QCL. *Applied Physics B*, **81**, 705–710, 2005. 13
-

- [37] J. Yu, A. Evans, S. Slivken, S. Darvish, and M. Razeghi. Temperature dependent characteristics of λ 3.8 μ m room-temperature continuous-wave quantum-cascade lasers. *Applied physics letters*, **88**, 251118, 2006. 13
- [38] S. Bartalini, S. Borri, and P. D. Natale. Doppler-free polarization spectroscopy with a quantum cascade laser at 4.3 μ m. *Optics Express*, **17**, 7440–7449, 2009. 13, 56, 60
- [39] L. Tombez, J. D. Francesco, S. Schilt, G. D. Domenico, J. Faist, P. Thomann, and D. Hofstetter. Frequency noise of free-running 4.6 μ m distributed feedback quantum cascade lasers near room temperature. *Opt. Lett.*, **36**, 3109–3111, 2011. 13
- [40] P. Maddaloni, M. Bellini, and P. De Natale. *Laser-based measurements for time and frequency domain applications: a handbook*. CRC Press, 6000 Broken South Parkway NW 300, Boca Raton, FL 33487-2742, USA, 2013. 13
- [41] G. Duxbury, N. Langford, M. T. McCulloch, and S. Wright. Quantum cascade semiconductor infrared and far-infrared lasers: from trace gas sensing to non-linear optics. *Chem. Soc. Rev.*, **34**, 921–934, 2005. 13
- [42] A. Castrillo, E. De Tommasi, L. Gianfrani, L. Sirigu, and J. Faist. Doppler-free saturated-absorption spectroscopy of CO₂ at 4.3 μ m by means of a distributed feedback quantum cascade laser. *Optics letters*, **31**, 3040–3042, 2006. 13
- [43] H.-W. Hübers, S. G. Pavlov, H. Richter, A. D. Semenov, L. Mahler, A. Tredicucci, H. E. Beere, and D. A. Ritchie. High-resolution gas phase spectroscopy with a distributed feedback terahertz quantum cascade laser. *Applied Physics Letters*, **89**, 061115, 2006. 13
- [44] S. Maithani and M. Pradhan. Cavity ring-down spectroscopy and its applications to environmental, chemical and biomedical systems. *Journal of Chemical Sciences*, **132**, 1–19, 2020. 13
- [45] X. Pang, O. Ozolins, L. Zhang, R. Schatz, A. Udalcovs, X. Yu, G. Jacobsen, S. Popov, J. Chen, and S. Lourduoss. Free-space communications enabled by quantum cascade lasers. *physica status solidi (a)*, **218**, 2000407, 2021. 13
- [46] N. Corrias, T. Gabbrielli, P. De Natale, L. Consolino, and F. Cappelli. Analog FM free-space optical communication based on a mid-infrared quantum cascade laser frequency comb. *Optics Express*, **30**, 10217–10228, 2022. 13, 119
- [47] X. Pang, R. Schatz, M. Joharifar, A. Udalcovs, V. Bobrovs, L. Zhang, X. Yu, Y.-T. Sun, G. Maisons, M. Carras, S. Popov, S. Lourduoss, and O. Ozolins. Direct modulation and free-space transmissions of up to 6 gbps multilevel signals with a 4.65- μ m quantum cascade laser at room temperature. *Journal of Lightwave Technology*, **40**, 2370–2377, 2022. 13
- [48] X. Pang, H. Dely, R. Schatz, D. Gacemi, M. Joharifar, T. Salgals, A. Udalcovs, Y.-T. Sun, Y. Fan, L. Zhang, E. Rodriguez, S. Spolitis, V. Bobrovs, X. Yu,

- S. Lourdudoss, S. Popov, O. Ozolins, A. Vasanelli, and C. Sirtori, 11 gb/s lwir fso transmission at 9.6 μm using a directly-modulated quantum cascade laser and an uncooled quantum cascade detector. in *2022 Optical Fiber Communications Conference and Exhibition (OFC)*. , 1–3, 2022. 13
- [49] G. Temporao, H. Zibinden, S. Tanzilli, N. Gisin, T. Aellen, M. Giovannini, J. Faist, and J. von der Weid. Feasibility study of free-space quantum key distribution in the mid-infrared. *Quantum Information and Computation*, **8**, 0001–0011, 2008. 13, 60
- [50] O. Spitz, A. Herdt, J. Wu, G. Maisons, M. Carras, C.-W. Wong, W. Elsäßer, and F. Grillot. Private communication with quantum cascade laser photonic chaos. *Nature communications*, **12**, 1–8, 2021. 13
- [51] A. Hugi, G. Villares, S. Blaser, H. Liu, and J. Faist. Mid-infrared frequency comb based on a quantum cascade laser. *Nature*, **492**, 229–233, 2012. 13, 14, 57, 58, 78, 123
- [52] T. W. Hänsch. Nobel lecture: passion for precision. *Reviews of Modern Physics*, **78**, 1297, 2006. 13, 56
- [53] E. P. Ippen, C. V. Shank, and A. Dienes. Passive mode locking of the cw dye laser. *Appl. Phys. Lett.*, **21**, 348–350, 1972. 14
- [54] T. Udem, J. Reichert, R. Holzwarth, and T. W. Hänsch. Absolute optical frequency measurement of the cesium D_1 line with a mode-locked laser. *Phys. Rev. Lett.*, **82**, 3568–3571, 1999. 14
- [55] T. Udem, J. Reichert, R. Holzwarth, and T. W. Hänsch. Accurate measurement of large optical frequency differences with a mode-locked laser. *Opt. Lett.*, **24**, 881–883, 1999. 14
- [56] S. A. Diddams, D. J. Jones, J. Ye, S. T. Cundiff, J. L. Hall, J. K. Ranka, R. S. Windeler, R. Holzwarth, T. Udem, and T. W. Hänsch. Direct link between microwave and optical frequencies with a 300 THz femtosecond laser comb. *Phys. Rev. Lett.*, **84**, 5102–5105, 2000. 14, 56
- [57] T. Udem, R. Holzwarth, and T. W. Hänsch. Optical frequency metrology. *Nature*, **416**, 233–237, 2002. 14, 56
- [58] T. Fortier and E. Baumann. 20 years of developments in optical frequency comb technology and applications. *Communications Physics*, **2**, 1–16, 2019. 14
- [59] N. Picqué and T. W. Hänsch. Frequency comb spectroscopy. *Nature Photonics*, **13**, 146–157, 2019. 14
- [60] A. Schliesser, N. Picqué, and T. W. Hänsch. Mid-infrared frequency combs. *Nat. Photon.*, **6**, 440–449, 2012. 14
- [61] E. Baumann, F. R. Giorgetta, W. C. Swann, A. M. Zolot, I. Coddington, and N. R. Newbury. Spectroscopy of the methane ν_3 band with an accurate midinfrared coherent dual-comb spectrometer. *Phys. Rev. A*, **84**, 062513, 2011. 14

- [62] A. Ruehl, A. Gambetta, I. Hartl, M. E. Fermann, K. S. E. Eikema, and M. Marangoni. Widely-tunable mid-infrared frequency comb source based on difference frequency generation. *Opt. Lett.*, **37**, 2232–2234, 2012. 14
- [63] F. Zhu, H. Hundertmark, A. A. Kolomenskii, J. Strohaber, R. Holzwarth, and H. A. Schuessler. High-power mid-infrared frequency comb source based on a femtosecond Er: fiber oscillator. *Opt. Lett.*, **38**, 2360–2362, 2013. 14
- [64] F. Keilmann and S. Amarie. Mid-infrared frequency comb spanning an octave based on an er fiber laser and difference-frequency generation. *Journal of Infrared, Millimeter, and Terahertz Waves*, **33**, 479–484, 2012. 14
- [65] I. Galli, F. Cappelli, P. Cancio, G. Giusfredi, D. Mazzotti, S. Bartalini, and P. De Natale. High-coherence mid-infrared frequency comb. *Optics Express*, **21**, 28877–28885, 2013. 14
- [66] F. Adler, K. C. Cossel, M. J. Thorpe, I. Hartl, M. E. Fermann, and J. Ye. Phase-stabilized, 1.5 W frequency comb at 2.8–4.8 μm . *Opt. Lett.*, **34**, 1330–1332, 2009. 14
- [67] L. Tombez, F. Cappelli, S. Schilt, G. Di Domenico, S. Bartalini, and D. Hofstetter. Wavelength tuning and thermal dynamics of continuous-wave mid-infrared distributed feedback quantum cascade lasers. *Appl. Phys. Lett.*, **103**, 031111, 2013. 14
- [68] P. Friedli, H. Sigg, B. Hinkov, A. Hugi, S. Riedi, M. Beck, and J. Faist. Four-wave mixing in a quantum cascade laser amplifier. *Appl. Phys. Lett.*, **102**, 222104, 2013. 14, 58, 78
- [69] S. Riedi, F. Cappelli, S. Blaser, P. Baroni, A. Müller, and J. Faist. Broadband superluminescence, 5.9 μm to 7.2 μm , of a quantum cascade gain device. *Optics Express*, **23**, 7184–7189, 2015. 14, 78
- [70] M. Levenson, R. Shelby, A. Aspect, M. Reid, and D. Walls. Generation and detection of squeezed states of light by nondegenerate four-wave mixing in an optical fiber. *Physical Review A*, **32**, 1550–1562, 1985. 14
- [71] R. Slusher, L. Hollberg, B. Yurke, J. Mertz, and J. Valley. Observation of squeezed states generated by four-wave mixing in an optical cavity. *Physical Review Letters*, **55**, 2409–2412, 1985. 14
- [72] C. McCormick, V. Boyer, E. Arimondo, and P. Lett. Strong relative intensity squeezing by four-wave mixing in rubidium vapor. *Optics letters*, **32**, 178–180, 2007. 14
- [73] A. Dutt, K. Luke, S. Manipatruni, A. L. Gaeta, P. Nussenzveig, and M. Lipson. On-chip optical squeezing. *Phys. Rev. Applied*, **3**, 044005, 2015. 14, 38, 82, 83
- [74] M. A. Foster, J. S. Levy, O. Kuzucu, K. Saha, M. Lipson, and A. L. Gaeta. Silicon-based monolithic optical frequency comb source. *Optics Express*, **19**, 14233–14239, 2011. 14

-
- [75] T. Gabbrielli, N. Bruno, N. Corrias, S. Borri, L. Consolino, M. Bertrand, M. Shahmohammadi, M. Franckić, M. Beck, J. Faist, A. Zavatta, F. Cappelletti, and P. De Natale. Intensity correlations in quantum cascade laser harmonic frequency combs. *Advanced Photonics Research*, **3**, 2200162, 2022. 14, 15, 16, 73, 77, 80, 92, 118
- [76] C. M. Caves. Quantum limits on noise in linear amplifiers. *Phys. Rev. D*, **26**, 1817–1839, 1982. 14, 78
- [77] S. Barbieri, M. Ravarò, P. Gellie, G. Santarelli, C. Manquest, C. Sirtori, S. P. Khanna, E. H. Linfield, and A. G. Davies. Coherent sampling of active mode-locked terahertz quantum cascade lasers and frequency synthesis. *Nature Photon.*, **5**, 306, 2011. 15, 57
- [78] T. Gensty and W. Elsässer. Semiclassical model for the relative intensity noise of intersubband quantum cascade lasers. *Opt. Commun.*, **256**, 171 – 183, 2005. 15
- [79] E. F. Zalewski and C. R. Duda. Silicon photodiode device with 100% external quantum efficiency. *Applied optics*, **22**, 2867–2873, 1983. 15
- [80] C. M. Natarajan, M. G. Tanner, and R. H. Hadfield. Superconducting nanowire single-photon detectors: physics and applications. *Superconductor science and technology*, **25**, 063001, 2012. 15
- [81] B. J. Lawrie, P. D. Lett, A. M. Marino, and R. C. Pooser. Quantum sensing with squeezed light. *Acs Photonics*, **6**, 1307–1318, 2019. 15
- [82] G. Frascella, S. Agne, F. Y. Khalili, and M. V. Chekhova. Overcoming detection loss and noise in squeezing-based optical sensing. *npj Quantum Information*, **7**, 1–6, 2021. 15
- [83] L. McCuller, C. Whittle, D. Ganapathy, K. Komori, M. Tse, A. Fernandez-Galiana, L. Barsotti, P. Fritschel, M. MacInnis, F. Matichard, *et al.* Frequency-dependent squeezing for advanced ligo. *Physical review letters*, **124**, 171102, 2020. 15
- [84] M. Tse, H. Yu, N. Kijbunchoo, A. Fernandez-Galiana, P. Dupej, L. Barsotti, C. D. Blair, D. D. Brown, S. E. Dwyer, A. Effler, M. Evans, P. Fritschel, V. V. Frolov, A. C. Green, G. L. Mansell, F. Matichard, N. Mavalvala, *et al.* Quantum-enhanced advanced LIGO detectors in the era of gravitational-wave astronomy. *Phys. Rev. Lett.*, **123**, 231107, 2019. 15
- [85] E. Polzik, J. Carri, and H. Kimble. Spectroscopy with squeezed light. *Physical review letters*, **68**, 3020, 1992. 15
- [86] Y. Michael, L. Bello, M. Rosenbluh, and A. Pe’er. Squeezing-enhanced Raman spectroscopy. *npj Quantum Information*, **5**, 1–9, 2019. 15
- [87] N. J. Cerf, M. Levy, and G. Van Assche. Quantum distribution of gaussian keys using squeezed states. *Physical Review A*, **63**, 052311, 2001. 16

- [88] D. Gottesman and J. Preskill, Secure quantum key distribution using squeezed states. in *Quantum Information with Continuous Variables.* , 317–356Springer, 2003. 16, 102
- [89] A. M. Marino and C. R. Stroud. Deterministic secure communications using two-mode squeezed states. *Phys. Rev. A*, **74**, 022315, 2006. 16
- [90] V. C. Usenko and R. Filip. Squeezed-state quantum key distribution upon imperfect reconciliation. *New Journal of Physics*, **13**, 113007, 2011. 16, 102
- [91] T. Eberle, V. Händchen, J. Duhme, T. Franz, F. Furrer, R. Schnabel, and R. F. Werner. Gaussian entanglement for quantum key distribution from a single-mode squeezing source. *New Journal of Physics*, **15**, 053049, 2013. 16, 102
- [92] M. Fanizza, M. Rosati, M. Skotiniotis, J. Calsamiglia, and V. Giovannetti. Squeezing-enhanced communication without a phase reference. *Quantum*, **5**, 608, 2021. 16
- [93] A. Ourjoumtsev, R. Tualle-Brouri, J. Laurat, and P. Grangier. Generating optical schrödinger kittens for quantum information processing. *Science*, **312**, 83–86, 2006. 16, 101, 102, 103, 104
- [94] K. Takase, A. Kawasaki, B. K. Jeong, M. Endo, T. Kashiwazaki, T. Kazama, K. Enbutsu, K. Watanabe, T. Umeki, S. Miki, H. Terai, M. Yabuno, F. China, W. Asavanant, J. ichi Yoshikawa, and A. Furusawa. Generation of schrödinger cat states with wigner negativity using a continuous-wave low-loss waveguide optical parametric amplifier. *Optics Express*, **30**, 14161–14171, 2022. 16, 102, 108
- [95] M. F. Melalkia, T. Gabbrielli, A. Petitjean, L. Brunel, A. Zavatta, S. Tanzilli, J. Etesse, and V. D’Auria. Plug-and-play generation of non-gaussian states of light at a telecom wavelength. *Optics Express*, **30**, 45195–45201, 2022. 16, 17, 101, 102, 103, 108, 114, 115, 118
- [96] R. Lescanne, M. Villiers, T. Peronnin, A. Sarlette, M. Delbecq, B. Huard, T. Kontos, M. Mirrahimi, and Z. Leghtas. Exponential suppression of bit-flips in a qubit encoded in an oscillator. *Nature Physics*, **16**, 509–513, 2020. 16
- [97] H. Takahashi, J. S. Neergaard-Nielsen, M. Takeuchi, M. Takeoka, K. Hayasaka, A. Furusawa, and M. Sasaki. Entanglement distillation from gaussian input states. *Nature photonics*, **4**, 178–181, 2010. 16, 102
- [98] A. Tipsmark, J. S. Neergaard-Nielsen, and U. L. Andersen. Displacement-enhanced entanglement distillation of single-mode-squeezed entangled states. *Optics Express*, **21**, 6670–6680, 2013. 16, 102
- [99] T. Gabbrielli, F. Cappelli, N. Bruno, N. Corrias, S. Borri, P. De Natale, and A. Zavatta. Mid-infrared homodyne balanced detector for quantum light characterization. *Optics Express*, **29**, 14536–14547, 2021. 16, 59, 60, 64, 67, 81, 83, 87, 117

-
- [100] R. Loudon. *The quantum theory of light*. OUP Oxford, 2000. 20, 21, 23, 24, 25, 26, 28, 29, 31, 38, 40, 41, 42, 43, 45, 46, 47, 59, 60, 61, 104, 105, 121, 122
- [101] C. Gerry, P. Knight, and P. L. Knight. *Introductory quantum optics*. Cambridge university press, 2005. 20, 31, 36, 37, 38, 46, 47, 103, 105, 114
- [102] M. O. Scully and M. S. Zubairy. *Quantum optics*. Cambridge University Press, 1997. 20, 31, 36, 37, 38, 103
- [103] U. Leonhardt. *Measuring the quantum state of light*. , vol. 22 Cambridge university press, 1997. 20, 47, 48, 105
- [104] G. Grynberg, A. Aspect, and C. Fabre. *Introduction to quantum optics, from the semi-classical approach to quantized light*. Cambridge University Press, 32 Avenue of the Americas, New York, NY 10013-2473, USA, 2010. 20, 31, 36, 37, 38
- [105] J. D. Jackson. *Classical Electrodynamics*. John Wiley & Sons, third ed., 1999. 31, 32
- [106] R. Boyd. *Nonlinear optics*. Elsevier/Academic Press, Amsterdam, The Netherlands, third ed., 2008. 31, 32, 33, 34, 35, 36, 78
- [107] L. Brunel, *Étude théorique et expérimentale de l'intrication hybride à variables discrètes et continues pour les réseaux de télécommunication quantique*. . Ph.d. thesis, Institut de Physique de Nice (INPHYNI), CNRS, UMR 7 010, 2022. 31, 36, 109
- [108] F. M. Mohamed, *Generation and manipulation of photonic states for Quantum communication*. . Ph.d. thesis, Institut de Physique de Nice (INPHYNI), CNRS, UMR 7 010, 2022. 31, 36, 37, 47, 102, 103, 105, 106, 108, 109, 110, 112, 113, 114, 115
- [109] O. Morin, *Non-Gaussian states and measurements for quantum information*. . PhD thesis, Université Pierre et Marie Curie - Paris VI, 2013. 31, 36, 46
- [110] A. Yariv. *Quantum Electronics*. John Wiley & Sons, New York, USA, third ed., 1989. 32, 50, 55
- [111] Y. K. Chembo. Quantum dynamics of Kerr optical frequency combs below and above threshold: Spontaneous four-wave mixing, entanglement, and squeezed states of light. *Phys. Rev. A*, **93**, 033820, 2016. 38, 39, 78
- [112] E. P. Wigner, On the quantum correction for thermodynamic equilibrium. in *Part I: Physical Chemistry. Part II: Solid State Physics*. , 110–120 Springer, 1997. 46, 47, 105
- [113] A. Ourjountsev, *Étude théorique et expérimentale de superpositions quantiques cohérentes et d'états intriqués non-gaussiens de la lumière*. . Ph.d. thesis, Université Paris Sud - Paris XI, 2007. 46, 47, 105
-

- [114] A. Kenfack and K. Życzkowski. Negativity of the wigner function as an indicator of non-classicality. *Journal of Optics B: Quantum and Semiclassical Optics*, **6**, 396, 2004. 47, 105
- [115] R. Köhler, A. Tredicucci, F. Beltram, H. E. Beere, E. H. Linfield, A. G. Davies, D. A. Ritchie, R. C. Iotti, and F. Rossi. Terahertz semiconductor-heterostructure laser. *Nature*, **417**, 156, 2002. 50
- [116] S. Bartalini, S. Borri, I. Galli, G. Giusfredi, D. Mazzotti, T. Edamura, N. Akikusa, M. Yamanishi, and P. De Natale. Measuring frequency noise and intrinsic linewidth of a room-temperature DFB quantum cascade laser. *Optics Express*, **19**, 17996–18003, 2011. 51
- [117] C. Sirtori, P. Kruck, S. Barbieri, P. Collot, and J. Nagle. GaAs/Al_xGa_{1-x}As quantum cascade lasers. *Appl. Phys. Lett.*, **73**, 3486–3488, 1998. 51
- [118] L. R. Wilson, P. T. Keightley, J. W. Cockburn, M. S. Skolnick, J. C. Clark, G. Hill, R. Grey, and M. Hopkinson. Comparison of performance of GaAs-AlGaAs and InGaAs-AlInAs quantum cascade lasers. *Electronics Letters*, **35**, 2034–2036, 1999. 51
- [119] S. Gianordoli, W. Schrenk, L. Hvozdar, N. Finger, K. Unterrainer, G. Strasser, and E. Gornik. Improved performance of GaAs-AlGaAs superlattice quantum cascade lasers beyond $\lambda = 13\mu\text{m}$. *IEEE Photonics Technology Letters*, **12**, 1144–1146, 2000. 51
- [120] F. Capasso, C. Gmachl, D. L. Sivco, and A. Y. Cho. Quantum cascade lasers. *Physics World*, **12**, 1999. 54
- [121] C. Sirtori, H. Page, C. Becker, and V. Ortiz. GaAs-AlGaAs quantum cascade lasers: physics, technology, and prospects. *IEEE J. Quantum Electron.*, **38**, 547–558, 2002. 54
- [122] S. Bartalini, S. Borri, P. Cancio, A. Castrillo, I. Galli, G. Giusfredi, D. Mazzotti, L. Gianfrani, and P. De Natale. Observing the intrinsic linewidth of a quantum-cascade laser: Beyond the Schawlow-Townes limit. *Phys. Rev. Lett.*, **104**, 083904–1–4, 2010. 54, 55
- [123] M. Yamanishi, T. Edamura, K. Fujita, N. Akikusa, and H. Kan. Theory of the intrinsic linewidth of quantum-cascade lasers: Hidden reason for the narrow linewidth and line-broadening by thermal photons. *IEEE J. Quantum Electron.*, **44**, 12–29, 2008. 54
- [124] D. J. Jones, S. A. Diddams, J. K. Ranka, A. Stentz, R. S. Windeler, J. L. Hall, and S. T. Cundiff. Carrier-envelope phase control of femtosecond mode-locked lasers and direct optical frequency synthesis. *Science*, **288**, 635–639, 2000. 56
- [125] R. Holzwarth, T. Udem, T. W. Hänsch, J. C. Knight, W. J. Wadsworth, and P. S. J. Russell. Optical frequency synthesizer for precision spectroscopy. *Phys. Rev. Lett.*, **85**, 2264–2267, 2000. 56

-
- [126] S. A. Diddams. The evolving optical frequency comb [Invited]. *J. Opt. Soc. Am. B*, **27**, B51, 2010. 56
- [127] P. Malara, R. Blanchard, T. S. Mansuripur, A. K. Wojcik, A. Belyanin, K. Fujita, T. Edamura, S. Furuta, M. Yamanishi, P. De Natale, and F. Capasso. External ring-cavity quantum cascade lasers. *Appl. Phys. Lett.*, **102**, 2013. 57
- [128] C. Y. Wang, L. Kuznetsova, V. M. Gkortsas, L. Diehl, F. X. Kärtner, M. A. Belkin, A. Belyanin, X. Li, D. Ham, H. Schneider, D. Grant, C. Y. Song, S. Haffouz, Z. R. Wasilewski, H. C. Liu, and F. Capasso. Mode-locked pulses from mid-infrared quantum cascade lasers. *Optics Express*, **17**, 12929–12943, 2009. 57
- [129] D. G. Revin, M. Hemingway, Y. Wang, J. W. Cockburn, and A. Belyanin. Active mode locking of quantum cascade lasers in an external ring cavity. *Nat. Commun.*, **7**, 11440, 2016. 57
- [130] F. Wang, H. Nong, T. Fobbe, V. Pistore, S. Houver, S. Markmann, N. Jukam, M. Amanti, C. Sirtori, S. Moudji, R. Colombelli, L. Li, E. Linfield, G. Davies, J. Mangeney, J. Tignon, and S. Dhillon. Short terahertz pulse generation from a dispersion compensated modelocked semiconductor laser. *Laser Photonics Rev.*, **11**, 1700013, 2017. 57
- [131] D. Burghoff, T.-Y. Kao, N. Han, C. W. I. Chan, X. Cai, Y. Yang, D. J. Hayton, J.-R. Gao, J. L. Reno, and Q. Hu. Terahertz laser frequency combs. *Nat. Photon.*, **8**, 462–467, 2014. 58, 123
- [132] D. Burghoff, Y. Yang, D. J. Hayton, J.-R. Gao, J. L. Reno, and Q. Hu. Evaluating the coherence and time-domain profile of quantum cascade laser frequency combs. *Optics Express*, **23**, 1190–1202, 2015. 58, 123
- [133] M. Singleton, P. Jouy, M. Beck, and J. Faist. Evidence of linear chirp in mid-infrared quantum cascade lasers. *Optica*, **5**, 948–953, 2018. 58, 123
- [134] G. Villares, A. Hugi, S. Blaser, and J. Faist. Dual-comb spectroscopy based on quantum-cascade-laser frequency combs. *Nat. Commun.*, **5**, 5192, 2014. 58
- [135] F. Cappelli, G. Campo, I. Galli, G. Giusfredi, S. Bartalini, D. Mazzotti, P. Cancio, S. Borri, B. Hinkov, J. Faist, and P. De Natale. Frequency stability characterization of a quantum cascade laser frequency comb. *Laser Photonics Rev.*, **10**, 623–630, 2016. 58
- [136] F. Cappelli, G. Villares, S. Riedi, and J. Faist. Intrinsic linewidth of quantum cascade laser frequency combs. *Optica*, **2**, 836–840, 2015. 58
- [137] F. Cappelli, L. Consolino, G. Campo, I. Galli, D. Mazzotti, A. Campa, M. Siciliani de Cumis, P. Cancio Pastor, R. Eramo, M. Rösch, M. Beck, G. Scalari, J. Faist, P. De Natale, and S. Bartalini. Retrieval of phase relation and emission profile of quantum cascade laser frequency combs. *Nature Photon.*, **13**, 562–568, 2019. 58, 76, 123
-

- [138] H. P. Yuen and V. W. Chan. Noise in homodyne and heterodyne detection. *Optics letters*, **8**, 177–179, 1983. 59
- [139] J. Shapiro. Quantum noise and excess noise in optical homodyne and heterodyne receivers. *IEEE Journal of Quantum Electronics*, **21**, 237–250, 1985. 59
- [140] M. Raymer, J. Cooper, H. Carmichael, M. Beck, and D. Smithey. Ultrafast measurement of optical-field statistics by dc-balanced homodyne detection. *JOSA B*, **12**, 1801–1812, 1995. 59, 60
- [141] A. Lambrecht, T. Coudreau, A. M. Steinberg, and E. Giacobino. Squeezing with cold atoms. *Europhysics Letters (EPL)*, **36**, 93–98, 1996. 59, 60
- [142] A. Zavatta, M. Bellini, P. L. Ramazza, F. Marin, and F. T. Arecchi. Time-domain analysis of quantum states of light: noise characterization and homodyne tomography. *JOSA B*, **19**, 1189–1194, 2002. 59, 60
- [143] M. Sasaki and S. Suzuki. Multimode theory of measurement-induced non-gaussian operation on wideband squeezed light: Analytical formula. *Physical Review A*, **73**, 043807, 2006. 59
- [144] R. Kumar, E. Barrios, A. MacRae, E. Cairns, E. Huntington, and A. Lvovsky. Versatile wideband balanced detector for quantum optical homodyne tomography. *Optics Communications*, **285**, 5259–5267, 2012. 59
- [145] B. L. Schumaker. Noise in homodyne detection. *Opt. Lett.*, **9**, 189–191, 1984. 60, 61
- [146] L. S. Costanzo, A. S. Coelho, N. Biagi, J. Fiurášek, M. Bellini, and A. Zavatta. Measurement-induced strong Kerr nonlinearity for weak quantum states of light. *Physical Review Letters*, **119**, 013601, 2017. 60
- [147] N. Biagi, L. S. Costanzo, M. Bellini, and A. Zavatta. Entangling macroscopic light states by delocalized photon addition. *Phys. Rev. Lett.*, **124**, 033604, 2020. 60
- [148] T. C. Ralph. Continuous variable quantum cryptography. *Phys. Rev. A*, **61**, 010303, 1999. 60
- [149] A. A. Semenov and W. Vogel. Quantum light in the turbulent atmosphere. *Phys. Rev. A*, **80**, 021802, 2009. 60
- [150] D. Elser, T. Bartley, B. Heim, C. Wittmann, D. Sych, and G. Leuchs. Feasibility of free space quantum key distribution with coherent polarization states. *New Journal of Physics*, **11**, 045014, 2009. 60
- [151] C. B. Carlisle and D. E. Cooper. Tunable-diode-laser frequency-modulation spectroscopy using balanced homodyne detection. *Optics letters*, **14**, 1306–1308, 1989. 60
- [152] W. Chen, G. Mouret, and D. Boucher. Difference-frequency laser spectroscopy detection of acetylene trace constituent. *Applied Physics B: Lasers & Optics*, **67**, 375–379, 1998. 60

-
- [153] D. M. Sonnenfroh, W. T. Rawlins, M. G. Allen, C. Gmachl, F. Capasso, A. L. Hutchinson, D. L. Sivco, J. N. Baillargeon, and A. Y. Cho. Application of balanced detection to absorption measurements of trace gases with room-temperature, quasi-cw quantum-cascade lasers. *Applied Optics*, **40**, 812–820, 2001. 60
- [154] M. Mancinelli, A. Trenti, S. Piccione, G. Fontana, J. S. Dam, P. Tidemand-Lichtenberg, C. Pedersen, and L. Pavesi. Mid-infrared coincidence measurements on twin photons at room temperature. *Nature communications*, **8**, 1–8, 2017. 60
- [155] J. Appel, D. Hoffman, E. Figueroa, and A. Lvovsky. Electronic noise in optical homodyne tomography. *Physical Review A*, **75**, 035802, 2007. 63, 64
- [156] A. I. Lvovsky and M. G. Raymer. Continuous-variable optical quantum-state tomography. *Reviews of modern physics*, **81**, 299–332, 2009. 67, 72, 106
- [157] F. Rice. A frequency-domain derivation of shot-noise. *American Journal of Physics*, **84**, 44–51, 2016. 68
- [158] N. Biagi, M. Bohmann, E. Agudelo, M. Bellini, and A. Zavatta. Experimental certification of nonclassicality via phase-space inequalities. *Physical Review Letters*, **126**, 023605, 2021. 72
- [159] M. G. Paris, M. Cola, and R. Bonifacio. Remote state preparation and teleportation in phase space. *Journal of Optics B: Quantum and Semiclassical Optics*, **5**, S360, 2003. 72
- [160] D. Dequal, L. Trigo Vidarte, V. Roman Rodriguez, G. Vallone, P. Villoresi, A. Leverrier, and E. Diamanti. Feasibility of satellite-to-ground continuous-variable quantum key distribution. *npj Quantum Information*, **7**, 3, 2021. 72
- [161] M. Piccardo, P. Chevalier, S. Anand, Y. Wang, D. Kazakov, E. A. Mejia, F. Xie, K. Lascola, A. Belyanin, and F. Capasso. Widely tunable harmonic frequency comb in a quantum cascade laser. *Applied Physics Letters*, **113**, 031104, 2018. 73, 76, 77
- [162] N. B. Colthup, Infrared spectroscopy. in *Encyclopedia of Physical Science and Technology (Third Edition)*. (R. A. Meyers, ed.), 793–816 Academic Press, New York, third edition ed., 2003. 74
- [163] D. Kazakov, M. Piccardo, Y. Wang, P. Chevalier, T. S. Mansuripur, F. Xie, C.-e. Zah, K. Lascola, A. Belyanin, and F. Capasso. Self-starting harmonic frequency comb generation in a quantum cascade laser. *Nature Photonics*, **11**, 789–792, 2017. 76
- [164] Y. Wang and A. Belyanin. Harmonic frequency combs in quantum cascade lasers: time-domain and frequency-domain theory. *Physical Review A*, **102**, 013519, 2020. 76
-

- [165] L. Lu, X. Zheng, Y. Lu, S. Zhu, and X.-S. Ma. Advances in chip-scale quantum photonic technologies. *Advanced Quantum Technologies*, **4**, 2100068, 2021. 77
- [166] Y.-q. Li and M. Xiao. Generation and applications of amplitude-squeezed states of light from semiconductor diode lasers. *Optics express*, **2**, 110–117, 1998. 77
- [167] Y. Yamamoto, S. Machida, and W. H. Richardson, Photon number squeezed states in semiconductor lasers. in *Confined Electrons and Photons*. , 879–884Springer, 1995. 77
- [168] T. Gensty, W. Elsässer, and C. Mann. Intensity noise properties of quantum cascade lasers. *Optics Express*, **13**, 2032–2039, 2005. 77, 78
- [169] L. Tombez, F. Cappelli, S. Schilt, G. Di Domenico, S. Bartalini, and D. Hofstetter. Wavelength tuning and thermal dynamics of continuous-wave mid-infrared distributed feedback quantum cascade lasers. *Appl. Phys. Lett.*, **103**, 031111, 2013. 77
- [170] S. Schilt, L. Tombez, C. Tardy, A. Bismuto, S. Blaser, R. Maulini, R. Terazzi, M. Rochat, and T. Südmeyer. An experimental study of noise in mid-infrared quantum cascade lasers of different designs. *Applied Physics B*, **119**, 189–201, 2015. 77
- [171] B.-B. Zhao, X.-G. Wang, J. Zhang, and C. Wang. Relative intensity noise of a mid-infrared quantum cascade laser: insensitivity to optical feedback. *Optics express*, **27**, 26639–26647, 2019. 77
- [172] S. Borri, S. Bartalini, P. C. Pastor, I. Galli, G. Giusfredi, D. Mazzotti, M. Yamanishi, and P. De Natale. Frequency-noise dynamics of mid-infrared quantum cascade lasers. *IEEE Journal of Quantum Electronics*, **47**, 984–988, 2011. 77
- [173] M. Yamanishi, T. Hirohata, S. Hayashi, K. Fujita, and K. Tanaka. Electrical flicker-noise generated by filling and emptying of impurity states in injectors of quantum-cascade lasers. *J. Appl. Phys.*, **116**, 183106, 2014. 77
- [174] Y. I. Khanin. *Principles of laser dynamics*. Newnes, 2012. 77
- [175] F. Rana and R. J. Ram. Current noise and photon noise in quantum cascade lasers. *Physical Review B*, **65**, 125313, 2002. 78
- [176] N. Opačak and B. Schwarz. Theory of frequency-modulated combs in lasers with spatial hole burning, dispersion, and Kerr nonlinearity. *Phys. Rev. Lett.*, **123**, 243902, 2019. 78
- [177] A. Trombettoni, F. Scazza, F. Minardi, G. Roati, F. Cappelli, L. Consolino, A. Smerzi, and P. De Natale. Quantum simulating the electron transport in quantum cascade laser structures. *Adv. Quantum Technol.*, **4**, 2100044, 2021. 78
- [178] M. Franckie, Optimization of broad gain and high optical nonlinearity of mid-infrared quantum cascade laser frequency combs. 2022. 78

-
- [179] T. S. Mansuripur, C. Vernet, P. Chevalier, G. Aoust, B. Schwarz, F. Xie, C. Caneau, K. Lascola, C.-e. Zah, D. P. Caffey, T. Day, L. J. Missaggia, M. K. Connors, C. A. Wang, A. Belyanin, and F. Capasso. Single-mode instability in standing-wave lasers: The quantum cascade laser as a self-pumped parametric oscillator. *Phys. Rev. A*, **94**, 063807, 2016. 78
- [180] B. Schneider, F. Kapsalidis, M. Bertrand, M. Singleton, J. Hillbrand, M. Beck, and J. Faist. Controlling quantum cascade laser optical frequency combs through microwave injection. *Laser & Photonics Reviews*, **15**, 2100242, 2021. 80
- [181] J. Taylor. *Introduction to error analysis, the study of uncertainties in physical measurements.* , 1997. 82, 86
- [182] V. Thiel, J. Roslund, P. Jian, C. Fabre, and N. Treps. Quantum-limited measurements of distance fluctuations with a multimode detector. *Quantum Science and Technology*, **2**, 034008, 2017. 83
- [183] A. V. Oppenheim. *Discrete-time signal processing.* Pearson Education India, 1999. 86
- [184] B. Yurke and D. Stoler. Generating quantum mechanical superpositions of macroscopically distinguishable states via amplitude dispersion. *Phys. Rev. Lett.*, **57**, 13–16, 1986. 101, 102
- [185] U. L. Andersen, T. Gehring, C. Marquardt, and G. Leuchs. 30 years of squeezed light generation. *Physica Scripta*, **91**, 053001, 2016. 102
- [186] A. I. Lvovsky. Squeezed light. *Photonics: Scientific Foundations, Technology and Applications*, **1**, 121–163, 2015. 102
- [187] B. Xiong, X. Li, S.-L. Chao, Z. Yang, W.-Z. Zhang, and L. Zhou. Generation of entangled schrödinger cat state of two macroscopic mirrors. *Optics Express*, **27**, 13547–13558, 2019. 102
- [188] D. V. Sychev, A. E. Ulanov, A. A. Pushkina, M. W. Richards, I. A. Fedorov, and A. I. Lvovsky. Enlargement of optical Schrödinger’s cat states. *Nature Photonics*, **11**, 379–382, 2017. 102
- [189] J. Laurat, T. Coudreau, G. Keller, N. Treps, and C. Fabre. Compact source of einstein-podolsky-rosen entanglement and squeezing at very low noise frequencies. *Physical Review A*, **70**, 042315, 2004. 102
- [190] M. Mehmet, S. Ast, T. Eberle, S. Steinlechner, H. Vahlbruch, and R. Schnabel. Squeezed light at 1550 nm with a quantum noise reduction of 12.3 db. *Optics express*, **19**, 25763–25772, 2011. 102
- [191] F. Kaiser, B. Fedrici, A. Zavatta, V. d’Auria, and S. Tanzilli. A fully guided-wave squeezing experiment for fiber quantum networks. *Optica*, **3**, 362–365, 2016. 102
-

- [192] F. Mondain, T. Lunghi, A. Zavatta, E. Gouzien, F. Doutre, M. De Micheli, S. Tanzilli, and V. D'Auria. Chip-based squeezing at a telecom wavelength. *Photonics Research*, **7**, A36–A39, 2019. 102
- [193] F. Lenzini, J. Janousek, O. Thearle, M. Villa, B. Haylock, S. Kasture, L. Cui, H.-P. Phan, D. V. Dao, H. Yonezawa, *et al.* Integrated photonic platform for quantum information with continuous variables. *Science advances*, **4**, eaat9331, 2018. 102
- [194] Y. Zhao, Y. Okawachi, J. K. Jang, X. Ji, M. Lipson, and A. L. Gaeta. Near-degenerate quadrature-squeezed vacuum generation on a silicon-nitride chip. *Physical Review Letters*, **124**, 193601, 2020. 102
- [195] J.-i. Yoshikawa, W. Asavanant, and A. Furusawa. Purification of photon subtraction from continuous squeezed light by filtering. *Phys. Rev. A*, **96**, 052304, 2017. 103, 113, 114
- [196] A. I. Lvovsky. Iterative maximum-likelihood reconstruction in quantum homodyne tomography. *Journal of Optics B: Quantum and Semiclassical Optics*, **6**, S556, 2004. 105
- [197] A. I. Lvovsky, P. Grangier, A. Ourjoumtsev, V. Parigi, M. Sasaki, and R. Tualle-Brouri. Production and applications of non-Gaussian quantum states of light. 2020. 108
- [198] M. Vaughan. *The Fabry-Perot interferometer: history, theory, practice and applications*. Routledge & CRC Press, 2017. 109
- [199] R. Drever, J. L. Hall, F. Kowalski, J. Hough, G. Ford, A. Munley, and H. Ward. Laser phase and frequency stabilization using an optical resonator. *Applied Physics B*, **31**, 97–105, 1983. 110
- [200] O. Morin, C. Fabre, and J. Laurat. Experimentally accessing the optimal temporal mode of traveling quantum light states. *Physical review letters*, **111**, 213602, 2013. 113, 114
- [201] K. Banaszek, G. M. D'Ariano, M. G. A. Paris, and M. F. Sacchi. Maximum-likelihood estimation of the density matrix. *Phys. Rev. A*, **61**, 010304, 1999. 114
- [202] A. I. Lvovsky and M. G. Raymer. Continuous-variable optical quantum-state tomography. *Rev. Mod. Phys.*, **81**, 299–332, 2009. 114
- [203] S. Mosca, M. Parisi, I. Ricciardi, F. Leo, T. Hansson, M. Erkintalo, P. Maddaloni, P. De Natale, S. Wabnitz, and M. De Rosa. Modulation instability induced frequency comb generation in a continuously pumped optical parametric oscillator. *Phys. Rev. Lett.*, **121**, 093903, 2018. 118
- [204] M. Scardigli, C. Crocini, C. Ferrantini, T. Gabbrielli, L. Silvestri, R. Coppini, C. Tesi, E. A. Rog-Zielinska, P. Kohl, E. Cerbai, C. Poggesi, F. S. Pavone, and L. Sacconi. Quantitative assessment of passive electrical properties of the

cardiac T-tubular system by FRAP microscopy. *Proceedings of the National Academy of Sciences*, **114**, 5737–5742, 2017.

- [205] M. Scardigli, C. Crocini, C. Ferrantini, T. Gabbrielli, L. Silvestri, R. Coppini, C. Tesi, E. A. Rog-Zielinska, P. Kohl, E. Cerbai, C. Poggesi, F. S. Pavone, and L. Sacconi. Reply to Entcheva: The impact of T-tubules on action potential propagation in cardiac tissue. *Proceedings of the National Academy of Sciences*, **115**, E562–E563, 2018.
- [206] N. Corrias, T. Gabbrielli, P. D. Natale, L. Consolino, and F. Cappelli. Analog FM free-space optical communication based on a mid-infrared quantum cascade laser frequency comb. *Optics Express*, **30**, 10217–10228, 2022.
- [207] T. Gabbrielli, F. Cappelli, N. Bruno, N. Corrias, S. Borri, P. De Natale, and A. Zavatta, Mid-infrared balanced detector for quantum light characterization. in *Quantum 2.0.*, QTh7B–5, Optical Society of America, 2020.
- [208] N. Bruno, T. Gabbrielli, F. Cappelli, N. Corrias, I. Mastroserio, P. Lombardi, F. Cataliotti, P. De Natale, and A. Zavatta, Multiplatform study of four wave mixing for quantum frequency comb generation. in *Frontiers in Optics / Laser Science.*, JW6A–29, Optical Society of America, 2020.
- [209] T. Gabbrielli, F. Cappelli, N. Bruno, N. Corrias, S. Borri, P. D. Natale, and A. Zavatta, Mid-infrared balanced detector for characterization of quantum light. in *OSA Optical Sensors and Sensing Congress 2021.*, SW5F.7, Optica Publishing Group, 2021.
- [210] T. Gabbrielli, N. Bruno, N. Corrias, S. Borri, L. Consolino, M. Bertrand, M. Shahmohammadi, M. Franckić, M. Beck, J. Faist, A. Zavatta, P. D. Natale, and F. Cappelli, Intensity correlation in harmonic comb emitted by quantum cascade laser. in *Optica Advanced Photonics Congress 2022.*, NpTu4F.2, Optica Publishing Group, 2022.
- [211] N. Corrias, T. Gabbrielli, P. D. Natale, L. Consolino, and F. Cappelli, Free-space optical communication with a quantum cascade laser frequency comb. in *Optica Advanced Photonics Congress 2022.*, NeTu4D.2, Optica Publishing Group, 2022.
- [212] M. Melalkia, T. Gabbrielli, A. Petitjean, A. Zavatta, L. Brunel, S. Tanzilli, J. Etesse, and V. D. Auria, Guided-wave solutions for non-classical state production. in *Quantum Technologies 2022.*, vol. 12133, 1213303, International Society for Optics and Photonics, SPIE, 2022.

List of Figures

I.1	Absorption coefficient of air gas mixture	12
I.2	Picture of a QCL fabricated at ETH Zürich taken using a mobile phone and a microscope.	13
1.1	Photon-number Poisson distribution characterizing a coherent state. . .	25
1.2	Representation of the quadrature operator's mean value and uncertainty for the squeezed vacuum state in the XY -quadrature phase space. . . .	27
1.3	Envelope of the noise band of the electric field for a vacuum squeezed state.	28
1.4	Schematic representation of an ideal beam splitter.	30
1.5	Phase-matching curves	34
1.6	Power spectra of pure amplitude and phase quadratures for different values of the squeezing parameter for a sideband-sideband photon number difference measurement.	39
1.7	Representation of a real detector with quantum efficiency $\eta < 1$	43
1.8	Homodyne detection scheme.	44
2.1	Energetic level of a quantum well.	50
2.2	QCL structure	52
2.3	QCLs band structure and cascade process	52
2.4	Band curvature of a standard semiconductor laser and of a QCL. . . .	55
2.5	Frequency noise spectrum of a MIR QCL	55
2.6	FWM process in Fabri-Pérot QCL and typical comb emission.	57
3.1	Scheme for a real balanced detector with losses.	62
3.2	Sketch of the implemented BHD.	65
3.3	Responsivity of the photovoltaic detectors used in the implemented BHD. .	66
3.4	INPSD retrieved via the FFT analysis done with the photocurrent outputs signals of the BHD and measurement of its CMRR in the frequency domain.	69
3.5	INPSD of the difference of the AC output signals as a function of the incident radiation power impinging onto the BHD.	70

3.6	MIR BHD FFT spectral response in terms of clearance.	72
4.1	FTIR setup used to measure the spectral emission of QCLs.	75
4.2	Typical emission of multimodal MIR QCLs at different values of driving current.	75
4.3	Harmonic comb and bilobed emission in multimodal QCLs	76
4.4	QCL's three-mode harmonic comb emission and experimental setup used to characterize its intensity correlation.	79
4.5	INPSD of a single sideband in a three-mode harmonic state, and INPSD of each mode compared with the one of the whole unsplit signal. . . .	84
4.6	RIN of each individual mode of the three-mode emission for two different values of the single sideband power	85
4.7	INPSD analysis of the sideband-sideband correlation and sideband-pump anti-correlation of a three-mode harmonic comb.	87
4.8	CMRR between sum and difference in the measurements of sideband-pump correlation and sideband-sideband correlation vs the power of the single sideband in case of a three-mode harmonic comb emission. . . .	89
4.9	INPSD comparison among individual modes and whole unsplit signal in case of three-mode harmonic comb emission.	90
4.10	LIV curve of "bilobed" QCL.	93
4.11	Spectral emission of the bilobed QCL.	93
4.12	Intermodal beat note, spectrum, and INPSDs of the MIR bilobed QCL. . . .	94
4.13	RIN vs driving current of a QCL showing bilobed emission.	95
4.14	INPSD of the single lobe composing the QCL bilobed emission.	96
4.15	INPSD analysis of the lobe-lobe correlation in a bilobed emission by a MIR QCL.	98
5.1	Wigner function of a Schrödinger's kitten state.	104
5.2	Experimental setup assemble for the kitten state generation and detection. . . .	107
5.3	Spectrum of the PPLN/RW.	109
5.4	Cavity locking setup used in the kitten state experiment.	110
5.5	Reflection signal from the cavity used in the kitten state experiment	111
5.6	Kitten state experiment: squeezed variance dependence of measuring time and on LO phase.	113
5.7	Temporal mode used to extract the kitten state quadrature from the raw homodyne data.	114
5.8	Wigner function retrieved in the kitten state experiments vs the Wigner function obtained by correcting for the detection efficiency.	115
A.1	FTIR optical spectrum analyzer and beat note setup	123

Curriculum vitæ & Publications list

Place and date of birth Figline Valdarno (FI) – May 25, 1993
Email addresses gabbrielli@lens.unifi.it
tecla.gabbrielli@ino.cnr.it
ORCID <https://orcid.org/0000-0001-5767-3036>

Work experience

Research in Physics
non-linear e non-classical optics

November 1, 2019 – today

- PHD STUDENT OF THE INTERNATIONAL DOCTORATE IN ATOMIC AND MOLECULAR PHOTONICS

Institute: University of Florence c/o LENS - European Laboratory for Non-Linear Spectroscopy, Via Nello Carrara 1, 50019 Sesto Fiorentino (FI) - Italy.

Thesis title & supervisor: "Chip-scale quantum light emitters" – Dr. Alessandro Zavatta

Main goal: Probing non-classicality/quantum correlations in quantum cascade laser comb emission

October 1, 2021 – March 31, 2022 (~ five months)

- GUEST PHD STUDENT - RESEARCH PERIOD ABROAD

Institute: Institut de Physique de Nice Université Côte d'Azur et CNRS Avenue Joseph Vallot, 06108 Nizza (Francia).

Project title & supervisors: "Chip-based squeezing at telecom wavelengths." – Dr. Alessandro Zavatta & Dr. Virginia D'Auria

Main goal: Implementation of a chip-based squeezing experiment, exploiting the combination of integrated optics and telecom technology ; generation of cat states

October 2016 – October 2019

- MASTER IN PHYSICS CURRICULUM PHYSICS OF MATTER (110/110 cum laude)

Institute: University of Florence (Italy)

Thesis title & supervisor: “Mid-infrared homodyne detector for quantum light characterization” – Dr. Alessandro Zavatta.

October 2012 – April 2016

- BACHELOR DEGREE IN PHYSICS (110/110 cum laude)

Institute: University of Florence (Italy)

Thesis title & supervisor: “Probing the diffusion in the tubular system of cardiac cells by FRAP microscopy” / Prof. Francesco Saverio Pavone & Dr. Leonardo Sacconi.

Publications List

Peer-reviewed articles

1. M. Scardigli, C. Crocini, C. Ferrantini, T. Gabbrielli, L. Silvestri, R. Coppini, C. Tesi, E. A. Rog-Zielinska, P. Kohl, E. Cerbai, C. Poggese, F. S. Pavone, and L. Sacconi. Quantitative assessment of passive electrical properties of the cardiac T-tubular system by FRAP microscopy. *Proceedings of the National Academy of Sciences*, **114**, 5737–5742, 2017
2. M. Scardigli, C. Crocini, C. Ferrantini, T. Gabbrielli, L. Silvestri, R. Coppini, C. Tesi, E. A. Rog-Zielinska, P. Kohl, E. Cerbai, C. Poggese, F. S. Pavone, and L. Sacconi. Reply to Entcheva: The impact of T-tubules on action potential propagation in cardiac tissue. *Proceedings of the National Academy of Sciences*, **115**, E562–E563, 2018
3. T. Gabbrielli, F. Cappelli, N. Bruno, N. Corrias, S. Borri, P. De Natale, and A. Zavatta. Mid-infrared homodyne balanced detector for quantum light characterization. *Optics Express*, **29**, 14536–14547, 2021
4. N. Corrias, T. Gabbrielli, P. D. Natale, L. Consolino, and F. Cappelli. Analog FM free-space optical communication based on a mid-infrared quantum cascade laser frequency comb. *Optics Express*, **30**, 10217–10228, 2022
5. T. Gabbrielli, N. Bruno, N. Corrias, S. Borri, L. Consolino, M. Bertrand, M. Shahmohammadi, M. Franckić, M. Beck, J. Faist, A. Zavatta, F. Cappelli, and P. De Natale. Intensity correlations in quantum cascade laser harmonic frequency combs. *Advanced Photonics Research*, **3**, 2200162, 2022
6. M. Seminara, T. Gabbrielli, N. Corrias, S. Borri, L. Consolino, M. Meucci, P. D. Natale, F. Cappelli, and J. Catani. Characterization of noise regimes in mid-IR free-space optical communication based on quantum cascade lasers. *Optics Express*, **30**, 44640–44656, 2022

7. M. F. Melalkia, T. Gabbrielli, A. Petitjean, L. Brunel, A. Zavatta, S. Tanzilli, J. Etesse, and V. D'Auria. Plug-and-play generation of non-gaussian states of light at a telecom wavelength. *Optics Express*, **30**, 45195–45201, 2022

Conference proceedings

8. T. Gabbrielli, F. Cappelli, N. Bruno, N. Corrias, S. Borri, P. De Natale, and A. Zavatta, Mid-infrared balanced detector for quantum light characterization. in *Quantum 2.0.*, QTh7B–5, Optical Society of America, 2020
9. N. Bruno, T. Gabbrielli, F. Cappelli, N. Corrias, I. Mastroserio, P. Lombardi, F. Cataliotti, P. De Natale, and A. Zavatta, Multiplatform study of four wave mixing for quantum frequency comb generation. in *Frontiers in Optics / Laser Science.*, JW6A–29, Optical Society of America, 2020
10. T. Gabbrielli, F. Cappelli, N. Bruno, N. Corrias, S. Borri, P. D. Natale, and A. Zavatta, Mid-infrared balanced detector for characterization of quantum light. in *OSA Optical Sensors and Sensing Congress 2021.*, SW5F.7, Optica Publishing Group, 2021
11. T. Gabbrielli, N. Bruno, N. Corrias, S. Borri, L. Consolino, M. Bertrand, M. Shahmohammadi, M. Franckić, M. Beck, J. Faist, A. Zavatta, P. D. Natale, and F. Cappelli, Intensity correlation in harmonic comb emitted by quantum cascade laser. in *Optica Advanced Photonics Congress 2022.*, NpTu4F.2, Optica Publishing Group, 2022
12. N. Corrias, T. Gabbrielli, P. D. Natale, L. Consolino, and F. Cappelli, Free-space optical communication with a quantum cascade laser frequency comb. in *Optica Advanced Photonics Congress 2022.*, NeTu4D.2, Optica Publishing Group, 2022
13. M. Melalkia, T. Gabbrielli, A. Petitjean, A. Zavatta, L. Brunel, S. Tanzilli, J. Etesse, and V. D. Auria, Guided-wave solutions for non-classical state production. in *Quantum Technologies 2022.*, vol. 12133, 1213303, International Society for Optics and Photonics, SPIE, 2022

International conferences and symposia (oral or poster)

CONFERENCE (YEAR)	PLACE	CONTRIBUTE NAME & TYPE
QTech2020 (2020)	Online	<i>Mid-Infrared balanced detector for quantum light characterization</i> Poster
OSA Quantum 2.0 Conference (2020)	Online	<i>Mid-Infrared Balanced Detector for Quantum Light Characterization</i> Poster

Curriculum vitae & Publications list

IQCLSW (2020) (2020)	Online	<i>Shot-Noise limited Mid-Infrared balanced detector</i> Poster
OSA Optical Sensors and Sensing Congress 2021 (2021)	Online	<i>Mid-infrared balanced detector for characterization of quantum light</i> Oral presentation
Perspectives on Quantum Simulation and Technologies - The Qombs Project Final Workshop (2022)	Firenze - Italy	<i>Towards the detection of quantum correlation in MIR QCL-combs emission</i> Oral presentation
OSA Advanced Photonics Congress 2022 (2022)	Maastricht - Netherlands	<i>Intensity correlation in harmonic comb emitted by quantum cascade laser</i> Oral presentation – <i>Free-space optical communication with a quantum cascade laser frequency comb</i> Oral presentation